Universidade do Vale do Paraiba
Instituto de Pesquisa e Desenvolvimento
Programa de Pós-graduação em Física e Astronomia

EBENEZER AGYEI-YEBOAH

MULTI-INSTRUMENT STUDY OF VARIOUS ASPECTS OF EQUATORIAL IONOSPHERIC IRREGULARITIES OVER AMERICAN AND AFRICAN SECTORS

São Jose dos Campos, SP
2022

EBENEZER AGYEI-YEBOAH

MULTI-INSTRUMENT STUDY OF VARIOUS ASPECTS OF EQUATORIAL IONOSPHERIC IRREGULARITIES OVER AMERICAN AND AFRICAN SECTORS.

Doctoral thesis submitted to the Post-graduate program in Physics and Astronomy in partial fulfilment of the requirements for the degree of Doctor of Philosophy in Space Physics.
Orientador: Prof. Dr. Paulo Roberto Fagundes
Co-orientador: Prof. Dr Alexandre Tardelli.

São Jose dos Campos, SP
2022

TERMO DE AUTORIZAÇÃO DE DIVULGAÇÃO DA OBRA

Ficha catalográfica

Agyei-Yeboah, Ebenezer
Multi-Instrument Study Of Various Aspects Of Equatorial Ionospheric Irregularities Over American And African Sectors / Ebenezer Agyei-Yeboah; orientador, Paulo Roberto Fagundes; co-orientador Alexandre Tardelli. - São José dos Campos, SP, 2022.
1 CD-ROM, 177 p.

Tese (Doutorado) - Universidade do Vale do Paraíba, São José dos Campos. Programa de Pós-Graduação em Física e Astronomia.

Inclui referências

1. Física e Astronomia. 2. Ionospheric irregularities. 3. Plasma bubbles. 4. Equatorial Spread-F. 5. Plasma blobs. I. Fagundes, Paulo Roberto, orient. II. Tardelli, Alexandre, co-orient. III. Universidade do Vale do Paraíba. Programa de Pós-Graduação em Física e Astronomia. IV. Título.

Eu, Ebenezer Agyei-Yeboah, autor(a) da obra acima referenciada:

Autorizo a divulgação total ou parcial da obra impressa, digital ou fixada em outro tipo de mídia, bem como, a sua reprodução total ou parcial, devendo o usuário da reprodução atribuir os créditos ao autor da obra, citando a fonte.

Declaro, para todos os fins e efeitos de direito, que o Trabalho foi elaborado respeitando os princípios da moral e da ética e não violou qualquer direito de propriedade intelectual sob pena de responder civil, criminal, ética e profissionalmente por meus atos.

São José dos Campos, 9 de Novembro de 2022.

Autor(a) da Obra

Data da defesa: 19 / 08 / 2022

UniVap
Universidade do Vale do Paraíba

P&D
Instituto de Pesquisa
e Desenvolvimento

EBENEZER AGYEI-YEBOAH

"MULTI-INSTRUMENT STUDY OF VARIOUS ASPECTS OF EQUATORIAL IONOSPHERIC IRREGULARITIES OVER AMERICAN AND AFRICAN SECTORS."

Tese aprovada como requisito parcial à obtenção do grau de Doutor, do Programa de Pós-Graduação em Física e Astronomia, do Instituto de Pesquisa e Desenvolvimento da Universidade do Vale do Paraíba – Univap, pela seguinte banca examinadora:

Prof. Dr. Valdir Gil Pillat	Valdir Gil Pillat
Prof. Dr. Paulo Roberto Fagundes	Paulo Roberto Fagundes
Prof. Dr. Alexandre Tardelli	Alexandre Tardelli
Prof. Dr. Arian Ojeda González	Arian Ojeda González
Prof. Dr. Igo Paulino	Igo Paulino
Prof.ª Dr.ª Inez Staciarini Batista	Inez Staciarini Batista

Prof.ª Dr.ª Lúcia Vieira
Diretora do IP&D – Univap
São José dos Campos, 02 de agosto 2022.

Av. Shishima Hifumi, 2911 - 12244-000
São José dos Campos – SP
www.univap.br

This thesis is dedicated to my late father Mr. J.K. Agyei, who inspired me to pursue my dreams, my mother Mrs. Comfort Kyeraa Agyei, my love Débora Maria dos Santos Agyei-Yeboah, and my son Nana Kwadwo Agyei-Yeboah

ACKNOWLEDGEMENTS

First and most importantly, I would like to thank God for the wisdom and strength to persist through this arduous academic journey and for bringing me to the conclusion of this defining point in my life. A special appreciation goes to my advisors Prof. Dr. Paulo Roberto Fagundes and Prof. Dr. Alexandre Tardelli for their guidance, patience, and support from the start of my Ph.D. studies - through the preparation and organization of this work to the thesis. They have constantly and consistently steered my efforts in the right direction with feedback, guidance, and encouragement in the gradual development of the work.

I would like to thank all the lecturers at the Laboratory of Physics and Astronomy especially Prof. Dr. Valdir Pillat and Prof. Arian Ojeda Gonzalez for all their diverse support. I also thank my colleagues at the lab.

My gratitude also goes to the thesis and defense board for their valuable input in the thesis.

I am also grateful to the Coordenação de Aperfeiçoamento de Pessoal de Nível Superior" (CAPES) for the financial support and to the leadership of the Post-Graduate Program in Physics and Astronomy at the Institute of Research and Development (IP&D) of University of Paraiba Valley (UNUVAP)

Special thanks go to my late father Mr. I.K. Agyei and my mother, Mrs. Comfort Kyeraa Agyei for always being there through prayers and unwavering support throughout the years. And to all my siblings - Vida Appiah-Agyei (late), Mercy Akrasi-Agyei, Samuel Kwasi Agyei, Frank Kwadwo Agyei, Richard Ofori-Agyei, Emmanuel Agyei-Mensah (late), Gifty Afua Faakyewa, Christiana Attaa Serwaa, and Christopher Atta Osei and my entire family.

Immense gratitude as always to my Debora for her patience, support and constantly listening to me rant and talk things out all these years through graduate school.

Ebenezer Agyei-Yeboah

ABSTRACT

This thesis is devoted to the study of ionospheric irregularities observed over Brazil and Africa using different instruments and observational techniques. First, the occurrence of ionospheric irregularities like plasma bubbles, blobs, and Spread-F (typical and atypical have been investigated using all-sky imaging systems and ionosondes located at Araguatins, Jataí, and São José dos Campos. Afterward, GPS-TEC data from 33 receiver stations located in different parts of Brazil and Africa were used in the investigation of ROT (rate of TEC change) phase fluctuations during the Antarctic Sudden Stratospheric Warming (SSW). Electron density measurements from the Swarm constellation have also been employed to aid in the analysis and discussion of some of the results obtained from ionosonde and ASI. The thesis focuses on two main studies. One study was dedicated to exploring the observation of the simultaneous occurrence of ionospheric plasma bubbles and blobs using an all-sky imaging system and the observation of atypical Spread-F on ionograms. Based on these observations, a novel methodology is proposed for the observation and studies of ionospheric plasma blobs using ionosondes. The proposed methodology employed a colocated all-sky imager and ionosonde at Araguatins to observe simultaneously occurring plasma bubbles and blobs and then the corresponding ionograms were analyzed. The characteristics of the echoes on the ionograms were compared with the observations from the OI 630 nm nightglow images from the all-sky imager for when there were no irregularities and when bubbles and/or blobs were present. The results showed that in the presence of bubbles and blobs, Spread-Fs with high-frequency echoes were drawn on the ionograms at almost the same time as the images were taken. The results also showed that the generation of plasma blobs could be influenced by the development of bubbles and that the equatorial ionization anomaly may play a major role in their development. The other focus of the thesis is the study of the effects of the 2019 minor Antarctic SSW event on the generation/suppression of ionospheric irregularities. The critical frequency obtained from the three ionosonde stations at Araguatins, Jataí, and São José dos Campos was used to monitor the ionospheric irregularities during the different phases of the SSW event. Spread-F (Brazil) and ROT phase fluctuations (Brazil, Africa) occurrence at different latitudes during different phases of the event were analyzed. Irregularity occurrence from a similar period in 2018 when no SSW event was recorded in the Antarctic region was also analyzed. The results showed a general decrease in occurrence rates during the peak phase of the event compared to the other phases in 2019. The results also showed a decrease in occurrence rate from the peak phase in 2018 (no SSW) to the peak phase in 2019 (SSW).

Keywords: ionospheric irregularities; plasma bubbles; plasma blobs; equatorial Spread-F; sudden stratospheric warming; ROT.

ESTUDO MULTI-INSTRUMENTOS DE DIVERSOS ASPECTOS DAS IRREGULARIDADES IONOSFÉRICAS EQUATORIAIS NOS SETORES AMERICANO E AFRICANO

RESUMO

Esta tese é dedicada ao estudo de irregularidades ionosféricas observadas no Brasil e na África utilizando diferentes instrumentos e técnicas observacionais. Inicialmente, a ocorrência de irregularidades ionosféricas como blobs e bolhas de plasma, e spread-F (típico e atípico) foram investigadas utilizando sistema de imageador All-sky e ionosondas localizados em Araguatins, Jataí e São José dos Campos. Depois, foram utilizados dados de GPS-TEC de 33 estações receptoras localizadas no Brasil e da África com a finalidade de investigar flutuações de fase ROT durante o aquecimento estratosférico súbito (em inglês: sudden stratospheric warming-SSW) na Antártida. Medidas de densidade eletrônica da constelação de Swarm também foram utilizadas para auxiliar na análise e discussão de alguns dos resultados obtidos da ionosonda e do imageador. A tese se concentra em dois estudos principais. O estudo foi dedicado a explorar a observação da ocorrência simultânea de blobs e bolhas de plasma ionosféricas usando um imageador all-sky e a observação de spread-F atípico em ionogramas. Baseado nessas observações, uma nova metodologia é proposta para a observação e estudos de blobs ionosféricos usando ionosondas. A metodologia proposta utiliza um imageador e ionosonda em Araguatins para observar simultaneamente bolhas e blobs de plasma e, em seguida, foram analisadas as ionogramas correspondentes. As características dos ecos nos ionogramas foram comparadas com as observações das imagens noturnas de OI 630 nm do imageador all-sky para períodos quando não houve irregularidades e quando bolhas e/ou blobs estavam presentes. Os resultados mostraram que, na presença de bolhas e blobs, spread-Fs com ecos de alta frequência foram observados nos ionogramas quase ao mesmo tempo em que as imagens foram adquiridas. Os resultados também mostraram que a geração de bolhas de plasma pode ser influenciada pelo desenvolvimento de blobs e que a anomalia de ionização equatorial pode desempenhar um papel importante em seu desenvolvimento. O outro foco da tese é o estudo dos efeitos do evento menor SSW antártico de 2019 sobre a geração/inibição de irregularidades ionosféricas. A frequência crítica obtida nas três estações de ionosonda em Araguatins, Jataí e São José dos Campos foi utilizada para monitorar as irregularidades ionosféricas durante as diferentes fases do evento SSW. Foram analisadas flutuações de fase spread-F (Brasil) e ROT (Brasil, África) em diferentes latitudes durante diferentes fases do evento. Também foi analisada ocorrência de irregularidade em um período semelhante em 2018, quando também não foi registrada nenhuma ocorrência de SSW na região Antárctica. Os resultados mostraram uma queda geral nas taxas de ocorrência durante a fase de pico do evento em relação às outras fases em 2019. Os resultados também mostraram queda na taxa de ocorrência da fase de pico em 2018 (sem SSW) para a fase de pico em 2019 (SSW).

Palavras-chaves: irregularidades ionosféricas; bolhas de plasma; blobs de plasma; spread-F equatorial;aquecimento estratosférico repentino; ROT.

LIST OF FIGURES

Pages

LIST OF TABLES

Pages

LIST OF ABBREVIATIONS AND ACRONYMS

ASI:	all-sky imager
BDS	BeiDou Navigation System
BG:	background
CADI:	Canadian Advanced Digital Ionosonde
CCD:	charged-coupled device
Dst:	Disturbance storm time
EEJ:	equatorial electrojet
EGNOS	European Geostationary Navigation Overlay Service
EIA:	equatorial ionization anomaly
EPB:	Equatorial plasma bubble
ESA:	European Space Agency
ESF:	Equatorial Spread
EUV:	Extreme UV
foF2	critical frequency
FOV:	field of view
FWHM:	full-width at half-maximum
GAGAN	GPS Aided Geo Augmented Navigation
GLONASS	Global’naya Navigazionnaya Sputnikovaya Sistema
GNNS	Global Navigation Satellite System
GPS:	global positioning system
GW:	gravity wave
h’f:	virtual height
HF:	high frequency
hpF2:	F-Layer peak height
HSA:	high solar activity
IBGE	Rede Brasileira de Monitoramento Contínuo
INPE:	Instituto Nacional de Pesquisas Espaciais
IP&D:	Instituto de Pesquisa e Desenvolvimento
IPP	ionospheric piercing point
LCU:	liquid circulation unit
LSA:	low solar activity

LT	Local time
MSA:	medium solar activity
MSAS	Multi-functional Satellite Augmentation System
MSTID:	medium-scale traveling ionospheric disturbance
PRE:	Pre-Reversal enhancement
PW:	planetary wave
QZSS	Quasi-Zenith Satellite System
RF:	radio frequency
ROT	Rate of TEC change
RTI:	Rayleigh-Taylor instability
SBAS	Satellite-Based Augmented Systems
SSW:	sudden stratospheric warming
STEC	slant TEC
TEC:	total electron content
TID:	traveling ionospheric disturbances
UASDA:	UNIVAP All-Sky Data Analysis
UDIDA:	UNIVAP Digital Ionosonde Data Analysis
UNIVAP:	Universidade do Vale do Paraíba
UT:	universal time
UV:	ultraviolet
VHF	very high frequency
vTEC	vertical TEC
WAAS	Wide Area Augmentation System

LIST OF SYMBOLS

$\vec{E}$	Electric field vector
$\vec{B}$	Magnetic field vector
q	Ion-electron pair production rate
h	height
χ	zenith angle
I_∞	unattenuated flux at the top of the atmosphere
τ	optical depth
n	neutral gas concentration
η	ionizing efficiency
σ	absorption cross-section
P	Production rate
L	Loss rate
N	Electron density
V	Plasma drift
t	time
M	Mass of ion
g	Acceleration due to gravity
B	Magnetic field
v_i	Drift velocity
e	Electron
J	Current density
γ_{RT}	Rayleigh-Taylor instability growth rate

L	Plasma density scale length
v_{in}	Ion-neutral collision frequency
Δt	Time of flight
c	Speed of light
N_e	Plasma density/flux tube electron content
f_p	Plasma frequency
f	Transmitted radio wave frequency/ GPS signal frequency
V_p	Upward plasma drift
K^F	F region flux tube electron content height gradient
$\sum_p^{F,E}$	flux tube integrated F and E region Pedersen conductivities
R_T	flux tube integrated recombination
E_z	upward electric field
δE	electric field due to polarization
v_{eff}	flux tube integrated effective ion-neutral collision frequency
U_L^P	vertical component of neutral wind velocity perpendicular to the magnetic field
$J_{\theta\phi}$	zonal westward Hall current
E_θ	electric field in polar coordinates
E_ϕ	zonal eastward electric field
$J_{\phi\phi}$	Pederson current
m_e	mass of electron
ε_o	the permittivity of free space
Φ	GPS signal phase
P	GPS signa pseudorange

I	Ionospheric delay
z	Zenith angle of a GPS satellite
R_E	Earth radius
h_m	height of peak plasma density

CONTENT

Pages

1 INTRODUCTION

1.1 Introduction

The ionosphere is the ionized part of the Earth's atmosphere comprising of free electrons and positive ions which are generally in equal numbers in an electrically neutral medium (HUNSUCKER; HARGREAVES, 2003; KELLEY, 2009) and strongly affected by neutral winds and electric fields. The ionosphere has a smooth profile during the daytime (BALAN; LIU; LE, 2018). During daytime when the E-region conductivity is strong, ionospheric drivers such as neutral winds and electric fields and their fluctuations do not control the generation of irregularities in the ionosphere, however, after sunset, the weakening E-region conductivity leaves the ionosphere susceptible to plasma irregularities of several scale sizes induced by ionospheric drivers (BALAN; LIU; LE, 2018; BOOKER; WELLS, 1938). These irregularities are observed on ionograms as Spread-F, plasma bubbles in optical images, plumes on radars, etc. and their sizes range from a few centimeters to several hundreds of kilometers. The ionosphere and the irregularities therein are of great scientific interest, as an irregular ionosphere affects radio waves that pass through them by sporadically modifying the phase and amplitudes of these waves thereby leading to what is known as scintillations. The existence of strong scintillations or irregularities in the ionosphere affects the accuracy of communication and navigation signals, which have become a major part of our technology and way of life.

Large-scale ionospheric plasma irregularities or equatorial plasma bubbles originate and occur through the collisional Rayleigh-Taylor instability (RTI) mechanism around equatorial and low-latitude regions where the geomagnetic field lines are almost horizontal. Just before sunset, through the pre-reversal enhancement (PRE), the $\vec{E} \times \vec{B}$ vertical plasma drift causes the F-region ionosphere to rise rapidly to higher altitudes where collision is low and the growth rate of the RTI is high. To better understand the dynamics and variability of ionospheric irregularities for the development of predictive techniques, different instruments, and observational techniques have been developed and used to study their occurrences and processes that lead to their generation and morphology.

Majority of ionospheric variability has been attributed to processes above like solar wind, and geomagnetic storms known as main drivers. According to Rishbeth, Mendillo (2001), and Zhao *et al*. (2008) about 20-33 % of ionospheric variability is not accounted for by the main drivers and this is even higher in the equatorial and low-latitude regions. On the other hand, it has been observed and reported that processes that occur in the lower atmosphere also contribute significantly to ionospheric variations and dynamics. In the low latitudes, ionospheric variability depends not only on lower atmospheric processes but also on atmospheric processes originating from higher latitudes like sudden stratospheric warming (SSW) (YADAV *et al*., 2017). The effect of SSWs on the equatorial and low-latitude ionosphere and their influence on the occurrence of ionospheric irregularities have been studied extensively over the years albeit from the Arctic region. The results from these studies have shown that there is a relationship between SSW events, ionospheric variations, and irregularities.

Plasma blobs, another type of equatorial ionospheric irregularities, are regions in the ionosphere with enhanced plasma density. Plasma bubbles and blobs have been observed in all-sky imaging systems and with satellites (HUANG *et al*., 2014; MCNAMARA *et al*., 2013; MILOCH *et al*., 2018; OYA; TAKAHASHI; WATANABE, 1986; PARK *et al*., 2003; PIMENTA *et al*., 2004; ZAKHARENKOVA; ASTAFYEVA; CHERNIAK, 2016). A few recent reports have shown that they can be observed using ionosondes. It also turns out that these blobs, like their bubble counterparts, could also contain small-sized irregularities that produce spread on ionograms (MCNAMARA *et al*., 2013; NARAYANAN *et al*., 2014; PIMENTA *et al*., 2004; 2007; WANG *et al*., 2019). There is evidence that the generation of plasma blobs could be related to the occurrence of plasma bubbles with observations of plasma bubbles together with blobs being reported (KIL *et al*., 2019; PARK *et al*., 2003; PIMENTA *et al*., 2004; TARDELLI-COELHO *et al*., 2017). Since the first observations of blobs by Oya, Takahashi and Watanabe (1986), Watanabe and Oya (1986), and various authors have studied the occurrence of plasma blobs either independently or accompanied by plasma bubbles using satellite, radar, or optical techniques (KIL *et al*., 2011; 2019; PARK *et al*., 2003; PIMENTA *et al*., 2004, 2007; TARDELLI-COELHO *et al*., 2017; WANG *et al*., 2019).

1.2 Aims and Objectives

Plasma bubbles, Spread F, and recently Plasma blobs have been studied in the equatorial and low latitude regions at different longitude sectors. These studies have focused on observation, methodology for ionospheric irregularities, the source of these irregularities, and their generation processes, leading to a better understanding of their variability. Long-term studies and the development of different methods of investigation of ionospheric irregularities are very essential aspects in the quest to better understand them. Better prediction models require long-term observational data. New methodologies are developed with the expectation that they overcome the observation limitations of their predecessors and improve upon them in the quest to determine the ionospheric drivers (sources) and their influence on ionospheric variability and dynamics, and the occurrence of ionospheric irregularities.

Observation of plasma blobs using ionosondes has been reported, however, no consolidated methodology has been developed where one can use ionograms to analyze the characteristics of the trace and determine whether or not the trace contained blobs. Developing a methodology such as this requires that the observation of the blob be confirmed with one or more instruments and that these instruments and the ionosonde capture the same structures for comparison. And so, taking advantage of the ionosonde and all-sky imager located in the same region, it was possible to characterize the blob features in the ionograms with complementary observations from the Swarm constellation and propose another way to observe blobs from the ground using ionosonde that could overcome the limitations of the ground-based optical method and thus this investigation was developed.

The occurrence of large- and small-scale irregularities in the ionosphere is important owing to the disruptive impact of these on communications and navigation (e.g., GNSS) signals Ionospheric irregularities have been studied by Space researchers quite extensively. One aspect of their occurrence is the role of SSW events play in their formation and thus understanding how SSWs affect the generation of irregularities is of considerable interest. Current reports are divided on the impact of SSWs on ionosphere irregularities, as some studies suggest that SSW events suppress the generation of irregularities and others have reported an enhancement in the generation and occurrence of irregularities making SSWs' effects on ionospheric irregularities thus inconclusive. This is therefore an area that requires considerable investigation and understanding. The warming event of the Antarctic region is rare due in part to the distribution of mountains, land, and sea in the region that tends to cause the planetary waves that drive SSW events to have lower amplitudes than their Arctic counterparts. Consequently, most if not all studies were done on the influence of SSWs on the ionosphere and especially ionospheric phenomena (irregularities) are based on the Arctic SSW events under different geomagnetic and solar activity conditions. As such, the occurrence of the 2019 minor Antarctic event occurring under relatively low geomagnetic and solar activity conditions provides a rare opportunity to study and understand how the warming event of the southern hemisphere affects the ionosphere and ionospheric irregularities and how it compares with events from the north. Thus, contributing to our current understanding of the influence of (Antarctic) SSW events on the occurrence of ionospheric irregularities.

With this background, the main objectives of these investigations separated into two parts, based on the different investigations, are.

a) to propose a new methodology that uses ionosonde to observe and study plasma blob occurrence with the following specific objectives
    - observe and identify plasma bubble and blob signatures in OI 630.0 nm nightglow images.
    - observe and identify Spread-F structures associated with plasma irregularities in ionograms.
    - Compare nightglow observations and ionograms and develop a methodology to observe plasma blobs in ionograms.
    - Characterize observed Spread-F features to determine the occurrence of plasma blobs/atypical ESF

and

b) to investigate the impacts of SSW events on the occurrence of ionospheric irregularities in the Brazilian and African sectors guided by these objectives
    - Study the occurrence of Spread-F during the different phases of the 2019 minor SSW event in the Antarctic region.
    - Study the occurrence of ROT phase fluctuations during the different phases of the SSW event.
    - Comparative study of the statistical occurrence of irregularities at the different phases, sectors, and latitudes.

1.3 Thesis Organization

The thesis will contain the following chapters which will provide insights into the investigations highlighted. Chapter 2 will present the background to the Earth’s atmosphere, the ionosphere, some equatorial ionospheric dynamic processes, and ionospheric irregularities - their formation, and characteristics. Chapter 3 will provide details on the instrument and techniques used in the studies. The study on Ground- and satellite-based observations of ionospheric plasma bubbles and blobs at 5.6^{o} latitude in the Brazilian sector, including methodology, result, discussion, and conclusions are elaborated in Chapter 4. In Chapter 5, the study on the effects of the 2019 minor Antarctic sudden stratospheric warming on the occurrence of ionospheric irregularities in Brazil and Africa – data, methods, discussions, and conclusions are detailed.

2 THE EARTH’S IONOSPHERE

2.1 The Neutral Atmosphere

Surrounding the Earth is a compressible fluid that is held in place by the force of gravity and consists of a stable mixture of several gases known as the terrestrial atmosphere (SAHA, 2017). The atmosphere starts from the surface of the Earth and becomes thinner with altitude to about 10, 000 km where it blends with the interplanetary space (SAHA, 2017). About three-quarters of the mass of the atmosphere is contained within about 11 km of the surface. The lower region of the atmosphere is composed of Nitrogen (78%), Oxygen (21%), and other gases (1%). The picture in Figure 1 shows the layers of the Earth’s atmosphere(SAHA, 2017).

Figure 1: Diagrams showing the different layers of the atmosphere of the Earth.

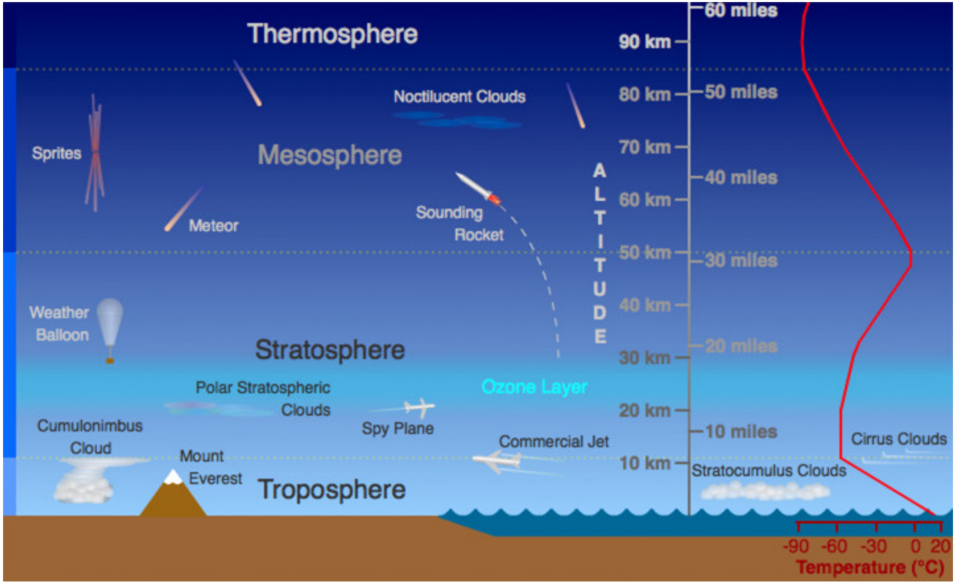

SOURCE: (“Layers of Earth’s Atmosphere | UCAR Center for Science Education,” [s.d.]).

The structure of the atmosphere is based principally on temperature, chemical composition, dynamics, and density. Based on the temperature gradient, the atmosphere is divided into four distinct regions which from the surface of the Earth: the Troposphere (up to 18 km), Stratosphere (10 km to 50 km), Mesosphere (50 km to 85 km), and thermosphere (85 km to 700 km) (BREKKE, 2013; KELLEY, 2009; SAHA, 2017). Also, the atmosphere can be divided into two main layers – the neutral atmosphere and the ionosphere – based on the ionization rate. The ionosphere, to be discussed in section 2.3, is found within the thermosphere. Figure 2 shows atmospheric temperature variation (left panel) and ionospheric plasma density variation for day and night times (right panel) with altitude.

Figure 2: Typical profiles of the neutral atmospheric temperature (left panel) and ionospheric plasma density(right panel).

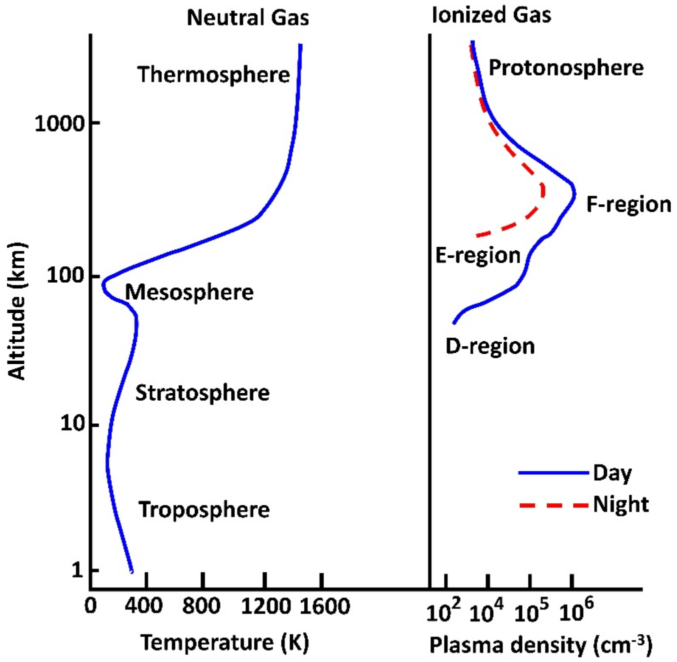

SOURCE: Adapted from KELLEY (2009).

2.2 Atmospheric layers

- ***Troposphere*** – This is the layer where a majority of the Earth's weather phenomena, like cloud formation, occur. It is the lowest of the layers in terms of altitude. Over the equator, it extends to around 18 km in altitude and decreases gradually to about 8 km at the poles. The troposphere contains almost all the water stream (~ 99 %) in the atmosphere which helps in regulating air temperature by absorbing solar energy and thermal radiation from the surface. It is made up of a mixed composition of molecular nitrogen and oxygen. It is the densest region of the atmosphere. The region is characterized by a continuous decrease in temperature with an altitude of about 7 K/km ((KELLEY, 2009). The upper part of this region is bounded by the tropopause.
- ***Stratosphere*** – This is located above the troposphere, and in this region, the temperature reverses, increasing with altitude. It extends from the tropopause to a height of up to 50 km. This region contains about 90 % of the atmosphere's ozone

with maximum ozone concentration located at about 30 km altitude. The stratospheric ozone absorbs harmful ultraviolet (UV) radiation from the Sun, preventing it from reaching the Earth's surface. This causes an increase in the temperature in this region. The stratosphere may be subdivided into two parts: the lower stratosphere with a constant temperature of ~ 217 K and the upper stratosphere above 20 km with a temperature of up to 273 K. This increase in temperature with height, limits vertical motion. During winter in the polar region, energy from the Sun is not sufficient to heat the ozone causing rapid cooling of the stratosphere. This creates a thermal imbalance between the polar stratosphere and the warm off-pole stratosphere resulting in a large pressure gradient. This pressure gradient combined with Coriolis effects creates a strong jet stream in the stratosphere directed eastward. This system known as a polar night jet contains a very strong polar vortex. The strength of the polar vortex depends on how cold the polar stratosphere is during winter. A strong polar vortex can lead to the occurrence of an ozone hole and the splitting of the polar vortex causing a rapid rise in the stratospheric temperature in a phenomenon known as sudden stratospheric warming. This phenomenon is known to potentially impact ionospheric variability and the generation of irregularities. The upper boundary of the stratosphere is the stratopause.

- ***Mesosphere*** – It is the coldest region of the atmosphere extending from 50 km to 80 km and sitting directly above the stratopause. The temperature in this region also decreases as altitude increases. Inside the mesosphere is where most meteorites that enter the Earth's atmosphere burn up. It absorbs very little solar energy and is mostly made up of molecular nitrogen and oxygen. It also contains some metals like iron and sodium from meteoric debris. The mesosphere is bounded on the upper side by the mesopause.
- ***Thermosphere*** – This region is the hottest of the four layers with temperatures almost constant with altitude. It also has a very low density. It includes the ionosphere and extends to hundreds of kilometers (~ 500 km). The temperature in this region increases due to heating by solar UV radiation.

The atmospheric layers described above are classified based on the temperature variation with altitude which is generally the most useful classification there is, however, there exist other forms of classifications based on the state of mixing, composition, or ionization. For example, the lowest part of the atmosphere is well mixed much like that at sea level save for a few minor components. This region is called the turbosphere or homosphere.

In the upper region, inside the thermosphere, the mixing is inhibited due to high temperatures, and the action of gravity on some species. As such the composition varies with altitude and this part is namely the heterosphere. Between the homosphere and the heterosphere is a boundary at about 100 km called turbopause. Above this boundary, gases separate by gaseous diffusion more rapidly than they are mixed by turbulence. Also, the regions of the heterosphere where helium or hydrogen is predominant are the heliosphere and the protonosphere, respectively (see Figure 1). The exosphere is the region above ~ 600 km where individual atoms can escape from the Earth's gravitational attraction. Earth's atmosphere can also be classified as the lower atmosphere (0-15 km), middle atmosphere (15-90 km), and upper atmosphere (above 90 km) based on the altitude (HUNSUCKER; HARGREAVES, 2002; SAHA, 2017; SHEPHERD, 2002).

2.3 The Ionosphere

The ionosphere is the ionized part of the Earth’s atmosphere comprising of free electrons and positive ions which are generally in equal numbers in an electrically neutral medium (HUNSUCKER; HARGREAVES, 2003; KELLEY, 2009) extending from about 60 km to 1000 km in altitude. The ionosphere is not a distinct layer of the atmosphere based on the temperature profile. The primary source of ionization in the low-latitude ionosphere is the photoionization of the neutral constituents by solar extreme ultraviolet radiation (EUV) and X-rays (RISHBETH; GARRIOTT, 1969) whereas ionization by energetic particles due to particle precipitation from the magnetosphere impacts the neutral atmosphere at high latitudes (KELLEY, 2009). The plasma interacts chemically with the neutral species and diffuses due to gravity and pressure gradients. The plasma is transported by neutral winds and electric fields under the influence of the Earth’s magnetic field creating altitude-dependent density profiles as shown in Figure 3. It is within the F-region (150 km - 1000 km; to be discussed later in this section) of this layer that equatorial ionospheric irregularities are observed and where the two investigations contained in this thesis were conducted.

Figure 3: Vertical profile of atmospheric species (electron, ion, and neutral).

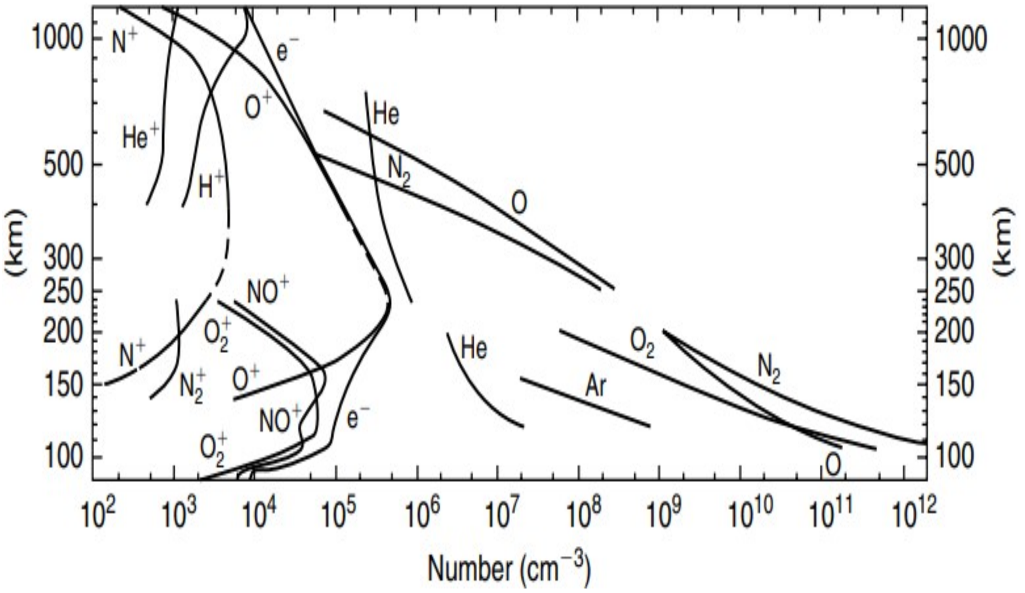

SOURCE: KELLEY (2009).

The rate at which ionization occurs depends on the density of atoms in the atmosphere and the intensity of the ultraviolet radiation - which varies with solar activity. Since the atmosphere is bombarded by UV radiation of different frequencies, several ionized layers are formed at different altitudes. Lower-frequency ultraviolet radiation penetrates the atmosphere the least; therefore, they produce ionized layers at higher altitudes. Conversely, higher frequencies penetrate deeper and produce layers at lower altitudes. An important factor in determining the density of the ionized layer is the elevation angle of the Sun, which changes continuously. For this reason, the height and thickness of the ionized layers vary, depending on the time of day and the season of the year. At the top of the atmosphere, there are very few particles and so little of the incoming ionizing radiation is absorbed at first. As the radiation penetrates further down, there is a greater density of neutral particles, and increased absorption takes place.

At a certain height, the rate at which the gas concentration increases downwards will be matched by the rate at which the strength of the radiation decreases downwards. So, at this height, the rate of production of electrons would be greatest and this level is called the peak of the ionospheric layer. The same thing indeed happens for the other species present and the appropriate wavelengths. The theory was derived in 1931 by CHAPMAN and the ideal ionospheric layer described is called the Chapman layer. The height and the rate of production of ionization of a Chapman layer are strongly influenced by solar zenith angle χ as depicted in equation 1 and shown in Figure 4.

The production rate of the ion-electron pair is given by the following expression.

$$q(h,\chi) = I_\infty \eta \sigma n(h) e^{-\tau(h,\chi)} \tag{1}$$

where $I_\infty, \tau, n(h), \eta, and\ \sigma$ are the unattenuated flux at the top of the atmosphere, optical depth, neutral gas concentration at a height h, ionizing efficiency, and absorption cross-section respectively (SCHUNK; NAGY, 2009).

Figure 4: Representation of ion production in the atmosphere as solar radiation intensity decreases with decreasing altitude and neutral density increases downward.

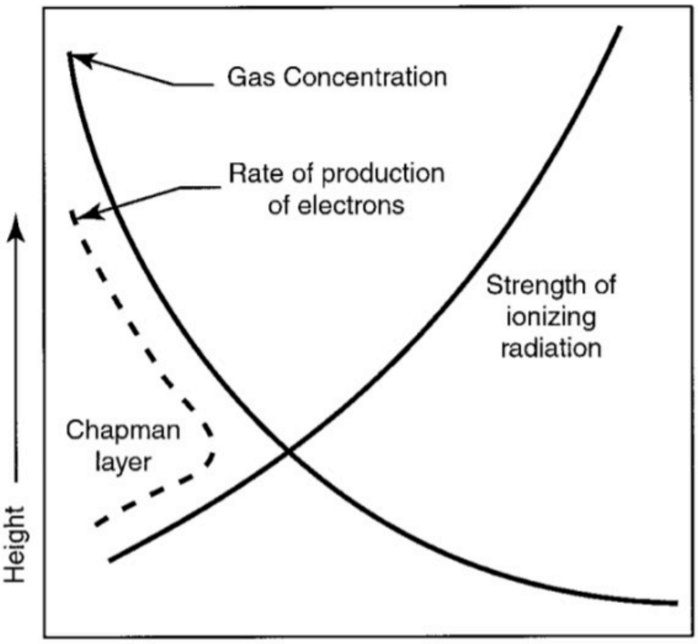

SOURCE: Adapted from BANKS; G. KOCKARTS (1973).

In addition to the production, the loss and the transport processes govern the altitude distribution of the electron densities. The important loss processes are the radiative recombination of atomic ions with electrons and the dissociative recombination of molecular ions with electrons. The charge exchange process assists in the loss of electrons at a certain altitude range. Moreover, the electron density distribution is also determined by the transport process. The plasma is transported mainly in two ways: plasma diffusion and transport owing to the presence of ambient electric field and geomagnetic field (RISHBETH, 2000). Thus, the altitude distribution of electron density depends upon the production, loss, and transport processes and can be described by the continuity equation,

$$\frac{\partial N}{\partial t} = P - L - \nabla(NV) \tag{2}$$

where, P, L, N, and V correspond to the production rate, loss rate, electron density, and drift of the plasma respectively (RISHBETH, 2000; RISHBETH; GARRIOTT, 1969).

Owing to the pervasive influence of gravity and as a result of density variations in the neutral composition and production rate, the ionosphere has vertical layer structures namely D, E, and F. The ionospheric layers are controlled by different physical and chemical processes that lead to different ion compositions. The D and E-layers are dominated by molecular ions like O_2^+, N_2^+, NO^+ (see Figure 3 and Figure 5). During post-sunset hours production rates are decreased in these layers leading to the disappearance of both layers after sunset. The dominant species in the F-region, however, are mostly atomic ions, O^+, H^+. Figure 5 shows the daytime electron distribution in the ionosphere with principal ions at the various layers and the main ionization radiations, respectively.

Figure 5: Average daytime electron distribution with principal ions in the various layers of the ionosphere and the principal ionizing sources at each layer.

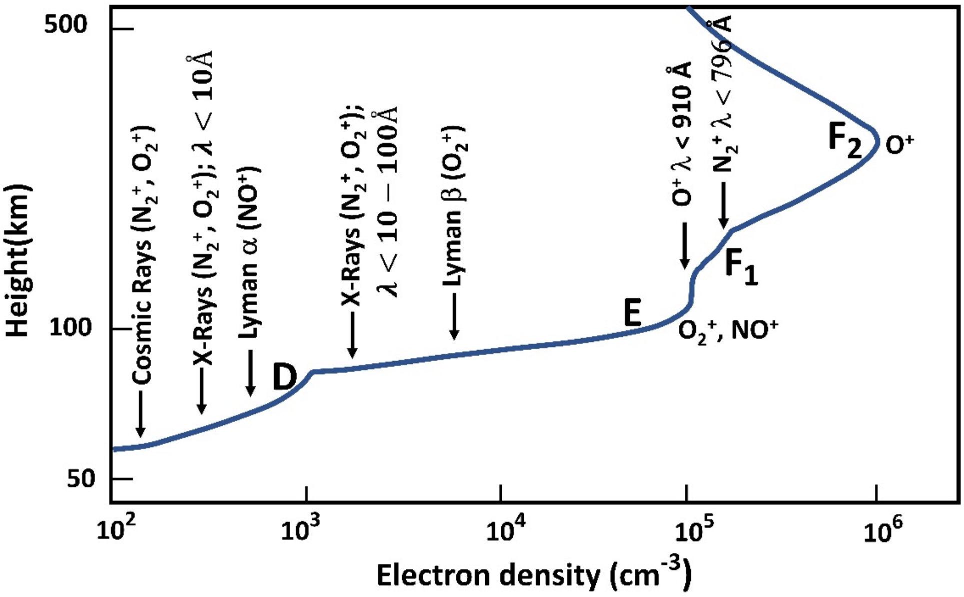

SOURCE: Adapted from BANKS; KOCKARTS (1973).

The rate of recombination in the ionosphere decreases with increasing altitude, as such the F-region does not disappear completely but part of it is maintained during nighttime hours. The plasma density in the ionosphere is maximum in the F-region. Above the F2 peak is the topside ionosphere where diffusion dominates, and the main chemical composition is H^+ and He^+. The variation in the vertical structure and density profile of the ionosphere depends on the production and loss processes which also vary with season, latitude, time of day, solar activity, etc. The vertical profile of the ionosphere for day and night during low and high solar activities is shown in Figure 6.

Figure 6: Day (continuous line) and night (dashed line) time ionospheric plasma density for solar maximum (red) and minimum (blue).

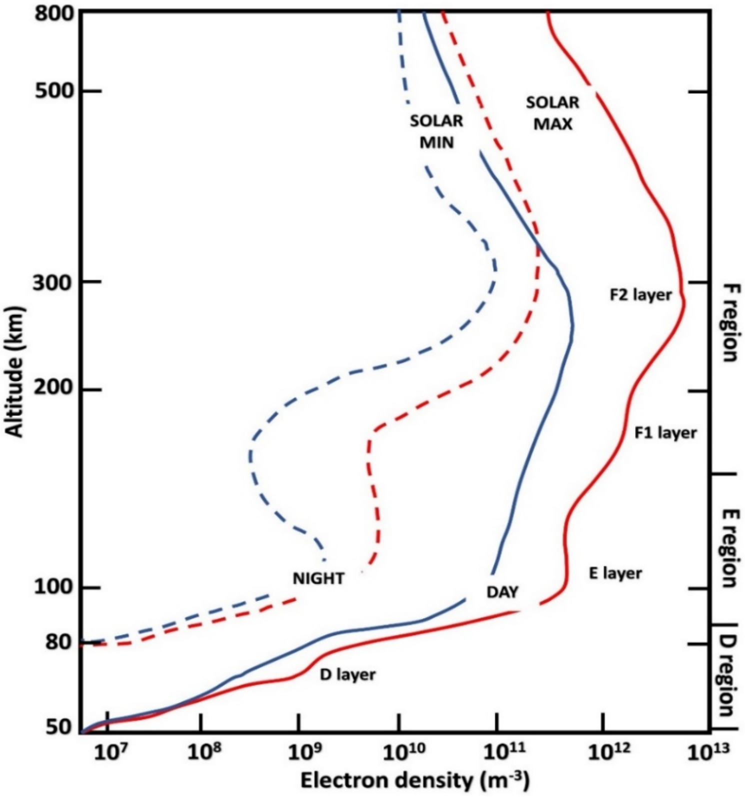

SOURCE: Adapted from GREBOWSKY; AIKIN (2008).

2.3.1 Layers of the ionosphere

- ***D-Layer*** – This layer is the lowest of the ionospheric layers located between 60-90 km altitude. It is only present during daytime hours and is controlled by the ionization of neutrals by solar x-rays, cosmic rays, and Lyman-α radiation. The layer is characterized by low plasma density and high ionization collision frequency between electrons and ions and neutral particles. The dynamics of this region are mostly dominated by the neutral atmosphere. The chemical processes present in this region are quite complex and O, O_2, O_3, and N_2 created by chemical processes are the most abundant neutral species among other species like NO_2, CO_2, H_2O, and alkali metals.

The electron concentration ranges between 10^7 and 10^{10} el/m^3, too low to reflect high-frequency (HF) radio waves. It mostly absorbs HF radio waves that pass through it.

- ***E-Layer*** – The E-layer was recognized because of its reflective properties in relation to radio waves used in telecommunications and it is characterized by increased electron density. It is situated between 90 km and 150 km in altitude. The main ionization comes from interaction with weak x-rays (λ > 10 Å), solar Lyman-β (1025.7 Å) and EUV (< 1000 Å) and EUV (< 900 Å). The region is dominated by N_2^+, O_2^+, NO^+ as its primary constituents. The region is weakly ionized and collisions between charged particles are not important. The electron density of the layer varies between 10^{10} and 10^{11} el/m^3 during the day and drops to 10^9 el/m^3 during the night due to recombination. The E region is also home to the sporadic E (Es) layers. These layers are formed due to different mechanisms. They are dense, highly variable, and thin with a thickness range of 0.6 km – 2 km. They are formed by the deposition of metal ions like Na^+, Mg^+, Fe^+, Ca^+, etc. by meteoric oblation. In the mid- and low-latitudes, they occur mostly in the summer and daytime and at high latitudes, they are frequently observed at nighttime.
- ***F-layer*** – This layer is located in the altitude range of 150 km – 1000 km and is the permanent region of the ionosphere. Major neutrals in this region are the N_2 and the atomic O with the dominant ion being O^+. The main ionizing sources are the EUV radiation and the Lyman continuum of hydrogen. The F region is sometimes characterized by two-electron concentration peaks corresponding to two sub-layers, the F1 and F2 layers. The inflection or the plasma density peak of the F1 layer is located around 180 km. Within this region, the transition from linear processes and quadratic loss takes place. The F2 layer occurs around the peak electron density at ~ 300 - 400 km. It is the densest region of the ionosphere in terms of ionization. It is formed mostly by winds and varies with solar activity. The concentration decreases at night due to the recombination of ions with neutrals and wind transport. The formation of a third layer, F3 in the equatorial region has been observed in Brazil and other regions (BALAN *et al*., 1998; PAZNUKHOV *et al*., 2007; TARDELLI *et al*., 2016, 2018; ZHAO *et al*., 2011). Evidence has shown that the F3 layer is a common feature of the magnetic equatorial region. The layer has seasonal, diurnal, and solar activity and geomagnetic activity variations (PAZNUKHOV *et al*., 2007; TARDELLI-COELHO *et al*., 2017; ZHAO *et al*., 2011). The peak electron density of the F3 layer

(NmF3) can exceed the peak electron density of the F2 layer (NmF2). The layer forms in the morning to noon hours in the equatorial region where the $\vec{E} \times \vec{B}$ drift and neutral winds provide vertically upward plasma drift at or above the F2 layer peak causing the F2 peak to drift upward forming the F3 layer while maintaining the normal F2 layer at lower heights through the usual photochemical and dynamical effects of the equatorial ionosphere (BALAN *et al*., 1998).

Table 1 below gives a summarized view of the ionospheric layers and some of their properties.

Table 1: Summary of the ionospheric layers and some properties

Layer	Altitude range (km)	Primary ionizing radiation	Daytime peak electron density (cm $^{-3}$)	Nighttime peak electron density (cm $^{-3}$)	Effect on radio signals	Signal (s) affected
D	60-90	Lyman- α	$< 10^2$	10^3	Attenuation/ absorption	LF, MF
E	90-150	Lyman-β	$1-2 \times 10^5$	2×10^3	Refraction	HF
F1	150-250	UV	$2-5 \times 10^5$	-	Reflection	HF
F2	> 200	UV	0.5×10^6	$2-5 \times 10^5$	Reflection	HF

SOURCE: Author**.**

Ionospheric plasma density does not only vary with altitude but also with time of day, latitude, longitude, season, solar activity, and geomagnetic activity. Recently, it has been shown to be affected also by processes below, like SSW which will be discussed in another section. Latitudinal variation has a distinctive behavior due to the geometry of the Earth's magnetic field lines. Hence the ionosphere can be classified by three latitudes controlled by different physical processes: the equatorial and low, middle, and high (aurora) latitude regions (HUNSUCKER; HARGREAVES, 2003; KELLEY, 2009).

2.4 Low-latitude and Equatorial ionosphere

A larger percentage of the solar radiation reaching the Earth's atmosphere is absorbed within ± 30^{o} – equatorial and low-latitude regions – as such the region is expected to have comparatively higher ionization. In these regions, the magnetic field lines are almost horizontal to the surface of the Earth, which restricts the motion of charged particles in the ionosphere within certain bounds resulting in ionospheric phenomena that are unique to the region.

2.4.1 Important Equatorial ionosphere phenomena.

The unique configuration of the eastward electric field, the geomagnetic field, and the plasma density gradient in the equatorial ionosphere lead to remarkable electrodynamic processes in the equatorial ionosphere. This leads to some unique and especially important geophysical phenomena such as Equatorial Electrojet (EEJ), Equatorial Ionization Anomaly (EIA), Pre-Reversal Enhancement (PRE), and generation of plasma irregularities (e.g., bubbles and blobs), etc. The generation, occurrence, characteristics, and morphology of these phenomena which vary with latitude, longitude, season, solar cycle, and geomagnetic activity have been studied over the years experimentally and/or theoretically (ABDU *et al*., 2003; FARLEY *et al*., 1986; FEJER *et al*., 1979).

2.4.2 Rayleigh-Taylor instability

Rayleigh-Taylor Instability (RTI) in the ionosphere is homologous to the hydrodynamic Rayleigh-Taylor instability in fluids. The RTI is the instability of an interface between two fluids of different densities in which the heavier fluid rests on top of the lighter one within a gravitational field. Any disturbance introduced at the boundary allows gravity to pull down the heavier fluid causing the lighter fluid to rise as bubbles through the heavier fluid inverting the density gradient. An illustration of the hydrodynamic RTI is shown in Figure 7. The RTI plays an important role in the formation of equatorial Spread-F and plasma bubbles.

Figure 7: Sequential sketches of hydrodynamic Rayleigh-Taylor instability showing the growth of the instability.

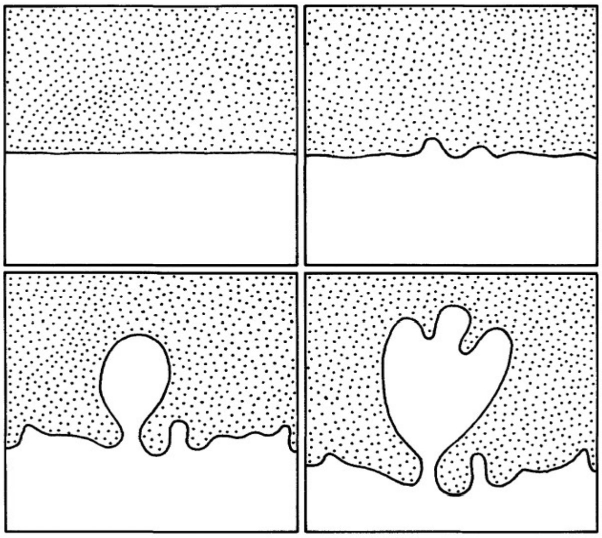

SOURCE: KELLEY (2009).

The bottom of the night side F region density gradient is shown as a gradient function with electron density n_1 in the F region and zero below it. At the equator, the magnetic field $\vec{B}$ is horizontal, which is into the plane of the page. The ions, which are more massive than electrons, will experience a downward gravitational force that is antiparallel to the density gradient. Assuming a collisionless magnetized plasma, this gravitational force creates a drift velocity given by

$$v_i = \frac{M\vec{g} \times \vec{B}}{eB^2} \tag{3}$$

where M is the mass of the ion. Hence the gravitational force produces a current density given as

$$J = \frac{nM\vec{g} \times \vec{B}}{B^2} \tag{4}$$

If there is a small disturbance at the bottom boundary of the F region, the current which flows close to the boundary meets the disturbance and is polarized in the way as shown in Figure 8. The gravity force and the magnetic field together drive the positive ions to one part of the disturbance which becomes positively charged and leaves the other part negatively charged. An electric field δE is developed due to this polarization. This electric field in turn produces a $\delta\vec{E} \times \vec{B}$ drift which is the same for electrons and ions. The direction of the drift is downwards (upwards) in regions where the boundary is bent downwards (upwards). This enhances the disturbance, and instability is created.

Figure 8: An illustration of the Rayleigh-Taylor instability.

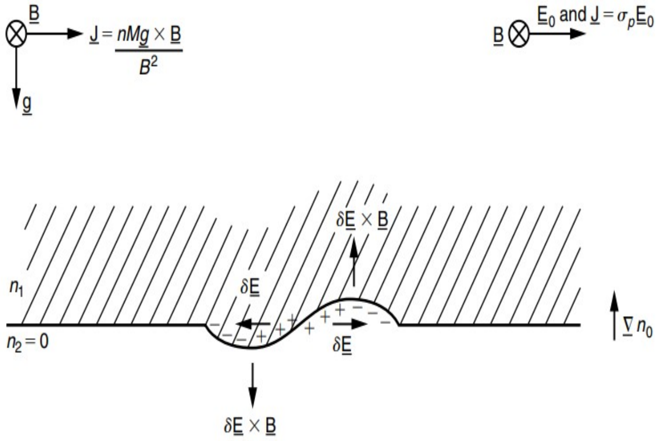

SOURCE: KELLEY (2009).

The linear growth rate of the RTI is given by

$$\gamma_{RT} = \frac{g}{L\nu_{in}} \tag{5}$$

where ν_{in} is the ion-neutral collision frequency, g is the acceleration due to gravity, $L = \left[\frac{1}{n_0}\frac{\partial n_0}{\partial z}\right]^{-1}$ is the plasma density scale length which is inversely proportional to the plasma density gradient $\frac{\partial n_0}{\partial z}$.

Other factors and processes such as meridional neutral winds, electric field shear effects, diffusion, and E-region conductivity, besides gravity, influence the stability of the equatorial ionosphere. Also, a strong vertical plasma density gradient at the bottomside of the F layer and a strong upward plasma drift during the night combine to destabilize the plasma (CARTER *et al*., 2016). Rayleigh-Taylor instability can be triggered whenever a certain geometric relationship holds between the electron density gradient in the equatorial ionosphere and the forces acting on the plasma. These parameters were incorporated in the RT instability theory and called the generalized RT theory which is understood to be the principal cause of ionospheric irregularities (EPBs/ESFs). The linear growth rate γ of generalized R-T instability dependent on local and flux tube integrated parameters has been studied and a formula derived based on these quantities (ABDU, 2001; CARTER *et al*., 2016; GENTILE; BURKE; RICH, 2006; SULTAN, 1996).

When conductivities at low F-region conjugate E-layers are important, γ would depend on the flux tube integrated quantities given in equation (6):

$$\gamma_{RT} = \frac{\Sigma_P^F}{\Sigma_P^E + \Sigma_P^F}\left(V_P - U_L^P - \frac{g_e}{\upsilon_{eff}}\right)K^F - R_T \tag{6}$$

$V_p = \frac{\vec{E}\times\vec{B}}{B^2}$ is the upward plasma drift, the vertical component of neutral wind velocity perpendicular to $\vec{B}$. $\frac{g_e}{\upsilon_{eff}}$ is the altitude-corrected gravity divided by the flux tube integrated effective ion-neutral collision frequency, weighted by the electron density. These terms in the brackets are multiplied by flux tube integrated F and E region Pedersen conductivities $\Sigma_P^{F,E}$ ratio and K^F, the F region flux tube electron content height gradient is given by $\frac{1}{N_e}\frac{\partial N_e}{\partial H}$ where N_e is the flux tube electron content. R_T is the flux tube integrated recombination.

In the postsunset hours, the magnitude of the RT linear growth rate, γ_{RT} depends strongly on the strength of the PRE, which is one of the most important prerequisites for the occurrence of equatorial ionospheric irregularities, in the upward plasma drift V_p which is known to have strong seasonal and longitudinal variations. Thus, the observed seasonal and longitudinal dependence of ionospheric irregularities can be explained by the seasonal and longitudinal variations in the V_p (BURKE *et al*., 2004; CARTER *et al*., 2016; GENTILE; BURKE; RICH, 2006).

The F-layer bottomside density gradient or its integrated density gradient defined by the K^F parameter, which is positive at the bottomside, is another factor that controls the growth rate of the RTI (ABDU, 2001; GENTILE; BURKE; RICH, 2006). The eastward component of the electric field and the downward component of the neutral wind velocity contribute to a positive growth rate of the RT instability. At a given location g and B are constants, as such RT growth rates are controlled by the variability of E_0, U_L^P, $\Sigma_P^{F,E}$, R_T, υ_{eff}, and through the flux-tube integrated quantities by the height of the F-layer (GENTILE; BURKE; RICH, 2006).

At lower heights, when conductivities are assumed zero and less important to the growth rate of RTI, then γ in its simplest form becomes:

$$\gamma = \left(V_p - \frac{g}{v_{in}}\right)\frac{\Delta n}{n} - R_T \qquad (7)$$

Where n is the ambient electron density and v_{in} is the ion-neutral collision frequency.

When the F-layer rises, the growth rate of the generalized Rayleigh Taylor instability increases since the neutral collision rates and the recombination rates are smaller in the background neutral density at higher altitudes decreases. A larger growth rate of the RTI implies that it is more likely for ionospheric irregularities to occur.

2.4.3 Pre-Reversal Enhancement

The equatorial ionosphere generally drifts upward during the day and downward in the nighttime due to the $\vec{E} \times \vec{B}$. The electric field is produced by the dynamo effect of E-region neutral winds. At sunset hours, the eastward daytime electric field in the F region of the equatorial ionosphere often shows a strong increase for 1-2 hours, increasing sharply the upward drift velocity, before reversing to its nighttime westward direction. This increase in the eastward electric field is called Pre-Reversal Enhancement, PRE (FARLEY *et al*., 1986; FEJER *et al*., 1991). The evening enhancement is known to be the result of the dynamo effect by F-region neutral winds and the effect of rapid changes in E-region electric conductivity at sunset. Figure 9 shows the mechanism that causes the pre-reversal enhancement and a simplified model of the physical principle of vertical drift formation.

According to Farley *et al*. (1986), the thermospheric neutral winds at equatorial F-region altitudes blow eastward toward the dusk terminator. The eastward motion of neutral particles causes only ions to drift upward through collision generating an electric field Ez in the F region (MARUYAMA, 2002) as shown in Figure 9. This electric field, due to the charge separation, is projected along the geomagnetic field lines, B onto the E region towards the equator, with the representation in polar coordinates of E_θ. This mapped electric field generates a zonal westward Hall current, $J_{\theta\phi}$ in the E-layer. The sudden drop in the nighttime E region electronic density causes the E region conductivity to become negligible. This causes an accumulation of negative charges at the terminator, inducing a zonal eastward electric field

(E_ϕ) to maintain the electrostatic balance. This field creates a Pederson current, $J_{\phi\phi}$ that cancels $J_{\theta\phi}$ in a steady state. Then E_ϕ is then mapped back to the F region, where it produces a sudden increase in vertical plasma drift ($\vec{E} \times \vec{B}$), the PRE.

Figure 9: Simplified model of the pre-reversal enhancement of the ionospheric electric field driven by the uniform F-region neutral wind, U.

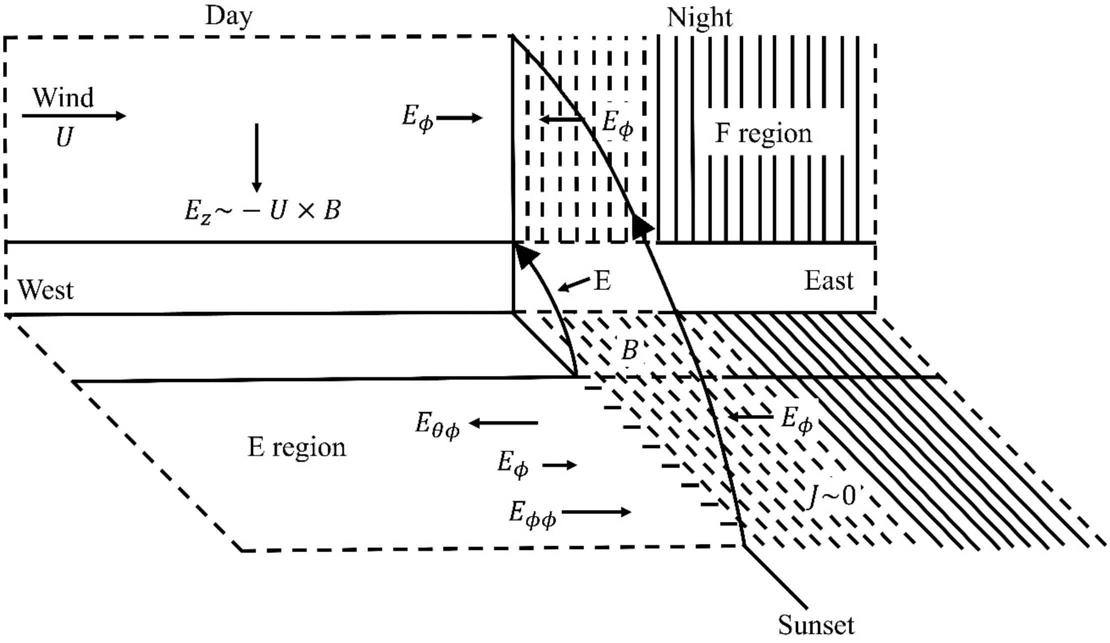

SOURCE: From FARLEY *et al.* (1986).

At equatorial latitudes, any change in the east-west electric field is reflected in the vertical drift driven by $\vec{E} \times \vec{B}$ mechanism. So, the upward daytime vertical drift also shows an enhancement before it reverses. The effect of the PRE in the ionosphere is especially important for the generation of ionospheric irregularities as it drives the F-layer plasma to higher altitudes where collision frequency is significantly reduced. The pre-reversal enhancement (PRE) of the vertical upward $\vec{E} \times \vec{B}$ drift and its fluctuations amplified during PRE provide the driving force and seed for the collisional RT instability mechanism for the intense irregularities, with neutral wind and gravity waves being the primary sources. The magnitude of the PRE depends on the season, solar activity, time of day, and geomagnetic activity as demonstrated in Figure 10. The PRE is shown to occur in all epochs except solar minimum solstices. At low solar activity especially in summer when the fast-varying PRE is absent, the slow varying gravity waves including large-scale waves (LSW) seem to act as both drivers and seeds for weak irregularities.

Figure 10: Average vertical plasma drifts measured from Jamaica during equinox, winter, and summer for three solar cycle periods from 1968, 1980 -1981, and 1984 – 1988.

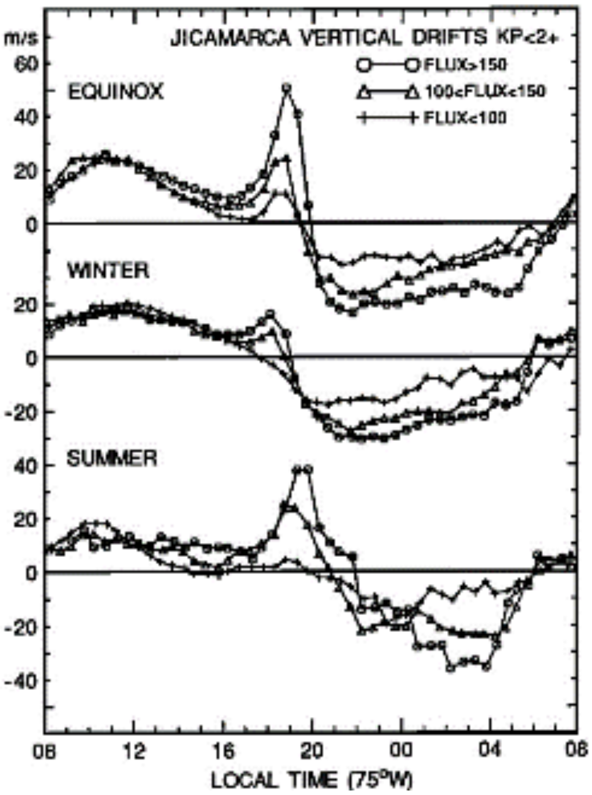

SOURCE: FEJER *et al*. (1991).

2.4.4 Equatorial Ionization Anomaly

The EIA, also the Appleton anomaly is one of the most prominent equatorial ionospheric/thermospheric processes which occurs in the low latitudes giving rise to plasma depletion at the equator and two plasma enhancements at low latitudes around ± 15° - 20°. The development process involves the vertical upward plasma drift that occurs as a result of a unique geometric configuration due to the cross of the Earth's magnetic field ($\vec{B}$) and the zonal electric field ($\vec{E}$) in the near-equatorial and low-latitude regions during quiet time in the daytime hours. The daytime eastward zonal electric field acts perpendicular to the north-south geomagnetic field lines (almost parallel to the Earth's surface at the equator and nearby latitudes) and gives rise to an upward vertical plasma drift of the F-layer known as the $\vec{E} \times \vec{B}$

upward vertical drift. This causes the F-layer plasma at the equator to rise to higher altitudes. As the plasma rises, it encounters the horizontal lines of force of the Earth's magnetic field and eventually gets deposited into the low latitude ionosphere along the geomagnetic field lines by the action of gravitational and pressure gradient forces in a process known as the fountain effect. The result of this is the formation of two crests of high plasma density in the northern and southern hemispheres between ± 15° and ± 20° dip-latitudes and a trough – low depleted plasma at the magnetic equator (FATHY; GHAMRY, 2017; MO *et al.*, 2017). The equatorial electrodynamics and the formation of the fountain effect leading to the EIA are shown in the schematic diagram of Figure 11.

Figure 11: Schematic illustration of the equatorial electrodynamics and the formation of the EIA on both sides of the magnetic equator.

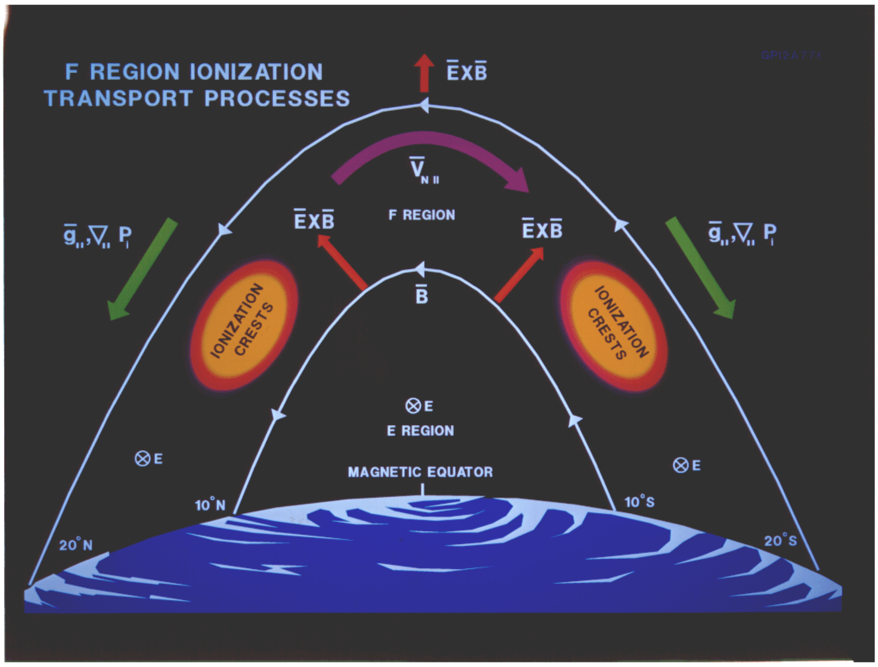

SOURCE: TSURUTANI; LAKHINA; HAJRA (2020).

The EIA appears in the morning around 10 h LT and becomes stronger during the day till it reaches its maximum in the afternoon. It gradually disappears as the sun sets based on geophysical conditions. Sometimes, however, just after sunset the zonal eastward electric field is intensified, which may lead to an intensification of the EIA after sunset. In this case, the EIA crests may persist a couple of hours after the PRE peak into the nighttime hours (BALAN; LIU; LE, 2018; BALAN; SOUZA; BAILEY, 2018).

The EIA structure is generally considered to exhibit regular and symmetric behavior; however, its intensity may have local time, seasonal, longitudinal, and solar cycle dependence and may exhibit asymmetric behavior in the latitudinal location and ionization densities between the northern and southern ionization crests and possible single crest formation due to an inter-hemispheric wind blowing from the summer to winter hemisphere (BALAN; LIU; LE, 2018; FATHY; GHAMRY, 2017; KELLEY, 2009). In the summer hemisphere, plasma moves upward along the geomagnetic field lines, while plasma moves downward in the winter hemisphere. Therefore, the plasma is transported from the summer hemisphere to the winter hemisphere. As result, the equatorial anomaly crests in the winter hemisphere are generally larger than in the summer hemisphere. Factors such as geomagnetic declination angle, and displacement of the geomagnetic equator may also play important roles in the hemispheric asymmetry of the EIA.

2.4.5 Ionospheric irregularities

Ionospheric irregularities are structures of various scale sizes in the ionospheric plasma density generally oriented so that the plasma density variations occur rapidly across the geomagnetic field but slowly (or not at all) along the geomagnetic field (PERKINS, 1975). They typically occur after sunset in the equatorial and low-latitude F-region. They are attributed to depletions and instabilities in the background plasma due to the generalized Rayleigh-Taylor instability first suggested in 1956 by DUNGEY. The RTI mechanism acts on disturbances introduced by seeding mechanisms like gravity waves at the bottomside of the F-layer inducing plasma instabilities that develop into irregularities. Generally, ionospheric irregularities have been used to refer to fluctuations and inhomogeneities in the ionospheric plasma density. Irregularities occur in all latitudes with different morphologies, formation mechanisms, and distribution.

Ionospheric irregularities come in varied spectral ranges, with a wide spatial scale ranging from a few centimeters to hundreds of kilometers, occurring from the F-region base to the topside of the layer (KELLEY; HYSELL, 1991). The different irregularity scale sizes require different techniques and instruments that are used to detect and observe. Depending on which instrument and/or technique used, different terms are associated with the type of observation giving various names to these observations. For example, plumes are small-scale irregularities of the order of about 3-5 m observed with radars in VHF, scintillations are produced in signals transmitted by UHF and VHF satellites like geostationary and GPS satellites and originate from irregularities with sizes ranging from hundreds of meters to tens of kilometers. Large-scale ionospheric irregularity structures consist of regions of lower plasma density referred to as plasma bubbles or depletions observed with optical instruments and as ionization holes observed with in-situ measurements. They are observed as scattered traces in ionograms. These structures in the equatorial ionospheric plasma density have spatial sizes of the order of tens to hundreds of kilometers, long life spans, and periods of 1 hour or more. They are generally oriented in such a way to have the plasma density variations occur rapidly across the geomagnetic field but slowly along these fields. At the topside of the ionosphere, these structures extend to form plumes.

The development, and long-term and medium-term variability of large-scale ionospheric structures are well understood, however, the day-to-day (or short-term) variability still baffles researchers. The development of the large-scale structure is understood through the generalized Rayleigh-Taylor instability processes. The smaller-scale irregularities coexist with large-scale irregularities, however, the mechanisms that lead to their development are different from that of the large-scale structures and are not fully understood.

The understanding of the dynamics and morphology of ionospheric irregularities is not only important to research but has great importance to telecommunications, and navigation. These irregularities can cause instabilities, scintillations, and strong interference in transionospheric communication signals or radio waves that pass through them causing errors in them. Some examples of large-scale equatorial ionospheric irregularities are traveling ionospheric disturbances (TID), Equatorial plasma bubbles (EPBs), and Spread-F.

2.4.5.1 Equatorial Spread-F

Equatorial Spread-F (ESF) was first discovered in 1938 by BOOKER and WELLS as diffuse echoes on ionograms. Later it became known that the ESF phenomenon that was seen as a spread in range and frequency (WOODMAN; LA HOZ, 1976) was also observed as plumes in coherent backscatter radar echoes (WEBER *et al.*, 1978), intensity bite-outs in OI 630 nm nightglow images (AARONS, 1982; BASU; KELLEY, 1977; YEH; LIU, 1982) and scintillations on amplitude and phase of VHF, UHF, and L-Bands (SCHUNK; NAGY, 2009).

ESFs are nighttime ionospheric irregularities that usually occur after sunset at the bottomside F-region. They can be seen in ionograms as diffused echoes generated by various plasma instability processes of which Rayleigh-Taylor instability plays a dominant role (BASU; COPPI, 1999; HYSELL; BURCHAM, 2002). Spread F can be classified mainly into three categories based on their appearance in the ionogram. They are,

1. ***Range spread F*** – refers to the diffuseness main along the horizontal part of the F-region trace on the ionograms giving raise the ambiguity in height as the critical frequencies are identifiable.
2. ***Frequency spread F*** – refers to the spreading near the critical frequencies causing ambiguity regarding the identification of the critical frequency of the F2 layer while the trace is sharp and clear at lower frequencies.
3. ***Complete/Mixed Spread F*** – occasionally, spreading is seen to be equally prominent in the height scale in the entire frequency range of the observed ionogram.

Figure 12 shows three ionograms showing the three types of Spread-Fs: a)Range Spread-F, b) Frequency Spread-F (FSF), and c) Mixed Spread-F (MSF)

Figure 12: Sample ionograms showing a) Range, b) Frequency, and c) Mixed Spread-F types.

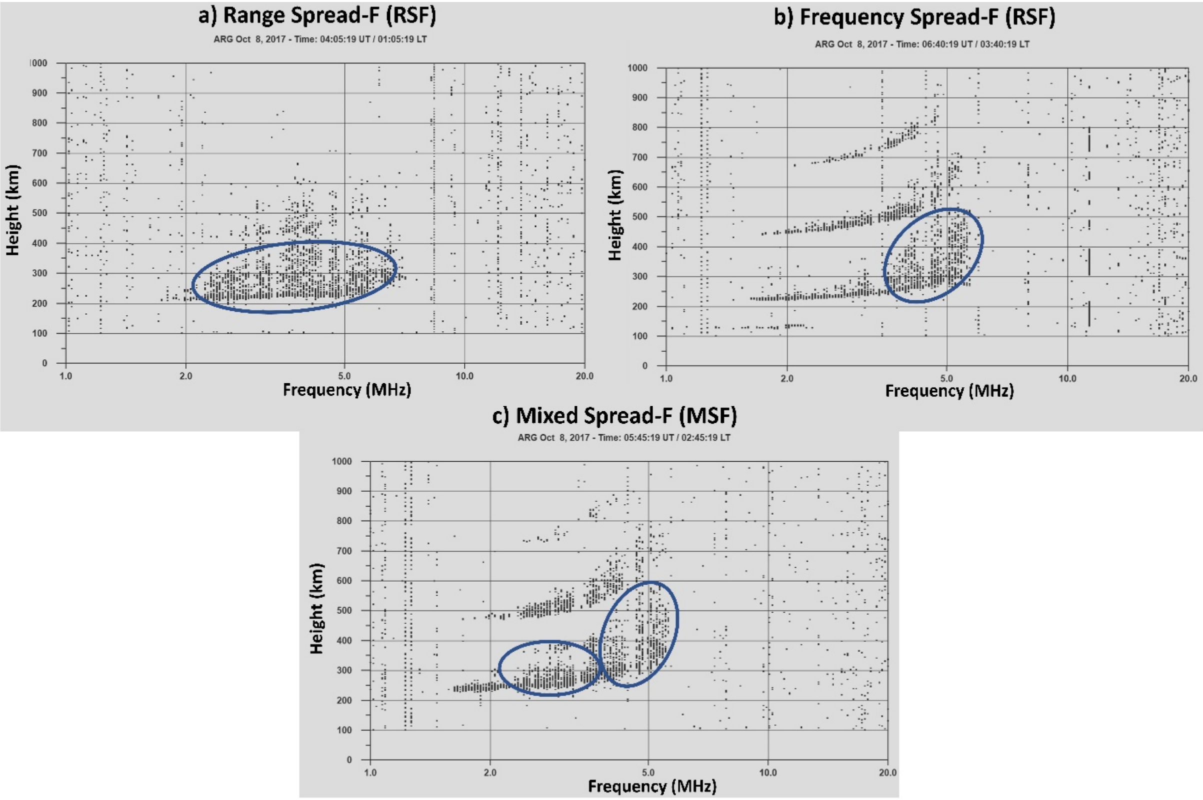

a) Range Spread-F (RSF)

ARG Oct 8, 2017 - Time: 04:05:19 UT / 01:05:19 LT

b) Frequency Spread-F (RSF)

ARG Oct 8, 2017 - Time: 06:40:19 UT / 03:40:19 LT

c) Mixed Spread-F (MSF)

ARG Oct 8, 2017 - Time: 05:45:19 UT / 02:45:19 LT

SOURCE: Author.

ESFs occur at all latitudes, however, the majority and most intense are observed around ± 20° geomagnetic latitudes, and their occurrence show variability with the season, local time, geographical location, and solar and magnetic activity (MA; MARUYAMA, 2006). The maximum probability of occurrence of ESF is during local summer and the equinoxes and the minimum occurs in local winter or June solstices (ABDU *et al*., 1998; ABDU; SOBRAL; BATISTA, 2000; ALFONSI *et al*., 2013; GONZÁLEZ, 2022) in the Brazilian sector.

2.4.5.2 Equatorial Plasma bubbles

Equatorial Plasma Bubbles (EPBs), also plasma bubbles or plasma depletions are large-scale structures with sizes ranging from 10s to 100s kilometers. These regions of reduced plasma densities relative to the ambient plasma in the equatorial ionosphere occur frequently in the bottomside F region and extend vertically to the topside ionosphere during the post-sunset hours (NARAYANAN *et al*., 2017; ZAKHARENKOVA; ASTAFYEVA; CHERNIAK, 2016). The structures are so-called because they are similar to bubbles rising through a liquid medium. They are observed as elongated, wedge-like structures as they rise in altitude extending to higher latitudes along the magnetic flux tube lines (CHERNIAK; ZAKHARENKOVA, 2016). They are normally observed within the equatorial and low-latitude regions but reports from Ma; Maruyama (2006) and Narayanan *et al*. (2017) have shown that during geomagnetic storms they can extend up to mid-latitude regions. EPBs are generally generated just after sunset when there is rapid recombination and reduced production rates in the E-region creating a steep vertical plasma gradient between E- and F-regions with the E-region on the lower side of the gradient. The plasma density gradient combined with the uplifting of the F-region by PRE action through the $\vec{E} \times \vec{B}$ upward plasma drift causes the bottomside equatorial ionosphere to drift to heights where the RTI growth rate is increased and recombination is decreased thereby generating EPBs (BOOKER; WELLS, 1938; KUMAR *et al*., 2016; NARAYANAN *et al*., 2017).

Plasma bubbles were first observed by Booker; Wells (1938) on ionograms as radio wave signals interacted with ionospheric layers and suffered multiple reflections (echoes). Plasma bubbles are known to introduce amplitude and phase fluctuations into radio signals that pass through them thereby causing deterioration in the signal integrity and causing errors in telecommunication and navigation systems. As such, the study of the occurrence of plasma bubbles is a particularly important research area leading to research that employs various techniques and instruments including incoherent scatter radar, ionosonde ionograms, airglow images from all-sky imaging systems, global positioning system – total electron content (GPS-TEC), satellite observations, etc.

The occurrence of plasma bubbles varies with season, solar and magnetic activity, local time, and latitude (AGYEI-YEBOAH *et al*., 2019; CHAPAGAIN; FEJER; CHAU, 2009; GENTILE; BURKE; RICH, 2006; KUMAR *et al*., 2016; SAHAI; FAGUNDES; BITTENCOURT, 1999, 2000; SOBRAL *et al*., 2002). The report from Sobral *et a*l. (2002) analyzes 22-year scanning photometer data and results from Agyei-Yeboah *et al*. (2019) with 11-year OI 630.0 nm nightglow data from an all-sky image located at São João do Cariri, north-east of Brazil showed that the solar cycle variation, seasonal and latitudinal dependence. Figure 13 shows the occurrence rates of plasma bubbles at different latitude stations (São João do Cariri and Cachoeira Paulista) during different solar activity levels (high, medium, and low). The results show that plasma bubbles are more frequent during high solar activity compared to medium and low activity periods. They are more likely to be observed in equatorial regions and less likely to be observed at higher latitudes. This is because, during the high solar activity (HSA), PRE that controls the occurrence of EPBs is known to have increased amplitude (LIN *et al*., 2007; SHARMA; NADE; GHODAWAT, 2013).

Figure 13: Plasma bubble occurrence rate at different solar activity phases observed at different longitudinal sectors – São João do Cariri, CAR (equatorial region), Cachoeira Paulista, CP (low-latitude region).

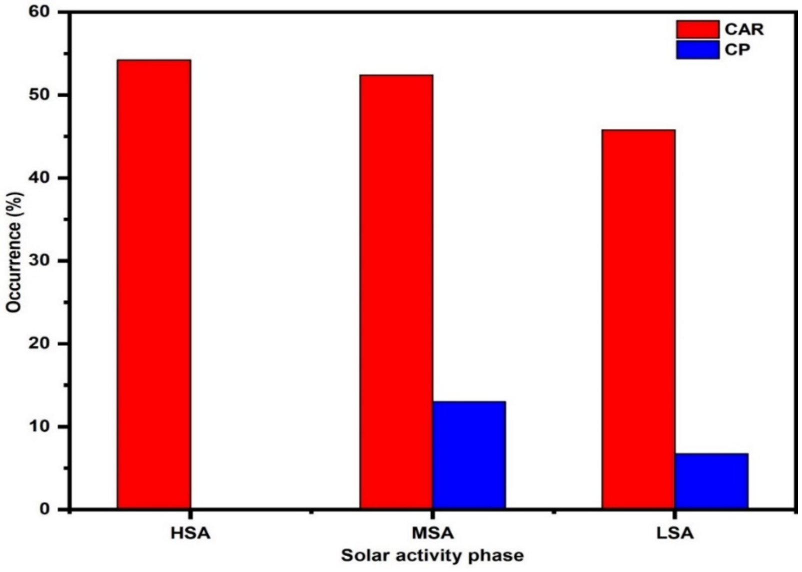

SOURCE: From AGYEI-YEBOAH *et al*. 2019).

Agyei-Yeboah *et al.* (2019) also observed seasonal variation in plasma bubble occurrence at both Cariri and Cachoeira Paulista during all solar activity periods with higher occurrence being recorded during the summer, autumn, spring, and winter recording the least occurrences as shown in Figure 14. In each season, plasma bubble occurrences showed solar activity dependence decreasing from HSA to low solar activity (LSA) at both stations. However, a departure was observed in the results where the LSA occurrence rate was higher than medium/moderate solar activity (MSA) in autumn at Cariri, and in summer at Cachoeira Paulista. This departure was attributed to the high incidence of gravity waves during low solar activity taking over the generation of plasma bubbles as PRE influence reduces during this period. The seasonal variation of plasma bubbles has been attributed to in part neutral winds and the strength of equatorial fountain effects. Tsunoda (1985) on the other hand have suggested that this seasonal variation is due to the variation in the relative alignment between the local meridian and sunset terminator such that the closer they are, the smaller the declination angle during equinox leading to increased PRE amplitude and consequently faster vertical upward drift.

Figure 14: Seasonal variation of EPBs under different solar activity phases at different latitude sectors

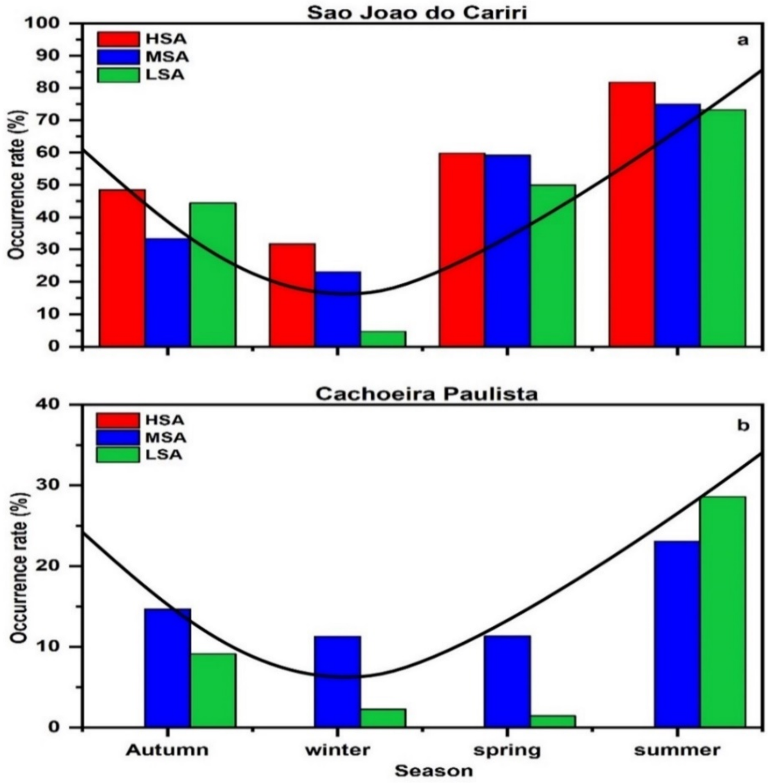

SOURCE: From AGYEI-YEBOAH *et al*. (2019).

2.4.5.3 Plasma blobs

Plasma blobs are ionospheric irregularities characterized by regions of enhanced plasma density of several orders higher than the background plasma which have been observed in the low-latitude ionosphere. They appear as upward spikes in plasma density measurements along the orbits of a satellite as shown in Figure 15. In airglow images, they are observed as bright regions, with emission intensities greater than the background nightglow emission, and in ionograms, they are observed as higher-frequency echoes observed beyond the critical frequency at the time (CHERNIAK; ZAKHARENKOVA, 2016; HUANG *et al.*, 2014; MCNAMARA *et al.*, 2013; PARK *et al.*, 2003; PIMENTA *et al.*, 2004). Since the first observation in 1986 by Watanabe and Oya using data from the Hinotori satellite, many other studies have been carried out using different techniques and instruments covering their generation, morphology, development, variations, etc.(HUANG *et al.*, 2014; LE *et al.*, 2003; PARK *et al.*, 2010; PIMENTA *et al.*, 2004; WANG *et al.*, 2019).

Figure 15: Plasma blobs as observed by DMSP 12 satellite during a) solar minimum and b), solar maximum

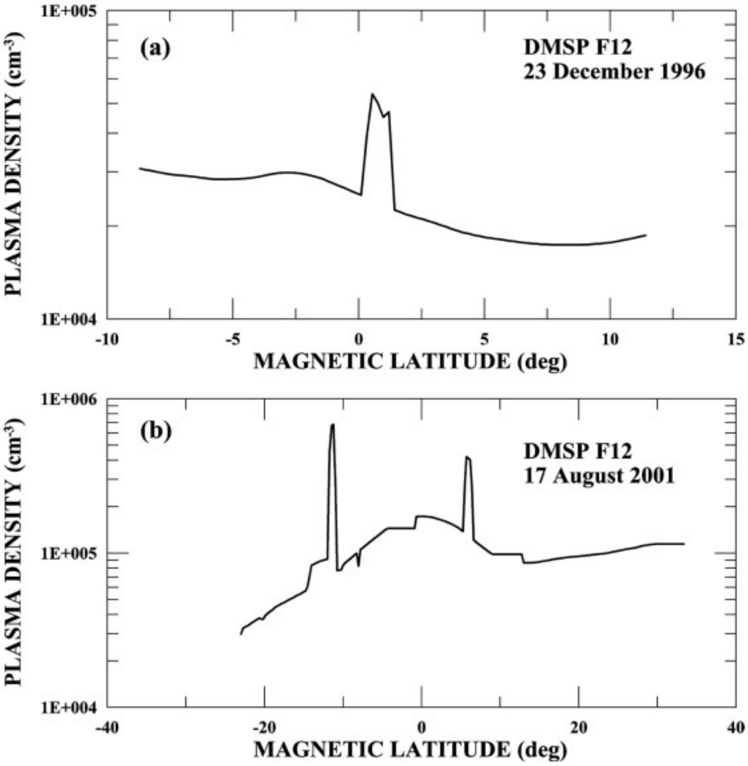

SOURCE: KIM; HEGAI (2016).

Plasma bubbles have been suggested to have an important role in the generation of plasma blobs (KIL *et al.*, 2019). Le *et al.* (2003) have reported that the eastward electric field inside an EPB would push up high-density plasma at the EIA crest when the EPB flux tube reaches EIA latitudes. This would result in the occurrence of a blob just above the EPB flux tube. Other studies have also suggested medium-scale traveling ionospheric disturbances

(MSTID) and gravity waves (GWs) as possible generators of plasma blobs (KIL *et al*., 2019; WANG *et al*., 2019).

2.5 Sudden Stratospheric Warming

Ionospheric variations are not only affected by processes above like solar wind and geomagnetic storms known as main drivers but also by processes occurring in the lower atmosphere. The ionospheric variability that is not accounted for by the main drivers is in the neighborhood of around 20-33% and even higher in the low latitudes (CHAU *et al*., 2012). In the lower latitudes, the variability in the ionosphere is not only affected by lower atmospheric processes but also by processes from higher latitudes (DE PAULA *et al*., 2015; YADAV *et al*., 2017). One such high-latitude process is sudden stratospheric warming or SSW.

SSW is a meteorological phenomenon that occurs in the polar stratosphere during winter. The phenomenon is characterized by a sharp increase in stratospheric temperature at high latitudes that occurs over several days. This temperature increase is caused by the disturbances caused by the interaction between upward propagating planetary waves (PWs) and the zonal wind. The eastward zonal wind sometimes decelerates (minor SSW) and often completely reverses direction westward (major SSW). The influence of SSW events extends beyond just the high-latitude stratosphere but has far-reaching consequences in the low-latitude ionosphere during and after an event (PEDATELLA *et al*., 2018). The amplified PWs and other waves like gravity waves and tides generated during SSW events may modify equatorial ionospheric dynamics which may influence plasma distribution in the low-latitude ionosphere (KUTTIPPURATH; NIKULIN, 2012; MCINTURFF, 1978). It usually occurs in the northern hemisphere but occasionally it does occur in the southern hemisphere (e.g., in 2002 and 2019). Figure 16 shows the coupling process that occurs in the ionosphere during an SSW event.

Figure 16: Coupling processes that occur in the atmosphere during SSW events. Red and blue circles denote regions of warming and cooling, respectively

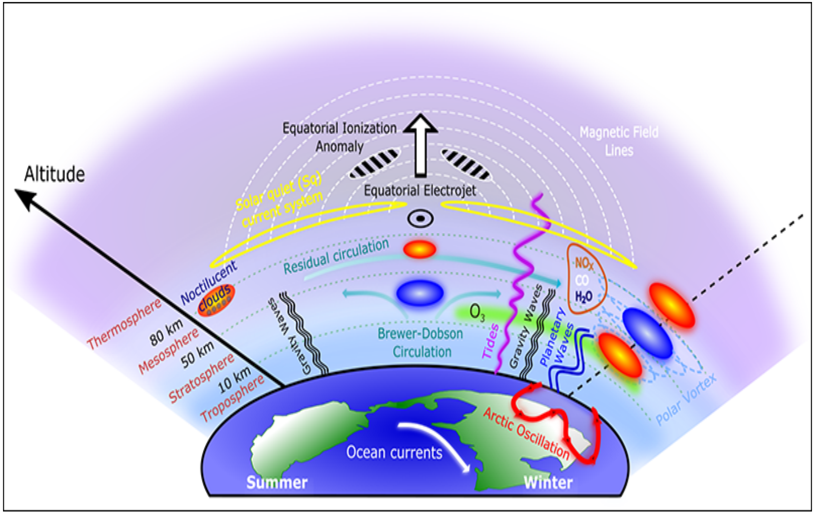

SOURCE: (PEDATELLA *et al.*, 2018).

An SSW event is said to be major when there is a temperature increase of at least 25 K at 10 hPa and 60° latitude followed by a reversal of the westerly winds to the east (CHATTOPADHYAY; MIDYA, 2006). A minor SSW, however, is characterized by an increase in temperature of at least 25 K at any stratospheric level in the winter hemisphere with a slowing down but not a reversal of the prevailing wind (PEDATELLA *et al.,* 2018).

3 INSTRUMENTS AND TECHNIQUES

Many ionospheric phenomena are best studied through long-term data collection. This is particularly true for aerodynamic measurements that are often sporadic due to weather conditions, or the relative locations of the moon and Sun. To study the temporal (time of day, seasonal, solar cycle, etc.) and spatial (longitudinal and latitudinal) variations of the ionosphere, different instruments and methods are employed under different geophysical conditions and geographical locations. These instruments and methods can be classified as in-situ and remote sensing. The objective of this chapter is to describe the instruments and techniques used in the investigations detailed in this thesis to set the stage for the presentation of the data collected, methods used, and subsequently, the results. This will give background to the results presented for better understanding.

3.1 All-Sky Imaging System

All-sky optical imaging is one of the main techniques employed in auroral and airglow studies. It takes high-resolution airglow emissions images. The imager consists of a fisheye lens, a charged-coupled device (CCD) camera, a set of lenses, a filter wheel interference system, a cooling system, and a microcomputer. A schematic structure of the all-sky imaging system is shown in Figure 17. The all-sky imager (ASI) performs two basic functions in airglow studies; to record complete images of the night sky airglow emissions and monitor the variations of airglow in real-time. The ASI is an important tool in the study of the morphology and dynamics of phenomena like gravity waves in the mesosphere and irregularities in the ionosphere. The study of airglow emissions using an all-sky imaging system has some inherent limitations which include environmental situations that cannot be controlled, among which are sky transmission, clouds, moonlight, etc. Among the airglow emissions that are observed with the imager are those due to atomic oxygen (OI 557.7 nm, OI 630 nm, and OI 777.4 nm), molecular oxygen O_2 (0, 1), mesospheric sodium (NaD), and Hydroxyl molecule and light from the night sky (Background or BG). A detailed treatment of airglow is provided in Appendix B on page 158.

The all-sky imager works similarly to a normal photographic camera. Measurements are made by directing the lens of the instrument to the desired emission (upwards). The emissions that enter the lens are projected along the system of the lens' photosensitive cells that associate the luminous intensity with digital information. The lens used by the system is a fisheye lens that provides a 180° field of view. The selection of the desired wavelengths of each emission is made by the interference filters, then the lens set projects the image to the CCD-type camera. The Cooling System keeps the temperature (~ - 35 °C) to reduce thermal noise. The whole system is monitored by a microcomputer that also manages the storage of the data on a hard drive. A description of the optics system of the All-sky imager (ASI) and how they operate can be found on page 165, Appendix C.

Figure 17: A schematic diagram of an All-sky imager showing ray paths.

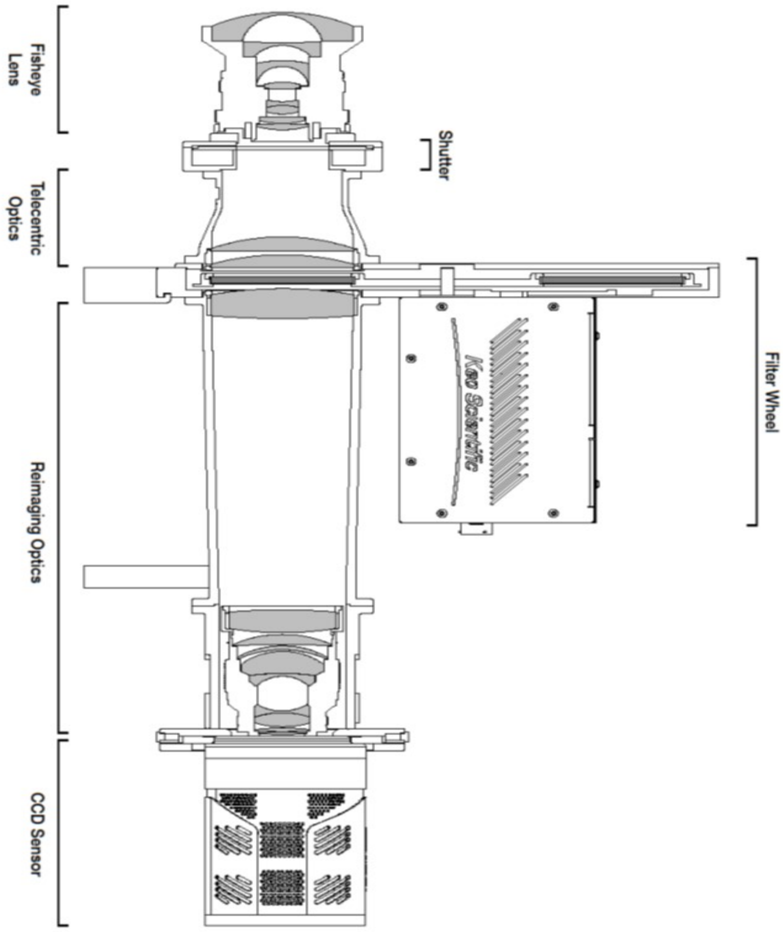

SOURCE: KEO Scientific.

3.1.1 Image Visualization, Treatment, and Analysis

Airglow image files are collected and stored as *.tif files. Each of these images is an array of 1024 x 1024 elements (the number of elements depends on the resolution of the CCD). Consequently, an element of these arrays is one pixel. The information contained in each pixel refers to the intensity of airglow that the corresponding CCD cell has received. The information recorded in the matrix elements varies on a scale from 0 to 65536 degrees gray, where 0 corresponds to the absence of light and 65536 to maximum intensity. UNIVAP All-Sky Data Analysis (UASDA), shown in Figure 18, has been developed at the UNIVAP to study airglow images obtained from all-sky imaging systems. The program has several useful features incorporated into it. It is used for the visualization, calibration, and linearization of airglow images among other features. And in Figure 19, a lecturer from the Space Physics Laboratory in practical class helps students to disassemble and mount an all-sky imaging system in a dark room.

Figure 18: The interface of UASDA of UNIVAP.

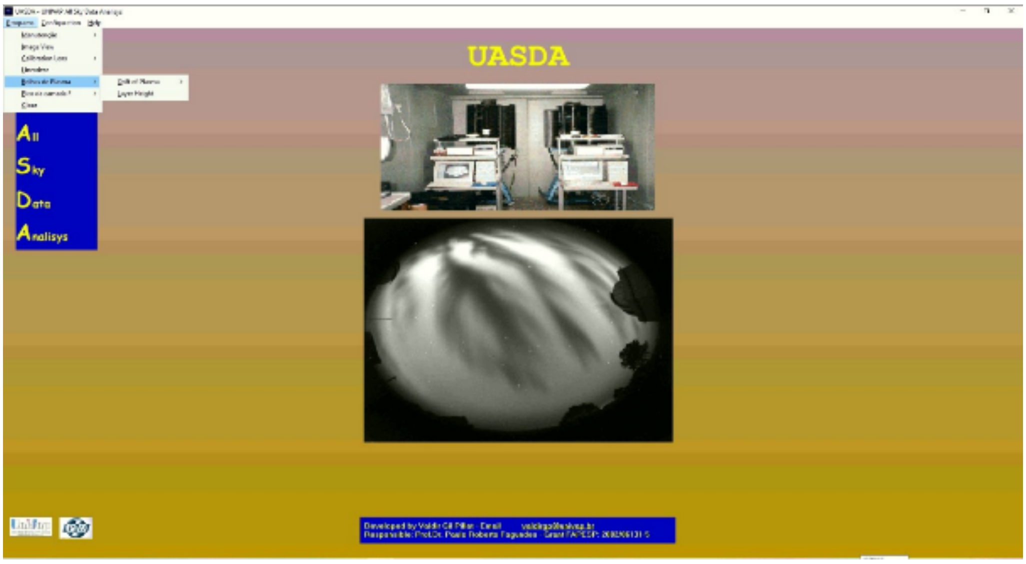

SOURCE: Author.

Figure 19: Some students and a lecturer mounting an all-sky imaging system in the darkroom of the Physics and Astronomy lab of IP&D, UNIVAP.

SOURCE: Author.

3.2 CADI ionosonde

The Canadian Advanced Digital Ionosonde (CADI) is a state-of-the-art, low-cost, full-featured ionosonde developed by the Canadian Space Research Network. It uses high-power radiofrequency pulses at vertical incidence with transmission frequencies from 1 up to 30 MHz. The operational principle of the ionosonde is described in Appendix D, page 173. It is ideal for both routine ionospheric monitoring and scientific research. The system integrates phase coding techniques, solid-state electronics, and PC technology to make CADI a significantly smaller and less expensive ionosonde. The system may be operated with single or multiple receivers. Observables include echo delay (height) versus frequency; the phase and amplitude of the echo; angle of arrival; and polarization of the echo. Drifts can also be measured using the spaced-antenna method. Figure 20 and Figure 21 show a CADI setup CADI transmission antenna installed at Araguatins in Brazil, respectively.

Figure 20: One of the CADI ionosondes used by UNIVAP for ionospheric studies.

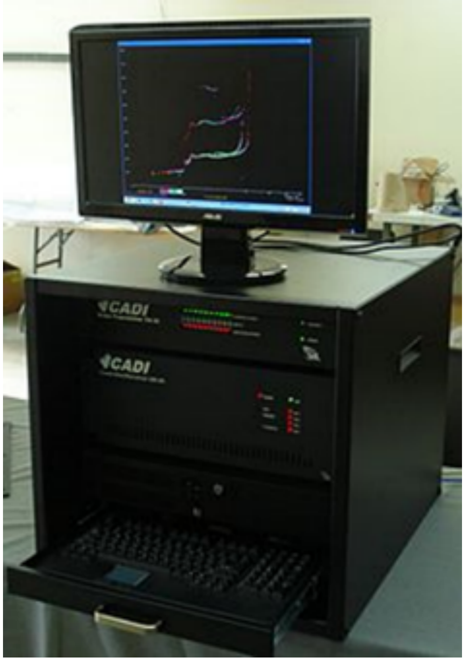

SOURCE: Author.

Figure 21: CADI transmission antenna installed at Araguatins observation station.

SOURCE: (BARBOSA, 2018).

The CADI ionosonde comprises a delta antenna transmitter, a four-dipole receiver, and a frequency synthesizer. The power requirement of the transmitter is ~ 600 W and provides the power amplification of radio frequency (RF) signals. The CADI transmission system uses the 13-bit pulse code (Baker code) and 40 μs pulse width, which corresponds to an output mode of 520 μs. The transmission antenna has a mast that rises to a height of 20 m. The receiver, consisting of a standard wideband RF amplifier, a mixer, and a narrow intermediate-frequency amplifier, amplifies and demodulates the returning signals. The frequency synthesizer uses the direct digital synthesis card, which produces two output frequencies from its two channels. The ionosonde covers an altitude range between ~ 90–1000 km with a ±3 km resolution from a pulse length of 40 μs. The system operates in two scanning modes, with the first being 180 frequencies every 300 seconds for normal ionogram output. The second mode scans 6 frequencies (3, 4, 5, 6, 7, and 8 MHz) every 100 seconds in higher temporal resolution. For noise suppression, the CADI ionosonde uses coherent pulse averaging to improve the signal-to-noise ratio. The ionogram data is stored daily, two files every hour with extensions .md4 and .md3 for ionograms with 180 and 6 frequencies, respectively. Each .md4 file has 12 ionograms of 180 specific frequencies generated every 5 minutes. The .md3 files have 36 ionograms each. Some specifications of the CADI are summarized in Table 2.

Table 2: Important specifications of the CADI ionosonde

Features	Specifications
Frequency Range	1-20 MHz
Frequency Generation	DDS-based synthesizer
Frequency Sweeps	100, 200, 400 linear or logarithmic steps
Pulse power	00 W
Pulse Coding	13-bit Barker or single pulse
Height Range	90 to 512 km (can be increased to 1000 km)
Height Resolution	6 km
Date /Time/Location identification	Recorded with each ionogram
Storage	Standard 120 MB tape backups
Compute	IBM compatible PC with at least two free 8-bit slots (5 slots for a four-receiver system)
Dimensions	Power amplifier cabinet 10 x 12 x 8 inches
Power Requirements	PC plug-in boards run off standard bus power. Power amplifier units require 110/220V, 50/60Hz, 100VA
Graphics	CGA for single receiver EGA/VGA for multiple receivers

SOURCE: CADI.

The Physics and Astronomy group of the Instituto de Pesquisa e Desenvolvimento (IP&D) operates four CADI ionosonde systems in Araguatins, São José dos Campos, Palmas, Jatai, and Manaus, all in Brazil. To process and analyze the ionograms from the CADIs, the UNIVAP Digital Ionosonde Data Analysis (UDIDA) program, developed at UNIVAP, is used. UDIDA has several features that allow for the visualization, analysis, and storage of ionograms obtained from CADI. The UDIDA allows for manual ionogram reduction/scaling where the ionospheric parameters are obtained by user inputs using mouse clicks to pick the parameters. It allows users to identify and classify Spread-F and Es layers if they are present. Figure 67 shows the interface of UDIDA showing an ionogram from Araguatins which displays ionospheric layers and how ionospheric parameters can be retrieved manually by the user. Figure 68 shows the occurrence of ESF and Es from an ionogram.

3.3 Swarm Constellation

The European Space Agency (ESA) Swarm constellation consists of three identical namely **A**lpha, **B**ravo, and **C**harlie launched into a circular near-pole orbit with 87^o inclination in November 2013 (FRIIS-CHRISTENSEN *et al*., 2008; FRIIS-CHRISTENSEN; LÜHR; HULOT, 2006; PEZZOPANE; PIGNALBERI, 2019). Initially, in the first two months, the three satellites followed each other at an altitude of 500 km. Later, they were reconfigured with Swarm A and C being lowered to fly side-by-side (lower pair), at an altitude of ~ 470 km with 1.4^o (approximately 6 minutes in local time) separation in longitude. The altitude of Swarm B, instead, was raised to 530 km in an orbital plane which has gradually gotten farther away from the other two satellites during the mission's lifetime – approximately 9 hours in local time after 4 years. The principal scientific objectives of the Swarm mission are to study fields originating both within and above the Earth and to characterize the ionospheric electric fields, currents, and other plasma processes that give rise to external magnetic fields. Figure 22 shows a picture of the three Swarm satellites before launch and Figure 23 shows the Swarm constellation projection at the equator (left panel) and the poles (right panel).

Figure 22: Picture of the three Swarm satellites before they launch.

SOURCE: ESA.

An Electric Field Instrument (EFI), consisting of a pair of Thermal Ion Imagers (TIIs), and a pair of Langmuir probes (LPs) is installed on all three satellites (KNUDSEN *et al.*, 2017). The TIIs have been designed to measure 3-D ion drift velocities and ion temperatures, and the LPs measure ion density from the high-gain probe (during the negatively biased portion of the sweep) and electron density (Te) from both high- and low-gain probes with a 2 Hz resolution (FRIIS-CHRISTENSEN *et al.*, 2008; FRIIS-CHRISTENSEN; LÜHR; HULOT, 2006; KNUDSEN *et al.,* 2017).

Figure 23: Projection of the Swarm overtime at the equator (left panel) and the poles (right panel).

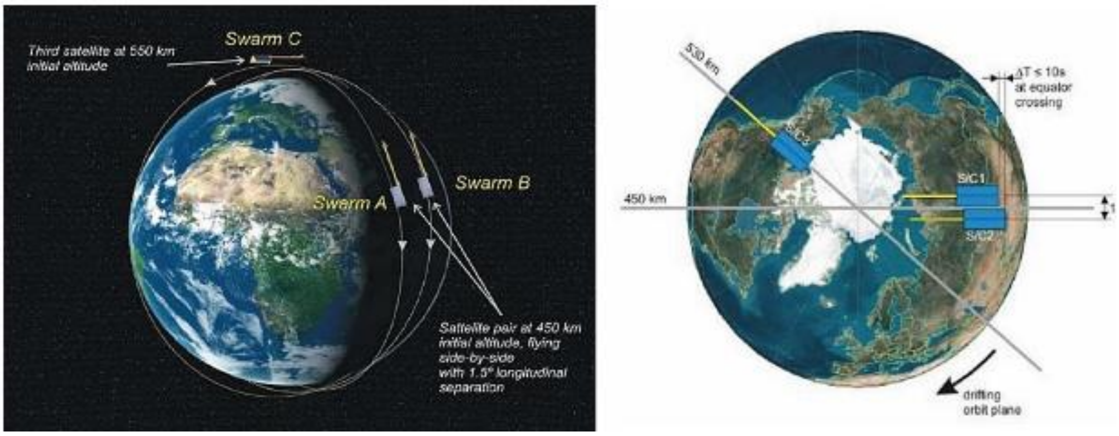

SOURCE: ESA.

3.4 Global Navigation Satellite System

Global Navigation Satellite System, GNSS, is the generic name given to systems of navigation satellites that are being developed and deployed by governments, commercial entities, etc. into orbit. They are constellations of satellites that provide position and timing signals from space around the globe. The ionosphere is assumed to be a thin layer in GNSS processing so signals from global navigation satellites must transit the ionosphere on their way to the receivers. GNSS provides for both military and civilian navigation and position use and has now become integrated into our daily lives. The GNSS receivers can also provide space scientists with a means to monitor ionospheric instabilities.

The United States of America department of defense developed a navigation system called the NAVSTAR in the 1960s, currently the Global Positioning Systems (GPS). It went into full operations globally in 1993. It is a satellite-based system made up of 32 or more artificial satellites orbiting the Earth in 6 distinct but uniformly distributed orbital planes at an altitude of 20, 200 km. Each GPS satellite circles the Earth every 12 hours with an orbital speed of about 14000 km/h in a precise orbit continuously transmitting signals that provide positioning, navigation, and timing information to military and civilian users worldwide using triangulation. GPS satellites are not in geosynchronous or geostationary orbits. The satellites are distributed such that at any point on Earth up to 12 satellites at one time or at least 4 satellites are always visible at any given time. Each satellite carries with it an atomic clock with an accuracy of 1 nanosecond to reduce errors.

The Global'naya Navigazionnaya Sputnikovaya Sistema, GLONASS was also developed in the 1980s by the Russians during the cold war for communication purposes. GLONASS is made of 24 satellites. Another well-known global navigation system is the Chinese BeiDou Navigation System (BDS) started deploying in the 2000s with the first generation, BeiDou-1 being launched with 4 satellites. The third and current generation, BeiDou-3 is made of 35 satellites and was launched in 2015. BDS provides global positioning services. BeiDou is an active system, and unlike other positioning systems interacts with the users.

Galileo is a satellite navigation system conceived as a joint public-private enterprise under civilian control which is financed and managed by the European Commission (EC), and the European Space Agency (ESA), with a constellation size of 30 satellites. Galileo went live in 2016. One of the aims of Galileo is to provide an independent high-precision positioning system so European nations do not have to rely on the US' GPS or the Russian GLONASS systems. In conjunction with an industry consortium, the Japanese government developed the Quasi-Zenith Satellite System (QZSS), also known as Michibiki. It is a regional system to transmit differential corrections to GPS and other GNSS satellites and was officially started in 2018.

Each of these systems employs a constellation of orbiting satellites working in conjunction with a network of ground stations. The accuracy, availability, and integrity of GPS for civil aviation are greatly improved by employing the use of augmentation systems such Satellite-Based Augmented Systems (SBAS) like the European Geostationary Navigation Overlay Service (EGNOS), Multi-functional Satellite Augmentation System (MSAS) in Japan, Wide Area Augmentation System (WAAS) in the USA, GPS Aided Geo Augmented Navigation (GAGAN) system of India.

Each GPS satellite continuously transmits two radio frequencies in L-band, generally referred to as Link 1 (L_1) and Link 2 (L_2), respectively. The L-band covers frequencies between 1 GHz and 2 GHz. It is a subset of the ultra-high frequency (UFH) band, specially coded, allowing the receiver to compute positioning, speed, and time. The L_1 and L_2 signals are obtained by multiplying a fundamental frequency of 10.23 MHz with 154 and 120, respectively. This effectively gives the frequency and wavelength of L_1 as 1575.42 MHz and 19.0 cm and L_2, 1227.60 MHz and 24.4 cm. It must be noted that each of the constellations or systems of GNSS uses frequencies that are different from those used by GPS. A new signal called L_5 with a frequency of 1176 MHz and a wavelength of 24.48 cm has recently been introduced (KAPLAN; HEGARTY, 2017). Table 3 itemizes the GPS L-bands used, their frequencies, and wavelengths.

Table 3: L-Band GPS radio frequencies and their wavelengths

L-Band	Frequency (MHz)	Wavelength (cm)
L_1	$f_1 = 1575.42$	$\lambda_1 = 19.05$
L_2	$f_2 = 1225.60$	$\lambda_2 = 24.45$

SOURCE: (KAPLAN; HEGARTY, 2017).

The signal after reaching the receiver from the satellite is decoded and the time and phase between the satellite and receiver can be calculated. This provides the pseudorange information, P_1 and P_2, and the phase, Φ_1, and Φ_2 of the signal. From this information, the dual-frequency GPS receivers at two lower-band GPS frequencies f_1 and f_2, can be used to determine the electron content of the ionosphere in each considered station (HOFMANN-WELLENHOF; LICHTENEGGER, 2001).

3.4.1 Calculating Total Electron Content

Radio waves that pass through the ionosphere are affected by the free electrons that inhabit the ionosphere. Radio signals with a frequency of 30 MHz or less are reflected back to the Earth when they meet the ionosphere making long-distance communication on the Earth possible. Higher frequency signals such as GPS signals, on the other hand, pass through but are slowed down (refracted). This is due to the dispersive nature of the ionosphere contributing to the GPS errors. The accuracy and reliability of GPS depend on system factors (associated with the three GPS segments: space, control, and user which include errors due to satellite clock and ephemeris information, hardware, and channel biases, satellite geometry effects, and thermal noise errors) and environmental factors - are associated with propagation phenomena which include electromagnetic interference from external sources, ionospheric effects (quiet and disturbed ionosphere), tropospheric delays, and multipath (KHADKA, 2018).

Total Electron Content (TEC) is defined as the line integral of electron density on a given ray path from the satellite to the receiver (Hofmann-Wellenhof & Lichtenegger, 2001). TEC is the total number of free electrons in a cylindrical path with a 1 m^2 cross-sectional area between a radio transmitter and a receiver. Radio waves are affected by the presence of these free electrons. More free electrons along this path mean the radio signal will be affected more. For ground-to-satellite communication and satellite navigation, TEC is a good parameter to monitor for possible space weather impacts. The variation in ionospheric plasma density is affected by changing solar Extreme Ultra-Violet radiation, solar activity, geomagnetic storms, atmospheric waves, and tides that propagate up from the lower atmosphere. Thus, TEC values will have local time, latitudinal, longitudinal, seasonal, solar cycle, geomagnetic, and tropospheric dependence. In light of this, TEC has been employed in space weather research in the investigation of ionospheric variability and plasma irregularities during different periods and space weather events. TEC is measured in TEC units – TECU, where 1 TECU = 10^6 el/m^2 and is given as

$$TEC = \int_s^r Ne\, ds \tag{8}$$

Ne represents the electron density, and ds is an element of length between the satellite (s) and the receiver (r).

Slant TEC, STEC is a measure of the total electron content of the ionosphere along the ray path from the satellite to the receiver. The ionosphere-free linear combination of two different frequencies helps calculate the STEC along the line of sight between the satellite and receiver, as illustrated as shown in Figure 24. The magnitude of the error due to ionospheric effects on GPS signals depends directly on the TEC present along the path traveled by the signal, which, in turn, is related to the ionization process in the ionosphere, and inversely proportional to the square of the signal frequency. The error due to ionospheric delay ($I_{1,2}$) obtained by the pseudorange is given in equation (9). The ionospheric or signal delay is proportional to the slant TEC and inversely proportional to the square of the frequency. Since the frequencies of GNSS signal are known, it follows that ionosphere signal delay is the only function of the slant TEC as shown:

$$I_{1,2} = \frac{40.3}{f_{1,2}^2} STEC \tag{9}$$

The STEC can thus be calculated as

$$TEC = \frac{1}{40.3}\left(\frac{f_1^2 f_2^2}{f_1^2 - f_2^2}\right)\{(P_2 - P_1) - (b_p^s + b_p^r)\} \tag{10}$$

Where b_p^s, and b_p^r are the pseudorange satellite and receiver delays respectively, $f_{1,2}$ are frequencies of GPS signals, $P_{1,2}$ are P-code pseudoranges and 40.3 is a coefficient constant.

3.4.2 Calculating vertical TEC

The vertical TEC is defined as

$$vTEC = cos(z') \; TEC \tag{11}$$

where z' is the zenith angle of the signal at the ionospheric piercing point (IPP) located at the mean altitude H_m described by the following equation:

$$Sin(z') = \frac{R_E}{R_E + h_m} Sin(z) \tag{12}$$

Where R_E is the average Earth radius, h_m is the height of peak plasma density and z is the zenith angle of the satellite ($z = 90^o$- El. El is the elevation angle shown in Figure 24).

Figure 24: Geometric path of GPS signal from a satellite to ground receiver through the ionosphere.

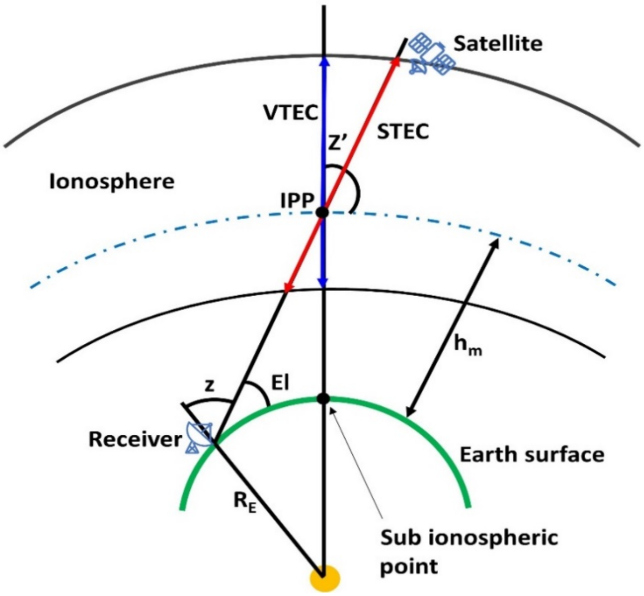

SOURCE: Adapted from (ESSIEN, 2020).

3.4.3 Rate of TEC Change

The rate of TEC change, ROT is the temporal rate of ionospheric delay. This parameter indicates the presence of large-scale ionospheric irregularities. It is calculated as the quotient between ionospheric delay and the time interval, and it is usually expressed in TECU per min. ROT is calculated as follows

$$ROT = \frac{\Delta TEC}{t_2 - t_1} \tag{13}$$

4 GROUND- AND SATELLITE-BASED OBSERVATIONS OF IONOSPHERIC PLASMA BUBBLES AND BLOBS AT 5.6^{O} LATITUDE IN THE BRAZILIAN SECTOR

4.1 Summary

This chapter describes the proposed methodology for the identification of plasma blobs in ionograms when they appear in the company of plasma bubbles in the ionosphere. Three instruments have been employed to accomplish this task. The ground-based remote sensing instruments are an all-sky imager and an ionosonde, both located at Araguatins (5.65° S, 48.07° W, and dip-latitude of 4.17° S). The two instruments located in the same region means that they will observe the same ionosphere irregularities that occur in the overhead ionosphere thereby providing a unique opportunity for the specific study. Simultaneous observation means that whatever will be observed in one instrument in time will be the same observed in the other. There will not be significant time lags that will introduce disparities in the observations between the two instruments. In-situ plasma density measurements from the Swarm constellation will be used to complement the results from the ground instruments to verify the occurrence of the structures at swarm altitudes. The methodology being proposed uses ionosonde to observe and study plasma blobs as this addresses the weather and lighting limitations of an optical instrument like the all-sky imager, allowing for continuous, observation and regions where only ionosonde is available. The results would be presented case-by-case (night-by-night) allowing for comparison among the three techniques employed in the study.

4.2 Background

The occurrence of plasma bubbles and blobs has been observed and studied using several instruments and techniques: from remote sensing to in-situ, optical to radio, etc. (CHERNIAK; ZAKHARENKOVA, 2016; HUANG *et al.*, 2014; OYA; TAKAHASHI; WATANABE, 1986; PIMENTA *et al.*, 2004, 2007; SIDDIQUI *et al.*, 2015; WU *et al.*, 2018). While plasma bubbles are plasma-depleted regions in the ionosphere, blobs are regions in the ionosphere where plasma density is enhanced. Oya; Takahashi; Watanabe (1986) and Watanabe; Oya (1986) first reported the observation of blobs, and since the study of the high plasma density ionospheric irregularity has been studied by various authors using satellite, radar, or optical techniques (KIL *et al*., 2011, 2019; PARK *et al*., 2003; PIMENTA *et al*., 2004, 2007; TARDELLI-COELHO *et al*., 2017; WANG *et al*., 2019).

Several theories have been proposed to explain the generation and source of plasma blobs with some suggesting that blobs occur simultaneously with bubbles and that bubbles could be causing the incidence of the blob (LE *et al*., 2003; PIMENTA *et al*., 2004, 2007) while others have reported that the occurrence of blobs could be due to medium-scale traveling ionospheric disturbances (MSTIDs) or gravity waves (GWs) (KIL et al., 2019b; MILLER *et al*., 2014; WANG *et al*., 2019). Still, plasma blobs have been observed in regions where plasma bubbles were reportedly absent (KIL *et al*., 2011), indicating that blobs could indeed be generated from other sources other than plasma bubbles. Based on the simultaneous observation of backscatter plumes and bubbles, and the observation of plasma density enhancements associated with plasma bubbles, it has been suggested that there is a link between bubbles and blobs occur at any altitude or latitude in the ionosphere during the generation and evolution of bubbles (HUANG *et al*., 2014; YOKOYAMA; SU; FUKAO, 2007).

All-sky imaging systems have been used over the year for the study of plasma blobs and/or bubbles in all sectors (PIMENTA *et al*., 2004, 2007; TARDELLI-COELHO *et al*., 2017). Even though ASIs are very important in ionospheric studies and the observation of plasma bubbles and blobs, the ground-based optical system has a few limitations such as moonlight and weather conditions (like cloud cover). This does not make them ideal for continuous observations all year round as such different techniques and instruments have been used for the study of plasma irregularities. One such instrument is the ionosondes which employ radio waves in their operations and therefore are not susceptible to the same limitations as the all-sky imagers. The ionosonde has been used for the study of plasma-depleted irregularities (bubbles) for many decades in a few studies for the observation of blobs (NARAYANAN *et al*., 2014; PIMENTA *et al*., 2004, 2007; WANG *et al*., 2019). The square of the reflected frequency is proportional to the plasma density of the ionosphere where the signal was reflected drawn on the ionograms such plasma depleted -bubble- regions of the ionosphere would reflect signals at lower frequencies while plasma-enhanced regions, blobs are expected to reflect signals of higher frequencies. Therefore, it is expected that plasma bubbles observed in all-sky images would be associated with low-frequency echoes, and plasma blobs are observed as higher-frequency Spread-F echoes on the ionograms.

Investigating equatorial spread-F echo characteristics, Calvert; Cohen (1961) reported that the main features of ESF echoes seen in ionograms depend on the scattering irregularities and their horizontal distribution with respect to the location of the ionosonde. According to Narayanan *et al.* (2014), the maximum frequency within Spread- F is dependent on the electron densities inside the irregularity and does not the virtual height when they move towards the ionosonde. So, in a uniformly stratified ionosphere, within the field of view of the ionosonde, the electron densities remain the same as that for both oblique and vertical incidence ray paths. Since the plasma frequency is proportional to the electron density, oblique reflections do not show any pseudo enhancement or reduction in the plasma frequency. However, when there is an incidence of plasma blob or bubble, the reflections will show high or low frequencies, respectively. Fagundes *et al.* (2012) observed Spread-F features in ionograms from São José dos Campos and Cachoeira Paulista which they christened as atypical Spread-Fs. They observed these features beyond the critical frequency and virtual height and associated them with MSTIDs but not plasma blobs. However, in other studies, Wang *et al.* (2019), Narayanan *et al.* (2014), and Pimenta *et al.* (2004; 2007) have observed high-frequency reflections on ionograms and have linked them to plasma blobs.

4.3 Data and Methodology

First, airglow images with the absence of plasma irregularities will be presented. The ionograms for this period will also be present to ascertain the nature of the ionosphere. In the absence of irregularities, the ionograms are not expected to show any Spread-Fs (neither high nor low-frequency spreads). Then airglow images showing the signatures of plasma bubbles will be shown together with corresponding ionograms. The ionograms corresponding to plasma bubbles in the airglow images should present low-frequency Spread-Fs. These two cases will highlight the difference in ionograms of the overhead ionosphere with the presence or absence of irregularities (that are not blobs). The third scenario will demonstrate the nature of the ionograms when ionospheric irregularities including bubbles and blobs are observed in the OI 630.0 nm nightglow images. In this scenario, the ionograms are expected to present Spread-Fs that cover low to high-frequency ranges (high- and low-frequency Spread-Fs) that correspond to the depleted (bubble) and enhanced (blob) density regions of the ionosphere at the time of the observation. The differences among these three types of ionograms due to the different observations in the airglow images will determine whether or not the ionosonde shows the occurrence of blobs in the ionograms or not.

4.3.1 Simultaneous observation of bubbles/blobs and ESFs

OI 630.0 nm nightglow images and ionograms from an all-sky imaging system and ionosonde located at Araguatins were used. Observations from 8 nights (nightglow images and ionosondes) were selected from 2017. These data were obtained from ARA (5.65° S, 48.07° W, and dip-latitude of 4.17° S), a near-equatorial station in Brazil. The OI 630.0 nm nightglow emission images used in this study were recorded at intervals of 3-4 min considering the operation sequence and the number of filters used by the imager system. The all-sky imaging system is capable of visually capturing and characterizing the morphology of plasma bubbles and blobs over wide regions of the sky (for example, at 250 km altitude, 75° zenith angle (Z.A)., the FOV of the ASI is approximately 1800 km in diameter – see Figure 25).

Figure 25: Map of South America showing the location of Araguatins in Brazil. geographic and magnetic equators and the FOVs of the imager system and ionosonde.

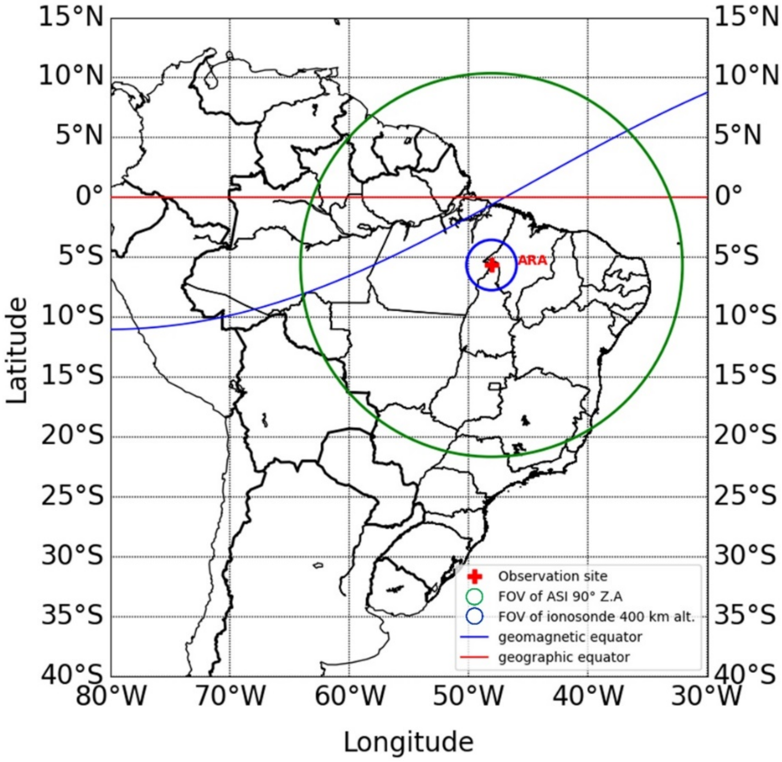

SOURCE: Author.

The magnitude of the FOV of the image coupled with the unique configuration of the geomagnetic equator around the Brazilian equatorial region makes the ASI at ARA uniquely positioned to observe the Spatio-temporal variation of OI 630.0 nm nightglow emission intensities and the development and morphology of ionospheric irregularities and waves. The imager has a FOV that spans from low-latitude southern hemisphere-equatorial regions and to-low-latitude in the northern hemisphere between 20° S to 10° N. The captured OI 630 nm nightglow images for each night were visually inspected and analyzed using the UASDA program to determine the presence or otherwise of plasma irregularities (bubbles and/or blobs). Specific airglow images were chosen from each night to demonstrate the occurrence or lack thereof of an irregularity and then were linearized using UASDA.

Ionograms from CADI, which operates at the same station as the imager provided the ionograms for this investigation. The ionograms used coincided with the nights of the nightglow images selected. The ionograms are stored at 5-minute intervals. The ionograms allow us to get ionospheric parameters and manually identify nighttime plasma density profiles and Spread-F configurations using UDIDA. The presence or absence of equatorial range Spread-F and its duration are observed and identified in the ionograms to compare with the structures observed in the OI 630 nm nightglow images.

The geographical location of Araguatins, ARA is shown on the Brazilian map in Figure 25. Also, on the map are shown the geographic (red line) and geomagnetic (blue) equators. The green circle is the imager's field of view at 90° zenith angle (Z.A) and 250 km altitude. At 90° Z.A., the ASI covers ~ ± 16° lat/lon which corresponds to a diameter of ~ 3500 km (NADE *et al.*, 2014; SHARMA *et al.*, 2018). The blue circle represents the FOV of the ionosonde at ~ 400 km altitude corresponding to a horizontal diameter of ~ 462 km which is approximately ± 2.1° lat/lon (PILLAT; FAGUNDES; GUIMARÃES, 2015).

Table 4 summarizes the selected nights into instruments and observed events. These nights were selected specifically to show the specific scenarios previously discussed. They show clear signatures of plasma bubbles and blobs or lack of irregularities with no clouds. Also, due to limitations of the ASI, resulting from weather and light conditions, it was difficult to get more data that depicted clearly the cases being discussed and to simultaneously observe bubbles and blobs at the same time to obtain corresponding ionograms. The selected nightglow images are linearized using UASDA, which is equipped with a linearization feature. The scanning method incorporated in the UASDA is used to determine the variation of OI 630.0 nm nightglow emission intensity across the images along scanning lines. The relative nightglow intensities along scanning lines are plotted against longitude for different nights as shown in Figure 26, right panel. This way, the occurrence of bubbles and blobs which corresponded to reduced and enhanced OI 630.0 nm nightglow emission intensities respectively can be verified.

Table 4: Summary of phenomena observed by the different instruments used.

Date	ASI observations		Ionosonde observation		SWARM depletion		
	Bubbles UT	Blobs UT	Spread-F UT	Atypical ESF (UT)	A (UT)	B (UT)	C (UT)
07 Mar	absent	absent	absent	absent	absent	n/a	absent
29 Sep	05:02	absent	05:00	absent	n/a	04:41-05:05	n/a
14 Sep	01:02	01:43	01:20	01:43	02:07-02:28	n/a	02:07-02:28
12 Oct	00:03	00:03	00:05	00:05	n/a	03:45-04:06	n/a
21 Oct	01:04	01:24	01:05	01:25	n/a	02:28-02:49	n/a
23 Oct	01:33	01:54	01:35	01:55	n/a	03:25-03:46	n/a
20 Nov	01:36	01:56	01:35	01:55	n/a	00:50-01:11	n/a
21 Dec	01:03	01:03	01:05	01:05	03:20-03:41	n/a	03:20-03:41

SOURCE: Author.

Figure 26-left panel shows linearized nightglow images and corresponding relative intensity variation plots. The blue circle indicates the FOV of the ionosonde at 400 km altitude. The red and green horizontal lines are the scanning paths on two images obtained at different times. The bubbles and blobs are seen in the middle and bottom panels and fall within the FOV of the ionosonde. The right panels are the OI 630.0 nm nightglow emission intensities determined across the red and green horizontal lines.

Figure 26: Linearized OI 630.0 nm nightglow images from Araguatins – Brazil (left panel), with scanning lines for different times (green and red lines), and OI 630.0 nm emission intensity plots (right panel)

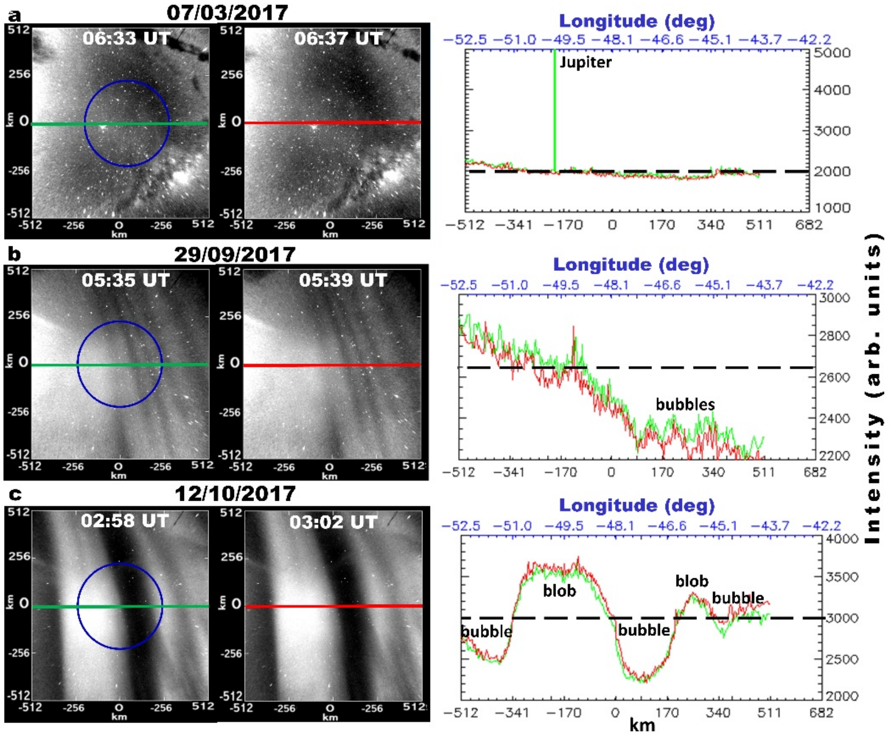

SOURCE: Author.

On the intensity plots, the black dashed lines represent the background OI 630.0 emission intensity at the time the images were recorded. Plasma blobs and bubbles are indicated on the plots where present. The background nightglow emission is determined from the undisturbed, smooth nightglow emission that is observed outside intensity enhancements or depletions from the image and can be determined quantitatively along any scanning line through the image. The OI 630.0 nm nightglow emission intensity for plasma blobs and bubbles is defined relative to the background intensity of the region and at the time of measurement (NADE *et al.*, 2014; SHARMA *et al.*, 2018). Based on this, the measured plasma intensities measured inside the blobs captured in this study presented intensities of up to 16 - 26 % of the background intensity and up to 100 % of the plasma bubble intensity.

With airglow images selected and analyzed for the occurrence of irregularities for these nights and irregularities confirmed from the intensity plots, corresponding ionograms were analyzed to determine the nature of the ionosphere or ESF structures if present. Sample comparison between OI 630.0 nm nightglow images and ionograms are shown in Figure 27.

Three different nights of observations are presented in Figure 27 – from top to bottom 07 March, 29 September, and 12 October 2017, respectively. In the left panel are the airglow images and the corresponding ionograms are shown on the right. Using these 3 examples from simultaneous observations with a collocated imager and ionosonde it is possible to compare the structures observed separately by each instrument and establish a methodology to identify in ionograms the plasma blobs in the company of plasma bubbles when they occur.

Figure 27: Comparison between different nightglow images showing various structures (or not) and ionograms recorded at the same time.

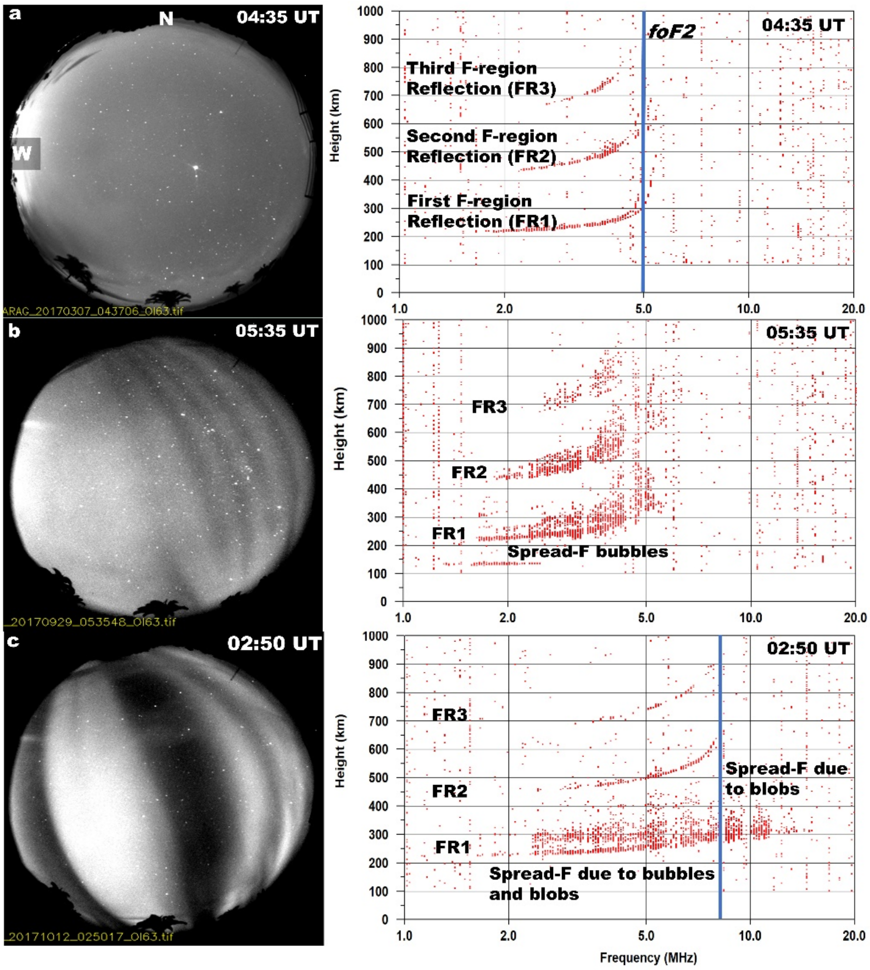

SOURCE: Author.

As a necessity, two test cases (nights) are chosen to compare the cases with the occurrence of blobs. These cases are chosen to test the nature of the ionogram behavior when there are no irregularities and when there are EPBs in the nightglow images. The OI 630.0 nightglow image in the first panel of Figure 27 shows no signatures of irregularities or waves with quasi-homogeneous nighttime ionospheric OI 630.0 nm nightglow emission. The corresponding simultaneous ionogram recorded shows a typical nighttime ionospheric F-layer profile with several other reflections. The ionogram also shows ordinary and extraordinary traces (echoes). Notice that all 3 F-region reflections, the first, second, and third reflections (FR1, FR2, and FR3 respectively) are quite similar in shape and have comparable foF2s. The blue vertical line demarcates the critical frequency. This gives a representation of the nature of the ionogram when there are no irregularities overhead.

The middle panel, OI 630.0 nm nightglow image shows the occurrence of plasma bubbles only. The corresponding ionogram recorded almost at the same time shows a typical range spread-F structure (PILLAT; FAGUNDES; GUIMARÃES, 2015). The echoes in the ionogram go up to 5 MHz and spread. This is a typical signature of reflections from irregularity-filled plasma-depleted regions. Notice that the first and second F reflection echoes recorded have quite similar shapes and characteristics. It is not possible to determine the exact foF2 from the ionogram in this case hence the absence of the blue vertical line.

The third case is shown in the bottom panel of Figure 27. The OI 630.0 nm nightglow image shows dark and bright north-south bands almost aligned to the Earth's geomagnetic field. These are the signatures of bubbles and blobs, respectively. This bright structure has homogeneous longitudinal intensity and is almost aligned with the magnetic field (following nearly the same latitudinal shape and orientation as the plasma bubble). The ionogram on the right presents an atypical kind of range Spread-F. First, the echoes of the range Spread-F frequencies extend up to and beyond 10 MHz. The FR1 trace is quite different from the FR2 and the FR3. In this specific case, the FR1 is particularly different from the FR2 and FR3, however, we observe that the higher-frequency echoes of the FR1 do not appear in the FR2 and FR3. While the FR1 contains spread, the FR2 and FR3 show typical profiles. The foF2 (blue vertical line) can only be determined from the higher-order reflections.

This ionogram corresponding to the airglow image during the occurrence of a blob shows a marked difference from the two previous events. The nature of the ionogram indicates that this ionogram recorded the superimposition of the signature of the bubbles and blobs. This assumption can only be put forward because of the advantage that is gained from using simultaneous observations from ASI and ionosonde located in the same place observing the same ionosphere above. Beyond the blue vertical line are the echoes at higher frequencies from high plasma density regions. The ESF structure observed here is dubbed atypical ESF and an ESF structure is considered “atypical” when high-frequency echoes reflected from high plasma density regions (blobs) occur together with low-frequency reflections (“typical” ESF) from low plasma density regions (bubbles).

4.3.2 Plasma Density measurements from Swarm.

The plasma density measurements from the LP on board the Swarm satellites presented in this thesis were obtained freely from the ESA website at ftp://swarm-diss.eo.int. Level 1b electron density measurements at a 2 Hz rate (EFIx_LP) made by Langmuir probes were used to make the plasma density plots (NIELSEN, 2019). The Level-1b products of the Swarm mission contain a time series of quality-screened, calibrated, and corrected measurements given in physical, SI units in geo-localized reference frames. Level-1b products are provided individually for each of the three satellites Swarm A, Swarm B, and Swarm C on a daily basis i.e., each product contains all available data for that day from 00:00 until (but not including) 24:00 UT time. The Level 1b data files were downloaded from ftp://swarm-diss.eo.int/Latest_baselines/EFIx_LP/. Daily zipped cdf has been organized into three folders each for one Swarm satellite. The cdf files contain the electron density measurements, information on Universal Time, and geographic coordinates.

Swarm's electron density data are provided with two flags, one indicating the source of measurements (*Flags_LP*), the other characterizing the plasma density measurements (*Flags_Ne*), as reported in the Swarm L1b Product Definition (NIELSEN, 2019). Only the most reliable measurements, those with *Flags_LP*=1 and *Flag_Ne*≤29 were used to make the graphs for the days and periods selected for this study.

Swarm data have been analyzed by developing a Python script to select, open and read cdf files, calculate Local Time and Quasi-Dipole magnetic coordinates, and filter measurements through flags. Selected data are stored in .txt files. Then, another Python script is used to plot the selected data to obtain the plasma density variation graphs. In these plots, Swarm electron density data are scattered along the satellite path at altitudes within the ionosphere (in-situ), no interpolation and smoothing has been applied to data to arrive at the results presented. Since the ground-based ionosonde and all-sky imaging systems observe the bubbles and blobs at the bottom of the F-region ionosphere, the Swarm data is used to complement the observations and show that the observations from the ground stations extend to the topside ionosphere at the Swarm altitudes.

4.4 Results and Discussion

4.4.1 Ionosphere without irregularities

OI 630.0 nm nightglow emission images from ARA from 07 March 2017 between 04:30 – 06:30 UT are selected. These images show no signatures of ionospheric plasma irregularities (blobs/bubbles) or waves. This night and time are chosen to demonstrate the nature of the OI 630.0 nm nightglow emission in the absence of plasma irregularities. The sequence of nightglow images shows smooth homogeneous OI 630.0 nm nightglow emission in Figure 28a. In the middle and at the upper left-hand corner of the images light from Jupiter and external sources are observed, respectively. The homogeneity observed in the OI 630.0 nm nightglow images is indicative of the absence of structure inside the ionosphere and the FOV of the imaging system.

Figure 28: a) OI 630.0 nm nightglow images over Araguatins 04:30 UT - 06:30 UT on 07 Mar 2017. The images depict an ionosphere devoid of irregularities and waves and b) Linearized nightglow images (upper panel), and nightglow emission intensity plot (lower panel).

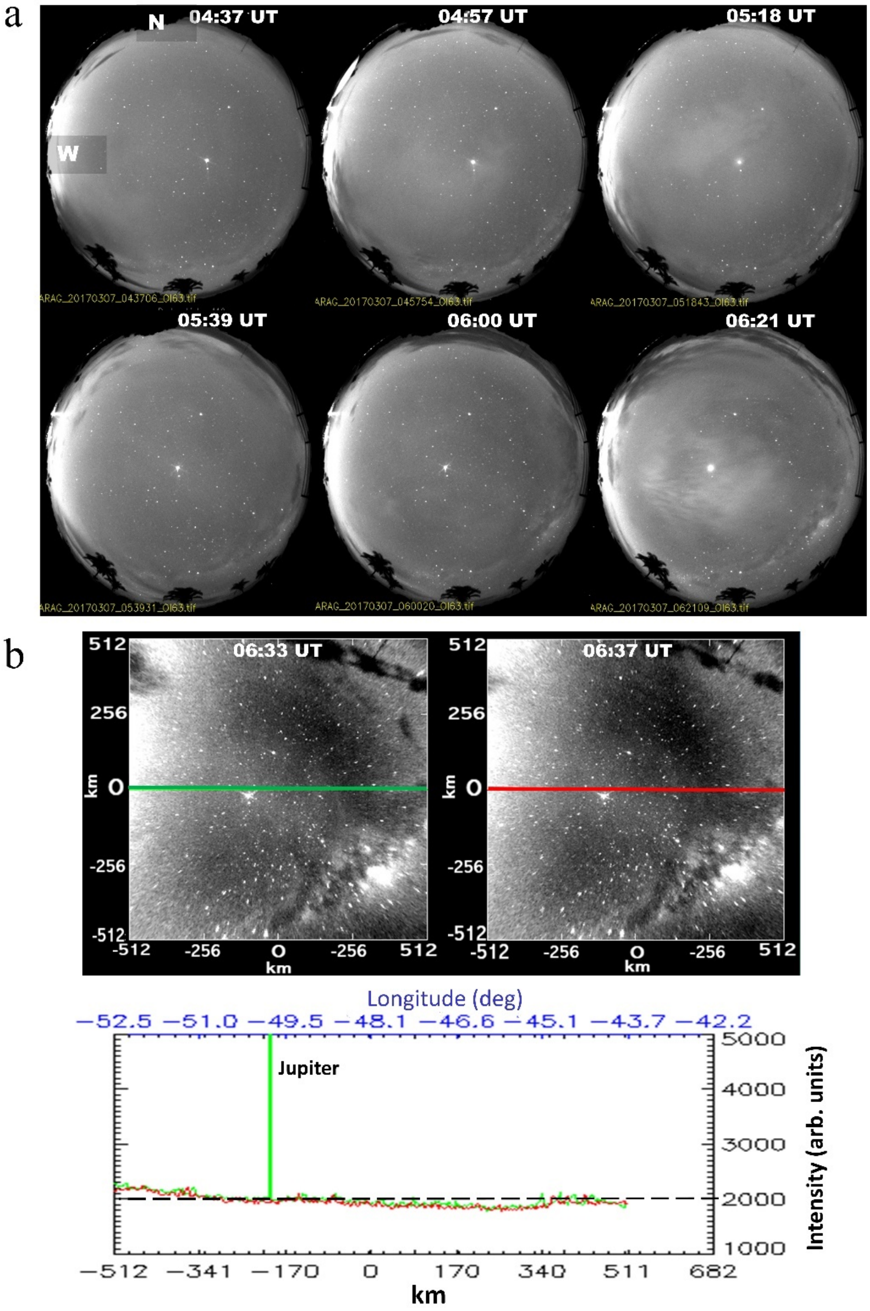

SOURCE: Author.

Figure 28b shows sample linearized OI 630.0 nm nightglow images. The relative nightglow emission intensities are determined across the horizontal lines (red and green) across the images and plotted to determine the emission intensity spikes or drops that represent blobs and bubbles, respectively. The plot shows an almost linear graph of the relative intensity with relatively no local highs or lows in the intensity profile, meaning there were no plasma enhancements, depletions, or even wave phenomena in the ionosphere at the time. This is typical of the background OI 630.0 nm emission intensity profile in the absence of blob, or bubble activity.

Figure 29 shows a sequence of ionograms recorded simultaneously as the OI 630.0 nm nightglow images. The ionograms show a typical nighttime ionospheric F-layer bottom side profile with no observable Spread-F signatures with ordinary and extraordinary traces. The ionograms also show the first, second, and even third F-region reflections of the ionosphere. All the reflections show similarities in their structures. The measured foF2, which is proportional to ionospheric plasma density, recorded was up to 5 MHz. The ionospheric profile presented in the ionograms depicts an ionosphere free of irregularities consistent with the nightglow emission intensity profile from the ASI presented in Figure 28a and b.

Figure 29: Simultaneous ionograms recorded with nightglow images depicting a typical nighttime ionospheric profile.

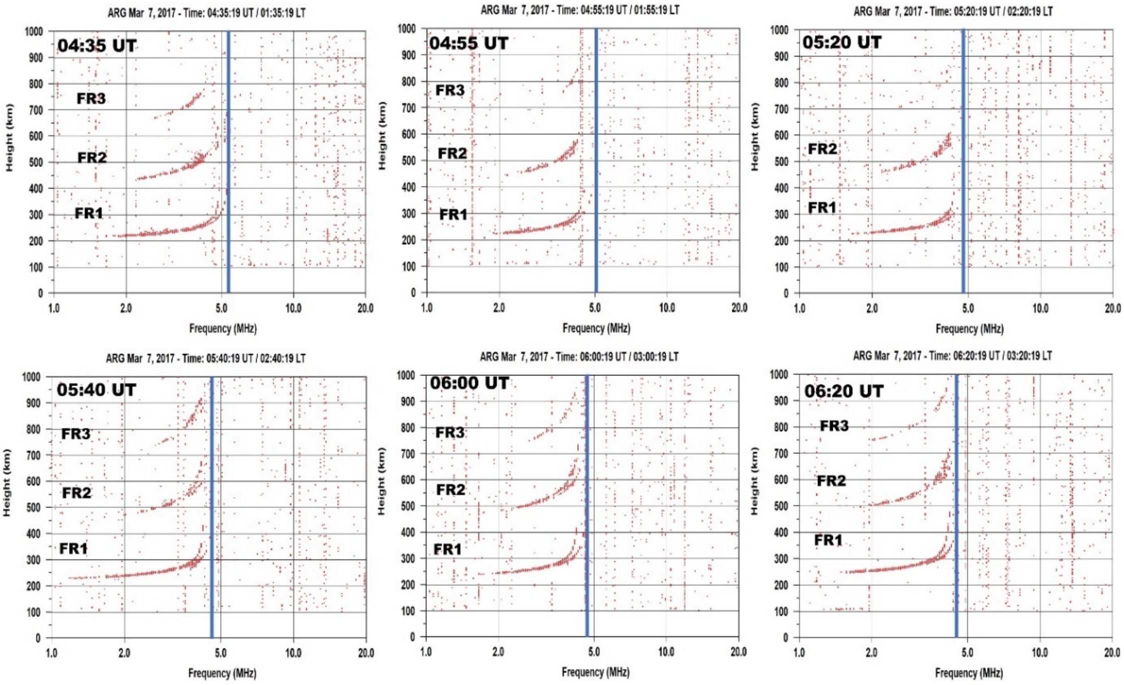

SOURCE: Author.

Plasma density variations at the top side of the ionosphere from Swam satellites A and C are shown in Figure 30. These paths are the closest the two satellites could get to the observation site on this night, 07 March 2017, within the period of the studies. Swarm A and C observations show plasma density measurements with high plasma density near the geomagnetic equator and wavelike oscillations at low latitude regions. These high plasma densities observed in the southern hemisphere could be a blob, but the two-ground-based observations could not pick them possibly due to altitude and the distance between the satellite paths and the observation area. This could explain the difference between remote sensing and in-situ observation within that time window.

Figure 30: Plasma density measurements from Swarm A and C. The left panel shows the map of South America with the location of Araguatins (black star), and the green and blues circles show the FOV of the imager and ionosonde, respectively. The multicolored vertical line is the path of the satellites, and the magenta is the magnetic equator. In the right panel, the dashed black line is the geographic latitude of the observation site, and the dashed magenta line shows the geographic latitude at the point the satellite crosses. The contour-colored curve shows the plasma density variations along the satellites' paths.

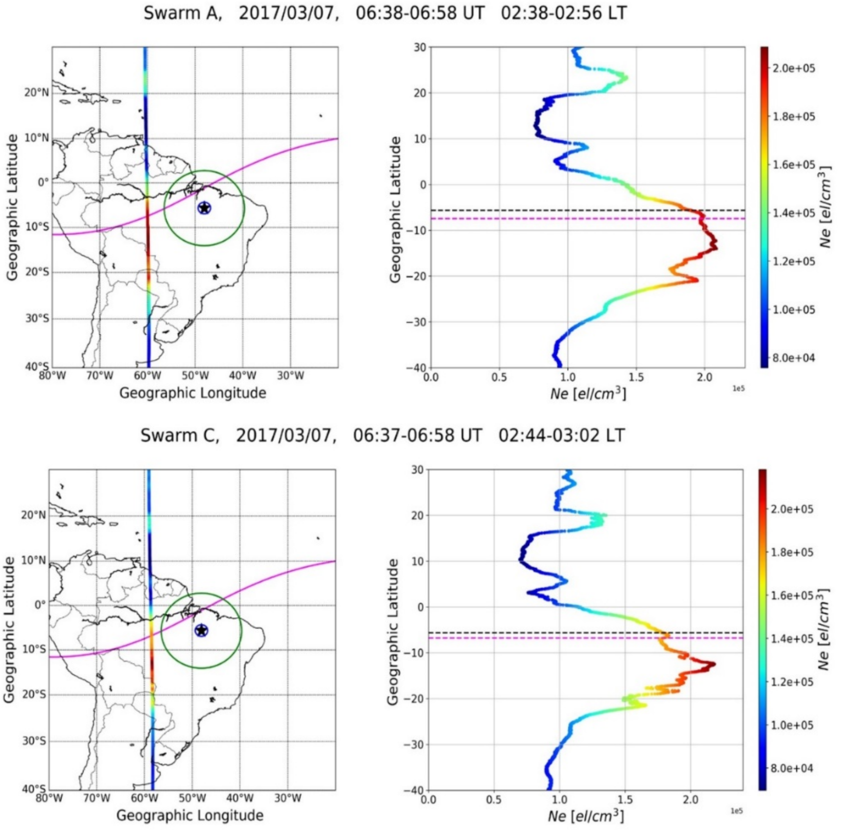

SOURCE: Author.

4.4.2 Ionosphere with plasma bubble occurrence

Figure 31a presents OI 630.0 nm nightglow emission images from 29 September 2017 showing the occurrence of multiple EPB signatures. The observations from this night show contrasting airglow intensity variations in Figure 28a. The sequence of images shows a series of depleted plasma density regions in the OI 630.0 nm nightglow emission background. From the sequence, it can be observed that the depleted density regions (bubbles) drift eastward across the FOV of the imaging system. The bright region on the left side of the images, however, consistently stayed in the same place throughout the observations without any change in position. This shows that this bright region could be resulting from external light sources and not from a blob.

Figure 31: a) Observation of plasma bubbles from OI 630.0 nm nightglow images obtained on the night of 29 September 2017 b) Linearized nightglow images for 29 September 2017 showing depleted plasma regions (above), relative OI 630.0 nm nightglow emission intensity plot (below) showing region of low intensity due to plasma depletion (bubble).

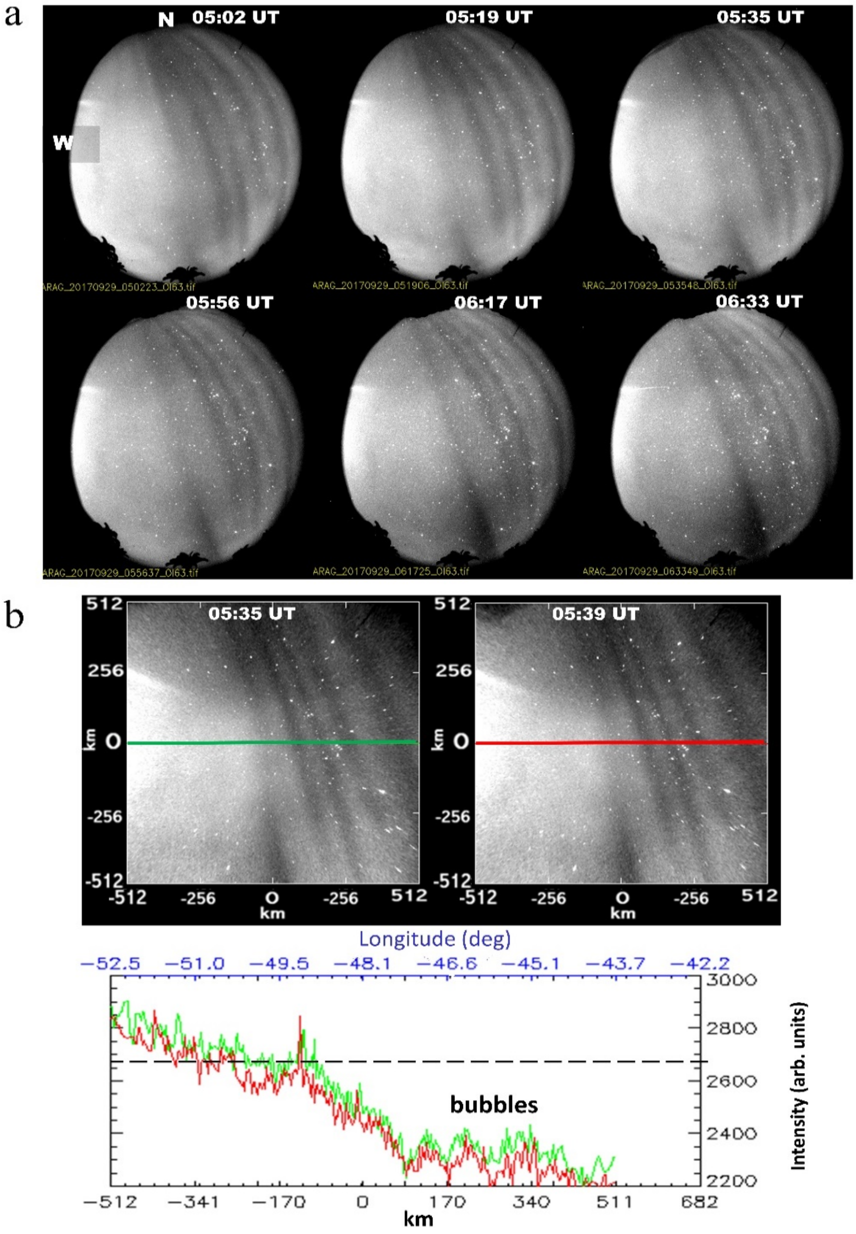

SOURCE: Author.

The OI 630.0 nm nightglow emission relative intensity plots obtained from selected linearized images within the observation period show a region of reduced nightglow emission intensity lower than the background intensity levels (horizontal black dashed line) for that period. This reduced intensity results from depleted plasma density regions as shown in Figure 31b**.** The depleted plasma density region contains several other small-scale irregularities. The variations observed in the intensity plot compare favorably with the intensity depletions in the raw nightglow images from Figure 31a but are different from the results from Figure 28b.

Accordingly, the sequence of simultaneous ionograms captured as shown in Figure 32 shows range type ESF occurrence. Since the spread (Spread-F) on ionograms are reflections from irregularities of different scale sizes from inside plasma bubbles above the ionosonde, ESFs provide evidence of the occurrence of plasma bubbles/irregularities in the ionosphere. Thus, the simultaneous observation of 'low-frequency' ESF on the ionograms indicates the occurrence of localized depleted plasma density region – EPBs as shown in Figure 31a and Figure 31b. The ionograms in Figure 32 show different structures and profiles from that presented in Figure 29 which does not show any form of spread but a typical nighttime F-region profile.

Figure 32: Ionograms obtained on the night of 29 September show equatorial Spread-F structures.

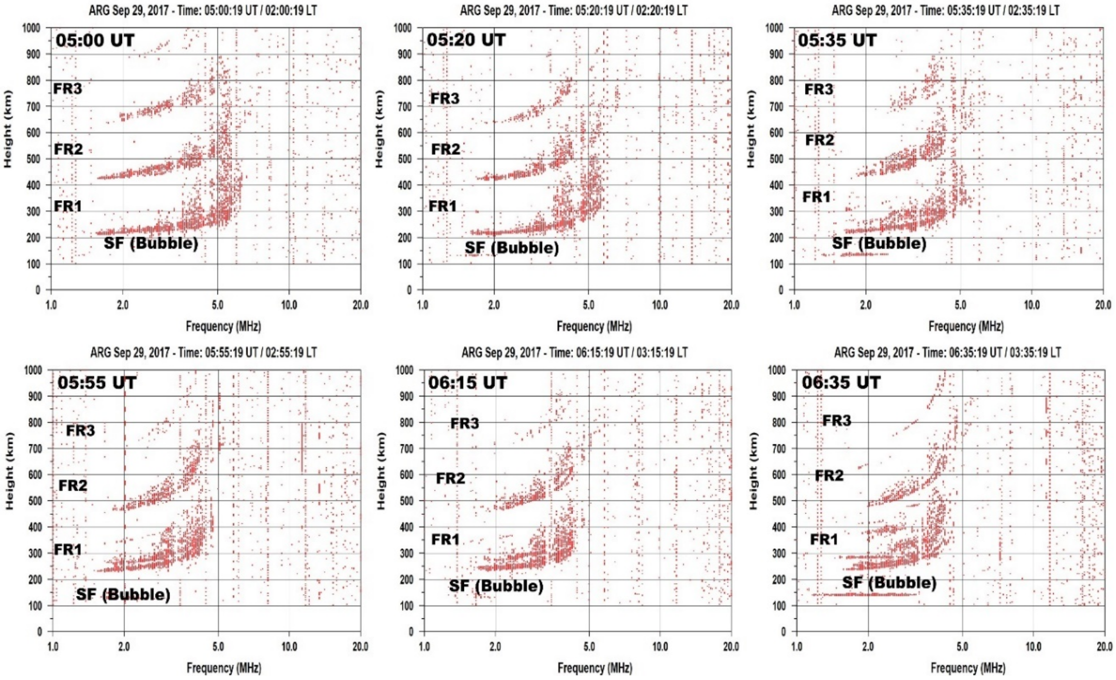

SOURCE: Author.

Since the plasma density of a region in the ionosphere is proportional to the critical frequency, it is expected that ESF that is normally associated with depleted plasma regions reflect radio signals at lower frequencies and show low-frequency echoes on ionograms below the critical frequency of the ionosphere at that region at that moment. It is not possible to measure accurately the critical frequency during an ESF event. It can however be shown that the echoes associated with the ESF show frequencies that are a little beyond 5 MHz initially and decreases with time. This decrease in frequency corresponds with the decrease in the overall plasma density of the overhead ionosphere. The ionograms from Figure 32 and Figure 29 have something in common though, that is the higher reflections, FR2 and FR3 look similar to the FR1 in both structure/form and frequency threshold. As will be shown in a later section, these features will be different when there is a blob event.

Within this observation period, the Swarm B satellite passed over the observation area. The plasma density measurements presented here are from this satellite only. The latitudinal plasma density measurement is presented in Figure 33. The plot shows significant latitudinal variation along the path of the satellite. Enhanced and depleted plasma density regions are observed between 15° north and 5° degrees south. Inside the depleted plasma density region, strong density variations associated with large-scale ionospheric irregularities are observed. This corresponds to the observed EPBs and ESFs observed in the OI 630.0 nm nightglow images and ionograms, respectively. The high plasma density peak observed in the southern hemisphere does not seem to have been observed by the ground instruments.

Figure 33: Plasma density measurement from Swarm A on 29 September 2017. Plot details are the same as in Figure 30.

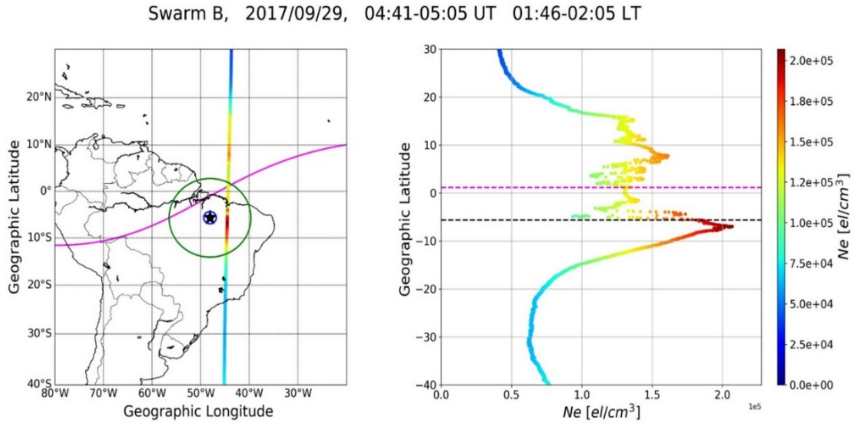

SOURCE: Author.

The disparity could be because the Swarm satellite measures the topside ionosphere, at altitudes even beyond Swarms A and C, while the ground-based observations are made at the bottomside of the ionosphere and as ESF is associated with irregularities at the bottom side, the plasma density peak observed might be only at higher altitudes above the F-layer peak height where plasma density could have been pushed by the $\vec{E} \times \vec{B}$ vertical drift. It could also be due to the small-time difference between the satellite passing and the commencement of the ground-based measurements thereby causing a temporal disparity in the structures observed from the two perspectives as shown in Figure 33.

4.4.3 Ionosphere with simultaneous bubbles and blobs

In the previous two sections, an effort was made to demonstrate the connection between the structures, or lack thereof, in airglow images and the nature of the traces in ionograms. The ionograms showed that when there are no irregularities above, the ionograms show a typical nighttime F-region profile devoid of ESF. On the contrary, when there is depleted plasma density above, the ionograms show ESF structures. However, both cases showed that the ionograms irrespective of whether there are bubbles or not, the other F region reflections show similar structures and that they have comparable “foF2” values.

In Figure 34a, a series of OI 630.0 nm nightglow images captured on the night of 14 September 2017 show the simultaneous occurrence of plasma bubbles (dark regions) and blobs (bright regions). The two structures are aligned almost along the geomagnetic field lines, an indication that they are plasma-density structures (KRALL *et al.*, 2010). Between 01:43 UT and 02:04 UT, a large-sized bubble is observed almost covering the entire surface of the image, with two bright regions seen at the west and eastmost edges of the image. However, as time passed, the blobs and bubbles drifted eastward as the west blob drifted to the center of the image, and the east blob drifted out of the field of view of the imager. By 03:27 UT, the eastmost blob had drifted completely out of view.

Figure 34: a) OI 630.0 nm nightglow emission images showing the occurrence of plasma bubbles and blob captured on 14 September 2017 b) Linearized nightglow images and emission intensity plot for 14 September 2017.

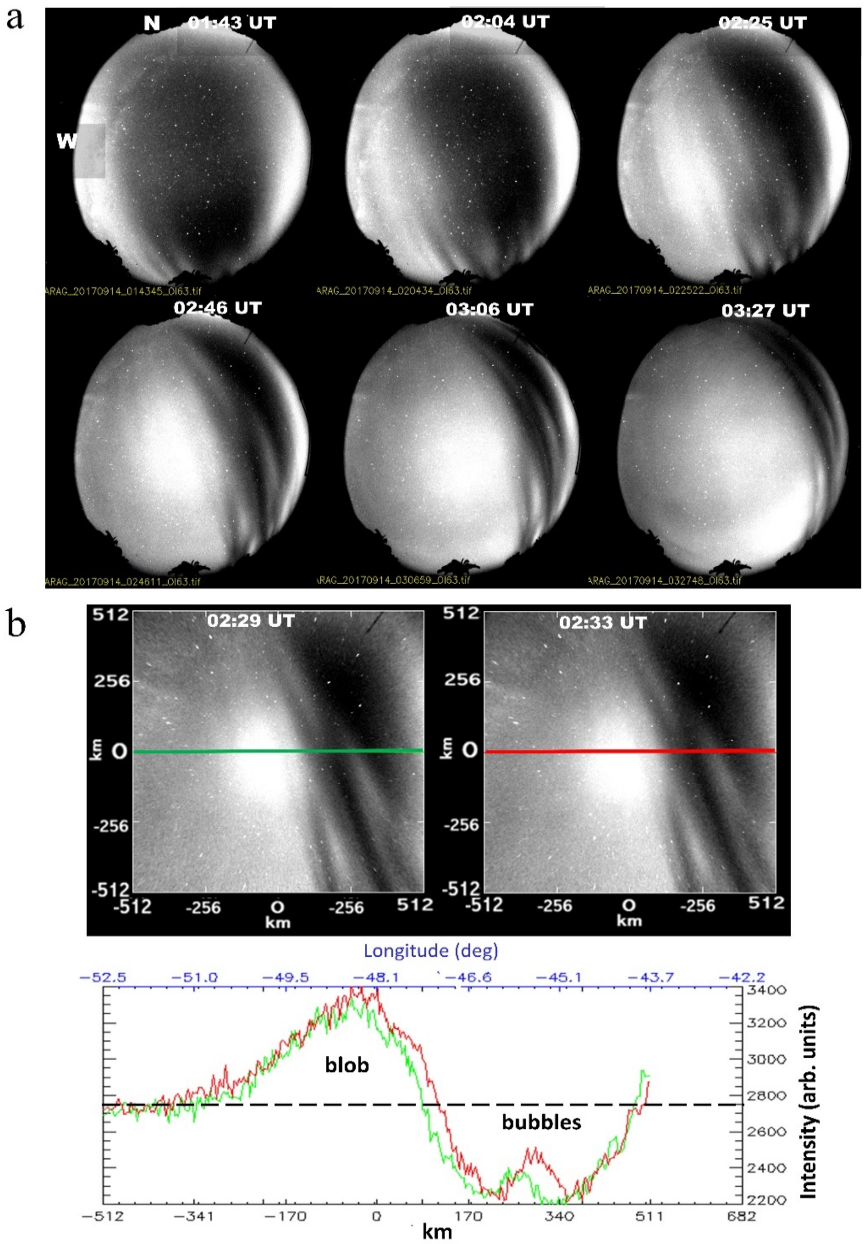

SOURCE: Author.

The upper panel of Figure 34b shows the scanning paths passing through the two plasma density structures – blob (bright region) and bubble (dark region) – at 02:29 UT and 02:33 UT in the linearized nightglow images. The nightglow emission intensity plot in the lower panel shows the two regions of relatively high and low emission intensities from the blob and bubble regions respectively as marked in the figure.

Figure 35 shows the occurrence of range-type ESF in the simultaneous ionograms similar to those observed in Figure 32. However, unlike the ionograms in Figure 32, the ESF structures observed here have some unique features that are different from the ionogram structures discussed in sections 4.4.1 and 4.4.2. First, it can be seen that the frequency of the ESF echoes extends to very high values greater than the foF2[*] of the ionosphere at the time of the observation- signifying higher plasma densities. The frequency of the echoes extended up to ~ 15 MHz. This means there exists a localized high plasma density region in the ionosphere above the ionosonde where the radio signals are bouncing off. As a result, the entire ESF structure could be a consequence of superposition reflections from low and high plasma density regions corresponding respectively to bubbles and blobs. This kind of ESF structure can be termed atypical ESF.

Figure 35: Atypical ESF structures observed on ionograms from 14 September 2017.

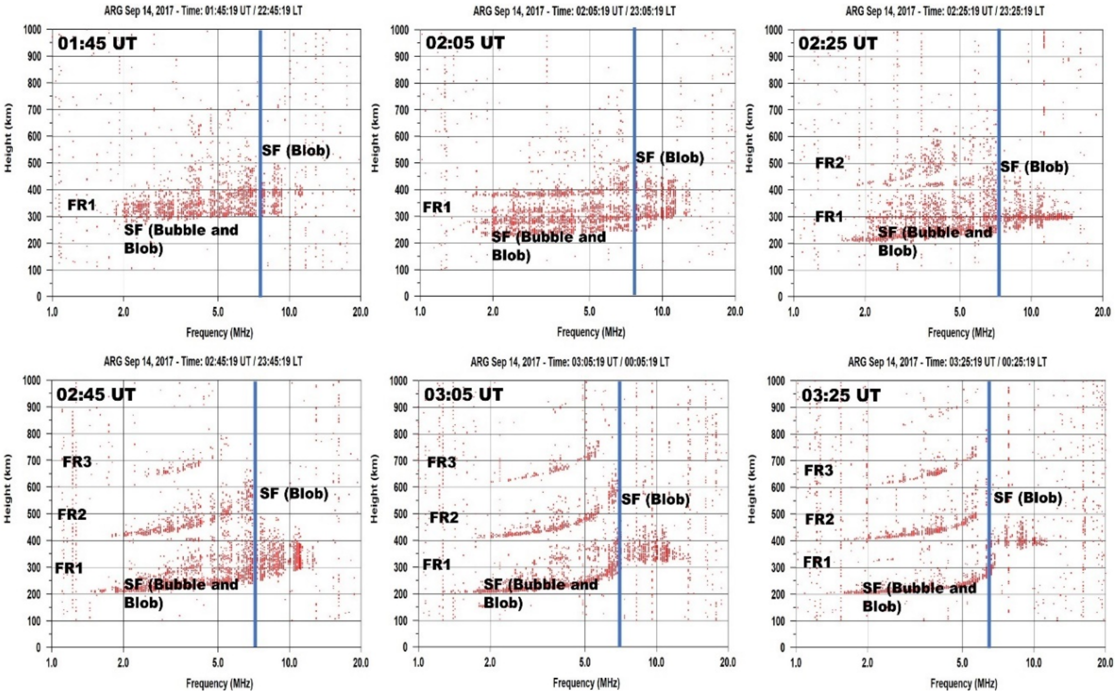

SOURCE: Author.

In this scenario, FR2 and FR3 reflections do not occur until around 02:25 UT. At this time, only FR2 occurs together with FR1. Later at about 02:45 UT, a third reflection FR3 is observed. While FR1 reflection is observed to extend beyond foF2, the FR2 and FR3

---

[*] The foF2 in this case, can be inferred more or less from the higher order reflections which have better defined form compared to the first F-region reflection.

reflections only extend up to the foF2 limit different from the results in Figure 29 and Figure 32. The higher frequency echoes from the blobs are not observed in the higher-order reflections, FR2 and FR3. The two cases from sections 4.4.1 and 4.4.2 show FR2 and FR3 reflections that look similar if not the same to FR1, however, FR2 and FR3 from this result look similar to each other and both look different from FR1 in appearance and form. This result shows the difference in the structure of ionograms and ESF when blobs occur together with bubbles.

Figure 36 shows electron density measurements from Swarm A and C satellites. The orbital paths of these two satellites are farther away from the observation region. At the Swarm altitudes, the remnants of the EIA are observable at 02:00 UT just outside of Brazil. The plots show the EIA crests and the trough. The signatures of the EIA could not be observed in the airglow images at that longitude and as a result, could not be shown in the emission intensity plot of Figure 34b.

Figure 36: Same as Figure 30 but for 14 September 2017.

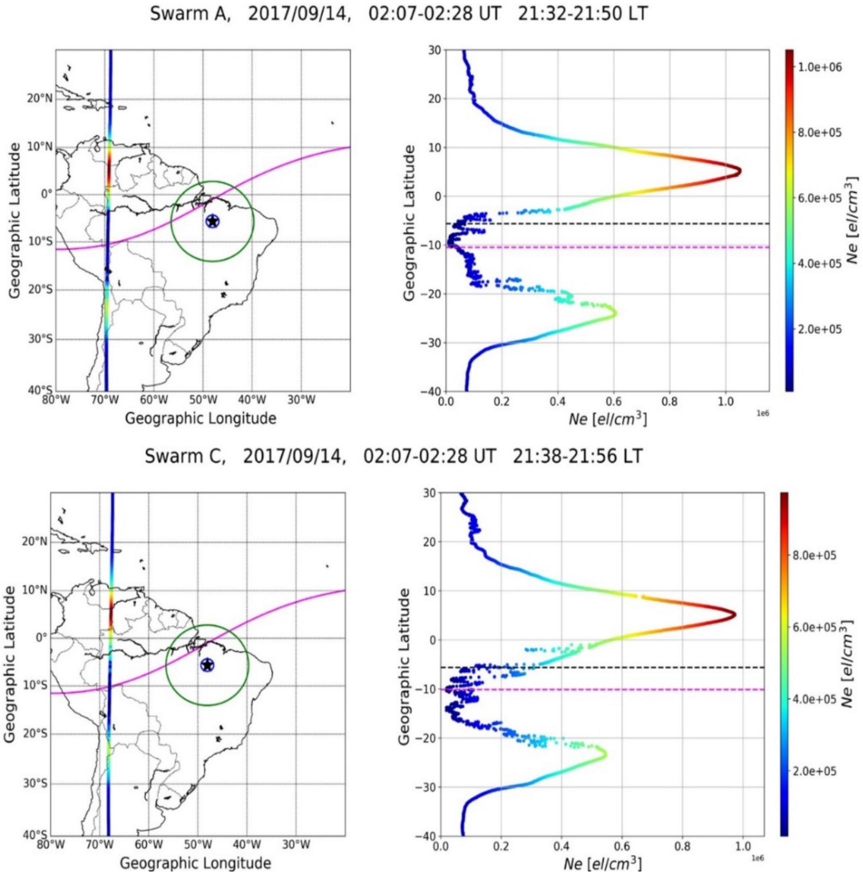

Swarm A, 2017/09/14, 02:07-02:28 UT 21:32-21:50 LT

Swarm C, 2017/09/14, 02:07-02:28 UT 21:38-21:56 LT

SOURCE: Author.

The ionograms also do not capture the EIA structure. The EIA crests shown in the plasma density plots could have influenced the background plasma density enhancement, especially from the northern hemisphere. And thus, observed as blobs in the nightglow images and as the atypical ESFs in the ionograms. The plasma density plots also show, between the two peaks, the EIA trough or depleted plasma density region with strong fluctuations around the observation site. These plasma density fluctuations could be signatures of the equatorial plasma bubbles observed in the nightglow observations. The results from the Swarm satellite measurements are consistent with the measurements from the ground.

Another case of the simultaneous occurrence of plasma bubbles and blobs observed in OI 630.0 nm nightglow images occurred on 12 October 2017 and is presented in Figure 37a. The dark and bright regions inclined along the geomagnetic field lines are bubbles and blobs, respectively. The blobs look like an extension of the southern hemisphere EIA crest. This is similar to the result from the previous case discussed. A possible explanation would be that the EIA plays a role in the formation and maintenance of plasma blobs of the EIA crest region by providing the background plasma density during the blob's lifetime. Figure 37b shows the nightglow emission intensity plot obtained from the linearization of two consecutive night glow images. The plot shows various high and low emission intensities along the scanning path associated with blobs and bubbles.

Figure 37: a) Blobs and bubbles observed in nightglow images on 12 October 2017, b) Same as Figure 34b but for 12 October 2017.

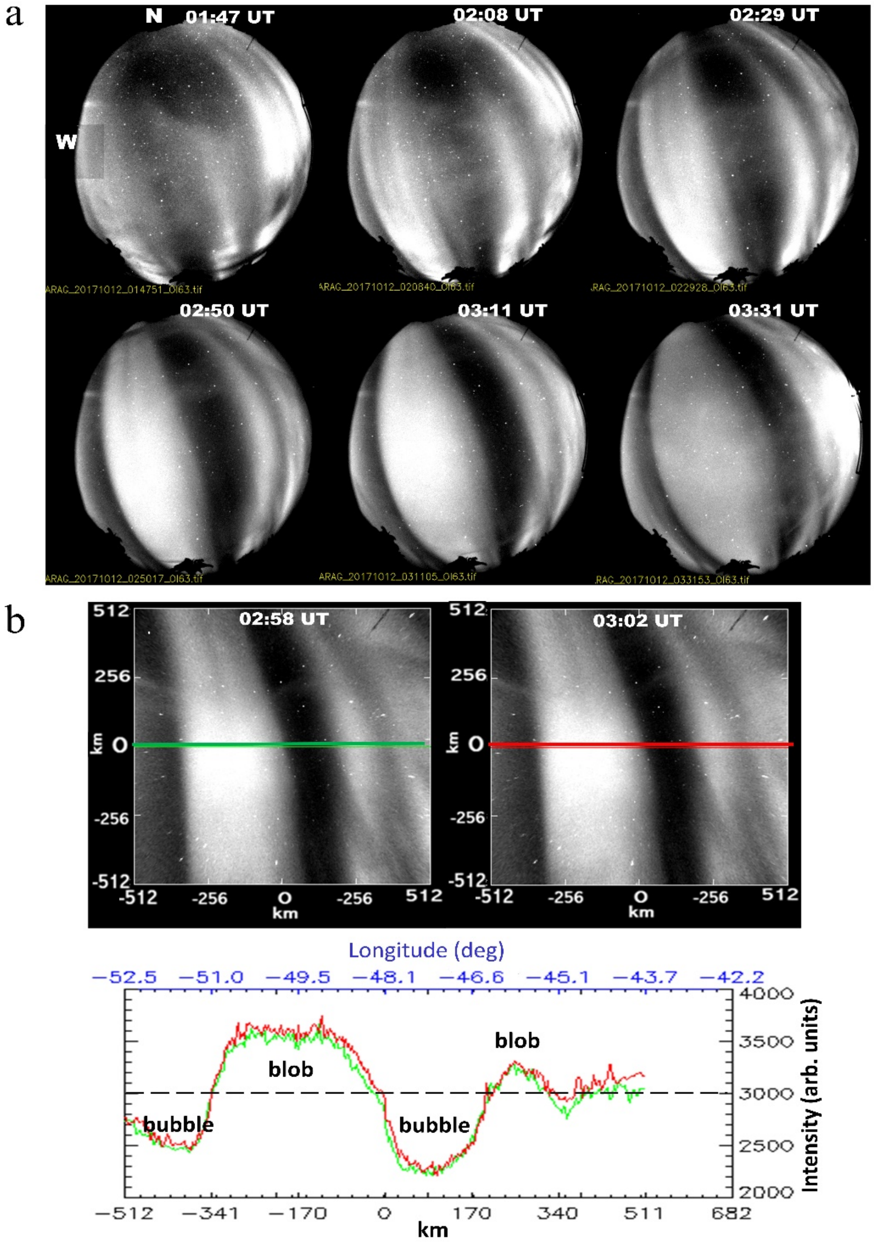

SOURCE: Author.

The ionograms in Figure 38 show atypical ESF with similar characteristics as in Figure 35. The atypical ESFs are associated with the simultaneous occurrence of plasma bubbles and blobs observed in the nightglow images. The atypical ESF structure shows low- and high-frequency echoes going up to and above ~10 MHz at different times. After 02:30 UT, FR2 and FR3 reflections are observed in the ionogram designated 02:50 UT. Similar to the previous case, the FR2 and FR3 reflections are different in appearance from the FR1 reflection. While the FR1 extends beyond the foF2, the FR2 and FR3 are just shy of the critical frequency limit. This difference between the first reflection and the higher-order reflections seems apparent only when plasma blobs are observed together with bubbles as demonstrated in sections 4.4.1, and 4.4.3.

Figure 38:Same as Figure 35 but for 12 October 2017.

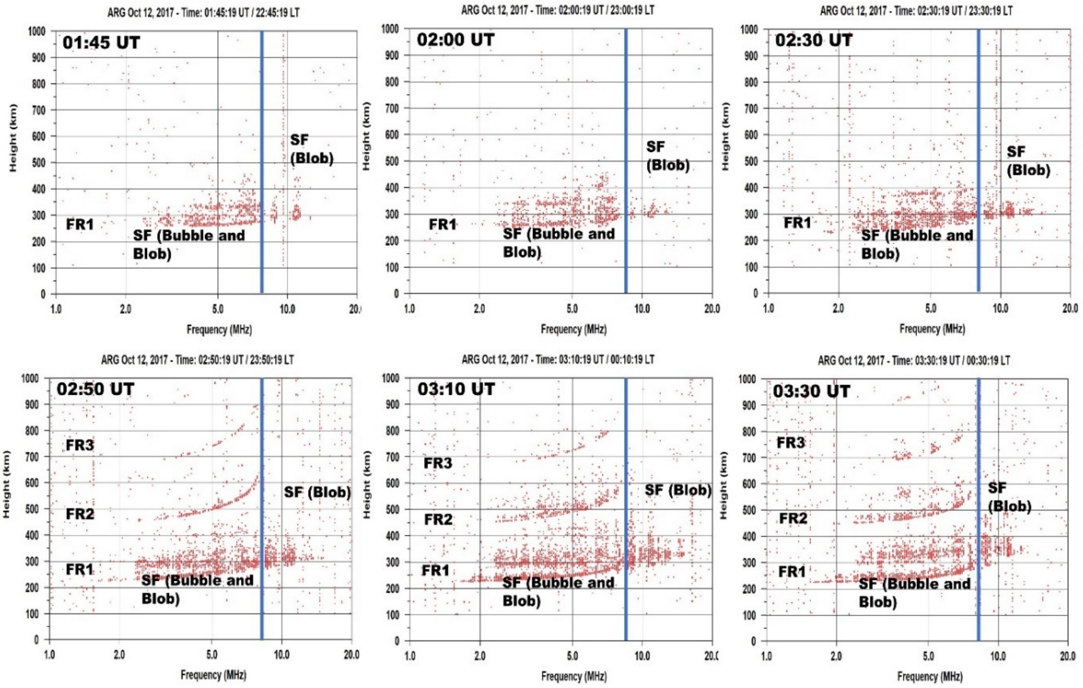

SOURCE: Author.

Figure 39 shows the electron density measurements from Swarm B Satellite on 12 October 2017. The satellite passed directly within the observation area after midnight universal time. Two plasma density crests are observed both in the northern and southern hemispheres and a trough is observed in the equatorial region. Plasma density fluctuations inside density maxima and minima are observed around the observation site. These could be plasma density irregularities observed inside both the enhanced (blob) and depleted (bubble) plasma density regions in agreement with the observations from the imaging system and ionogram.

Figure 39: Plasma density measurements from Swarm satellite B on 12 October 2017.

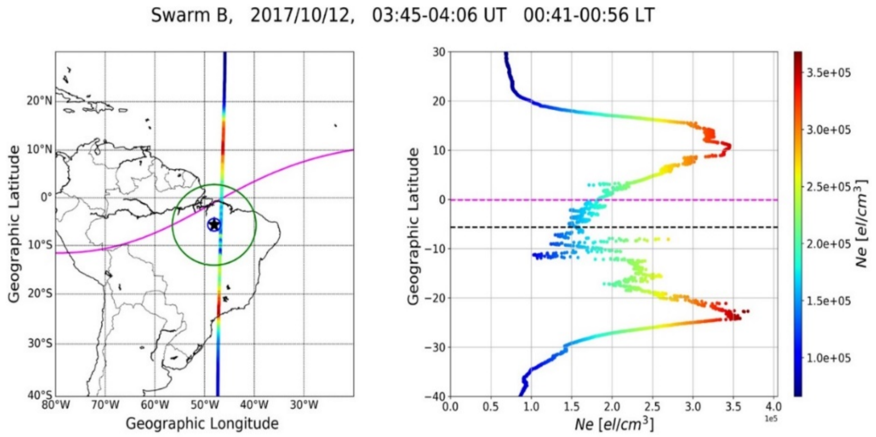

SOURCE: Author.

The observed plasma density crests and trough could be the EIA signature that lingered past midnight hours. The EIA crests fall outside the radius of the observation area, this means the enhanced plasma density observations implied from the high-frequency echoes and high nightglow emission intensities from the ionosonde and imager system are not from the EIA but blobs. However, the effects of the high plasma density in these regions due to the EIA could indirectly serve as background plasma to fuel the generation and development of the blobs.

The observed density fluctuations inside crests and trough could be an indication of irregularities in the bubble and blob. This could explain why the atypical structures have range spreads even at higher frequencies. Further shows that just like bubbles, blobs could contain several small-scale irregularities. The observations and results from 14 September and 12 October when plasm blobs occur with bubbles agree but contrast the results from 7 March when there are no irregularities and 29 September when only plasma bubbles are observed.

The OI 630.0 nm nightglow images and the intensity plots from the two cases before showing the occurrence of plasma blobs together with bubbles. Studies have shown that blobs can be generated through the same mechanisms that lead to the formation of plasma bubbles like the $\vec{E} \times \vec{B}$ upward drift and the fountain effect and that plasma bubbles could potentially be responsible for the occurrence of blobs (LE *et al*., 2003; PIMENTA *et al*., 2004, 2007). The occurrence altitude and latitude of a blob depend on the development phase of the bubble associated with it, i.e., in the development phase, the blob is observed above the bubble near the magnetic equator (equatorward edge of the bubble) due to the uplifting of the ionosphere and for a fully developed bubble, the blob is observed at the poleward edge of the bubble of the magnetic equator due to the fountain effect (HUANG *et al*., 2014). Figure 40 depicts the different blob locations with respect to the bubble at the different stages of the bubble development.

Figure 40: Schematic illustration of the location (altitude and latitude) of a blob in relation to the development phase of a bubble according to HUANG et al. (2014).

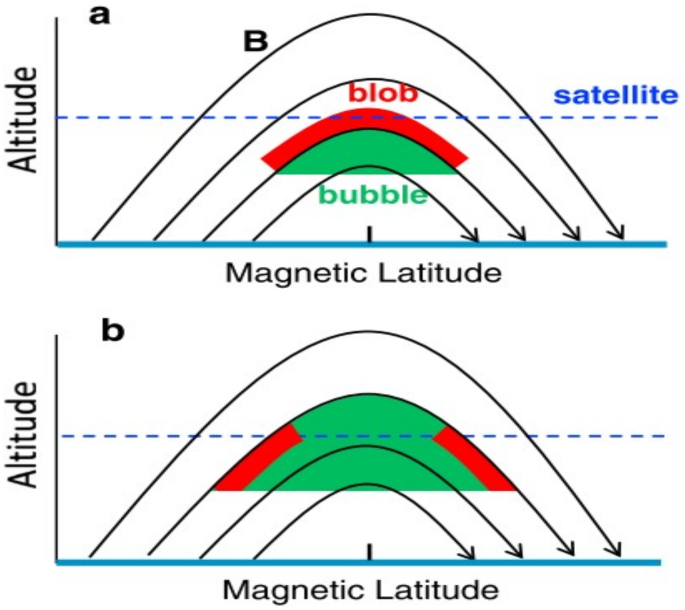

SOURCE: (KIL et al., 2015).

Pimenta *et al*. (2004), after observing plasma blobs in the EIA crest region alongside plasma bubbles near the magnetic equator during the upward motion of plasma bubbles, explained that the field-aligned plasma pressure gradient at the poleward edges of plasma depletions produces an equatorward force causing the plasma particles to move to the equator consequently restricting the density depletions to the anomaly crests regions. As a result, the polarization electric fields inside the depletion region can be mapped to higher latitudes and move the high-density plasma near the anomaly crest to increase plasma density just above the flux tubes. This explanation was supported by simulations from Yokoyama, Su and Fukao (2007) and observations from Tardelli-Coelho *et al*. (2017) and Wang *et al*. (2019) reported blobs at the poleward edges of the bubbles, while Huang *et al*. (2014) and Narayanan *et al*. (2014) reported the observations of blobs at the equatorward edges of EPBs. It shows that plasma blobs could potentially occur at the poleward edges EPBs and that the blobs presented here are not necessarily anomaly crests.

When there are no irregularities in the ionosphere, the nighttime F-layer profile is observed with no spread, and a normal nighttime ionospheric profile is observed with a well-defined critical frequency that can be measured precisely from the ionograms. However, it is not possible to precisely measure the critical frequency of the ionosphere on ionograms when ESF is present. The ESF trace associated with plasma depletion irregularities is expected to occur at or below the critical frequency of the ionosphere. In the case of bubbles occurring in the company of blobs, the ionograms exhibit the atypical Spread-F structures that present high-frequency echoes that extend beyond the normal critical frequency of the ionosphere at the region and at the time. This atypical ESF trace can reach up to about 15 MHz on the ionograms. These high-frequency portions of the atypical ESFs are observed either at or above the F layer virtual height.

During the lifetime of the atypical ESFs on the ionograms, the maximum frequencies observed related to the atypical ESFs did not vary significantly. From the airglow images, it could be seen that the blobs drifted eastward and moved horizontally along with the bubbles passing overhead of the observation area. During the drift, the maximum frequency remained virtually unchanged. The fact that the frequency related to the irregularities on the ionograms did not change widely suggests that the frequency of ESF depends on the plasma densities of the irregularities and not the virtual height when they move away or to the observation site. Since plasma frequency is dependent on the square of plasma density, the frequencies of ESF echoes associated with plasma bubbles are not expected to be higher than the critical frequency overhead of the ionosphere. On the other hand, high plasma density (with irregularities) regions associated with blobs are expected to bounce radio signals at higher frequencies greater than the critical frequency of the background ionosphere.

The spreads observed inside the high-frequency portion of the atypical ESF imply that smaller-scale irregularities could potentially exist inside blobs just as they exist inside plasma bubbles. As such, the identification of echoes (structures) at low and high frequencies on ionograms can be the first step in distinguishing and identifying reflections from low and high plasma density regions above the observation and related to bubbles and blobs.

The ionograms also show that in the presence of plasma blobs, simultaneously observed with bubbles, show that the FR2 and FR3 structures when present are always different in shape from the FR1. Their frequencies are always limited to the critical frequency or less unlike the FR1 (atypical ESF) which extends well beyond the critical frequency. The higher-frequency part of the atypical ESF associated with the blobs does not undergo further reflections. On the contrary, in the absence of plasma blobs, the observed F-layer reflections as shown observed when only bubbles occur or when there are no irregularities have FR1, FR2, and FR3 exhibiting similar shapes and comparable foF2.

In most of the cases, we observe first the typical ESF with or without the high-frequency trace associated with the blobs. Then it develops into atypical ESF with the high-frequency trace very prominent accompanied by the FR2 and possibly FR3 traces. This could be another identifying characteristic of plasma blobs on ionograms. Then the high-frequency trace starts separating or merging as the structure starts developing into the F-layer trace. This may indicate that the ionosonde superimposed the signatures of the bubbles and blobs in the ionograms along the development phases of the bubble. Ionograms are produced from the scattering from irregularities (individual scattering centers[†]) superimposed (CALVERT; COHEN, 1961), and in our case, irregularities from high and low plasma density region scatterers.

The collocation of the ASI and the ionosonde and simultaneous observations from these instruments provides a unique observation context to make this assumption. As such this could be a way to identify plasma blobs in ionograms when they occur in the company of plasma bubbles. And this proposed novel methodology could be especially useful in several ionospheric studies with the availability of only ionosonde data. This is the second step in identifying plasma blobs using ionograms.

OI 630.0 nm nightglow emission showing plasma bubble and blob signatures for four different nights is presented in Figure 41 as a, b, c, and d for 21 October 2017, 23 October 2019, 20 November 2017, and 21 December 2017, respectively. Like the first two cases presented earlier with simultaneous plasma bubble and blob occurrence, these cases also present bright and dark regions that are north-south aligned. The structures are similar and almost inclined to the geomagnetic field lines. In Figure 41 a and b, the blobs seem round in the middle but like the other figures (c and d) they extend to or from the southern crest region of the EIA. That may imply the influence, at least in part, of the EIA on the observed plasma blobs in OI 630 nm nightglow images.

[†] In the ionosphere this could be irregularities inside localized high or low plasma density regions

Figure 41: Same as but for a) 21 October 2017, b) 23 October 2017, c) 20 November 2017, and d) 21 December 2017.

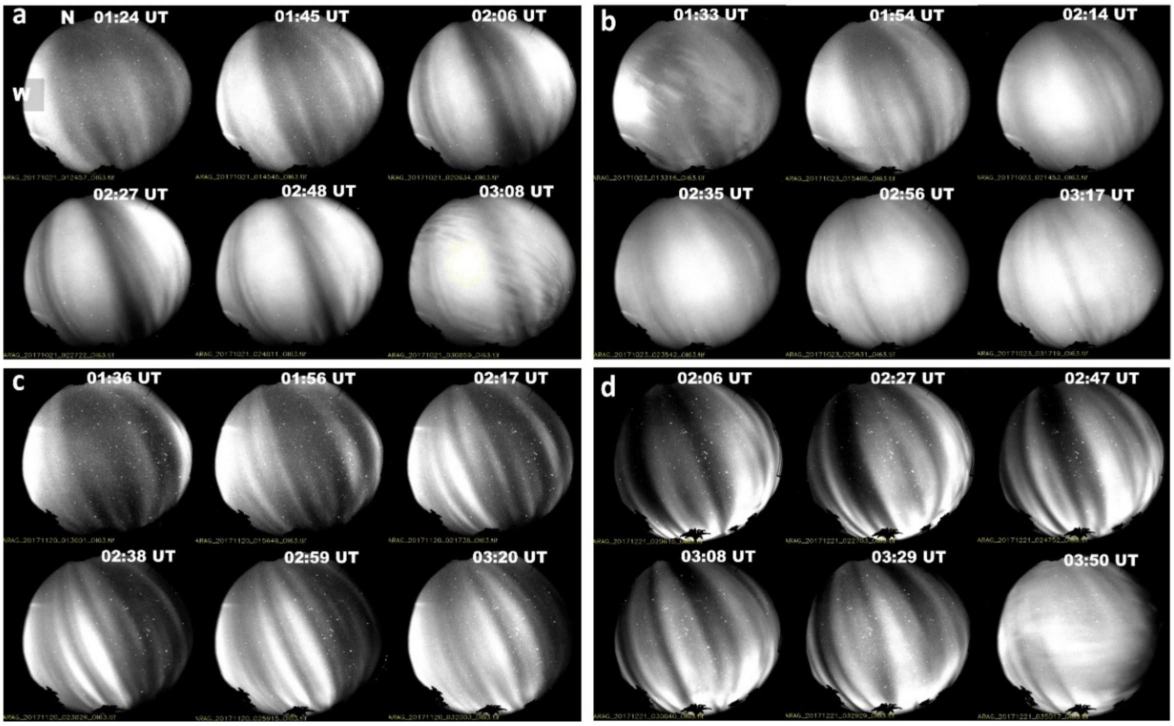

SOURCE: Author.

OI 630.0 nm nightglow emission intensity plots corresponding to the nights 21 October 2017, 23 October 2019, 20 November 2017, and 21 December 2017 are shown in Figure 42a, b, c, and d, respectively. High and low-intensity regions with respect to the background intensity have been indicated as blobs and bubbles, respectively. The blob and bubbles regions agree with the bright and dark regions observed in raw nightglow images. The results agree with high and low OI 630.0 nm emission intensities associated with enhanced and depleted plasma density regions associated with blobs and bubbles.

Figure 42: Nightglow emission intensity plots for the nights: a) 21 October 2017, b) 23 October 2017, c) 20 November 2017, and d) 21 December 2017 corresponding to the images in Figure 41.

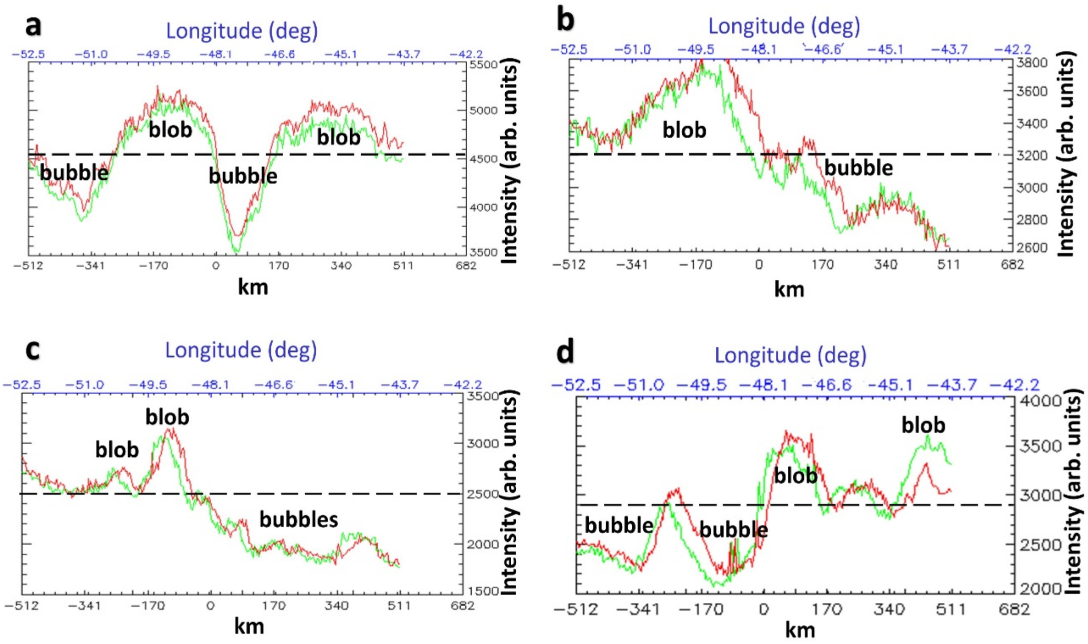

SOURCE: Author.

Figure 43 a, b, c, and d for 21 October 2017, 23 October 2019, 20 November 2017, and 21 December 2017 shows atypical ESF structures on the ionograms. These ionograms were recorded simultaneously on the same nights as the OI 630.0 nm nightglows images in Figure 41. The echoes for the atypical ESFs reach up to ~ 15 MHz which is an indication of the presence of localized high plasma density regions and agrees with the plasma blobs observed in the nightglow images. The ionograms, similarly in these cases, also show the difference between FR1 and FR2, and FR3. The higher frequency portions of the FR1 from the blue vertical line cannot be seen in the FR2 and FR3 structures suggesting the superposition of plasma blobs and bubbles or at least the presence of blobs in the overhead ionosphere.

Figure 43: Same as but for a) 21 October 2017, b) 23 October 2017, c) 20 November 2017, and d) 21 December 2017.

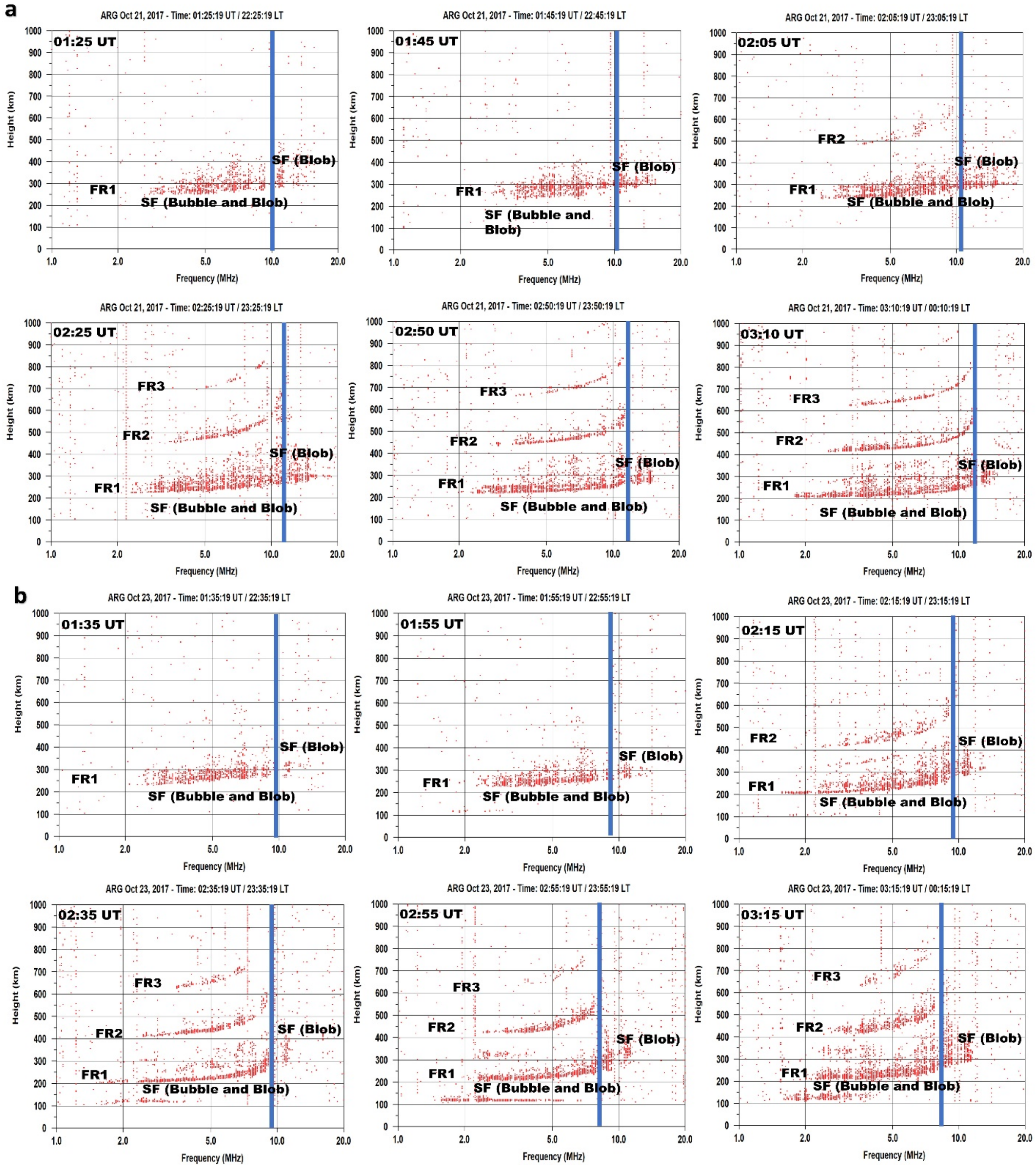

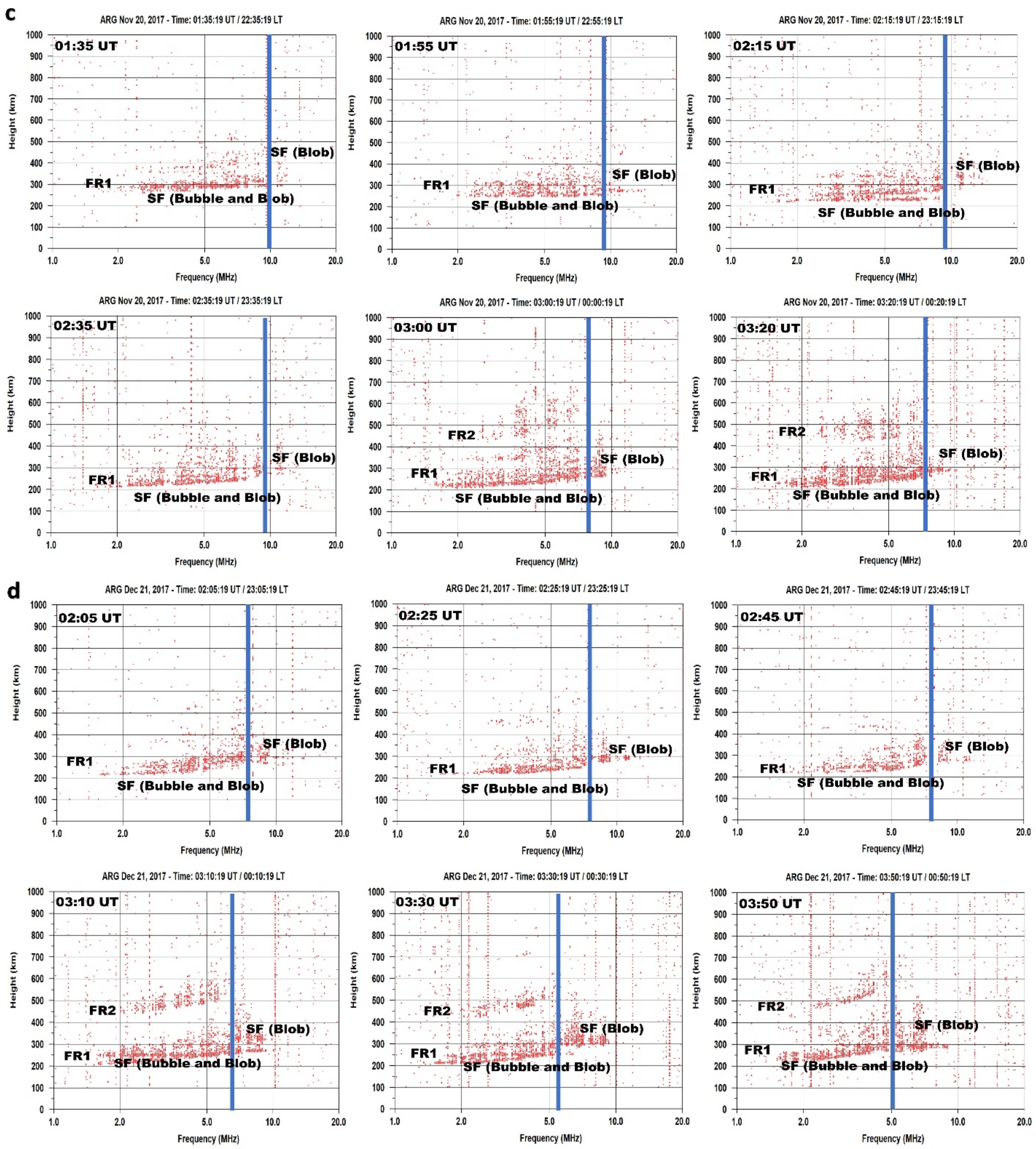

SOURCE: Author.

Similar structures like the atypical ESFs discussed have been reported by (NARAYANAN *et al.*, 2014; PIMENTA *et al.*, 2004; 2007; WANG *et al.*, 2019). They observed patches of ESF at frequencies higher than the background critical frequency at higher altitudes than the F-layer base height in ionograms. They suggested that these patches could be a result of plasma blobs at the overhead ionosphere causing the beams to be reflected at higher frequencies.

Wang *et al.* (2019) also reported the observation of low- and high-frequency range Spread-F in ionograms observed over Vanimo (Papua New Guinea) and Hainan (China) and attributed them to plasma bubbles and blobs, respectively. Pimenta *et al.* (2004; 2007) observed similar Spread-F structures in ionograms in a low-latitude station at Cachoeira Paulista–Brazil, in a study using ground-based instruments and satellite data. They reported that the high-frequency ESF structures appeared in the ionograms only when plasma blobs were observed in the nightglow images. The results from these studies agree with the current investigation.

These atypical spread-F structures are also similar to those reported by Fagundes *et al.* (2012) over Brazil using two ionosondes located in the low-latitude stations of São José dos Campos and Cachoeira Paulista. However, their report associated the observed atypical Spread-F with MSTIDs propagating at or above the F2-layer peak. Nevertheless, the structures look similar.

Meanwhile, Kil *et al.* (2019) and Miller *et al.* (2014) have linked MSTIDs to the generation of blobs using data from Swarm satellite measurements and optical/CINDI measurements. They concluded that the characteristics of the observed plasma blobs were consistent with MSTID-generated structures which are in line with the conclusion from Fagundes *et al.* (2012) that MSTIDs may have been the source of atypical ESFs observed in ionograms. This could just mean that the blobs generated by MSTIDs and the atypical ESFs structures are the same (blobs) observed on the ionograms and MSTIDs could be one of the generating sources of the irregularity.

Calvert, Cohen (1961) in the ionograms from Huancayo at the magnetic equator observed structures like those reported in the present study. However, the origins of the structures observed by Calvert; Cohen (1961) were linked with plasma bubbles from the midlatitudes unlike those reported by Fagundes *et al.* (2012) and those reported in this study.

Plasma density measurements from Swarm B for the nights of 21 October 2017, 23 October 2019, and 20 November 2017 and Swarm A and C for 21 December 2017 are shown in Figure 44a, b, c, and d, respectively. Figure 44a shows two plasma density peaks, at 10^{o} N and 2.2^{o} S with the southern peak exhibiting density fluctuations as opposed to the northern peak. The satellite passed directly at the edge of the observation area such that it could have observed similar structures as the ground instruments. The plasma density peaks in the density plots could be the crests of the EA which could have shifted northward moving the observation south peak closer to the observation site. The shifting of the EIA peaks could be explained by the movement of the meridional winds. This could have moved plasma from the daytime EIA crest region to the ionosphere over the observation site during the nighttime hours and played a significant role in the occurrence of the plasma blob observed in the airglow images and observed as atypical ESF in the ionograms.

Figure 44: Plasma density measurements from Swarm satellites. a) Swarm B, 21 October, b) Swarm B, 23 October, c) Swarm B, 20 November, and d) Swarm C, 21 December.

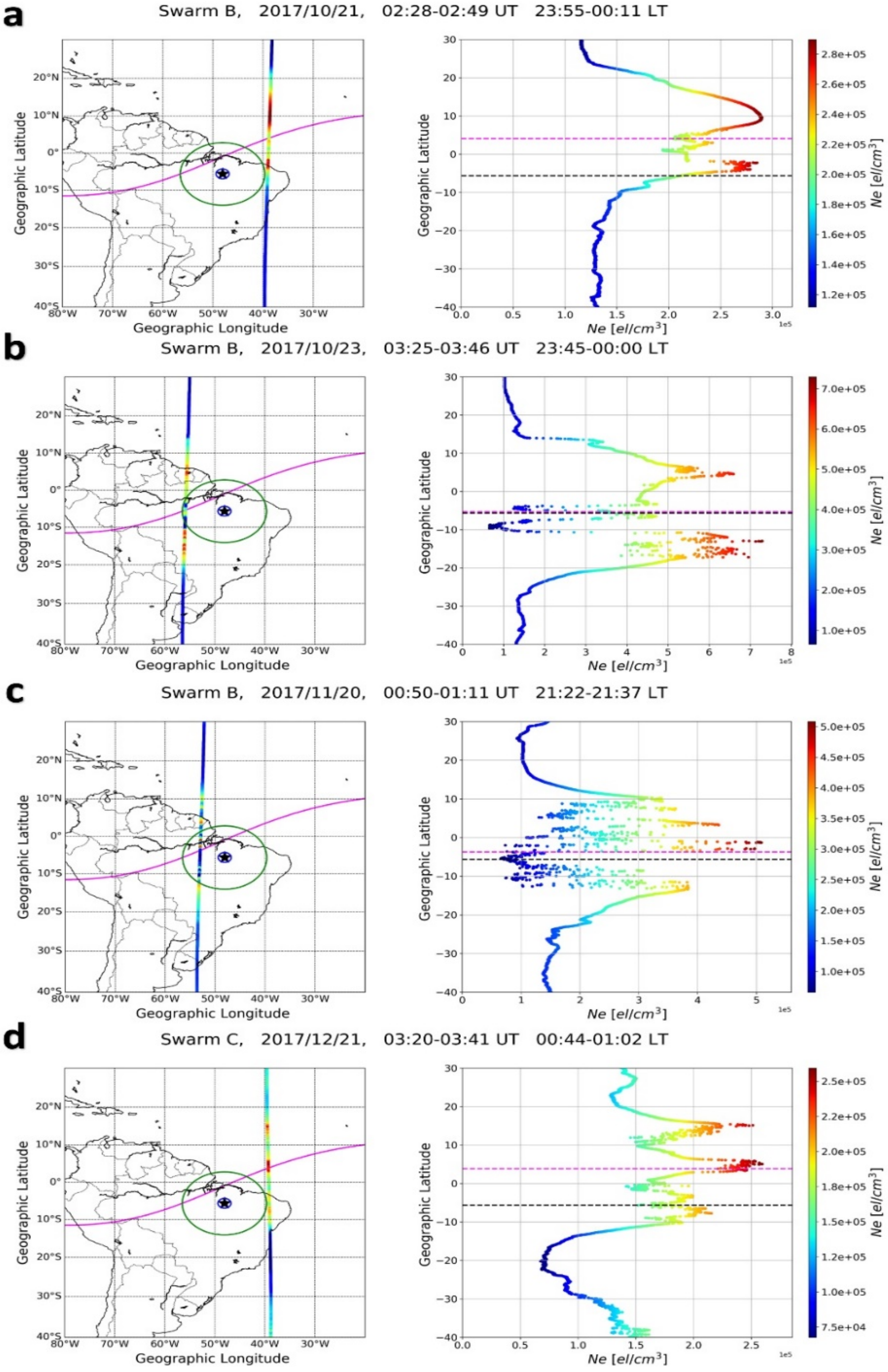

SOURCE: Author.

In Figure 44b, the plasma density measurement highlights significant plasma density fluctuations along the satellite path. The path of the satellites was at the western edge of the observation area. The density peaks that occur at ~ 4.5° N and 12° S are different from the locations of EIA crests during daytime hours, however, again, this could have been caused by the meridional winds. Notwithstanding, the plasma observations in the ionograms and nightglow images may be indeed plasma bubbles whose development could have been influenced by the anomaly crest. In the plasma density minima, strong fluctuations are observed which could be related to the observed plasma bubbles in the ground instruments.

The density measurements in Figure 44c are plagued with strong plasma density fluctuations and substructures exhibiting various highs and lows between ± 10°. This series of enhancements and depletions are observed in the airglow images as several blobs and bubbles and atypical ESF in the ionograms. The results from all three techniques agree. On the opposite edges of these fluctuations, we observe some semblance of the anomaly crests which have been which has reduced. The EIA could have contributed in part to the increased plasma density in the region observed as blobs.

Figure 44d highlights the measurements from Swarm C. Various degrees of density enhancements are observed at different latitudes with localized density fluctuations. Depleted plasma density regions with fluctuations were also observed. Swarm C presents three peaks of plasma density at different latitude regions. Plasma-depleted regions are observed in the measurement of both satellites. The results confirm the observation of plasma blobs in the OI 630.0 nightglow images and atypical ESF in the ionograms.

The EIA is caused by the upward vertical drift ($\vec{E} \times \vec{B}$) of the F-layer moving ionospheric plasma at the equator to higher altitudes which eventually gets deposited at low latitude ionosphere via the magnetic field lines by gravitational and pressure gradient forces in a mechanism known as the fountain effect. This results in the abnormally formed high ionization in the low-latitudes (crests) in either hemisphere around ± 15° and ± 20° dip-latitudes and low ionization around the equator (trough) during daytime hours. Although, the EIA is a daytime phenomenon, sometimes just after sunset the intensified zonal eastward electric field (PRE) may lead to an intensification of the EIA, however, the EIA may disappear after the PRE since the zonal electric field reverses westward during nighttime, moving the F-layer downwards at the equatorial region the EIA crests.

Most of the plasma density measurements from Swarm satellites presented here show high plasma density peaks which could be the crests of the anomaly. The location and intensity of the EIA crests and trough vary in local time, season, and solar activity which leads to asymmetry in ionization densities and latitudinal location (BALAN; LIU; LE, 2018;

LE *et al*., 2003). This asymmetry is maybe principally by the thermospheric neutral winds which transport composition, energy, and momentum thereby modifying the F region electron density distribution around the magnetic equator producing the EIA crests Kil *et al*. (2019). Depending on the nature and direction of the meridional thermospheric winds (north to south), the EIA may or may not intensify and may be shifted poleward or equatorward. The meridional wind may cause the plasma in the F region to be driven upward to higher altitudes along the magnetic field lines where recombination is slower leading to higher peak plasma density resulting in the enhancement of ionospheric plasma. As such, the meridional winds could be responsible for the observed asymmetry in the plasma density peaks but more importantly play an important role in the formation of plasma blobs with the EIA as background plasma Kil *et al*. (2019). Therefore, it is important to emphasize at this point that the structures are seen throughout the OI 630.0 nm nightglow images showing high OI 630.0 nm nightglow intensity emission intensities, although occurring in the nighttime could be remnants of the EIA moving plasma from the crest region to observation site which is observed as the signature of blobs.

4.5 Conclusions

All-sky imagers have been used for the observation and studies of plasma bubbles and to some extent blobs. However, these imaging systems are plagued with limitations such as moonlight and weather conditions that do not allow the system to make continuous observations. The ionosonde does not have these limitations as its mode of operations relies on radio waves which are not affected by weather or light. Even though the ionosonde has been used for the study of ESF (plasma bubbles), it has yet to be adopted fully for use in plasma blob observations and studies. Notwithstanding a few observations have been reported of blobs with ionosonde.

In this study, the author sought to propose a novel methodology that could use only ionosonde to observe and study plasma blobs when in the company of bubbles. The proposed methodology discussed the characteristic of atypical ESF on ionograms when plasma blobs were present. This was achieved by taking advantage of the rare colocation of an all-sky imaging system and ionosonde at Araguatins in Brazil and simultaneous observations from these instruments. OI 630.0 nm nightglow images from all-sky were analyzed to determine the structures in the ionosphere above, then ionograms were compared for different structures observed in the OI 630.0 nm nightglow images. Plasma density measurements from Swarm A, B, and C were also used to complement the ground-based observations.

Three cases were analyzed from the OI 630.0 nm nightglow images, a night with no irregularities, a night with only plasma bubbles, and several nights with plasma bubbles and blobs. The corresponding ionograms for these nights were analyzed to determine the different characteristics. The observations have been presented in this study and the conclusions are as below.

1. Corresponding ionograms for nightglow images with no irregularities showed a typical nighttime ionospheric F region profile. The ionograms showed first, second and third reflections which in appearance looked similar. The FR2 and FR3 extended only to the critical frequency and could not pass that point. The ionograms showed no spread and the critical frequency was well defined which allows for precise measurement of same. The critical frequency, for the period, showed that plasma density in the region at the time was quite low.

2. In the case where only plasma bubbles were observed in the nightglow images, the corresponding ionograms showed equatorial spread structures of range type associated with plasma-depleted regions known as bubbles. First, second and third reflections were observed with similar appearances. Because of the spread, the critical frequency could not be precisely measured from the FR1 but could be estimated from the other ionospheric reflections. The estimated critical frequency was low – meaning that in the ionosphere there were regions of low plasma density. The limit of the FR2 and FR3 in terms of maximum frequency was the “foF2” which was a little more than 5MHz.

3. When plasma bubbles and blobs were simultaneously observed in the OI 630.0 nm nightglow images, the corresponding ionograms also showed equatorial spread-F structures with echoes spreading from lower to higher frequencies implying the existence of both high and low plasma density regions which correspond to plasma blobs and bubbles, respectively. The maximum frequency for the ESF with the occurrence of blobs could reach up to 15 MHz or more than the critical frequency of the region at the time.

4. The ionospheric reflection was present however, the second and third reflections appeared with time. When the FR2 and FR3 were present, their appearances were also different from the FR1. The FR1 extended to higher frequencies beyond the critical frequency but

the FR2 and FR3 were always limited to the critical frequency. The higher-frequency portion of the ESF associated with plasma blobs in the FR1 is not observed with the FR2 and FR3. The first F-layer reflection observed when there is atypical ESF is different in shape from the second, third, and higher-order reflections. This could mean that when plasma bubbles and blobs occur simultaneously, the signatures are superimposed on each other. This is not observed when only bubbles occur or in the absence of blobs.

5. The observations showed the entirety of the atypical ESF contained spread originating from echoes from depleted and enhanced plasma density regions above the ionosonde which was superimposed. This suggests that plasma blobs, just like plasma bubbles could contain small-scale size irregularities in them.

6. The results also showed that plasma blobs indeed do occur together with plasma bubbles and that bubbles could be a factor in the generation of plasma blobs.

5 THE EFFECTS OF THE 2019 MINOR ANTARCTIC SUDDEN STRATOSPHERIC WARMING ON THE OCCURRENCE OF IONOSPHERIC IRREGULARITIES IN BRAZIL AND AFRICA

5.1 Summary

This chapter discusses the results obtained from the analysis of ionograms from three ionosonde stations and GPS-TEC data from 33 ground-based GPS-receiver stations in Brazil and Africa during different phases of the 2019 minor sudden stratospheric warming that occurred in the southern hemisphere. The occurrence of SSW in the southern hemisphere, major/ minor, is very infrequent compared to the northern hemisphere due to the weaker planetary wave (PW) forcing resulting from smaller topographical differences and land-sea contrasts. The only SSW event to occur in the region in the past couple of decades are the major SSW event that happened in 2002, which incidentally is the only major SSW to have been recorded from the Antarctic region, and the recent 2019 minor event. This study, therefore, investigates the occurrence statistics of ionospheric irregularities during the recent SSW event from the Antarctic region and tries to fill in some of the knowledge gaps on the SSW effects on the occurrence of ionospheric irregularities, especially from the southern hemisphere. The critical frequency of the ionosphere, ESF, and ROT phase fluctuation occurrence variations before, after, and during the event have been analyzed for different longitudes and latitudes.

5.2 Background

The ionosphere is an especially essential element in satellite communication and navigation systems and the existence of disturbances and irregularities therein is an important consideration in the accuracy of these systems and the ionospheric electrodynamics, particularly in the equatorial region. In the space-weather environment, it has been realized that ionospheric variations, disturbances, and the occurrence of irregularities are not due only to forcings from above the ionosphere but also from phenomena below. The main drivers of ionospheric variabilities are solar winds and geomagnetic storms (RISHBETH; MENDILLO, 2001; ZHAO *et al.*, 2008). The occurrence of ionospheric irregularities mostly depends on the plasma density gradient, $\vec{E} \times \vec{B}$ upward vertical drift due to PRE of the eastward electric field, and the growth rate of the generalized Rayleigh-Taylor instability after sunset hours (ABDU, 2001; CARTER *et al*., 2014; HUANG, 2018). The long-term, medium-term, and short-term or day-to-day variability in the development and occurrence of these irregularities depend on the solar cycle (defined by the number of sunspots and solar flux), season, longitude and solar, and seeding of upward propagating atmospheric waves (e.g. Planetary waves, gravity waves, and semidiurnal solar and lunar tides), respectively have been studied extensively over the years (ABDU, 2019; CARTER *et al*., 2014; CHANG *et al*., 2010; ECCLES *et al*., 2011; FORBES, 1996; ONOHARA; BATISTA; TAKAHASHI, 2013; PAULINO *et al*., 2011, 2020; SAHAI; FAGUNDES; BITTENCOURT, 2000; SOBRAL *et al*., 2002; TAKAHASHI *et al*., 2009).

However, phenomena below the ionosphere like sudden stratospheric warmings, SSWs, and even volcanic eruptions have been observed to have significant influences on ionospheric variations and the occurrence of ionospheric irregularities (AA *et al*., 2022; YADAV *et al*., 2017). SSWs are described as one of the most spectacular meteorological fluctuations in the polar stratosphere during the wintertime and are considered one of the strongest manifestations of vertical coupling of the atmosphere (CHAU *et al*., 2012; GONCHARENKO *et al*., 2010a; TAROH MATSUNO, 1971). These warming events are known to contribute to large-scale electrodynamic and morphological variations in the ionosphere and their influence extend beyond the high-latitude stratosphere and into the low-latitude and equatorial ionosphere during and after the event (CHAU *et al*., 2012; FAGUNDES *et al*., 2015; GONCHARENKO *et al*., 2013; YU *et al*., 2020). Semidiurnal perturbations could be observed in the ionospheric $\vec{E} \times \vec{B}$ vertical drifts, equatorial electrojet (EEJ), peak electron density (NmF2), and total electron content (TEC) during SSW events, and this variability in the ionosphere is controlled by the dynamic processes of the equatorial ionization anomaly (CHAU; FEJER; GONCHARENKO, 2009; GONCHARENKO *et al*., 2010b; 2010a). The amplified PWs and other waves like gravity waves (GWs) and tides generated during SSW events may modify equatorial ionospheric dynamics which may influence plasma distribution in the low-latitude ionosphere due to the effects of E region dynamo which is driven by large-scale winds (DE PAULA *et al*., 2015; GONCHARENKO *et al*., 2010a; YADAV *et al*., 2017).

Unlike the rare Antarctic SSW events, the effects due to Arctic SSW events on the occurrence of ionospheric irregularities have been investigated and studied quite a bit (DE PAULA *et al*., 2015; JOSE; VINEETH; PANT, 2017; YU *et al*., 2020). Weakening of ionospheric scintillations, and modulation of ESF start times through planetary wave activity during different SSW events have been observed (DE PAULA *et al*., 2015; JOSE; VINEETH; PANT, 2017; YE *et al*., 2021; YU *et al*., 2020). Jose; Vineeth; Pant (2017) reported that quasi-16-day planetary waves affected the start times of ESFs significantly during SSW events. These quasi-16-day planetary waves predominant during SSW events, can enter the ionospheric dynamo region from below and modify electrodynamical processes like the EEJ and the PRE-a precursor factor for ionospheric irregularities (JOSE; VINEETH; PANT, 2017; MATTHIAS; ERN, 2018; PARK *et al*., 2012; PEDATELLA; LIU, 2013; YAMAZAKI *et al*., 2020).

5.3 Data and Methodology

Figure 45 is a map of South America, and Africa showing the locations of the ionosondes, and GPS receivers employed in this study. The ionosondes located at Araguatins, Jataí, and São José dos Campos are indicated on the map as ARA, JAT, and SJC gold circles on the South American section of the map, and the GPS receivers are indicated by the red squares. The ionosondes are maintained and managed by the Laboratory of Physics and Astronomy - UNIVAP. The GPS receivers selected are part of the Brazilian GPS receiver network, Rede Brasileira de Monitoramento Contínuo (IBGE), and UNAVCO. The GPS data used can be downloaded from http://www.ibge.gov.br and https://www.unavco.org.

Figure 45: Map of South America and Africa showing the locations of all ground-based GPS receiver stations (red dots) and ionosondes (gold dots) used in the study. The black curve is the geomagnetic equator, and the green line is the geographic equator.

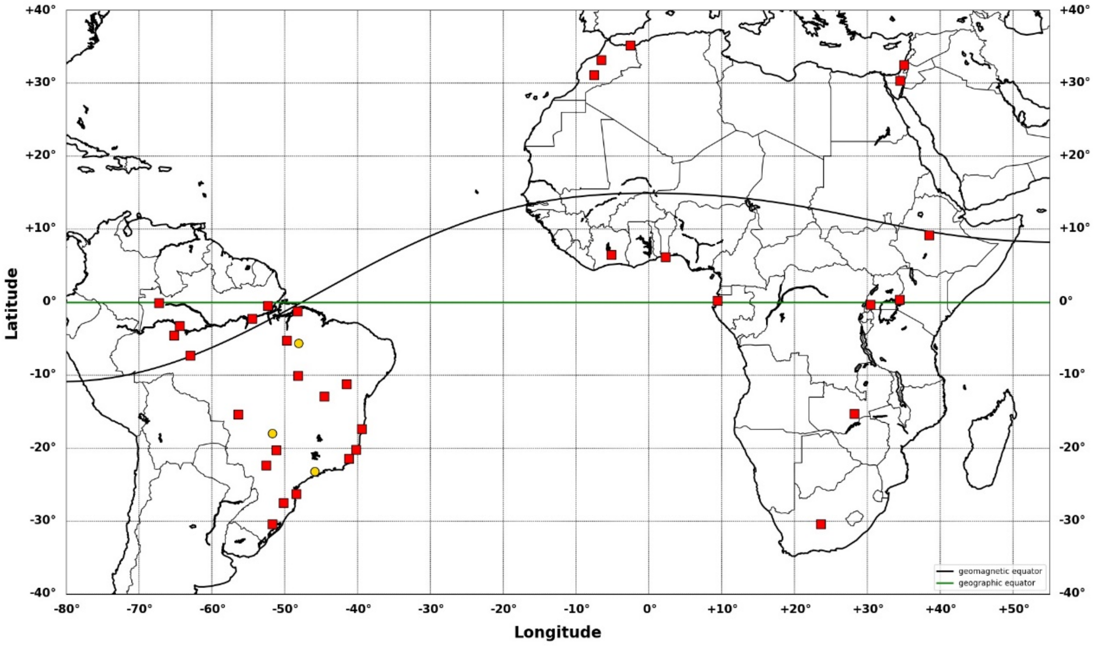

SOURCE: Author.

Data collected from GPS receivers and ionosondes over Brazil (South America) and Africa were used to study the occurrence characteristics of ionospheric irregularities – Equatorial Spread-F (ESF) and Rate of TEC change (ROT) – over Brazil and Africa during the 2019 Antarctic minor SSW. Details on the geographic coordinates and dip latitudes of the ionosondes and GPS receivers are given in Table 5 and Table 6, respectively. The GPS receivers were divided into 4 sectors based on their locations – Brazil west and east, and Africa west and east sectors. The stations from the Brazil sectors, were selected along 2 imaginary lines perpendicular to the geomagnetic equator in the western and eastern parts of Brazil. Due to the low numbers of receivers located in Africa, especially in the western part, stations were selected where receivers and data were mostly available within the 2 blocks – west and east. The occurrence frequencies of the ionospheric irregularities (ESFs and ROT phase fluctuations) for any period were calculated using equation (38) below.

$$Occ.freq.\% = \frac{number\ of\ days\ of\ occurrence\ (period)}{total\ number\ of\ days\ of\ observation\ (period)} \times 100 \qquad (14)$$

The GPS receiver and ionosonde stations are sub-categorized into equatorial, low-latitude, and beyond EIA crest regions based on their dip-latitudes (refer to Table 5 and Table 6). The criteria for the latitudinal classification of the GPS receiver and ionosonde stations are given as follows:

a) Equatorial region: 5^o N ≥ dip latitude ≤ 5^o S,

b) Low-latitude region: 20^o N > dip latitude > 5^o N and 20^o S > dip latitude > 5^o S and

c) Beyond EIA crest regions: dip latitude ≥ 20^o N and dip latitude ≥ 20^o S.

5.3.1 Ionosonde data

The study of Equatorial Spread-F (ESF) was carried out over Brazil using 3 ionosondes located at Araguatins-ARA (near-equatorial region), Jataí-JAT (low-latitude region), and São José dos Campos-SJC (beyond EIA crest region). Spread-F occurrence and critical frequency (foF2) information were collected from ionograms from the 3 ionosondes. The parameters collected from August to October 2019 (SSW) and 2018 (no SSW) were analyzed to investigate their variations at various periods of the study. The locations of the ionosondes are shown in gold circles on the map in

Figure 45 and Table 5 gives a list of the ionosondes, their geographical coordinates, and dip latitude.

Table 5: Summary list of ionosondes and their coordinates used.

Station	Code	Geo. Lat. (-S)	Geo. Lon. (-W)	Dip Lat (-S)	Reg.
Araguatins	**ARA**	**-5.7**	**48.1**	**-5.0**	**Near Equatorial S**
Jataí	**JAT**	**-19.0**	**51.7**	**-13.4**	**Low-Latitude S**
São José dos Campos	**SJC**	**-23.2**	**45.9**	**-20.2**	**Beyond EIA S**

SOURCE: Author.

5.3.2 GPS-TEC ROT

Figure 45 shows a map indicating the locations of all 33 ground-based GPS-receiver stations (red squares) in Brazil and Africa used in the study. The stations cover a range of latitudes from the equatorial region to the anomaly region in all designated sectors except where there were no receivers or data available. Using GPS receivers from all these longitude and latitude locations does not only allow for the analysis and comparison of the occurrence of ionospheric irregularities in the different longitudinal sectors but in different latitudes as well. The descriptions of the locations of the stations are summarized in Table 6 for the Brazilian and African sectors.

From the GPS-TEC data obtained from these stations, ROT phase fluctuations plots were made using UTECDA from UNIVAP. The plots were made for all receivers in all sectors with data. ROT allows for the detection of small-scale irregularities in the ionosphere. The rate of TEC, ROT is usually expressed in TECU per min and is calculated using equation (13) in section 3.4.3. In this equation, ΔTEC is the difference in TEC values at two consecutive times, t_2 - t_1. A graph of ROT shows random fluctuations in the presence of ionospheric irregularities. The ROT parameter (i.e., the fluctuations) depends on the amplitude of the irregularity and the background electron density. ROT has been used by space scientists in ionospheric studies for the identification of large-scale ionospheric irregularities.

Table 6: Summary of the locations of the GPS receiver stations in the Brazilian and African regions.

St. Name	Code	G. Lat. (-S)	G. Lon. (-W)	Dip Lat. (-S)	LT	Reg.
Brazil West Sector						
São Gabriel da Cachoeira	SAGA	-0.09	-67.30	8.9	LT = UT-3	Low-Lat. N
Tefé	AMTE	-03.21	-64.42	5.0	LT = UT-3	Equatorial N
Coari	AMCO	-4.52	-65.20	3.9	LT = UT-3	Equatorial N
Humaitá	AMHA	-07.31	-63.02	0.7	LT = UT-3	Equatorial N
Cuiabá	CUIB	-15.33	-56 4	-9.4	LT = UT-3	Low-Lat. S
Ilha Solteira	ILHA	-20.26	-51.21	15.8	LT = UT-3	Low-Lat. S
Rosana	ROSA	-22.31	-52.57	-16.6	LT = UT-3	Low-Lat. S
Araquari	SCQA	-26.23	-48.44	-21.6	LT = UT-3	Beyond EIA S
Lages	SCLA	-27.48	-50.18	-21.8	LT = UT-3	Beyond EIA S
Porto Alegre	POAL	-30.4	-51.7	-22.9	LT = UT-3	Beyond EIA S
Brazil East Sector						
Laranjal do Jari	APLJ	-00.49	-52.30	3.3	LT = UT-3	Equatorial N
Santareno - INCRA	PASM	-0.26	-54.44	1.5	LT = UT-3	Equatorial N
Belém INPE	BEPA	-1.27	-48.26	-1.0	LT = UT-3	Equatorial S
Marabá	MABA	-5.21	-49.70	-4.2	LT = UT-3	Equatorial S
Palmas	TOPL	-10.10	-48.20	-8.9	LT = UT-3	Low-Lat. S
Barreiras	BABR	-1. 90	-44.59	-12.6	LT = UT-3	Low-Lat. S
Irecê	BAIR	-11.18	-41.52	-13.7	LT = UT-3	Low-Lat. S
Teixeira de Freitas	BATF	-17.33	-39.45	-20.2	LT = UT-3	Beyond EIA S
Vitória	CEFE	-20.19	-40.19	-22.0	LT = UT-3	Beyond EIA S
Campos dos Goytacazes	RJCG	-21.45	-41.19	-22.5	LT = UT-3	Beyond EIA S

			Africa West Sector			
Melilla	MELI	35.17	-2.57	29.2	LT = UT	Beyond EIA N
Rabat-Emi	RABT	33.60	-6.51	27.5	LT = UT	Beyond EIA N
Oukaimeden	OUCA	31.12	-7.52	24.1	LT = UT	Beyond EIA N
Yamoussoukro	YKRO	6.52	-5.14	-5.8	LT = UT	Low-Lat. S
Cotonou	BJCO	6.23	2.27	-6.3	LT=UT+1	Low-Lat. S
N’Koltang	NKLG	0.21	9.40	-14.0	LT=UT+1	Low-Lat. S
			Africa East Sector			
Haifa	BSHM	32.47	35.01	29.7	LT= UT+2	Beyond EIA N
Mitzpe Ramon	RAMO	30.35	34.46	27.0	LT= UT+2	Beyond EIA N
Addis Ababa	ADIS	9.2	38.46	1.6	LT= UT+3	Equatorial N
Asumbi	ASUM	0.37	34.37	-3.2	LT= UT+3	Equatorial S
Mbarara	MBAR	-0.36	30.44	-10.3	LT= UT+3	Low-Lat. S
Lusaka	ZAMB	-15.25	28.19	-31.6	LT= UT+2	Beyond EIA S
De Aar	DEAR	-30.39	23.59	-44.3	LT= UT+2	Beyond EIA S

SOURCE: Author.

A ROT phase fluctuation graph is a plot of universal time (UT) on the horizontal axis against the pseudo-random noise (PRN) codes of different satellites on the vertical axis as shown in Figure 46. In this study, the PRNs of the satellites have been color-coded, shown on the far-right side of the figure. The PRN numbers range from 1 to 32 depending on the availability. A group of colored horizontal points represents the ROT for different satellites corresponding to the PRNs, the length of which is an indication of the time in UT within which the satellite was in the FOV of the receiver. Sample ROT phase fluctuation graphs are shown in Figure 46 for a) SAGA, a low-latitude station with a dip latitude of 8.6^{o} N in the Brazil west (BW) sector, and b) ADIS, an equatorial station with a dip latitude of 1.6^{o} N in the Africa east sector.

Figure 46: Sample ROT plot from a low-latitude GPS- receiver station, SAGA on 24-10-2019 (SSW). The Figure shows ROT 32 satellites with PRNs 1 to 32. The blue vertical line with timestamps shows the start and end times of the irregularities.

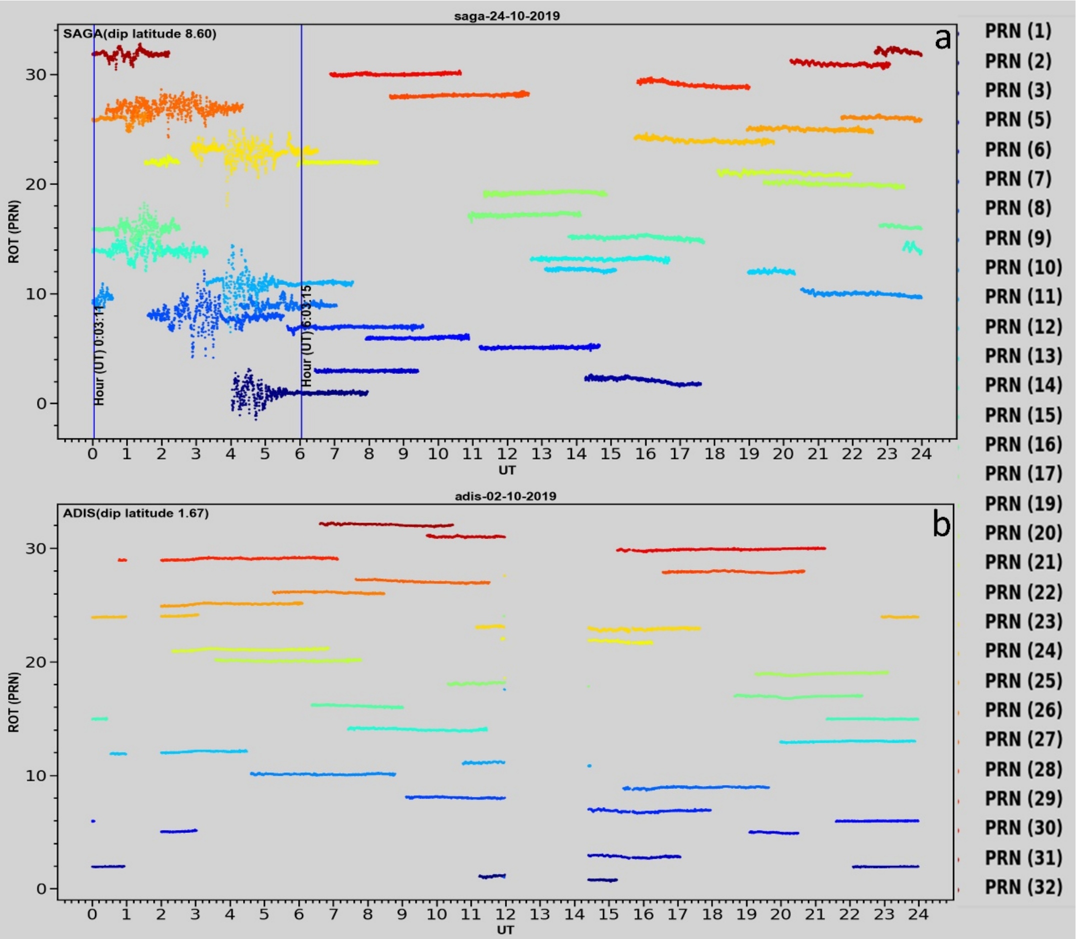

SOURCE: Author.

In the presence of irregularities, the ROT show phase fluctuations show vertically spread-out points (from the plot: fluctuating in the vertical plane) along the lifespan of the irregularity (Figure 46a). On the other hand, in the absence of irregularities along the signal path between the satellite and the receiver, the ROT phase fluctuations show almost straight horizontal lines with no spread, an example is shown in Figure 46b. The blue vertical lines with timestamps indicate the start and end of the observed irregularities when they occur. The irregularities associated with the different PRNs may start and end at different times as ionospheric irregularities are local and mobile causing the signals from different satellites connected to a receiver to pass through the irregularities at different times. Therefore, in this investigation, irregularities occur when one or more satellite signals show phase fluctuations. The start and end times of the irregularities for a given day will be given by the start time of the first and last satellite signals, respectively, that show phase fluctuations. For example, in

Figure 46a, the irregularities of the night started at 0:03:11 UT and ended at 6:03:15 UT, lasting for ~ 6 hours. Since ionospheric irregularities are nighttime phenomena, they generally occur between dusk and dawn.

5.3.3 September 2019 Antarctic Sudden Stratospheric Warming

In this study, the occurrence of ionospheric irregularities during the 2019 Antarctic minor SSW event is compared with the occurrence from 2017/018 (no SSW) from August to October. The stratospheric, solar, and geomagnetic conditions during the study period for 2019, 2018, and 2017 are shown and compared in Figure 47Figure 48, and Figure 51 respectively. The periods investigated in 2019, 2018, and 2017 are divided into 5 phases based on the 2019 T 90º S variation as pre-SSW, ascending, peak, descending, and post-SSW phases separated in the figures by black vertical lines (continuous and dashed). The stratospheric parameters were obtained from the Modern-Era Retrospective Analysis for Research and Applications, Version 2 (MERRA-2) reanalysis data at NASA's Goddard Earth Sciences Data and Information Services at https://acd-ext.gsfc.nasa.gov/Data_services/met/ann_data.html and the solar and geomagnetic parameters were obtained from NASA's https://omniweb.gsfc.nasa.gov/form/dx1.html.

Figure 47 shows the stratospheric, solar, and geomagnetic conditions during the period under investigation from 1 August 2019 to 31 October 2019. Figure 47a shows the stratospheric temperature at 90° S at 10 hPa increased from 201.76 K on 29 August 2019, crossing the 39-year climatological mean, and reaching a peak of ~ 272.84 K on 29 September 2019. The event ended on 16 October 2019. Between 5-11 September 2019, the polar temperature increased sharply from ~ 206.45 K to 266.72 K, with a difference of over 50 K in one week. In Figure 47b the mean zonal wind is seen to decrease from ~ 86 m/s to ~ 10 m/s between 28 August 2019 and 17 September 2019 without reversing (indicating a minor event) before the warming event commenced. In Figure 47c, it can be observed that the stationary planetary wave (PW1) increased strongly from ~ 0.13 km to ~ 1.52 km between 1 and 20 August 2019. It later dipped to 1.09 km on 25 August 2019 before rising again to 2.01 km on 2 September 2019. On September 4, the magnitude decreased again to 1.74 km before rising to the maximum of 2.18 km in the entire study period on 7 September. The PW1 enhancements occurred just before the commencement of the SSW event contributing to the weakening of the zonal mean flow referred to as preconditioning. The PW2 does not show any significant variations. Figure 47d, e, and f show respectively F10.7, Dst, and Kp indices.

The solar and geomagnetic indices show that during the entire period of investigation in 2019, geomagnetic and solar conditions were low with an average F10.7 flux under 74 s.f.u, Dst ≥ -40 nT and Kp < 5. This helps to isolate the effects of the SSW event on the ionosphere and the generation of irregularities. Although the SSW event of 2019 is considered minor, it involved a strong stationary PW1, a large rise in temperature over a short period and it occurred during the solar minimum in the transition between solar cycles 24 and 25.

Figure 47: Overview of the stratospheric conditions during the 2019 minor southern hemisphere SSW 2019. From top to bottom: a) Stratospheric temperature at 90°N at 10 hPa (red line), 39-year historic temperature (blue line) b) zonal mean zonal wind, c) amplitudes of the Planetary wave zonal wave numbers, PW1 and PW2. d) solar flux, e) Dst, and f) Kp. The black vertical lines show the different phases in the SSW under investigation. The two black vertical dashed lines mark the start and end of the event.

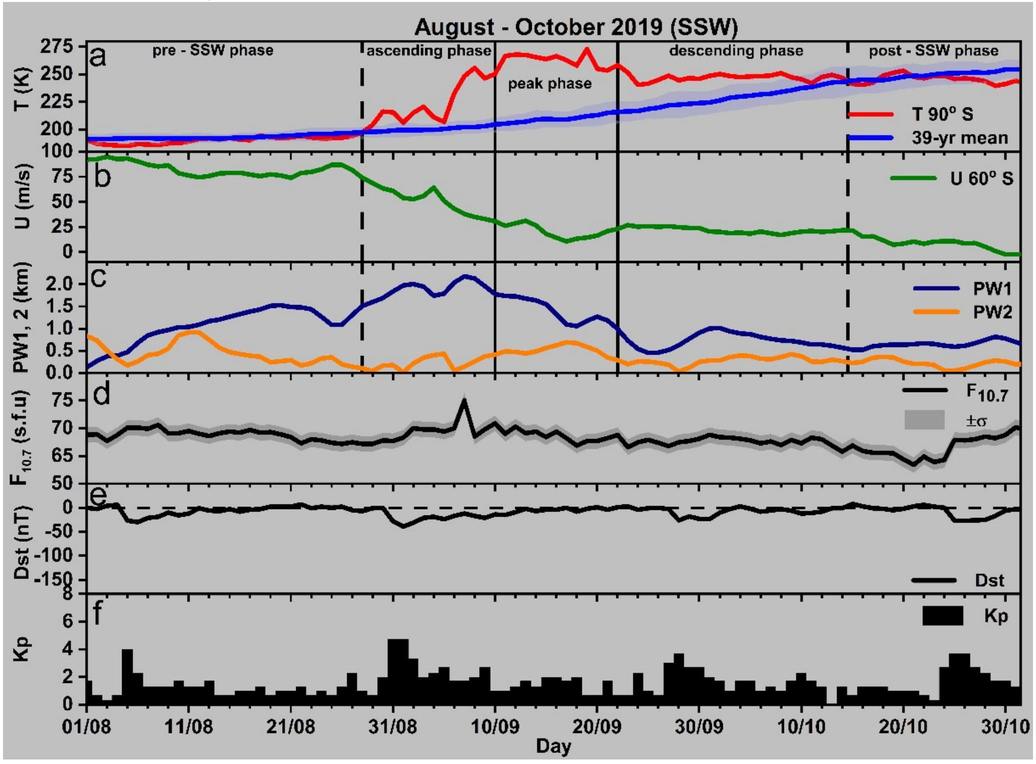

SOURCE: Author.

The SSW event started on 28 August 2019 and ended on 14 October. The start and end of the event were determined from the point where the stratospheric temperature at 90° S at 10 hPa crossed the climatological mean upward in the case of the start and when it crossed it downward in the case of the end. Pre-SSW phase is described as the period before the event commencement, between 1 and 28 August (28 days). The ascending phase starts from 29 August to 9 September (12 days) which is the period where the temperature increases rapidly. The peak phase occurred from 10 – 22 September (13 days). The peak phase is the period where the event attained the highest temperatures. The stratospheric temperature started decreasing from 23 September to 13 October (21 days), this is the descending phase. On October 14, the stratospheric temperature crossed the climatological mean temperature and marked the start of the post-SSW phase which ended on 31 October (18 days).

Figure 48 shows the stratospheric, solar, and geomagnetic conditions for the same period in 2018 (No SSW) as in 2019 (SSW). The stratospheric temperature at 90° S at 10 hPa does not show any variation large enough to induce an event as shown in Figure 48a. The zonal mean zonal wind and planetary waves (both PW1 and PW2) do not show any significant variations (Figure 48b and c). In the lower panel of Figure 48, the solar flux is low but still with an average higher than in 2019. In Figure 48b, a strong geomagnetic storm is observed with its main phase starting on 25 August and ending on 26 August 2018. The recovery phase lasted for about 3 days, fully recovering around 31 August 2018. The Dst daily average reached a minimum value of - 104 nT with the Kp value rising to over 5. The storm started days before the beginning of the ascending phase in 2018. The Dst values for all other days are comparable. The Kp indices recorded for both periods – 2018 (No SSW) and 2019 (SSW) – are also comparable. Barring minor deviations, the solar and geomagnetic conditions for the two periods are similar enough to compare.

Figure 48: Same Figure 47 as but for 2018 without SSW event. The blue overlay shows the initial phase of a geomagnetic storm, the yellow overlay shows the main phase of the storm, and the black arrow indicates the recovery phase.

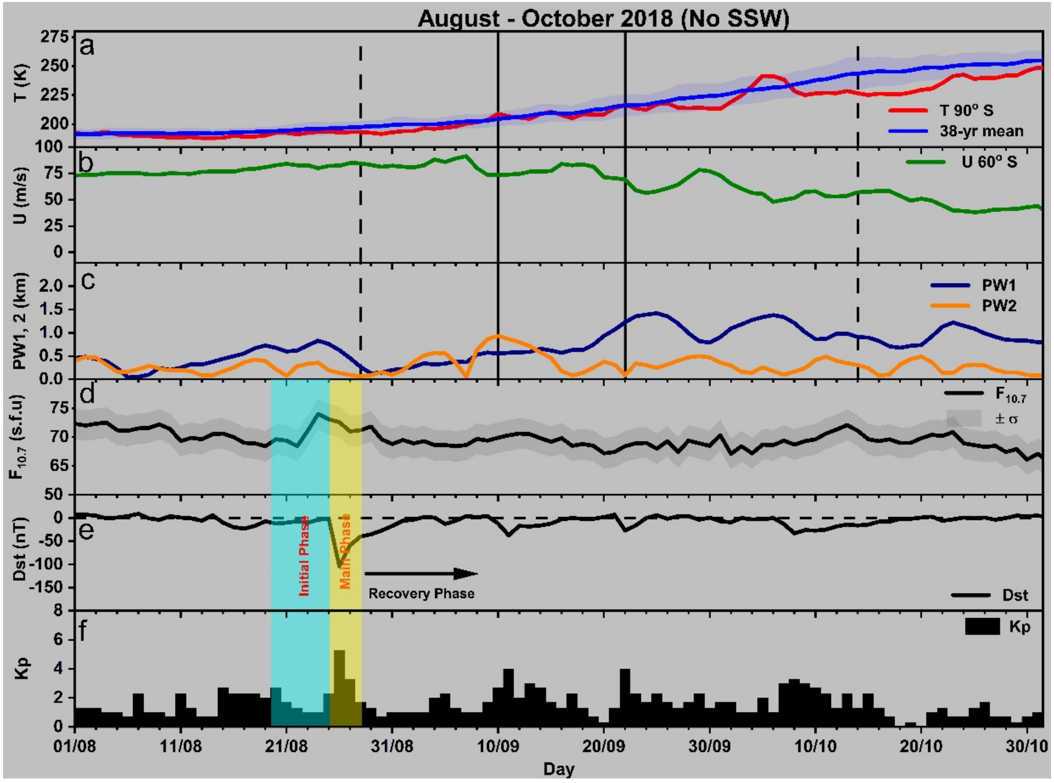

SOURCE: Author.

5.4 Results

The main aim of the study was to investigate the effect of SSW events in the generation or suppression of ionospheric irregularities by comparing irregularity occurrence rates during the different phases of the warming process. Irregularity occurrence characteristics during a period with an SSW event (2019) and two other periods with no SSW (2018/2017) are also compared to investigate and confirm the role of SSW in the generation or suppression of ionospheric irregularities over Brazil and Africa.

5.4.1 ESF Occurrence

Figure 49 shows the day-to-day occurrence of Equatorial Spread-F (range + frequency types) observed from ARA, JAT, and SJC stations in 2019 (left panel) and 2018 (right panel) between August and October. The black curves show the stratospheric temperatures within the same period in 2019 and 2018, respectively. The black vertical lines (continuous and dashed) indicate the different SSW phases (pre, ascending, peak, descending, and post) as described in section 5.3.3 and shown in Figure 47. The gray rectangles with black diagonal lines indicate dates when there was no data. The total ESF occurrence (range + frequency) rates for the different phases were calculated from equation (14). The results show an overall higher occurrence frequency in 2019 than in 2018 for all three stations ARA, JAT, and SJC. The occurrence frequencies between August and October 2019 at all three stations were ~ 89 % compared to 85.2 %, 71.9 %, and 85.2 % at ARA, JAT, and SJC respectively in 2018.

Figure 49: Day-to-day variation of range (red) and (blue) frequency type Spread-Fs from ionosondes located at different latitudinal regions in Brazil (Araguatins, Jataí São José dos Campos) in a) 2019 (SSW) b) 2018 (No SSW). The black vertical lines demarcate the SSW phases (pre, ascending, peak, descending, and post) as shown in Figure 47 and the gray rectangles with black diagonal lines indicate when there are absent.

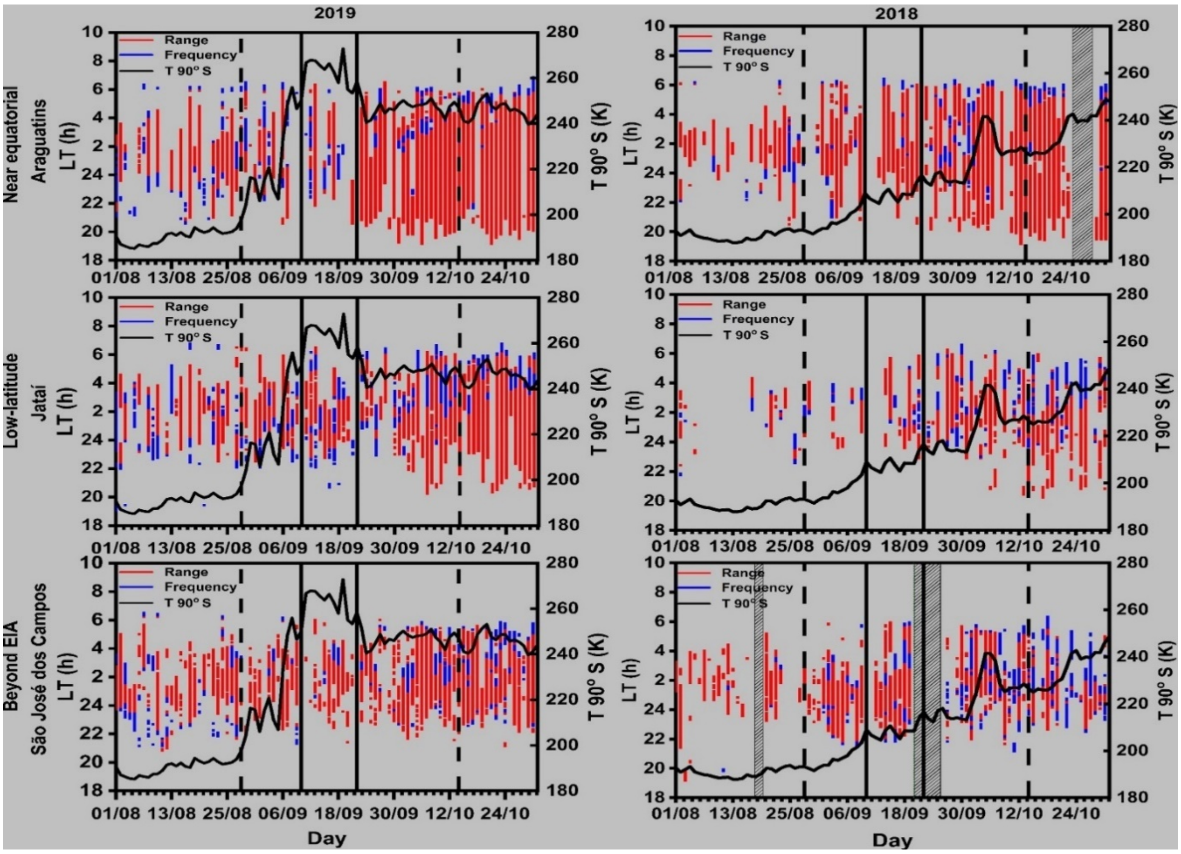

SOURCE: Author.

Figure 49 also shows a decrease in ESF occurrence from the equatorial station to the EIA crest region, ARA to JAT, and SJC. This is because ionospheric irregularities generally originate from the equatorial regions and extend to higher latitudes as they rise higher in the ionosphere. Thus, irregularities are observed more often in the equatorial regions and become less frequent as you move to higher latitudes. The results also show higher occurrence rates from the stations in the eastern sector (ARA) than in the western sector (JAT, SJC), although that can also be attributed to their latitudinal locations with respect to each other. Although the occurrence frequencies at the 3 stations in 2019 were similar, the total occurrence in hours over the entire study period decreased from ARA, a near-equatorial with ~ 489.16 h, followed by JAT, a low-latitude station with 398.49 h, and then SJC, beyond EIA region with 331.33 h. In 2018 also, ARA recorded 401.42 h, JAT recorded 240.92 h and SJC recorded 198.17 h. This implies that the total occurrence of ESF in hours also decreases with increasing latitude.

In 2019 at ARA, the Spread-F occurrence frequency decreased from 85.71 % during the pre-phase to 83.33 % at the ascending phase. The occurrence decreased further at the peak phase at 69.23 % before increasing to 100 % at the descending and post-SSW phases. The occurrence frequencies for each phase for 2019 and 2018 at all three ionosonde stations are summarized in Table 7. This trend is also observed in the total occurrence in hours of the recorded ESF at the different phases with the pre-phase recording 83.83 h and decreasing to 36.25 h and 42.58 h for the ascending and peak phases, respectively. The descending and post-SSW phases recorded a total of 155 h and 171.50 h, respectively. At JAT and SJC, the occurrence rates increased from the pre to the ascending phase and decreased at the peak phase, however, the occurrence frequencies at both stations were higher than ARA during the ascending and peak phases. This could be due to the shifting or extension of the southern EIA peak equatorward during SSW events, thereby increasing the background plasma density around JAT (MO *et al.*, 2017). After the peak phase, the occurrence increased at the descending and post phases following the ESF seasonal occurrence patterns in the Brazilian region. The occurrence patterns of JAT and SJC are similar to that of ARA. On the other hand, ESF occurrence frequency at ARA in 2018 increased from the pre-phase to the ascending phase following the seasonal variation of ESF in the Brazilian region increasing from August to October in the absence of a warming event. The total occurrence in hours at JAT and SJC followed a similar trend as the occurrence at ARA in 2018.

Table 7: ESF Occurrence rates (%) for the different SSW phases observed in all three stations in 2019 and 2018.

Station/Phase	Pre	Ascending	Peak	Descending	Post
			2019 (SSW)		
ARA	85.71	83.33	69.23	100.00	100.00
JAT	78.57	91.67	84.62	95.24	100.00
SJC	78.57	91.67	84.62	95.24	100.00
TOF	80.95	88.89	79.49	96.83	100.00
			2018 (No SSW)		
ARA	75.00	83.33	84.62	95.24	92.86
JAT	42.86	50.00	100.00	90.48	94.44
SJC	78.57	100.00	69.23	94.12	88.89
TOF	65.47	77.78	83.33	93.22	92.00

Tot. Occ. Freq. (TOF).: The average occurrence frequency over all the stations for every phase

SOURCE: Author.

From the pre-SSW phase in August going through the peak and to the post-SSW phase in October, in the absence of a warming event, the occurrence of ESF in the Brazilian region is expected to increase in that order. Many studies from that region have reported the seasonal variation of ESF/plasma bubbles (AGYEI-YEBOAH *et al.*, 2019; PIMENTA *et al.*, 2001; SAHAI; FAGUNDES; BITTENCOURT, 2000) where ESF occurrence frequencies increase from August to October. Their results are different from what has been reported here, as in September, around ascending and peak phases of the SSW event, ESF occurrence frequency decreased before increasing during the recovery and post-SSW phases as shown in Table 7.

The influence of SSW on the occurrence of ionospheric irregularities has been reported (DE PAULA *et al.*, 2015; JOSE; VINEETH; PANT, 2017; YE *et al.*, 2021; YU *et al.*, 2020). DE PAULA *et al.* (2015) reported low-latitude scintillation weakening during Arctic SSW events of 2001/2002, 2002/2003, and 2013/2013 using GPS receivers at São José dos Campos - near the southern EIA crest. The SSW events were moderate to major under low Kp conditions. Their result is consistent with the observations ESF reported here from SJC under the 2019 Antarctic warming event. YU et al. (2020) also observed a 30% decrease in F-layer scintillation from pre- to SSW days using the COSMIC/FOMOSAT-3 satellite during the January 2013 southern hemisphere major warming.

The daily foF2 variation of the ionospheric plasma during the period of study in both 2019 (SSW) and 2018 (No SSW) are shown in Figure 50 left and right panels, respectively. The average foF2 day-to-day variations were obtained from ARA, JAT, and SJC ionosonde stations. The black vertical lines (continuous and dashed) indicate the different SSW phases (pre, ascending, peak, descending, and post) as described in section 5.3.3 and shown in Figure 47 The gray rectangles with black diagonal lines indicate dates when there were no data. The white regions show the periods when ESFs were observed and as such foF2 values could not be obtained. From Figure 50, the results from 2019 show that the foF2 values increase from the pre-SSW phase to the ascending phase at ARA, JAT, and SJC stations and decrease during the peak phase. The plasma frequency then starts to increase again from the descending phase to the post-SSW phase. This implies that plasma density around these regions might have decreased during the highest temperatures of the Antarctic warming event. This could have affected the occurrence frequencies of the ionospheric irregularities (ESF) recorded by the respective ionosondes located at ARA, JAT, and SJC. This result is consistent with the ESF variation presented here in this paper. Comparing with the foF2 plots from 2018 from the same stations, it can be observed that the foF2 increased steadily from August to

October – following all the phases of the event. Thus, the results show a difference between foF2 variation in the presence or absence of a warming event.

Figure 50: Day-to-day critical frequency (foF2) variation obtained from three ionosonde stations over Brazil for pre-, peak, and post-SSW phases in 2019. a) Araguatins, Jataí, São José dos Campos in 2019 b) same as but for 2018 (No SSW). The black vertical lines demarcate the SSW phases (pre, ascending, peak, descending, and post) as shown in Figure 47 and the gray rectangles with black diagonal lines indicate when there was no data.

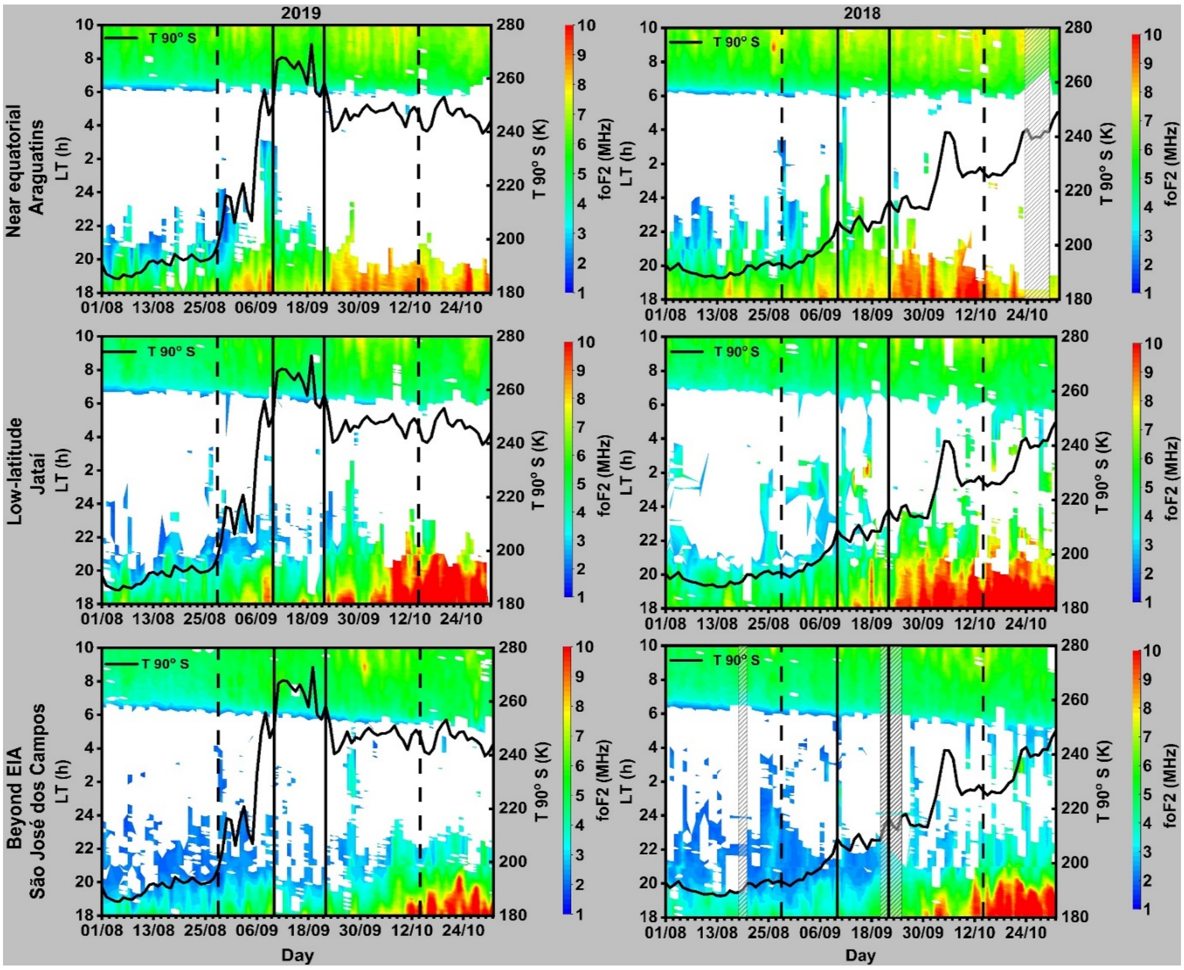

SOURCE: Author.

The effect of SSW on the ionospheric plasma density has been linked to the decrease in TEC, F-layer electron density, and EIA intensity at different times in the day during and sometimes after an SSW event (AZEEM; CROWLEY; HONNIBALL, 2015; GONCHARENKO *et al*., 2010a; VIEIRA *et al*., 2017; YASYUKEVICH, 2018). (FAGUNDES *et al*., 2015) saw a decrease in the foF2 parameter in the afternoon-evening period during the 2009 warming event which is consistent with the observations presented in this investigation.

VIEIRA *et al.* (2017), over Brazil, used 72 GPS receivers located from the equatorial region of Brazil to the southern EIA crest and beyond and spanning between 35- and 65-degree longitudes west to study TEC disturbances during SSW events. They studied the ionospheric F-layer response to the minor warming of 2012 using VTEC from GPS-TEC data. They observed that all over Brazil, the VTEC decreased by 30% in the daytime during and after the SSW event. In this study, we saw the plasma density decrease during the peak phase, however, the plasma density values after the peak phase just followed the seasonal ionospheric electron density trend and increased in the latter part of September and October. YASYUKEVICH (2018) also studied ionospheric peak electron density (NmF2) variation during 12 northern hemisphere SSWs using vertical sounding data from DPS-4 ionosonde located in Norilsk (88.0°E, 69.2°N). They observed that generally, the NmF2 responded negatively in the evolution and peak phases of an SSW event and positively during the recovery phase which is comparable to the results presented here.

Ionograms from August to October 2017, from ARA, JAT, and SJC were also analyzed for Spread-F occurrence and foF2 variations during all 5 phases. Figure 51 shows the stratospheric, solar, and geomagnetic conditions during the study period in 2017. Each plot is divided into phases separated by black vertical lines. The stratospheric temperature at 90° S (K) variation during this period shows that there was no SSW event in the Antarctic region at the time. Even though there was a temperature increase during the period, this increase was not as dramatic as it increased from a little under 200 K to about 260 K in about three months as shown in Figure 51a. In 2019 (SSW), a similar temperature rise occurred within a week. The solar (Figure 51b) and geomagnetic (Figure 51c and d) activity conditions indicate high solar and geomagnetic activities with peak values in the ascending phase with F10.7, Dst, and Kp reaching maximum values of 185.5 s.f.u on September 4, 2017, - 87 nT and 6 on September 8, 2017, respectively.

Figure 51: a) T 90° S, b) $F_{10.7}$ c) Dst, and d) Kp variations between August and October 2017. The black vertical lines (dashed, and continuous) show the various phases of the SSW event mentioned.

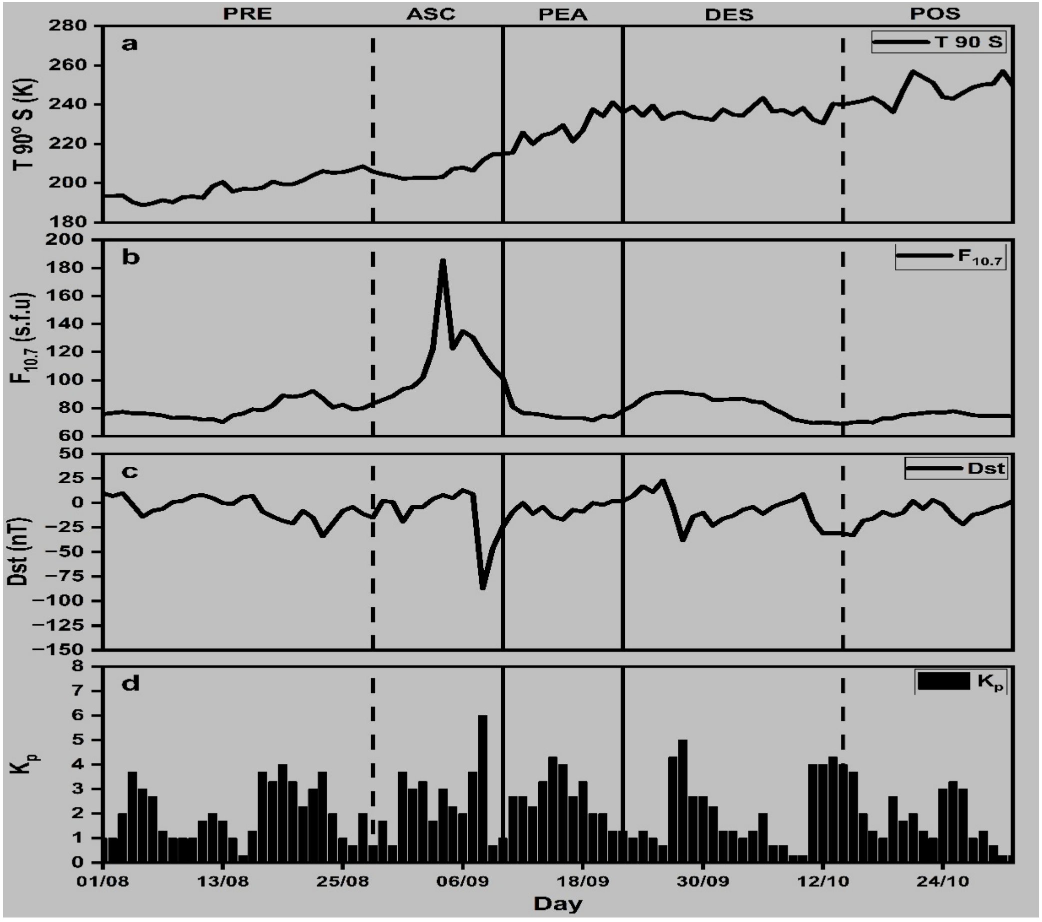

SOURCE: Author.

Figure 52 shows the day-to-day Spread-F occurrences in the left panel for ARA, JAT, and SJC in the upper. In the right panel of

Figure 52, the foF2 variations are shown for ARA, JAT, and SJC. The top, middle, and bottom panels are respectively for ARA, JAT, and SJC. The stratospheric temperature at 90° S (black curve) variation during this period is shown on the plots. The total occurrence rates for ARA, JAT, and SJC were 88%, 81%, and 90% respectively.

Figure 52 Day-to-day variation Spread-F (left panel) and critical frequency (right panel) variation from ARA (upper panel), JAT (middle panel), and SJC (lower panel) in 2017 – no SSW, through all 5 phases.

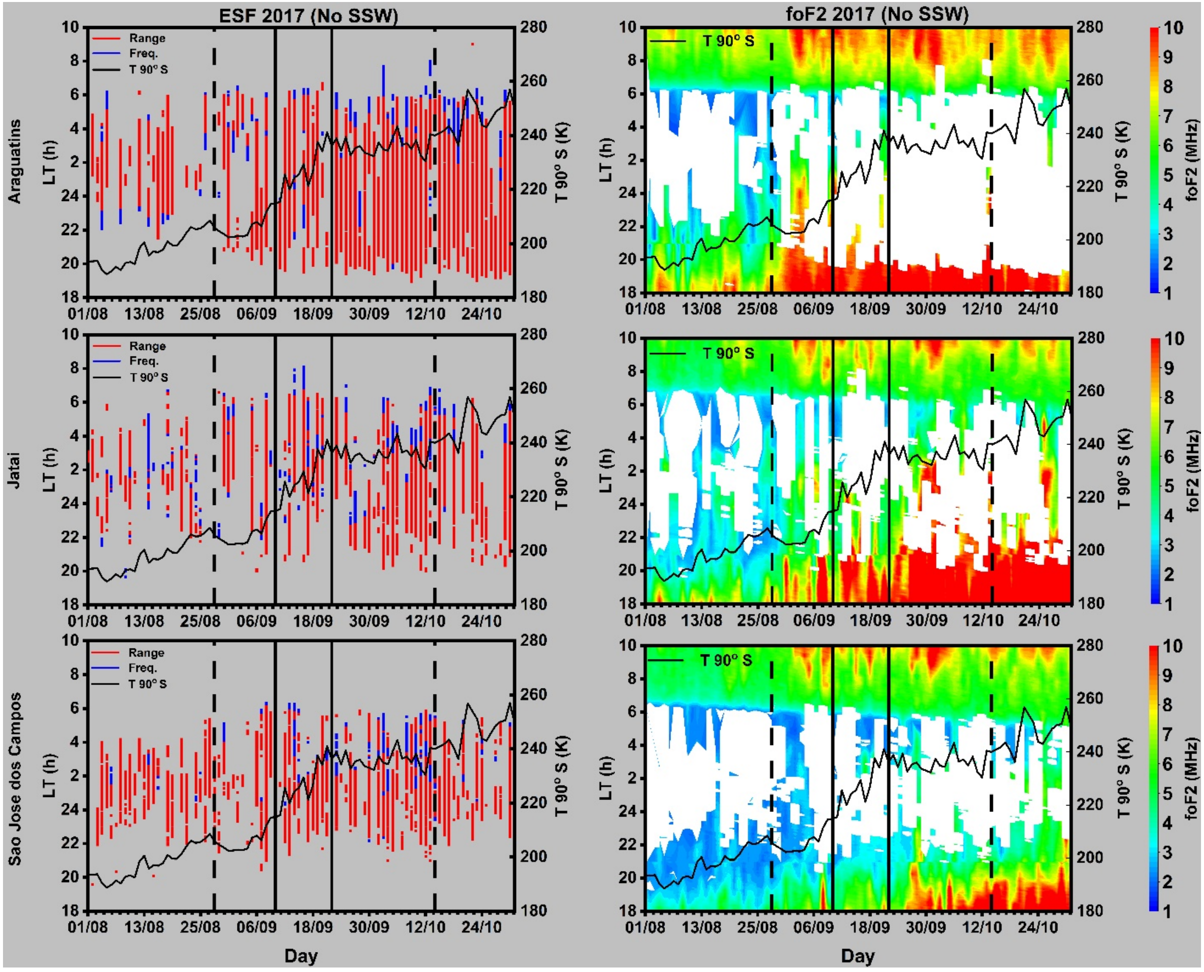

SOURCE: Author.

The occurrence rates followed the solar and geomagnetic activity variation with ESF occurrence rates increasing from the pre-phase to the ascending phase in ARA and SJC. The occurrence rate decreased in the peak phase and increased again in the descending phase before decreasing again in the post-phase along with the solar activity. In Jatai, however, the ESF occurrence rates increased from the pre-, ascending- phase to the peak phase and decreased in the descending and post phases. Unlike in 2019 and similar to 2018, the foF2 increased consistently from pre-phase to post-phase in JAT. However, in ARA and SJC, during the ascending phase, the foF2 increased from the pre-phase and decreased during the peak phase and descending phases similar to 2018 (no SSW).

Again, just like in 2018, the occurrence rates in the peak phase in 2017 (no SSW) are higher in all stations compared to the occurrence rates in 2019. In this scenario, the results are more similar to that from 2018 (no SSW) where the occurrence rates and foF2 variations are controlled not only by season but also by solar and geomagnetic activities than in 2019 (SSW). Whereas in 2017/2018, season, solar and geomagnetic activities influenced the occurrence frequency of ESF, in 2019, the only factor influencing the occurrence rates was the SSW event in the absence of any major solar or geomagnetic activity. The solar activity caused the occurrence rate to increase very rapidly in the ascending phase and decrease in the peak phase due to the decreased solar activity. Thus, causing a crest between the ascending and descending phases. In both 2017/2018 (no SSW), the behavior of ESF occurrence rate depends on season, solar or geomagnetic activity while in 2019, ESF occurrence rate behavior seems to have been influenced by the SSW event.

5.4.2 ROT phase fluctuation occurrence

5.4.2.1 Brazil Sector

Figure 53 shows the day-to-day variations of ROT phase fluctuations from several stations located within different latitudinal regions for the West (a) and East (b) Brazil sectors from August to October 2019. Vertical black lines are used to distinguish the different phases of the warming event described in an earlier section of the thesis. The start and end times in LT are shown in the figure. The stations in the figure are arranged in decreasing dip latitude from top to bottom indicating the latitudinal regions where the stations are located. The stations used from each sector are detailed in Table 6. In general, the ROT phase fluctuations in Figure 53 show the occurrence of irregularities decreasing as one moves further from the equator to higher latitudes. It also shows that in the equatorial and low-latitude stations, the majority of irregularities occurred during the descending and post-SSW phases in October.

Figure 53: Day-to-day ROT phase fluctuations from selected ground-based GPS receivers from Brazil a) West and b) East sectors in 2019, SSW period. The black dark vertical lines indicate the start and end of the SSW event. The entire study period is divided into pre-SSW, ascending, peak, descending, and post-SWW phases shown by the black vertical lines (continuous and dashed) as shown in Figure 47.

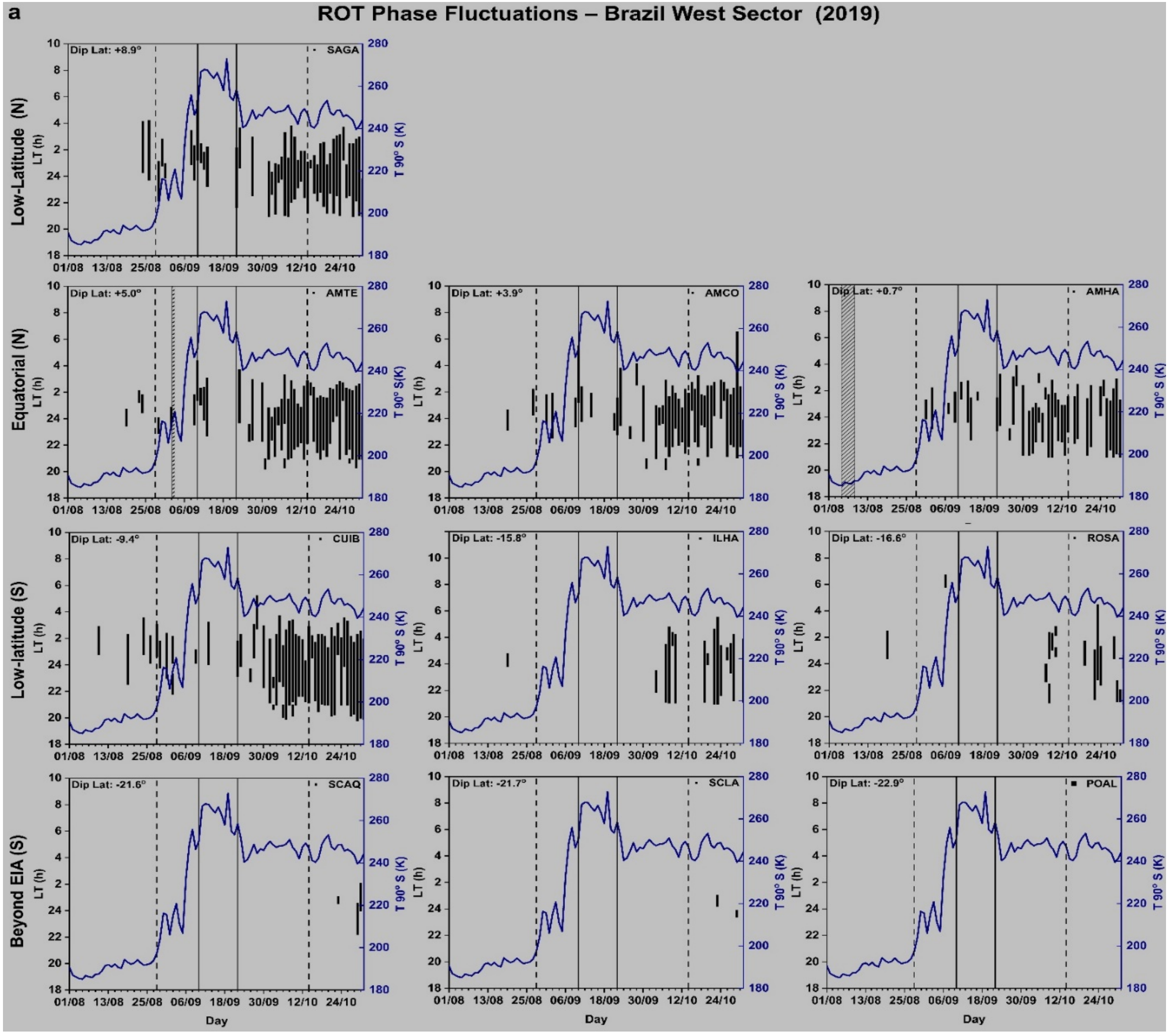

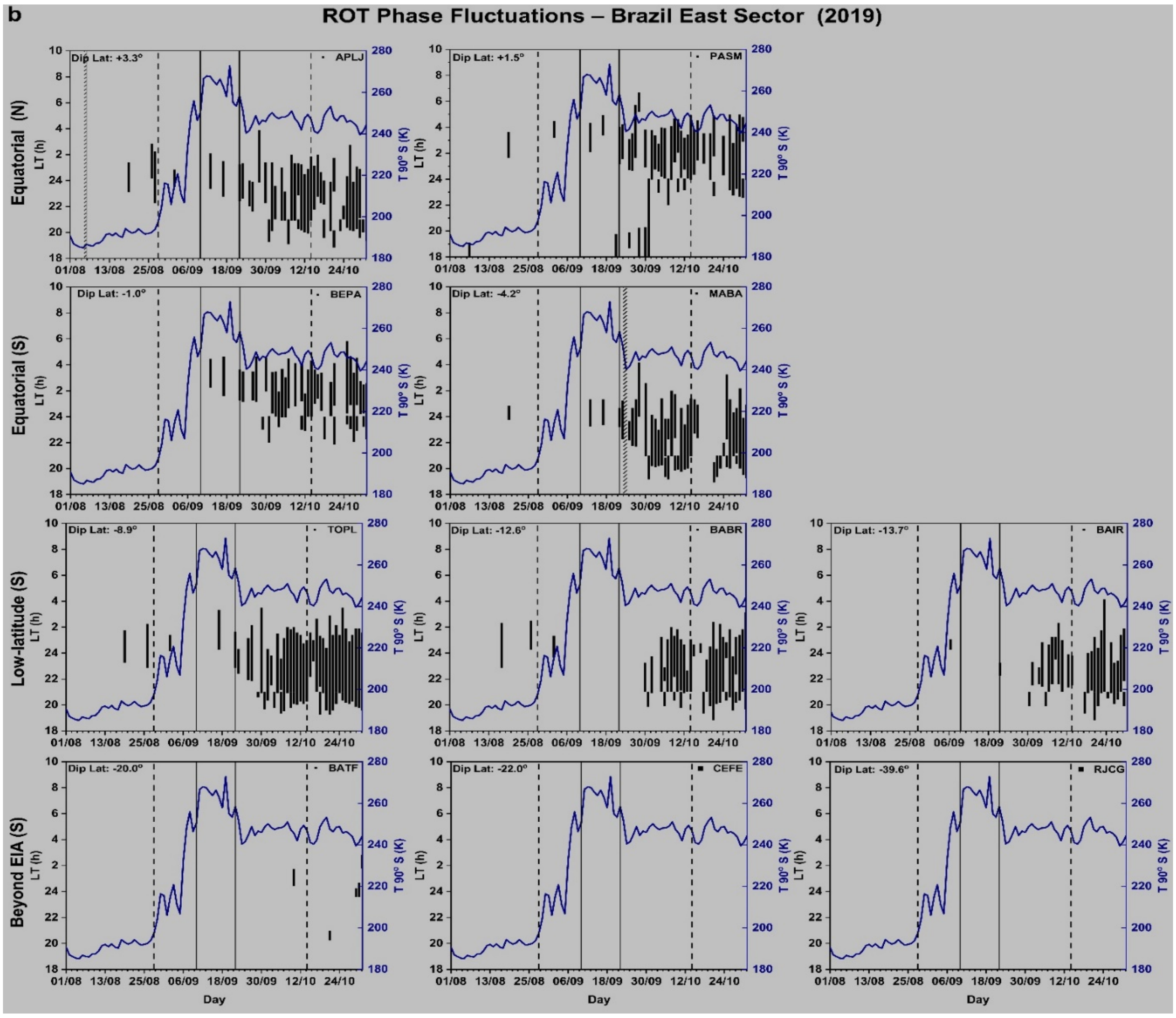

SOURCE: Author.

The results from AMHA, AMCO, in the west sector, and APLJ, MABA, TOPL, and PASM in the east sector, show a seasonal trend in the occurrence of ROT phase fluctuations with occurrence increasing from August to October and from the pre-SSW phase to post SSW phase. AMTE, SAGA, CUIB, and ROSA in the west sector show a decrease in ROT occurrence frequency from the ascending phase to the peak phase from 40.00 % to 30.77 %, 41.67 % to 38.46 %, 41.67 % to 15.38 %, 8.33 % to 0.00 % respectively, before increasing again during the descending and post phases of the event. Similar results are observed in the east sector, BAIR, and BABR, where the occurrence frequency decreased from 8.33 % to 0.00 % and 8.33 % to 7.69 % respectively, and then returned to the seasonal trend during the descending and post phases of the SSW event. The results here agree with the results presented on the ESF occurrence in the previous section.

Figure 54 shows the daily ROT fluctuations for the same stations as Figure 53 but from 2018 when no SSW event occurred. The latitudinal and seasonal trends are similar to the results from 2019 and observations from other studies from the Brazilian region. The figures show decreasing ROT phase fluctuation occurrence the farther away from the equator. All the stations from the west and east sectors show only seasonal variations as the occurrence rates increase with the phases – from pre, ascending, peak, and descending to the post-SSW phase. The occurrence rates during the peaks phase are generally higher in 2018 than in 2019 at all receiver stations, even for those that showed similar occurrence trends as in 2019. These results are similar to the results from the ESF occurrence shown earlier and show that SSW may affect the occurrence of irregularities, especially during the peak phase at the highest temperatures.

Figure 54: Same as Figure 53 but for 2018 – No SSW.

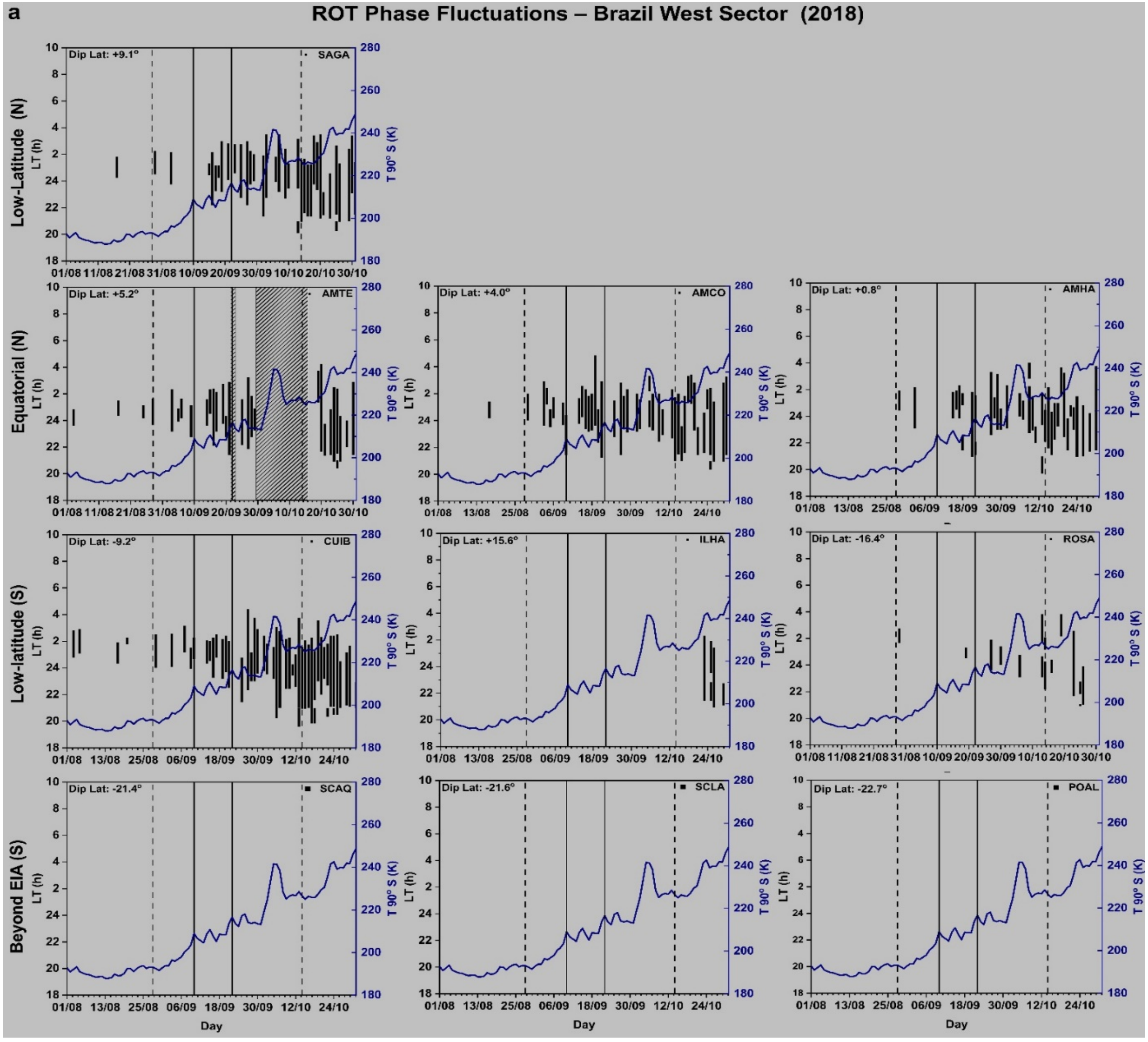

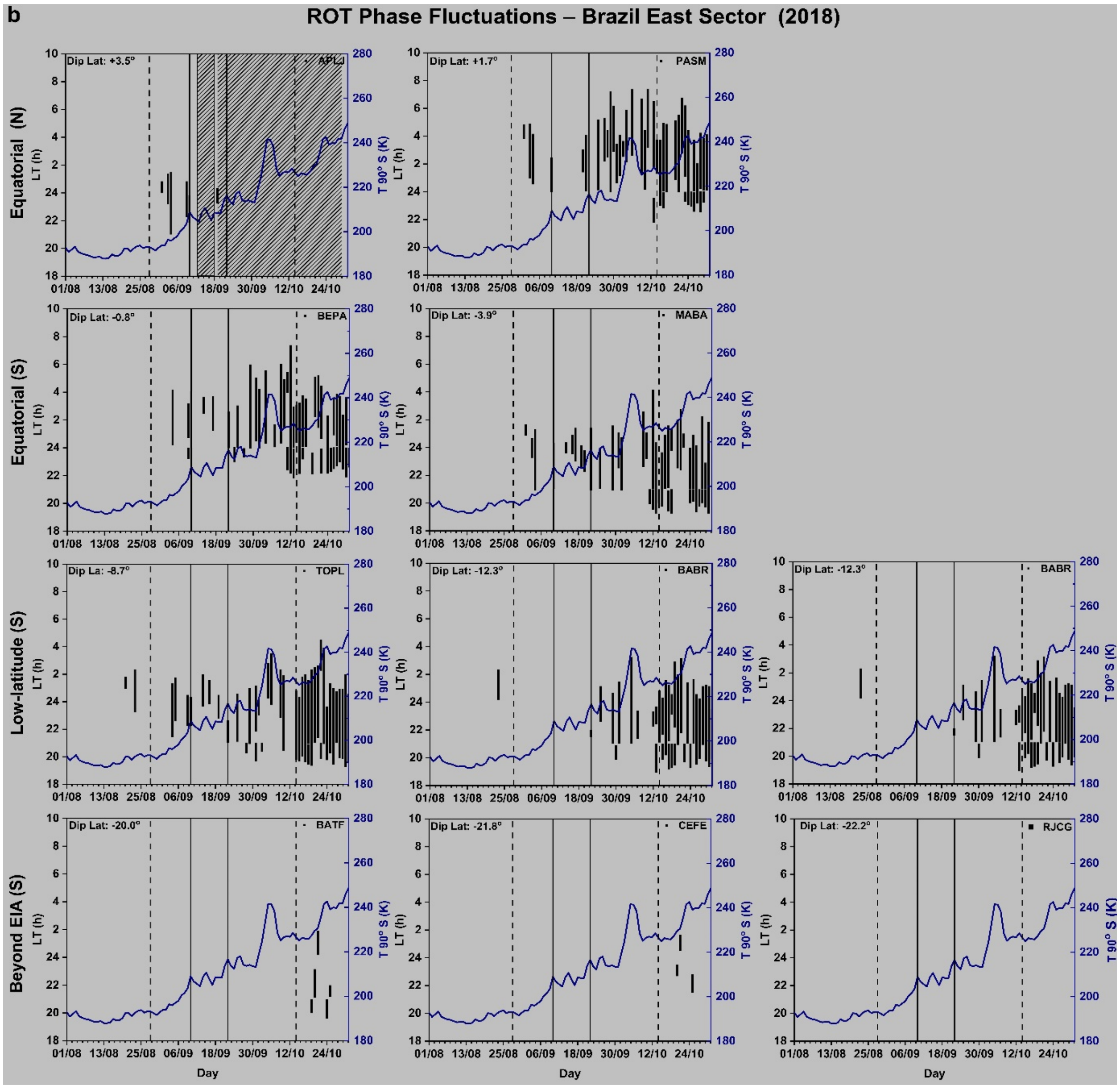

SOURCE: Author.

In 2018, the average F10.7 index was higher (still low solar activity) than in 2019. This means that in general, the occurrence frequency of ROT phase fluctuation should be higher in 2018 than in 2019 as the occurrence of ESF has been linked with solar activity (AGYEI-YEBOAH *et al.*, 2019; PIMENTA *et al.*, 2001; SAHAI; FAGUNDES; BITTENCOURT, 2000). The results show higher occurrence rates from 2019 at almost all phases for ESFs and ROTs alike. However, in 2018, there was a strong geomagnetic storm just before the ascending phase. This might have affected the occurrence of irregularities during the period. Geomagnetic storms are known to have considerable suppression or intensification effect on ionospheric irregularities in some longitude regions and latitudes (BASU *et al.*, 2010; DUGASSA; HABARULEMA; NIGUSSIE, 2019; SAHAI *et al.*, 2009).

Notwithstanding, the occurrence frequency showed the usual seasonal characteristics for the region.

The occurrence of ionospheric irregularities as observed from the ROT phase fluctuations show increasing occurrence from August to October for both 2019 (SSW) and 2018 (no SSW) in both the west and east sectors in the equatorial region which is the usual occurrence pattern of irregularities in the Brazilian ionosphere around this time of the year. However, at most of the stations, the occurrence rates were generally greater in 2019 than in 2018. Considering the different phases, it can be observed that in 2019, the occurrence rates decreased from the pre-SSW phase to the peak phase, then increased during the descending and the post-phases. In 2018 on the other hand, the occurrence of irregularities increased from pre-to-peak- to post-SSW phases consistent with the seasonal occurrence of ionospheric irregularity observations.

5.4.2.2 Africa Sector

Figure 55a and b show ROT phase fluctuations in the Africa west and east sectors from 2019. In the west sector, the figure only presents results from low-latitude south and beyond northern EIA crest regions due to the low number of stations and lack of data at some receiver stations during the study period from this sector. The east sector is no different as many stations available here did not have data within the period of study. The results from both east and west sectors show clear latitudinal variation in ROT phase fluctuation occurrence. It is observed in the west sector that YKRO, NKLG, and BJCO (mostly without data) in the low latitude region show the occurrence of irregularities while MELI, RABT, and OUCA, in the higher latitudes, beyond EIA, show no occurrence of irregularities. In the east sector, the equatorial and low latitude stations ADIS, MBAR, and ASUM present a small number of irregularities compared to the west sector as the higher latitudes show no occurrence of irregularities.

Figure 55: Day-to-day ROT phase fluctuations from selected ground-based GPS receivers from Africa a) West and b) East sectors in 2019, SSW period. The black dark vertical lines indicate the start and end of the SSW event.

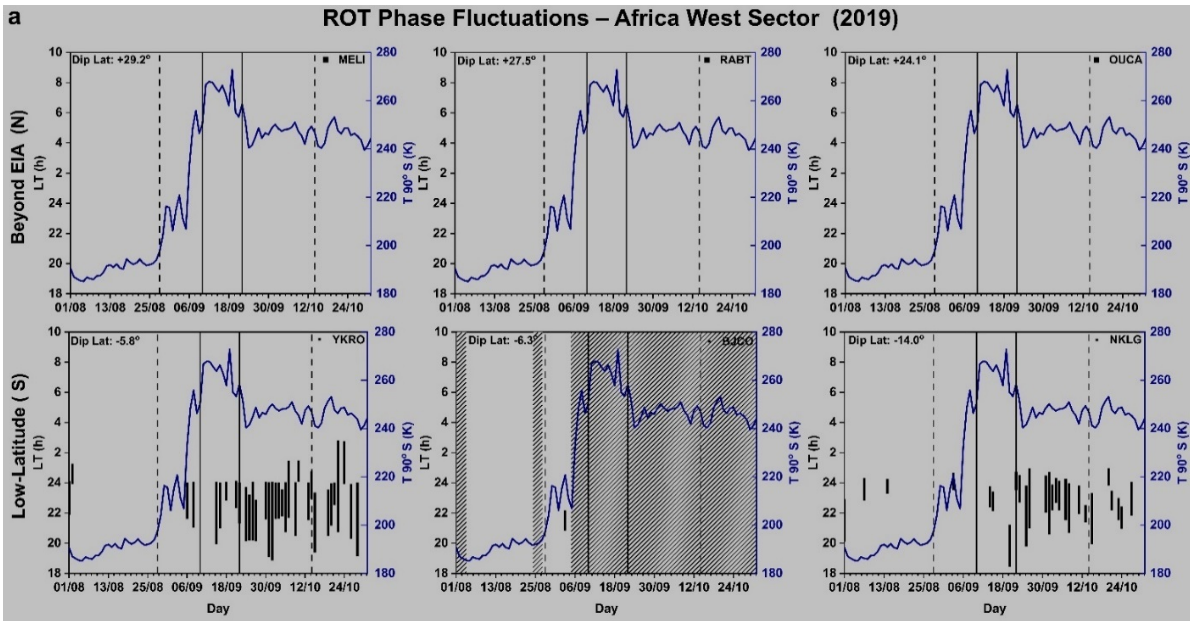

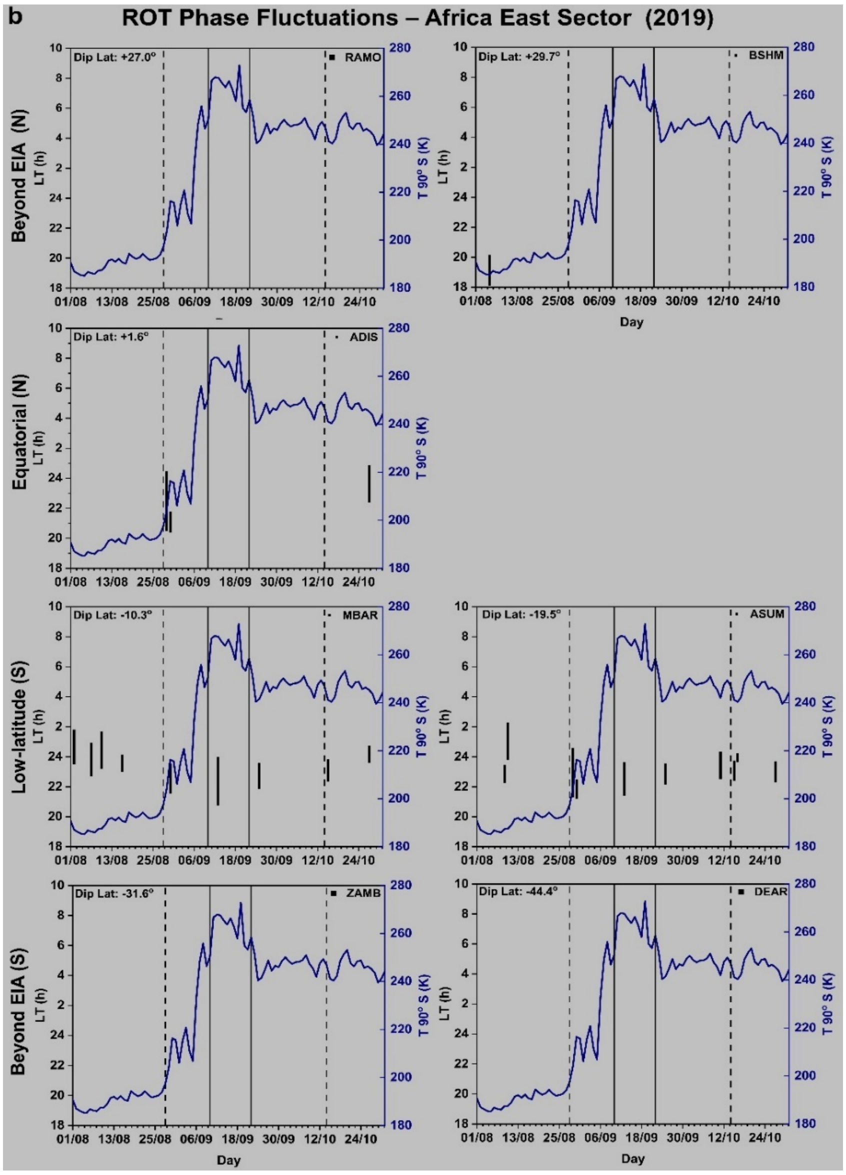

SOURCE: Author.

It can be seen that the occurrence of irregularities in the west sector is higher than in the east sector consistent with the occurrence characteristics of irregularities in the African sector. In the African sector ionospheric irregularities are known to have higher occurrence frequencies from January to April and September to December in the west and between May and July in the east (NISHIOKA; SAITO; TSUGAWA, 2008; OLWENDO; CILLIERS; MING, 2021). The results from YKRO and NKLG demonstrate this seasonal trend in the Africa sector. The combined occurrence rates of the ascending peak phase 16.67 % and 38.46 % respectively from YKRO and 8.33 % and 30.77 % from NKLG are comparable to or lower than the occurrence frequency of descending (post) SSW phase with occurrence rates of 71.43 % (50.00 %) and 57.14 % (38.89 %) for YKRO and NKLG, respectively. September and

October are within irregularity peak season in the West African region. The results from ADIS, MBAR, and ASUM show a distribution of ROT phase fluctuations over the period under investigation from the Africa east sector. ADIS, MBAR, and ASUM show a decrease in occurrence frequency from 16.67 % to 0.00 %, 8.33 % to 7.69 %, and 16.67 to 7.69 % respectively from ascending to the peak SSW phase consistent with results reported in an earlier section.

Figure 56a and b show similar results as Figure 55a and b but for 2018 with no SSW event. The latitudinal, longitudinal, and seasonal trends are consistent with the observations from 2019. Combined occurrence rates for the ascending and peak phases of 16.67 % and 69.23 % for YKRO and 50.00 % and 46.15 for NKLG are higher than the individual descending and post-SSW phases of 71.43 %, 72.22 %, and 55.56 %, 66.67 %. This is in contrast to the results from the same stations in 2019 (SSW) where the ascending and peak occurrence rates combined are less than the occurrence frequencies of the individual phases of descending and post SSW.

Figure 56: Same as Figure 5 but for 2018 – no SSW

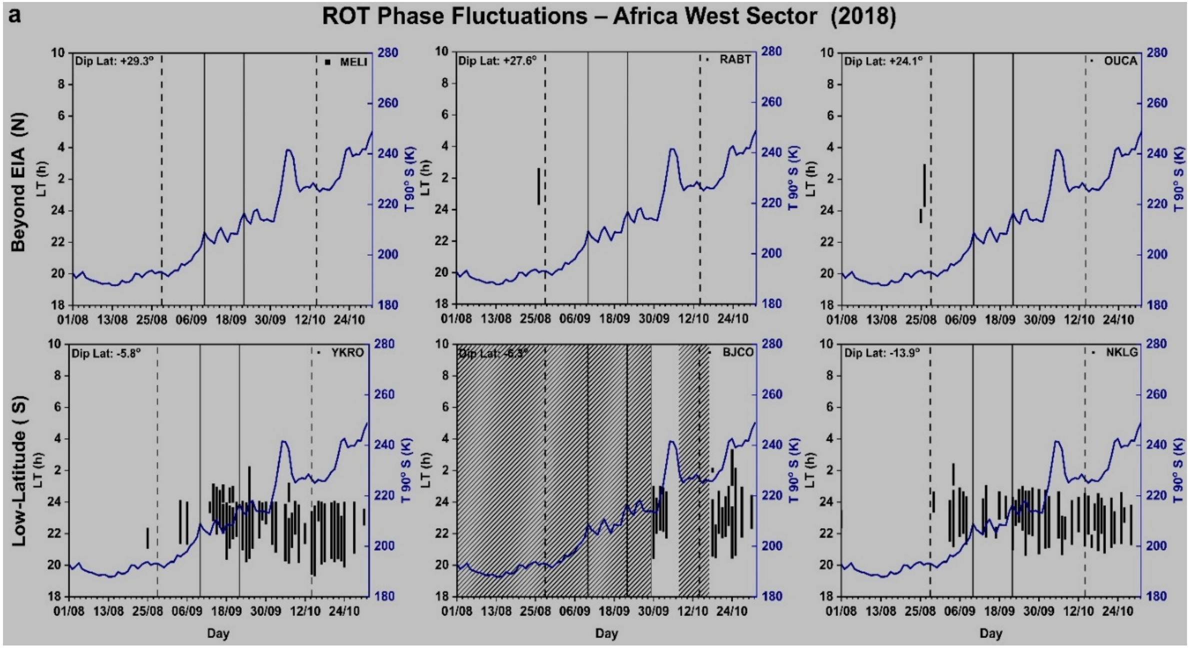

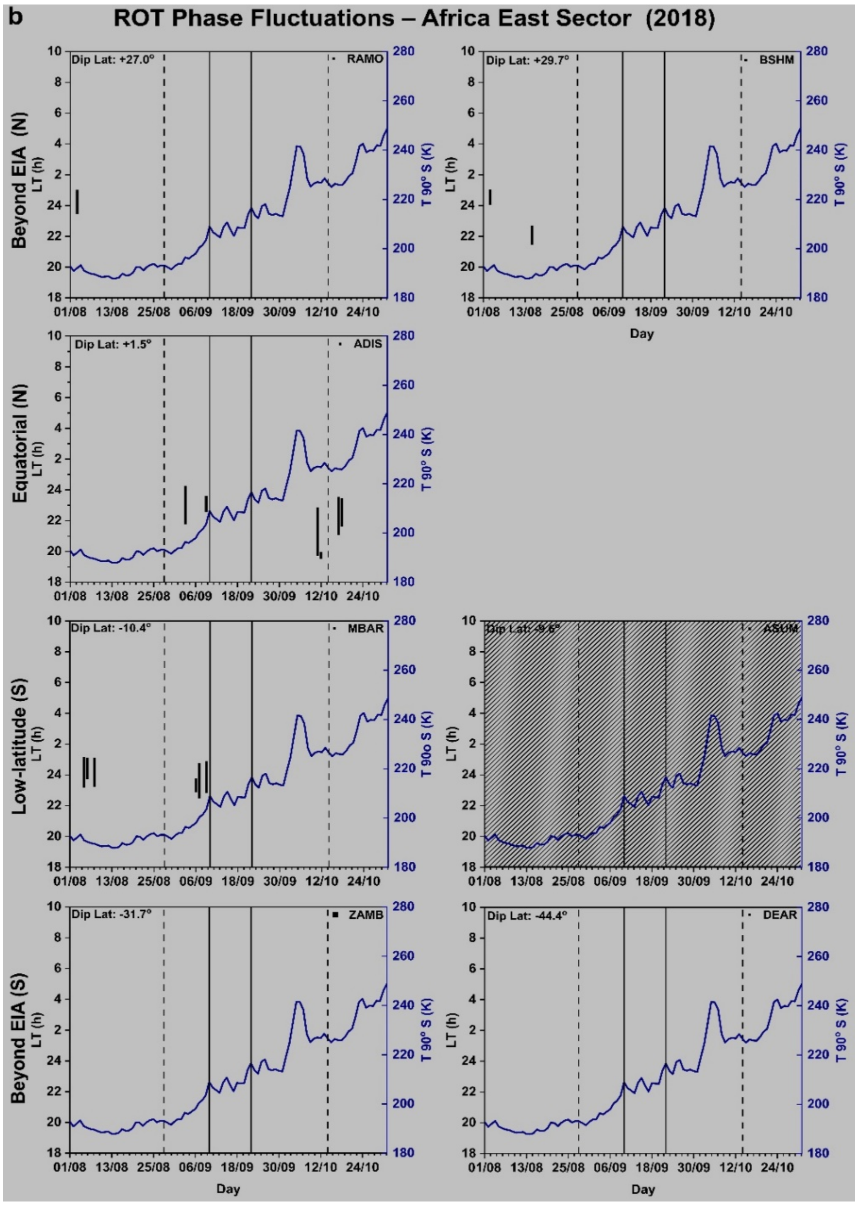

SOURCE: Author.

Table 8 gives the occurrence frequencies in percentage of ROT phase fluctuations for GPS receiver stations in all sectors. The table shows a decrease in ROT phase fluctuation occurrence frequencies in the peak SSW phase in some stations in 2019, especially in the west Brazil sector. This trend is not observed in 2018 (no SSW). In 2018, the occurrence frequencies increase from the pre- to post-SSW phases. Comparing the occurrence frequency in the peak phases in 2019 and 2018, also show a decrease in occurrence frequencies for the majority of the stations shown in Table 8 except for the Africa east (AE) sector.

Table 8: ROT Phase fluctuations occurrence rates (%) for all sectors and phases in 2019 and 2018.

Station/Phase	pre	asc	pea	des	pos	pre	asc	pea	des	pos
	2019 (SSW)					2018 (no SSW)				
Brazil West										
AMHA	0.00	33.33	38.46	85.71	66.67	0	16.67	46.15	52.38	77.78
AMCO	7.14	33.33	38.46	76.19	100.00	3.57	50.00	69.23	52.38	77.78
AMTE	10.71	40.00	30.77	80.95	100.00	14.29	33.33	58.33	100.00	58.82
SAGA	7.14	41.67	38.46	66.67	100.00	3.57	16.67	46.15	61.90	77.78
CUIB	17.86	41.67	15.38	80.95	100.00	14.29	33.33	61.54	71.43	88.89
ROSA	3.57	8.33	0.00	19.05	44.44	0.00	8.33	7.69	19.05	33.33
SCLA	0.00	0.00	0.00	0.00	11.11	0.00	0.00	0.00	0.00	0.00
SCQA	0.00	0.00	0.00	0.00	16.67	0.00	0.00	0.00	0.00	0.00
ILHA	3.57	0.00	0.00	23.81	50.00	0.00	0.00	0.00	0.00	27.78
POAL	0.00	0.00	0.00	0.00	0.00	0.00	0.00	0.00	0.00	0.00
Brazil East										
APLJ	11.54	8.33	23.08	80.95	88.89	0.00	33.33	66.67	/	0.00
MABA	3.57	0.00	23.08	100.00	72.22	0.00	25.00	53.85	42.86	88.89
TOPL	7.14	8.33	15.38	85.71	100.00	7.14	25.00	38.46	52.38	100.00
BABR	7.14	8.33	0.00	57.14	94.44	3.57	0.00	7.69	38.10	100.00
BAIR	0.00	8.33	7.69	52.38	77.78	0.00	0.00	0.00	42.86	100.00
BATF	0.00	0.00	0.00	4.76	22.22	0.00	0.00	0.00	0.00	27.78
CEFE	0.00	0.00	0.00	0.00	0.00	0.00	0.00	0.00	0.00	16.67
PASM	3.57	16.67	30.77	90.48	72.22	0.00	25.00	23.08	66.67	83.33
BEPA	0.00	0.00	23.08	76.19	83.33	0.00	16.67	30.77	61.90	88.89
RJCG	0.00	0.00	0.00	0.00	0.00	0.00	0.00	0.00	0.00	0.00
Africa West										
YKRO	7.14	16.67	38.46	71.43	50.00	3.57	16.67	69.23	71.43	72.22
NKLG	10.71	8.33	30.77	57.14	38.89	3.57	50.00	46.15	66.67	66.67
BJCO	0.00	16.67	/	/	/	/	/	/	55.56	66.67
Africa East										
ADIS	0.00	16.67	0.00	0.00	5.56	0.00	16.67	0.00	9.52	11.11
MBAR	14.29	8.33	7.69	4.76	11.11	10.71	25.00	0.00	0.00	0.00
RAMO	0.00	0.00	0.00	0.00	0.00	3.57	0.00	0.00	0.00	0.00
BSHM	3.57	0.00	0.00	0.00	0.00	7.14	0.00	0.00	0.00	0.00
ASUM	7.14	16.67	7.69	9.52	16.67	/		/	/	/

SOURCE: Author.

Figure 57 shows in the left panel, the ESF occurrence frequencies for all ionosonde stations and the total occurrence frequency (green line with the inverted triangles) for the stations combined in 2019 (a) and 2018 (c). The plot shows how the ESF occurrence frequencies varied during the peak phase of the warming event in 2019 and how it compared with the same period in 2018. The right panel is shown the total occurrence frequencies of the ROT phase fluctuations for each sector in 2019 (b) and 2018 (d) as listed in Table 8. The graphs show the occurrences frequencies variation through all the phases for 2019 and 2018.

Figure 57: Left panel: ESF phase occurrence frequency variation for all stations for a) 2019 and c) 2018, right panel: Total ROT phase fluctuation phase occurrence frequencies for each sector for b) 2019 d) 2018 for all phases.

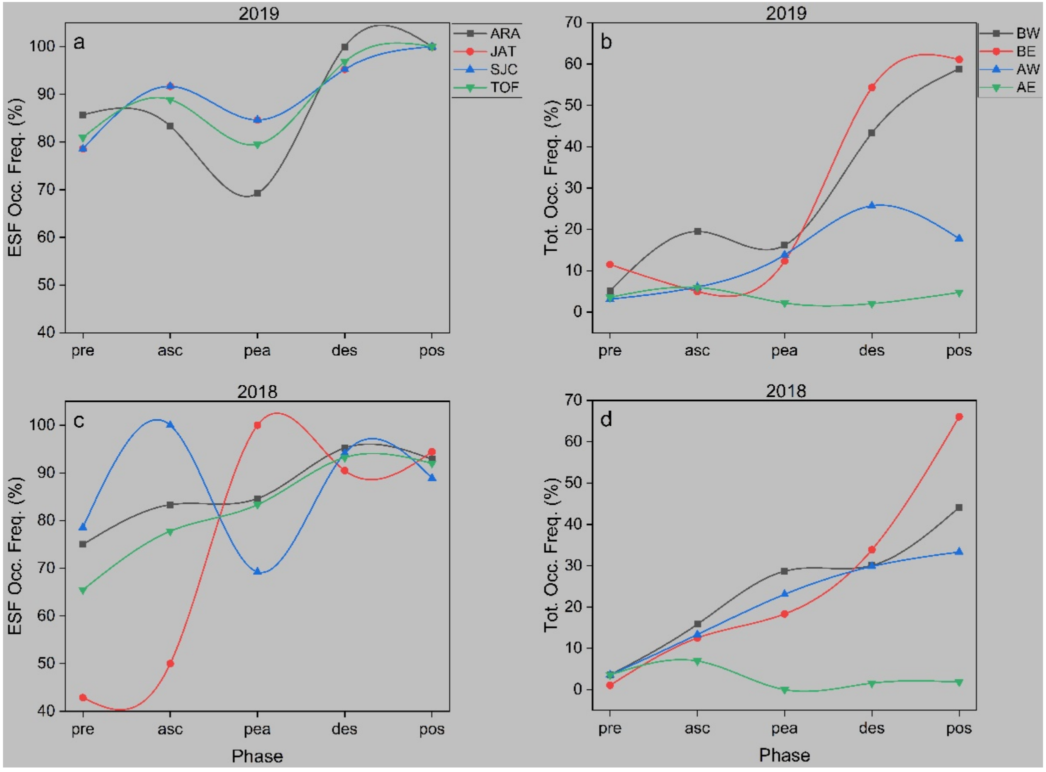

SOURCE: Author.

From Table 7 and Figure 57a and c, it can be observed that the ESF occurrence rates in 2019 decreased for all the stations in the peak phase from the pre and ascending SSW phases and increased again after the peak phase in the descending and post-phases. The total occurrence frequency in 2019 also shows a decrease in occurrence frequency during the peak phase. In 2018 (no SSW), except for SJC, there was no such decrease in occurrence frequency during the peak phase including the total occurrence frequency. However, on the contrary, the occurrence rates in 2018 increased from the pre-phase to the post-phase following the normal ESF occurrence behavior in the Brazilian sector during this season. From the graphs, it can be observed that the occurrence rates in the peak phase were higher in 2018 (no SSW event) than in 2019 (SSW) for all stations (again except SJC) and the average occurrence frequencies.

In Figure 57b right panel, the graph shows a decrease in ROT phase fluctuations occurrence frequency during the peak phase in the Brazil west and Africa east sectors in 2019. In the Brazil east (BE) sector, we observe a decrease in occurrence frequency only during the ascending phase of the event. In 2018, all sectors show a continuous increase in occurrence frequency from the pre- to post-phase except for the Africa east sector where the occurrence frequency decreases during the peak phase. However, this decrease during the peak phase in the Africa east sector in 2018 is similar to the results in 2019 as in both years the occurrence frequency is zero. In the Africa east sector, around this time of the year, there are little to no ionospheric irregularities. As such, the occurrence of the SSW event could not have significantly affected the occurrence of the rate of irregularities in the region. In all sectors, (again except for Africa east sector), the occurrence frequencies during the peak phase are higher in 2018 (no SSW) than in 2019 (SSW). The other phases do not show these higher occurrence rates in 2018 than in 2019. For example, the pre-phase occurrence rate is almost the same for 2018 as in 2019. In the ascending, descending, and post phases, the frequencies are at times higher in 2018 and other times higher in 2019.

5.5 Discussions

In this present work, using three ionosondes located in Brazil and a network of GPS receivers located in both Brazil and Africa, the occurrence characteristics of ionospheric irregularities during the 2019 minor Antarctic SSW event were investigated.

The results from the large-scale equatorial ionospheric irregularities (ESF) and small-scale ionospheric irregularities (ROT) from ionosonde and GPS respectively, showed a seasonal-longitudinal trend in the occurrence frequency in the west and Brazil east/Africa sectors in 2019 and 2018/2017. In 2019, there was an observed decrease in occurrence frequency during the peak phase and sometimes the ascending phase, possibly due to the influence of SSW. The occurrence frequency in 2019, however, began increasing during the descending and post-SSW phases in 2019. The seasonal characteristics of ionospheric irregularities in the Africa and Brazil sectors have been studied and discussed over the years (AGYEI-YEBOAH *et al.*, 2019; AKALA *et al.*, 2011; MUNGUFENI; HABARULEMA; JURUA, 2016; NISHIOKA; SAITO; TSUGAWA, 2008; OLADIPO *et al.*, 2014; OLWENDO; CILLIERS; MING, 2021). Their results showed that in the Brazil west and east sectors, ionospheric irregularity occurrence rates increased from August to October (Spring). In the Africa west (AW) sector, the occurrence rates increased in the first and last 4 months of the year while in the Africa east sector, the occurrence frequency is more pronounced in the June solstice - May to August. The highest occurrence rates are observed in the Brazil (South American) sector followed by the Africa west sector, then the Africa east sector. During this time of the year, irregularities are more frequent and predominant in the west Africa sector than in the east sector (OLWENDO; CILLIERS; MING, 2019, 2021).

Several theories have been suggested to explain the seasonal – longitudinal variation of ionospheric irregularities. KIL (2004), KIL; DEMAJISTRE; PAXTON (2004) suggested that the seasonal longitudinal variations of plasma bubbles may come about as the result of varying nighttime plasma density in the nighttime F-region at different seasons and longitudes They explained that the strong EPB activities during equinoctial periods were as a result of increased plasma densities at most longitudes, and weak EPB activity was due to low plasma density in the June solstice in the American- Atlantic sector. According to SU; CHAO; LIU (2008), the seasonal-longitudinal variations of quiet time postsunset vertical drift velocities correlate favorably with the seasonal-longitudinal variations of ionospheric irregularity occurrences. They showed at three different longitude zones of magnetic declination that vertical drift velocities variations agree with the irregularity occurrences for all seasons suggesting the averaged postsunset vertical drift velocities to be a useful indicator for equatorial density irregularities in a longitude region of similar magnetic declination. Another explanation by Tsunoda (1985) is considered the most plausible. They explained that the seasonal-longitudinal variation of plasma bubbles is controlled by the alignment between the local meridian and the sunset terminator (TSUNODA, 1985). Thus, when the angle between the local meridian and the terminator is minimum, the intensity of the PRE of the eastward electric field increases and causes rapid $\vec{E} \times \vec{B}$ vertical plasma drift near the equator leading to maximum plasma bubbles occurrence.

The latitudinal trend for the large-scale irregularities, ESFs show a decrease in the occurrence rates from the equatorial region through the low-latitude and beyond EIA regions, i.e., ARA, JAT, and SJC respectively, in all phases except during the ascending and peak phases where occurrence rates increased from the equatorial region to the higher latitudes in 2019. This could be due to the shifting or the spreading of plasma density from the EIA crest region to the low-latitude region thereby increasing the plasma density around these latitudinal regions and consequently increasing the rate of irregularity occurrence. KIL; DEMAJISTRE; PAXTON (2004) have stated that increased plasma density can increase the rate of occurrence of plasma bubbles in a region and MO *et al*. (2017) have reported movement of the EIA crest during SSW. The result of foF2 observations (Figure 50), shows an overall increase in foF2 over JAT, a low-latitude region, compared to ARA, and SJC in 2019. These results agree with the ESF observations. Azeem; Crowley; Honniball (2015), Goncharenko *et al*. (2010a), Vieira *et al*. (2017), and Yasyukevich (2018) have all reported a decrease in plasma density during SSW events. The results from ROT phase fluctuations (small-scale irregularities) however, clearly show latitudinal variation. Higher occurrence rates were recorded in the equatorial regions than in the low-latitude and beyond EIA at all sectors. The ROT phase fluctuations are concentrated in the equatorial and low-latitude regions with little to no observations in the EIA crest regions unlike large-scale irregularities (ESF). At higher latitudes, it is expected that only large-scale irregularities that rise to higher altitudes at the geomagnetic equator and extend along the magnetic field lines into the higher latitudes can be observed as the small-scale irregularities are filtered in the equatorial and low-latitude regions.

The observations show a decrease in the Spread-F, and ROT phase fluctuations in the west, Brazil east, west, and Africa east sectors in the equatorial/low-latitude region during the ascending and/or peak phases of the SSW event 2019. The occurrence frequency started to increase during the descending and post-phases. AMHA and AMCO in the Brazil west sector, APLJ, MABA, TOPL, and PASM in the Brazil east sector, and YKRO and NKLG in the Africa west sector did not show a decrease in irregularity occurrence frequency during the ascending to peak SSW phases. However, a comparison with results from the same period in 2018 demonstrates the difference in occurrence frequencies between when there is an SSW event and when there is not, occurrence frequencies during the 2018 peak phase (no SSW) are observed to be higher than occurrence frequencies during 2019 peak phase (SSW). Unlike the 2019 (SSW) occurrences, the 2017/2018 (No SSW) occurrence rates depended on season, longitude, solar, and geomagnetic influences. The occurrence frequency did not decrease during the ascending to peak phases in all but three stations from the Africa sector – NKLG, ADIS, and RAMO. Furthermore, the occurrence frequencies during the peak phase of the event in 2019 were mostly lower than in 2018 for both ESF and ROT observations. Again, the stations from 2019 that did not show any decrease during the peak and ascending phases presented occurrence frequencies lower than their counterparts in 2018 where there was no SSW but a strong magnetic storm at the onset of the ascending phase. The decrease in occurrence frequency from pre to ascending/peak phase and from 2018 to 2019 (peak phase only) ranges between 8 % and 46 %. This implies that the decrease in the irregularity occurrence rates from the pre to ascending/peak phase in 2019 during the warming event cannot be attributed to seasonal or month-to-month behavior of irregularity occurrence alone.

The generalized Rayleigh-Taylor instability (RTI) is the main factor responsible for the occurrence of ionospheric irregularities. The RTI is known to be controlled by the pre-reversal enhancement which is responsible for the upward $\vec{E} \times \vec{B}$ vertical drift, the flux tube integrated conductivity associated with meridional wind-induced hemispheric plasma density distribution symmetry and seeding mechanisms like gravity waves introduce perturbations at the bottomside F-layer (ABDU, 2001; DE PAULA *et al*., 2015; YU *et al*., 2020). A decrease in equatorial vertical plasma drifts before sunset was reported by De Paula *et al*. (2015) and Goncharenko *et al*. (2013). This reduction in the vertical plasma drift is thought to be related to PRE suppression during a warming event (DE PAULA *et al*., 2015; YU *et al*., 2020). PRE is known to have a controlling effect on the growth rate of generalized RTI and the generation of ionospheric irregularities hence the decrease in irregularities observed during the peak of this event.

It has been reported that the decrease in the critical frequency of the F-layer – foF2 occurs in the near evening sector with frequencies of up 6 MHz in the Brazilian sector during the 2009 sudden stratospheric warming (FAGUNDES *et al*., 2015). Their results are consistent with the findings presented here. The current findings show an average decrease in the foF2 parameter from 2018 (No SSW) to 2019 (SSW) especially during the peak SSW phase. This means that there was a decrease in the PRE vertical drift which is not favorable for the uplifting of the ionospheric F2 layer peak height (hmF2) after sunset consequently leading to the decrease in the development of ionospheric irregularities during the peak phase of the event.

Another explanation for the suppression of ionospheric irregularities as presented in this paper could be attributed to the thermospheric meridional/Transequatorial winds which can enhance the field line integrated conductivity of unstable flux tube resulting in a reduction in the growth of plasma instability (DE PAULA *et al*., 2015) that can lead to the suppression or the generation of ionospheric irregularities during a warming event (YU *et al*., 2020). The hemispheric asymmetry in plasma density distribution due to meridional/equatorward thermospheric effects during SSW events together with the weakening of the vertical drift caused by the warming events can also contribute to the suppression of ionospheric irregularities. Goncharenko *et al*. (2013), and Vieira *et al*. (2017) have reported TEC variations in either EIA crests in some regions which might be due to tidal forcing.

5.6 Conclusions

In this investigation, we have presented and discussed the observations and results of ionospheric irregularities from 3 ionosondes and 33 ground-based GPS receiver stations spread over Brazil and Africa during the minor Antarctic SSW event of 2019. A summary of the results from the study is presented as follows:

1. The overall occurrence frequencies of equatorial Spread-F and ROT phase fluctuations from all stations were generally higher in 2019 (SSW) than in 2018 (no SSW).
2. The results from the ionosondes do not show clear latitudinal dependence, as the ESFs are observed almost equally at all latitudes in the Brazilian sector, however, the ROT phase fluctuations show latitudinal dependence with ROT occurrence being concentrated in the equatorial and low-latitude regions and little to no observations in the beyond EIA region.
3. From the ESF results, it is observed that in 2019 during the ascending and peak phases, the occurrence rates are lower in the equatorial region than in the low-latitude and beyond EIA regions while in the rest of the phases the occurrence rates in the equatorial region are higher or equal to the low-low latitude and beyond EIA regions.
4. The occurrence frequencies followed the seasonal and monthly occurrence trends in Brazil and Africa in 2017, 2018, and 2019 in ESF occurrence frequencies with solar and geomagnetic activities accounting for ESF occurrence increases in 2017/2018 during the ascending phase. The ESF occurrence rates in 2017 correlated with the solar activity variation during the study period. The ROT phase fluctuations also presented seasonal/month-to-month and longitudinal variations in both 2018 and 2019.
5. The ROT phase fluctuations presented more occurrences in Brazil (west and east) sectors than in west Africa. Africa east presented the least occurrence of ROT phase fluctuations within this period which was the off-peak season for irregularity occurrence in that sector while Brazil and west Africa sectors were in peak irregularity periods.
6. In 2019, the occurrence rates decreased during the ascending/peak phase before increasing accordingly in the descending and post phases. Like the ESF results, in 2019 (SSW) the occurrence rates decreased in most ROT phase fluctuation results during the ascending and /or peak phases of the warming event from the pre-phase and increased again during the descending phases post-phases. A comparison of the peak and ascending phases of 2017/2018 (no SSW) and 2019 (SSW) showed a decrease in occurrence rate from 2017/2018 to 2019 in both ESF and ROT phase fluctuation results implying that the warming in 2019 could have played a part in the decrease in irregularity generation during the increasing or peak warming temperatures.

7. The foF2 ionospheric parameter also showed a phase-to-phase variation in 2019, decreasing from the pre-SSW phase to the peak phase and then increasing in the descending and post-SSW phases. On the contrary, in 2018 (no SSW), the foF2 increased from the pre-SSW phase to the post-SSW phase in the peak irregularity period.

6 FINAL THOUGHTS

The two topics discussed in this thesis sought to seek and elaborate on different ways to observe ionospheric irregularities and the influence of ionospheric drivers on the occurrence of ionospheric irregularities. They both in different ways help better our understanding of the occurrence of ionospheric irregularities, how to observe and measure them, and possibly help improve the prediction capabilities of existing models or develop new ones. This will ultimately in the mitigation of space weather effects on radio wave-based space technologies that have become part of our modern way of life with the understanding of how these irregularities occur and what are the factors that have major influences on their generation or suppression, especially in the equatorial and low latitude ionosphere based on ground-based observations. The thesis started in the Introduction, giving a brief background, elaborating on the motivations for both investigations, then their main and specific objectives. Then in the Earth's ionosphere, the structure of the Earth's atmosphere and ionosphere were described. The low latitude ionosphere, its variability, important phenomena unique to the equatorial and low latitude ionosphere like EIA, and some ionospheric irregularities like EPBs and ESFs were summarized. The physics and mechanisms behind some of these phenomena are also presented Sudden stratospheric warming, SSW, a lower atmospheric phenomenon was also summarized here. The instruments and techniques section follows, and it provides descriptions of instruments and techniques from ground and space used, their modes of operation, the principles behind their operations, and the data they collect that were used in the investigations.

In the subsequent two main sections, the proposed methodology for the observation of plasma blobs using ionosonde and the effect of the 2019 minor Antarctic SSW event on the occurrence of ionospheric irregularities are discussed in that order. The geographical locations, data, periods, and methods for each investigation are elaborated on in their respective sections. The results and discussions of these studies are presented with conclusions. With this background and here in this section the main, conclusions from the two investigations of this thesis are summarized as follows.

6.1 Observation of Blobs using Ionosondes

Ground-based all-sky imager and ionosonde, both located at the Araguatins observation site, and the Swarm satellite constellations were used to investigate the occurrence of ionospheric plasma blobs. With the analysis described in Chapter 4, a methodology was proposed for the observation and investigation of plasma blobs using ionosonde. This investigation was contingent on the fact that the two ground-based instruments were located in the same geographical area and that they observed the same ionosphere and phenomenon in the ionosphere a few minutes apart. Plasma density measurements from the Swarm satellites were used to complement the ground-based observations.

The observations showed that when plasma blobs were observed in the nightglow images, the corresponding ionograms at that moment showed equatorial Spread-F trace that extended beyond the critical frequency of the night. This trace associated with the blobs and bubbles showed an extension into the higher-frequency part of the frequency scale beyond the critical frequency that does not show in the second and third ionospheric reflections. The echoes of the atypical ESF reached up to 15 MHz Contrary to the trace of Spread-F associated with low plasma density, which shows similar first, second, and third reflections where the first only to the critical frequency. The trace associated with plasma blobs shows spread just like observed in the trace associated with bubbles, an indication that small-scale irregularities exist with the blobs as well. Although the study sample was limited, the conclusions were based on the case studies that were presented in this study. Similar characteristics have been observed in studies reported by Narayanan *et al*. (2014) and Wang *et al*. (2019) from different longitudinal sectors even though they did not make particular reference to these characteristics.

6.2 Effects of 2019 minor Antarctic SSW on the occurrence of ionospheric irregularities

The occurrence characteristics of ionospheric irregularities during the 2019 minor Antarctic sudden stratospheric warming have been explored and compared with data from 2018/2017 (no SSW) using ionosonde (ESF and foF2) located in Araguatins, Jatai, and São José dos Campos, all in Brazil, and GPS-receivers (ROT) spread over Brazil and Africa. The study period between August and October was divided into different phases (pre, ascending, peak, descending, and post). These phases were compared within 2019 and with results from 2017/2018. The observation period in 2019 showed no significant solar or geomagnetic activity. In 2017 strong geomagnetic and high solar activities were observed during the ascending phase and then the solar activity started decreasing till the end of the period. In

2018, the solar activity variation was comparable to 2019, however, there was a strong geomagnetic storm at beginning of the ascending phase, inside the pre-phase.

The results from the ESF and ROT phase fluctuation present a decrease in occurrence frequency during the peak phase in ARA, JAT, and SJC and in most of the GPS-receiver stations especially in Brazil in 2019 (SSW). In 2018 (no SSW), however, no such decrease was observed. Occurrence frequencies generally increased from the pre-phase to post-phases. In 2017 (no SSW), the observed decrease in occurrence frequency from the ascending phase to the peak phase was associated with solar and geomagnetic activity. The results also showed a decrease in occurrence frequencies of the irregularities during the peak from 2017/2018 (no SSW) to 2019 (SSW). Thus, during the peak phase, 2017/2018 occurrence frequencies were generally higher than in 2019. The foF2 from ionosonde also showed decreased values during the peak phase at SJC and SJC unlike 2017/2018 where the parameter increased from pre-phase to post-phase. The results also showed seasonal, longitude, latitudinal, solar, and geomagnetic variations. The effect of the SSW event on suppressing the occurrence of ionospheric irregularities was evident in the occurrence frequencies and the foF2 proxy.

REFERENCES

AA, E. *et al*. Significant equatorial plasma bubbles and global ionospheric disturbances after the 2022 Tonga volcano eruption. **Space Weather,** v. 20, n. 7, 2022.

AARONS, J. Global Morphology of Ionospheric Scintillations. **Proceedings of the IEEE**, v. 70, n. 4, p. 360–378, 1982.

ABDU, M. A. *et a*l. Equatorial spread-F occurrence statistics in the American longitudes: Diurnal, seasonal and solar cycle variations. **Advances in Space Research**, v. 22, n. 6, p. 851–854, Jan. 1998.

ABDU, M. A. Outstanding problems in the equatorial ionosphere-thermosphere electrodynamics relevant to spread F. **Journal of Atmospheric and Solar-Terrestrial Physics**, v. 63, n. 9, p. 869–884, 2001.

ABDU, M. A. *et al.* Equatorial evening prereversal electric field enhancement, and sporadic E layer disruption: A manifestation of E and F region coupling. **Journal of Geophysical Research: Space Physics**, v. 108, n. A6, p. 1610–1617, 2003.

ABDU, M. A. Day-to-day and short-term variabilities in the equatorial plasma bubble/spread F irregularity seeding and development. **Progress in Earth and Planetary Science**, v. 6, n. 1, p. 11, 1 Dez. 2019.

ABDU, M. A.; SOBRAL, J. H. A.; BATISTA, I. S. Equatorial spread F statistics in the American longitudes: Some problems relevant to ESF description in the IRI scheme. **Advances in Space Research**, v. 25, n. 1, p. 113–124, jan. 2000.

AGYEI-YEBOAH, E. *et al*. Seasonal variation of plasma bubbles during solar cycle 23–24 over the Brazilian equatorial region. **Advances in Space Research**, v. 64, n. 7, p. 1365–1374, 1 Oct. 2019.

AKALA, A. O. *et al*. Statistics of GPS scintillations over South America at three levels of solar activity. **Radio Science**, v. 46, n. 5, 2011.

ALFONSI, L. *et al*. Comparative analysis of spread-F signature and GPS scintillation occurrences at Tucumán, Argentina. **Journal of Geophysical Research: Space Physics**, v. 118, n. 7, p. 4483–4502, 2013.

AZEEM, I.; CROWLEY, G.; HONNIBALL, C. Global ionospheric response to the 2009 sudden stratospheric warming event using Ionospheric Data Assimilation Four-Dimensional (IDA4D) algorithm. **Journal of Geophysical Research: Space Physics**, v. 120, n. 5, 2015.

BALAN, N. *et a*l. Physical mechanism, and statistics of occurrence of an additional layer in the equatorial ionosphere. **Journal of Geophysical Research: Space Physics**, v. 103, n. A12, p. 29169–29181, 1 Dec. 1998.

BALAN, N.; LIU, L.; LE, H. A brief review of equatorial ionization anomaly and ionospheric irregularities. **Earth and Planetary Physics**, v. 2, n. 4, p. 1–19, 2018.

BALAN, N.; SOUZA, J.; BAILEY, G. J. Recent developments in the understanding of equatorial ionization anomaly: A review. **Journal of Atmospheric and Solar-Terrestrial Physics**, v. 171, n. July 2017, p. 3–11, 2018.

BAMFORD, R. A. The oblique ionospheric sounding final report. [s.l: s.n.], 2000.

BANKS, P. M.; KOCKARTS, G. Aeronomy Part A. **Academic Press**, 1973

BARBOSA, F. R. E. Estudo Das Irregularidades Ionosféricas De Grande E Média Escala Durante Períodos Geomagneticamente Calmo E Perturbado. [s.l: s.n.], 2018.

BASU, B.; COPPI, B. Relevance of plasma and neutral wind velocities to the topology and the excitation of modes for the onset of the equatorial spread F. **Journal of Geophysical Research: Space Physics**, v. 104, n. A1, p. 225–231, 1 Jan. 1999.

BASU, S. *et al*. Specification of the occurrence of equatorial ionospheric scintillations during the main phase of large magnetic storms within solar cycle 23. **Radio Science**, v. 45, n. 5, p. 1–15, 2010.

BASU, S.; KELLEY, M. C. Review of equatorial scintillation phenomena in light of recent developments in the theory and measurement of equatorial irregularities. **Journal of Atmospheric and Terrestrial Physics**, v. 39, n. 9–10, p. 1229–1242, Sep. 1977.

BOOKER, H. G.; WELLS, H. W. Scattering of radio waves by the F -region of the ionosphere. **Journal of Geophysical Research**, v. 43, n. 3, p. 249, 1938.

BREKKE, A. **Physics of the Upper Polar Atmosphere**. Berlin, Heidelberg: Springer Berlin Heidelberg, 2013. v. 5

BURKE, W. J. *et al*. Seasonal-longitudinal variability of equatorial plasma bubbles. **Annales Geophysicae**, v. 22, n. 9, p. 3089–3098, 2004.
CADI. Disponível em: https://www.sws.bom.gov.au/IPSHosted/INAG/web-60/cadi.htm. Acesso em: 15 abr. 2021.

CALVERT, W.; COHEN, R. The interpretation and synthesis of certain spread- F configurations appearing on equatorial ionograms . **Journal of Geophysical Research**, v. 66, n. 10, p. 3125–3140, 1961.

CARTER, B. A. *et al*. An analysis of the quiet time day-to-day variability in the formation of postsunset equatorial plasma bubbles in the Southeast Asian region. **Journal of Geophysical Research: Space Physics**, v. 119, n. 4, p. 3206–3223, Apr. 2014.

CARTER, B. A. *et al*. Global equatorial plasma bubble occurrence during the 2015 St. Patrick's Day storm. **Journal of Geophysical Research A: Space Physics**, v. 121, n. 1, p. 894–905, 2016.

CHANG, L. C. *et al*. Response of the thermosphere and ionosphere to an ultra-fast Kelvin wave. **Journal of Geophysical Research: Space Physics**, v. 115, n. A8, 1 Aug. 2010.

CHAPAGAIN, N. P.; FEJER, B. G.; CHAU, J. L. Climatology of postsunset equatorial spread F over Jicamarca. **Journal of Geophysical Research: Space Physics**, v. 114, n. 7, p. 1–7, 2009.

CHAPMAN, S. The absorption and dissociative or ionizing effect of monochromatic radiation in an atmosphere on a rotating earth. **Proceedings of the Physical Society**, v. 43, n. 1, p. 26–45, 1 Jan. 1931.

CHATTOPADHYAY, R.; MIDYA, S. K. Airglow emissions: Fundamentals of theory and experiment. **Indian Journal of Physics**, v. 80, n. 2, p. 115–166, 2006.

CHAU, J. L. *et al*. Equatorial and low latitude ionospheric effects during sudden stratospheric warming events : Ionospheric effects during SSW events. **Space Science Reviews**, v. 168, n. 1–4, p. 385–417, 2012.

CHAU, J. L.; FEJER, B. G.; GONCHARENKO, L. P. Quiet variability of equatorial e × B drifts during a sudden stratospheric warming event. **Geophysical Research Letters**, v. 36, n. 5, 2009.

CHERNIAK, I.; ZAKHARENKOVA, I. First observations of super plasma bubbles in Europe. **Geophysical Research Letters**, v. 43, n. 21, p. 11,137-11,145, 2016.

DE PAULA, E. R. *et al.* Low-latitude scintillation weakening during sudden stratospheric warming events. **Journal of Geophysical Research: Space Physics**, v. 120, n. 3, p. 2212–2221, 2015.

DUGASSA, T.; HABARULEMA, J. B.; NIGUSSIE, M. Longitudinal variability of occurrence of ionospheric irregularities over the American, African, and Indian regions during geomagnetic storms. **Advances in Space Research**, v. 63, n. 8, p. 2609–2622, 2019.

DUNGEY, J. W. Convective diffusion in the equatorial F region. **Journal of Atmospheric and Terrestrial Physics**, v. 9, n. 5–6, p. 304–310, 1956.

ECCLES, V. *et al*. Lunar atmospheric tidal effects in the plasma drifts observed by the Low-Latitude Ionospheric Sensor Network. **Journal of Geophysical Research: Space Physics**, v. 116, n. A7, p. 1–8, 1 Jul. 2011.

ESSIEN, P. **Study on medium-scale traveling ionospheric disturbances observed in the south american equatorial region.** Thesis (Doctorate) - Space Geophysics, 2020.

FAGUNDES, P. R. *et al*. Atypical nighttime spread-F structure observed near the southern crest of the ionospheric equatorial ionization anomaly. **Journal of Geophysical Research: Space Physics**, v. 117, n. 4, p. 1–9, 2012.

FAGUNDES, P. R. *et al*. Ionospheric response to the 2009 sudden stratospheric warming over the equatorial, low, and middle latitudes in the South American sector. **Journal of Geophysical Research: Space Physics**, v. 120, n. 9, p. 7889–7902, 9 Sep. 2015.

FARLEY, D. T. *et al*. The prereversal enhancement of the zonal electric field in the equatorial ionosphere. **Journal of Geophysical Research**, v. 91, n. A12, p. 13723, 1986.

FATHY, A.; GHAMRY, E. A statistical study of single crest phenomenon in the equatorial ionospheric anomaly region using Swarm A satellite. **Advances in Space Research**, v. 59, n. 6, p. 1539–1547, 2017.

FEJER, B. G. *et al*. Dependence of Equatorial F Region Vertical Drifts on Season and Solar Cycle. **Journal of Geophysical Research**, v. 84, n. A10, p. 5792–5796, 1979.

FEJER, B. G. *et al*. Average vertical and zonal F region plasma drifts over Jicamarca. **Journal of Geophysical Research: Space Physics**, v. 96, n. A8, p. 13901–13906, 1991.

FORBES, J. M. Planetary Waves in the Thermosphere-Ionosphere System. **Journal of geomagnetism and geoelectricity**, v. 48, n. 1, p. 91–98, 20 Jan. 1996.

FRIIS-CHRISTENSEN, E. *et al*. Swarm - An Earth Observation Mission investigating Geospace. **Advances in Space Research**, v. 41, n. 1, p. 210–216, 2008.

FRIIS-CHRISTENSEN, E.; LÜHR, H.; HULOT, G. Swarm: A constellation to study the Earth's magnetic field. Earth. **Planets and Space,** p.351-358, 2006

GENTILE, L. C.; BURKE, W. J.; RICH, F. J. A global climatology for equatorial plasma bubbles in the topside ionosphere. **Annales Geophysicae**, v. 24, n. 1, p. 163–172, 2006.

GONCHARENKO, L. *et al*. Ionospheric effects of sudden stratospheric warming during moderate-to-high solar activity: Case study of January 2013. **Geophysical Research Letters**, v. 40, n. 19, p. 4982–4986, 2013.

GONCHARENKO, L. P. *et al*. Impact of sudden stratospheric warmings on equatorial ionization anomaly. **Journal of Geophysical Research: Space Physics**, v. 115, n. 10, p. 1–11, 2010a.

GONCHARENKO, L. P. *et al*. Unexpected connections between the stratosphere and ionosphere. **Geophysical Research Letters**, v. 37, n. 10, 2010b.

GONZÁLEZ, G. DE L. Spread-F characteristics over Tucumán near the southern anomaly crest in South America during the descending phase of solar cycle 24. **Advances in Space Research**, v. 69, n. 3, p. 1281–1300, 1 Feb. 2022.

GREBOWSKY, J. M.; AIKIN, A. C. Planetary ionospheres – sources and dynamic drivers. **Proceedings of the International Astronomical Union**, v. 4, n. S257, p. 499–510, 2008.

HARGREAVES, J. K. **The Solar-Terrestrial Environment**. [s.l: s.n.].

HOFMANN-WELLENHOF, B.; H. LICHTENEGGER, J. C. **Global positioning system, theory, and practice**. 5th edition ed. [s.l: s.n.], 2001.

HUANG, C. S. *et al*. Relationship between Plasma bubbles and density enhancements: Observations and interpretation. **Journal of Geophysical Research A: Space Physics**, v. 119, n. 2, p. 1325–1336, 2014.

HUANG, C. S. Effects of the postsunset vertical plasma drift on the generation of equatorial spread F. **Progress in Earth and Planetary Science**, v. 5, n. 1, p. 1–15, 1 Dec. 2018.

HUNSUCKER, R. D.; HARGREAVES, J. K. **The high-latitude ionosphere and its effects on radio propagation**. [s.l.] Cambridge University Press, 2002.

HUNSUCKER, R. D.; HARGREAVES, J. K. **The high-latitude ionosphere and its effects on radio propagation**. [s.l: s.n.].

HYSELL, D. L.; BURCHAM, J. D. Long-term studies of equatorial spread F using the JULIA radar at Jicamarca. **Journal of Atmospheric and Solar-Terrestrial Physics**, v. 64, n. 12–14, p. 1531–1543, 2002.

JONAS BREGNHØJ NIELSEN. **Swarm Level 1b Product Definition**. [s.l: s.n.]. Disponível em: https://earth.esa.int/documents/10174/1514862/Swarm_L1b_Product_Definition.

JOSE, L.; VINEETH, C.; PANT, T. K. Impact of Stratospheric Sudden Warming on the Occurrence of the Equatorial Spread-F. **Journal of Geophysical Research: Space Physics**, v. 122, n. 12, p. 12544–12555, 2017.

KAPLAN, E. D.; HEGARTY, C. J. **Understanding GPS/GNSS Principles, and Applications**. [s.l: s.n.], 2017.

KELLEY, M. C. **The Earth's Ionosphere Second Edition**. [s.l: s.n.], 2009

KELLEY, M. C.; HYSELL, D. L. Equatorial spread-F, and neutral atmospheric turbulence : a review and a comparative anatomy. **Journal of Atmospheric and Terrestrial Physics**, v. 53, n. 8, p. 695–708, 1 Aug. 1991.

KHADKA, S. M. **Multi-diagnostic investigations of the equatorial and low-latitude ionospheric electrodynamics and their impacts on space-based technologies.** Requirements (graduation) – Boston College, Boston, 2018.

KIL, H. Coincident equatorial bubble detection by TIMED/GUVI and ROCSAT-1. **Geophysical Research Letters**, v. 31, n. 3, p. L03809, 2004.

KIL, H. *et al.* Onset conditions of bubbles and blobs: A case study on 2 March 2009. **Geophysical Research Letters**, v. 38, n. 6, p. 1–5, 2011.

KIL, H. *et al.* The causal relationship between plasma bubbles and blobs in the low-latitude F region during a solar minimum. **Journal of Geophysical Research: Space Physics**, v. 120, n. 5, p. 3961–3969, 1 May 2015.

KIL, H. *et al.* Daytime Evolution of Equatorial Plasma Bubbles Observed by the First Republic of China Satellite. **Geophysical Research Letters**, v. 46, n. 10, p. 5021–5027, 2019.

KIL, H. *et al.* Plasma Blobs Associated With Medium-Scale Traveling Ionospheric Disturbances. **Geophysical Research Letters**, v. 46, n. 7, p. 3575–3581, 2019b.

KIL, H.; DEMAJISTRE, R.; PAXTON, L. J. F -region plasma distribution seen from TIMED/GUVI and its relation to the equatorial spread F activity. **Geophysical Research Letters**, v. 31, n. 5, p. 1-5, 16 Mar. 2004.

KIM, V. P.; HEGAI, V. V. Low latitude plasma blobs: A review. **Journal of Astronomy and Space Sciences**, v. 33, n. 1, p. 13–19, 2016.

KNUDSEN, D. J. *et al*. Thermal ion imagers and Langmuir probes in the Swarm electric field instruments. **Journal of Geophysical Research: Space Physics**, v. 122, n. 2, p. 2655–2673, 2017.

KRALL, J. *et al*. Density enhancements associated with equatorial spread F. **Annales Geophysicae**, v. 28, n. 2, p. 327–337, 2010.

KUMAR, S. *et al*. Effects of solar and geomagnetic activity on the occurrence of equatorial plasma bubbles over Hong Kong. **Journal of Geophysical Research: Space Physics**, v. 121, n. 9, p. 9164–9178, 2016.

KUNG CHIE YEH; CHAO-HAN LIU. Radio wave scintillations in the ionosphere. **Proceedings of the IEEE**, v. 70, n. 4, p. 324–360, 1982.

KUTTIPPURATH, J.; NIKULIN, G. A comparative study of the major sudden stratospheric warmings in the Arctic winters 2003/2004-2009/2010. **Atmospheric Chemistry and Physics**, v. 12, n. 17, p. 8115–8129, 2012.

LAYERS of Earth's Atmosphere | UCAR Center for Science Education. Disponível em: https://scied.ucar.edu/learning-zone/atmosphere/layers-earths-atmosphere. Acesso em: 21 apr. 2021.

LE, G. *et al*. Plasma density enhancements associated with equatorial spread F: ROCSAT-1 and DMSP observations. **Journal of Geophysical Research: Space Physics**, v. 108, n. A8, p. 1–14, 2003.

LIN, C. H. *et al*. Motions of the equatorial ionization anomaly crests imaged by FORMOSAT-3/COSMIC. **Geophysical Research Letters**, v. 34, n. 19, p. 1–6, 2007.

MA, G.; MARUYAMA, T. A super bubble detected by dense GPS network at east Asian longitudes. **Geophysical Research Letters**, v. 33, n. 21, p. 1–5, 2006.

MARUYAMA, T. Ionosphere, and Thermosphere: Ionospheric Irregularities. **Journal of the Communications Research Laboratory**, v. 49, n. 3, p. 163–179, 2002.

MATTHIAS, V.; ERN, M. On the origin of the mesospheric quasi-stationary planetary waves in the unusual Arctic winter 2015/2016. **Atmospheric Chemistry and Physics**, v. 18, n. 7, p. 4803–4815, 2018.

MCINTURFF, R. M. Stratospheric warmings: Synoptic, dynamic, and general-circulation aspects. **National Aeronautics and Space Administration, Scientific and Technical Information Office**, n. January 1978, 1978.

MCNAMARA, L. F. *et al*. Signatures of equatorial plasma bubbles in VHF satellite scintillations and equatorial ionograms. **Radio Science**, v. 48, n. 2, p. 89–101, 2013.

MILLER, E. S. *et al*. Topside signature of medium-scale traveling ionospheric disturbances. **Annales Geophysicae**, v. 32, n. 8, p. 959–965, 2014.

MILOCH, W. J. *et al*. Ionospheric plasma irregularities studied with Swarm satellites. **E3S Web of Conferences**, v. 62, 2018.

MO, X. H. *et al*. Meridional movement of northern and southern equatorial ionization anomaly crests in the East-Asian sector during 2002–2003 SSW. **Science China Earth Sciences**, v. 60, n. 4, p. 776–785, 2017.

MUNGUFENI, P.; HABARULEMA, J. B.; JURUA, E. Trends of ionospheric irregularities over African low latitude region during quiet geomagnetic conditions. **Journal of Atmospheric and Solar-Terrestrial Physics**, v. 138–139, p. 261–267, 2016.

NADE, D. P. *et al*. Observations of Plasma Blobs by OI 630 nm Using ASI and Photometer over Kolhapur, India. **Earth, Moon and Planets**, v. 112, n. 1–4, p. 89–101, 2014.

NARAYANAN, V. L. *et al*. A statistical study of satellite traces and evolution of equatorial spread F Space science. **Earth, Planets and Space**, v. 66, n. 1, p. 1–13, 2014.

NARAYANAN, V. L. *et al*. Some new insights of the characteristics of equatorial plasma bubbles obtained from Indian region. **Journal of Atmospheric and Solar-Terrestrial Physics**, v. 156, n. August 2016, p. 80–86, 2017.

NISHIOKA, M.; SAITO, A.; TSUGAWA, T. Occurrence characteristics of plasma bubble derived from global ground-based GPS receiver networks. **Journal of Geophysical Research: Space Physics**, v. 113, n. 5, p. 1–12, 2008.

OLADIPO, O. A. *et al*. Large-scale ionospheric irregularities occurrence at Ilorin, Nigeria. **Space Weather**, v. 12, n. 5, p. 300–305, May 2014.

OLWENDO, J.; CILLIERS, P. J.; MING, O. Comparison of Ground-Based Ionospheric Scintillation Observations With In Situ Electron Density Variations as Measured by the Swarm Satellites. **Radio Science**, v. 54, n. 10, p. 852–866, 16 Oct. 2019.

OLWENDO, J.; CILLIERS, P. J.; MING, O. Monthly trends in temporal and spatial distribution of Ionospheric Irregularities across the African region during the descending phase of solar cycle 24. **Advances in Space Research**, v. 67, n. 10, p. 3187–3201, 2021.

ONOHARA, A. N.; BATISTA, I. S.; TAKAHASHI, H. The ultra-fast Kelvin waves in the equatorial ionosphere: Observations and modeling. **Annales Geophysicae**, v. 31, n. 2, p. 209–215, 2013.

OYA, H.; TAKAHASHI, T.; WATANABE, S. Observation of Low Latitude Ionosphere by the Impedance Probe on Board the Hinotori Satellite. **Journal of geomagnetism and geoelectricity**, v. 38, n. 2, p. 111–123, 1986.

PARK, J. *et al*. Plasma blob events observed by KOMPSAT-1 and DMSP F15 in the low latitude nighttime upper ionosphere. **Geophysical Research Letters**, v. 30, n. 21, p. 2–5, 2003.

PARK, J. *et al*. Field-aligned current associated with low-latitude plasma blobs as observed by the CHAMP satellite. **Annales Geophysicae**, v. 28, n. 3, p. 697–703, 2010.

PARK, J. *et al*. Effect of sudden stratospheric warming on lunar tidal modulation of the equatorial electrojet. **Journal of Geophysical Research: Space Physics**, v. 117, n. 3, p. 1–9, 2012.

PAULINO, I. *et al*. Mesospheric gravity waves and ionospheric plasma bubbles observed during the COPEX campaign. **Journal of Atmospheric and Solar-Terrestrial Physics**, v. 73, n. 11–12, p. 1575–1580, 1 Jul. 2011.

PAULINO, I. *et al*. Semimonthly oscillation observed in the start times of equatorial plasma bubbles. **Annales Geophysicae**, v. 38, n. 2, p. 437–443, 31 Mar. 2020.

PAULINO, I. *et al*. Influence of the semidiurnal lunar tide in the equatorial plasma bubble zonal drifts over Brazil. **Annales Geophysicae**, v. 39, n. 6, p. 1005–1012, 10 Dec. 2021.

PAZNUKHOV, V. V. *et al*. Formation of an F3 layer in the equatorial ionosphere: A result from strong IMF changes. **Journal of Atmospheric and Solar-Terrestrial Physics**, v. 69, n. 10- 11 SPEC. ISS., p. 1292–1304, jul. 2007.

PEDATELLA, N. M. *et al*. How Sudden stratospheric warmings affect the whole atmosphere. **Eos (United States)**, v. 99, n. 6, p. 35–38, 2018.

PEDATELLA, N. M.; LIU, H.-L. The influence of atmospheric tide and planetary wave variability during sudden stratosphere warmings on the low latitude ionosphere. **Journal of Geophysical Research: Space Physics**, v. 118, n. 8, p. 5333–5347, ago. 2013.

PERKINS, F. W. Ionospheric irregularities. **Reviews of Geophysics**, v. 13, n. 3, p. 884, 1975.

PEZZOPANE, M.; PIGNALBERI, A. The ESA Swarm mission to help ionospheric modeling: a new NeQuick topside formulation for mid-latitude regions. **Scientific Reports**, v. 9, n. 1, p. 1–12, 2019.

PILLAT, V. G.; FAGUNDES, P. R.; GUIMARÃES, L. N. F. Automatically identification of Equatorial Spread-F occurrence on ionograms. **Journal of Atmospheric and Solar-Terrestrial Physics**, v. 135, p. 118–125, 2015.

PIMENTA, A. A. *et al*. Relevant aspects of equatorial plasma bubbles under different solar activity conditions. **Advances in Space Research**, v. 27, n. 6–7, p. 1213–1218, 2001.

PIMENTA, A. A. *et al*. Plasma blobs observed by ground-based optical and radio techniques in the Brazilian tropical sector. **Geophysical Research Letters**, v. 31, n. 12, p. n/a-n/a, 2004.

PIMENTA, A. A. *et al*. Ionospheric plasma blobs observed by OI 630 nm all-sky imaging in the Brazilian tropical sector during the major geomagnetic storm of April 6–7, 2000.

Geophysical Research Letters, v. 34, n. 2, p. L02820, 27 Jan. 2007.

REES, M. H. **Physics, and chemistry of the upper atmosphere**. New York: Cambridge University Press, 1989.

RISHBETH, H. The equatorial F-layer: progress and puzzles. **Annales Geophysicae**, v. 18, n. 7, p. 730–739, 2000.

RISHBETH, H.; GARRIOTT, O. K. **Introduction to ionospheric physics**. [s.l.] Academic Press, 1969. v. 14

RISHBETH, H.; MENDILLO, M. Patterns of F2-layer variability. **Journal of Atmospheric and Solar-Terrestrial Physics**, v. 63, n. 15, p. 1661–1680, 1 out. 2001.

SAHA, K. **The Earth's Atmosphere**. [s.l: s.n.], 2017. v. 53

SAHAI, Y. *et al*. Observations of the F-region ionospheric irregularities in the South American sector during the October 2003 "Halloween Storms". **Annales Geophysicae**, v. 27, n. 12, p. 4463–4477, 2009.

SAHAI, Y.; FAGUNDES, P. R.; BITTENCOURT, J. A. Solar cycle effects on large scale equatorial plasma depletions. **Advances in Space Research**, v. 24, n. I, p. 1477–1480, 1999.

SAHAI, Y.; FAGUNDES, P. R.; BITTENCOURT, J. A. Transequatorial F-region ionospheric plasma bubbles: solar cycle effects. **Journal of Atmospheric and Solar-Terrestrial Physics**, v. 62, n. 15, p. 1377–1383, 2000.

SCHUNK, R.; NAGY, A. **Ionospheres**. Cambridge: Cambridge University Press, 2009.
SHARMA, A. K. et al. Study of equatorial plasma bubbles using all-sky imager and scintillation technique from Kolhapur station: a case study. **Astrophysics and Space Science**, v. 363, n. 4, 2018.

SHARMA, A. K.; NADE, D.; GHODAWAT, S. Occurrence of Equatorial Plasma Bubbles Over Kolhapur. n. June 2016, 2013.

SHEPHERD, G. G**. Spectral Imaging of the Atmosphere**. [s.l.]: Elsevier, 2002. v. 82.

SIDDIQUI, T. A. *et al*. Relation between stratospheric sudden warming and the lunar effect on the equatorial electrojet based on Huancayo recordings. **Annales Geophysicae**, v. 33, n. 2, p. 235–243, 2015.

SOBRAL, J. H. A. *et al*. Ionospheric plasma bubble climatology over Brazil based on 22 years (1977-1998) of 630 nm airglow observations. **Journal of Atmospheric and Solar-Terrestrial Physics**, v. 64, n. 12–14, p. 1517–1524, 2002.

SU, S. Y.; CHAO, C. K.; LIU, C. H. On monthly/seasonal/longitudinal variations of equatorial irregularity occurrences and their relationship with the postsunset vertical drift velocities. **Journal of Geophysical Research: Space Physics**, v. 113, n. 5, p. 1–16, 2008.

SULTAN, P. J. Linear theory, and modeling of the Rayleigh-Taylor instability leading to the occurrence of equatorial spread F . **Journal of Geophysical Research: Space Physics**, v. 101, n. A12, p. 26875–26891, 1996.

TAKAHASHI, H. *et al*. Simultaneous observation of ionospheric plasma bubbles and mesospheric gravity waves during the SpreadFEx campaign. **Annales Geophysicae**, v. 27, n. 4, p. 1477–1487, 2009.

TARDELLI, A. *et al*. Seasonal and solar activity variations of F3 layer and quadruple stratification (StF-4) near the equatorial region. **Journal of Geophysical Research: Space Physics**, v. 121, n. 12, p. 116-125, 2016.

TARDELLI, A. *et al*. Study of the F3 and StF4 Layers at Tucumán Near the Southern Crest of the Equatorial Ionization Anomaly in Western South America. **Journal of Geophysical Research: Space Physics**, v. 123, n. 3, p. 2156–2167, 2018.

TARDELLI-COELHO, F. *et al*. Plasma blobs associated with plasma bubbles observed in the Brazilian sector. **Advances in Space Research**, v. 60, n. 8, p. 1716–1724, 2017.

TAROH MATSUNO. A Dynamical Model of the Stratospheric Sudden Warming. **Journal of the Atmospheric Sciences**, v. 28, n. 8, p. 1479–1494, 1 Nov. 1971.

TSUNODA, R. T. Control of the Seasonal and Longitudinal Occurrence of Equatorial Scintillations By the Longitudinal Gradient in Integrated E Region Pedersen Conductivity. **Journal of Geophysical Research**, v. 90, n. A1, p. 447–456, 1985.

TSURUTANI, B. T.; LAKHINA, G. S.; HAJRA, R. The physics of space weather/solar-terrestrial physics (STP): What we know now and what the current and future challenges are. **Nonlinear Processes in Geophysics**, v. 27, n. 1, p. 75–119, 25 Feb. 2020.

VIEIRA, F. *et al*. Total electron content disturbances during minor sudden stratospheric warming, over the Brazilian region: A case study during January 2012. **Journal of Geophysical Research: Space Physics**, v. 122, n. 2, p. 2119–2135, 2017.

WANG, Z. *et al*. Plasma Blobs Concurrently Observed With Bubbles in the Asian-Oceanian Sector During Solar Maximum. **Journal of Geophysical Research: Space Physics**, v. 124, n. 8, p. 7062–7071, 2019.

WATANABE, S.; OYA, H. Occurrence characteristics of low latitude ionosphere Irregularities observed by impedance probe on board the Hinotori satellite. **J. Goemag. Geoelectr.**, n. 38, p. 125–149, 1986.

WEBER, E. J. *et al*. North-south aligned equatorial airglow depletions. **Journal of Geophysical Research**, v. 83, n. A2, p. 712, 1978.

WOODMAN, R. F.; LA HOZ, C. Radar observations of F region equatorial irregularities. **Journal of Geophysical Research**, v. 81, n. 31, p. 5447–5466, 1 Nov. 1976.

WU, K. *et al*. Edge Plasma Enhancements of Equatorial Plasma Depletions Observed by All-Sky Imager and the C/NOFS Satellite. **Journal of Geophysical Research: Space Physics**, v. 123, n. 10, p. 8835–8849, 2018.

YADAV, S. *et al*. Impact of Sudden Stratospheric Warming of 2009 on the Equatorial and Low-Latitude Ionosphere of the Indian Longitudes: A Case Study. **Journal of Geophysical Research: Space Physics**, v. 122, n. 10, p. 10,486-10,501, 2017.

YAMAZAKI, Y. *et al*. September 2019 Antarctic Sudden Stratospheric Warming: Quasi-6-Day Wave Burst and Ionospheric Effects. **Geophysical Research Letters**, v. 47, n. 1, p. 1–12, 2020.

YASYUKEVICH, A. S. Variations in Ionospheric Peak Electron Density During Sudden Stratospheric Warmings in the Arctic Region. **Journal of Geophysical Research: Space Physics**, v. 123, n. 4, p. 3027–3038, 2018.

YE, H. *et al*. Ionospheric F-Layer Scintillation Variabilities Over the American Sector During Sudden Stratospheric Warming Events. **Space Weather**, v. 19, n. 8, p. 1–20, 2021.

YOKOYAMA, T.; SU, S. Y.; FUKAO, S. Plasma blobs, and irregularities concurrently observed by ROCSAT-1 and Equatorial Atmosphere Radar. **Journal of Geophysical Research: Space Physics**, v. 112, n. 5, p. 1–7, 2007.

YU, T. *et al*. Ionospheric F Layer Scintillation Weakening as Observed by COSMIC/FORMOSAT-3 During the Major Sudden Stratospheric Warming in January 2013. **Journal of Geophysical Research: Space Physics**, v. 125, n. 9, p. 1–10, 2020.

ZAKHARENKOVA, I.; ASTAFYEVA, E.; CHERNIAK, I. GPS and in situ Swarm observations of the equatorial plasma density irregularities in the topside ionosphere. **Earth, Planets and Space**, v. 68, p. 120, 2016.

ZHAO, B. *et al*. Anomalous enhancement of ionospheric electron content in the Asian-Australian region during a geomagnetically quiet day. **Journal of Geophysical Research: Space Physics**, v. 113, n. 11, p. 1–12, 2008.

ZHAO, B. *et al*. Features of the F3 layer in the low-latitude ionosphere at sunset. **Journal of Geophysical Research: Space Physics**, v. 116, n. 1, 2011.

Appendix A

LIST OF PUBLICATIONS

This thesis consists of a review of the author's work in the area of ionospheric irregularities over Brazil and Africa and the following is a list of the author's publications:

I. Vieira F., Fagundes, P.R., Pillat, V.G., **Agyei-Yeboah, E**., Venkatesh, K., Arcanjo, M.O. ***"Ionospheric disturbances over the American and African sectors due to the 2019 major Sudden Stratospheric Warming (SSW 2019), under low solar activity conditions,"*** Journal of Atmospheric and Solar-Terrestrial Physics. https://doi.org/10.1016/j.jastp.2022.105945

II. **Ebenezer Agyei-Yeboah**, Paulo Roberto Fagundes, Tardelli, Alexandre, Valdir Gil Pillat, Francisco Vieira, Mateus de Oliveira Arcanjo. "***Occurrence of ionospheric irregularities over Brazil during the minor southern sudden stratospheric warming of 2019,***" Advances in Space Research. https://doi.org/10.1016/j.asr.2022.08.065

III. **Ebenezer Agyei-Yeboah**, Paulo Roberto Fagundes, Tardelli, Alexandre, Valdir Gil Pillat, Alessio Pignalberi, Kavutarapu, Venkatesh, Michael Pezzopane, Francisco Vieira. ***"Ground and satellite-based observations of ionospheric plasma bubbles and blobs at 5.65° latitude in the Brazilian sector,"*** Advances in Space Research**, 67(8),** 2416-2438 (2021). https://doi.org/10.1016/j.asr.2021.01.034

IV. Igo Paulino, Ana Roberta Paulino, Ricardo Y. C. Cueva, **Ebenezer Agyei-Yeboah**, Ricardo Arlen Buriti1, Hisao Takahashi, Cristiano Max Wrasse, Angela M. Santos, Amauri Fragoso de Medeiros, Inez S. Batista. ***"Semimonthly oscillation observed in the start times of equatorial plasma bubbles,"*** Annales Geophysicae., **38(2)**, 437–443(2020). https://doi.org/10.5194/angeo-38-437-2020

V. **Ebenezer Agyei-Yeboah**, Igo Paulino, Amauri Fragaso Medeiros, Ricardo Arlen Buriti, Ana Roberta Paulino, Patrick Essien, Solomon Otoo Lomotey, Hisao

Takahashi, Cristiano Max Wrasse. "***Seasonal variation of plasma bubbles during solar cycle 23–24 over the Brazilian equatorial region,***" Advances in Space Research, **64(7)**, 1365-1374 (2019). https://doi.org/10.1016/j.asr.2019.06.041

VI. Patrick Essien, Igo Paulino, Cristiano Max Wrasse, Jose André V. Campos, Ana Roberta Paulino, Amauri F. Medeiros, Ricardo Arlen Buriti, Hisao Takahashi, **Ebenezer Agyei-Yeboah**, and Aline N. Lins. "***Seasonal characteristics of small- and medium-scale gravity waves in the mesosphere and lower thermosphere over the Brazilian equatorial region,"*** Annales Geophysicae, **36(3)**, 899–914 (2018). https://doi.org/10.5194/angeo-36-899-2018

Appendix B

Airglow

The Earth's upper atmosphere is home to a wide variety of photochemical, chemical, and dynamical processes. It is continuously being excited by the flux of energy coming from the Sun and so electromagnetic radiation is considered a radiation agent for the excitation of the neutral atmosphere. Molecules and atoms throughout the atmosphere are excited by solar energy in the presence of the Sun. The excited atmospheric molecules and atoms return to their ground-state emitting electromagnetic radiation in space which becomes clearly observable at the night referred to as airglow. Airglow is thus the emission of photons of atmospheric constituents excited directly or indirectly by electromagnetic radiations from the Sun. Figure 58 shows an image of the airglow taken from the sky. Simply, airglow (nightglow) is a faint emission of light by a planetary atmosphere (upper). The unit representing the luminescence measurements is given by Rayleigh (R) which is equivalent to the emission of 10^6 photons/s cm^2 column.

Figure 58: Atmospheric airglow image of different lines shot from the international space station.

SOURCE: NASA.

During the night, the dominant light sources are the moon's reflection of the sun, light from the stars, and also from the scattering of surface lights. The Sun and stars generate a light spectrum of continuous frequencies governed by the Planck distribution. These sources can be approximated as black-body sources – high-temperature. On the other hand, the faint airglow is an emission spectrum of discrete frequencies observed as a band or line emissions with sharp intensity peaks. as in Figure 59.

Figure 59: Nightglow spectrum between 5000 Å and 8000 Å.

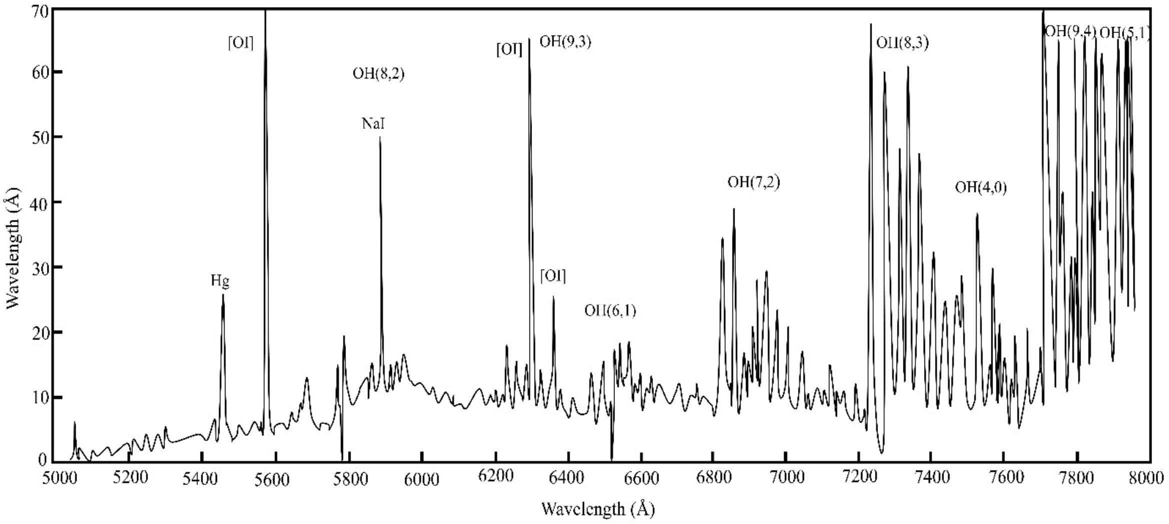

SOURCE: from Rees (1989)**.**

The airglow photons are the result of several chemical reactions in the upper atmosphere. The species that take part in the reactions together with the physical processes involved determine the wavelength and energy of the emitted photon. This makes it possible to determine which reactions/species produced which wavelength of photons. The principal source of energy for airglow reactions is the Sun, thus airglow can be defined as the optical emissions driven by excited atmospheric species whose source of energy arises from solar radiation. Unlike aurora which occurs at higher latitudes due to the impact excitation of energetic particles moving along the magnetic field lines, airglow emissions are global and weak.

Most airglow reactions excite an atom, molecule, or its ionic species. These excited species return to their ground states by emitting photons in the electromagnetic spectrum. These species return to their ground states by emitting photons in the electromagnetic spectrum, from ultraviolet to infrared. Considerable numbers of these deexcitation processes are prohibited in the electric dipole transitions and thus reach their respective ground states through metastable states. The lifetimes for deexcitations vary for different metastable states resulting in altitude-dependent emissions. The height of a particular emission depends on the collision rates, presence of specific species, and density of reactants[‡]. Based on these factors, different airglow emissions are concentrated at specific heights and consequently provide information on the reactants at their altitudes of origin.

Airglow emissions have been monitored by photometers and high-resolution spectrometers, which have provided a wealth of information on the behavior of the emitting regions, their temperature, densities, and dynamics. Airglow emissions occur at all times. The airglow that occurs in the nighttime is called the "nightglow," during twilight, is the "twilight-glow" and during daytime is the "dayglow."

Airglow Classification

Airglow is divided into three classes: nightglow, twilight-glow, and dayglow.

- ***Nightglow***: occurs at night when all sunlight is virtually absent. This occurs when the zenith angle of the Sun is greater than approximately 110 degrees. Nightglow is weakest at the zenith and is most intense towards the horizon with the maximum occurring 10 degrees above the horizon. Typically, nightglow emissions have very low intensities of the order of a few hundred Rayleighs.
- ***Twilight glow***: occurs at dusk or dawn and is characterized by the moment when the Sun is shining in the emitting region of the atmosphere, with the lower part and the solar zenith angle being between 90 and 110 degrees. The twilight glow is not as intense as the dayglow but stronger than the nightglow. Most of the processes that lead to twilight glow are direct excitation by sunlight. The night twilight is more energetic because the Sun sweeps the atmosphere during the day. Twilight can have intensities of several kilo Rayleighs.
- ***Dayglow***: The dayglow is more prominent but cannot be observed easily due to the brightness of the Sun's light in the background and the Rayleigh scattering effects. The dayglow is observed when sunlight enters the atmosphere from

---

[‡] Greater reactant density means higher emission intensity.

above at a zenith angle of between 0 and 90 degrees. Dayglow intensities can vary up to Mega-Rayleighs. In daylight, there is a strong diffuse background of continuous sunlight as such airglow instruments for observing spectral emissions should be able to isolate the emission resource of interest and provide the intensity of the isolated line emission. The daytime photometer makes use of a narrow-bandwidth interference filter to isolate the wavelength of interest.

Observed Emissions

Airglow emission is sampled by both TRACE and TRACE Port image capturers using 2 nm bandwidth filters centered on air emission wavelengths of 557.7 nm, 589.3 nm, 630.0 nm, and 777.4 nm with typical exposure times of two minutes. The emission lines of interest like OI 630.0 nm, OI 557.7 nm, and OI 777.4 nm will be discussed in the subsequent subsections. The names of the filters, central wavelength (λ), species, and altitude of origin are summarized in Table 10. The spectroscopic transition of the green line (557.7 nm) occurs when oxygen decays from a ^{1}S excited state to a ^{1}D quantum state emitting photons with energies around 2.2 eV. The red line (630.0 nm) transition occurs when oxygen moves from ^{1}D state to the ^{3}P. This transition emits photons of slightly lower energy of ~1.96 eV. The emission of the OI 777.4 nm emissions line happens when excited oxygen transitions from the excited ^{5}P state to the level ^{5}S state. In this emission, the energy of the dissociation energy is divided between the excited oxygen atom and the emitted photon. The characteristics of the main F-region emission lines are summarized in Table 9 and Figure 60 shows the spectroscopic transitions that produce these emission lines that are observed in atomic oxygen in both the auroral and airglow phenomena.

Table 9: Characteristics of the main F-region emissions

Atmospheric emission (nm)	Intensity (R)	Species	Altitude (km)
555.7	60	Atomic oxygen $O(1S) + O(1D)$	96 – 250
630.0	300	Atomic oxygen $O(1D)$	230 – 300
777.4	20	Atomic oxygen $O^+ + OH$	300 – 400

SOURCE: Author.

Figure 60: Spectral transitions in atomic oxygen that have been observed in airglow or aurora.

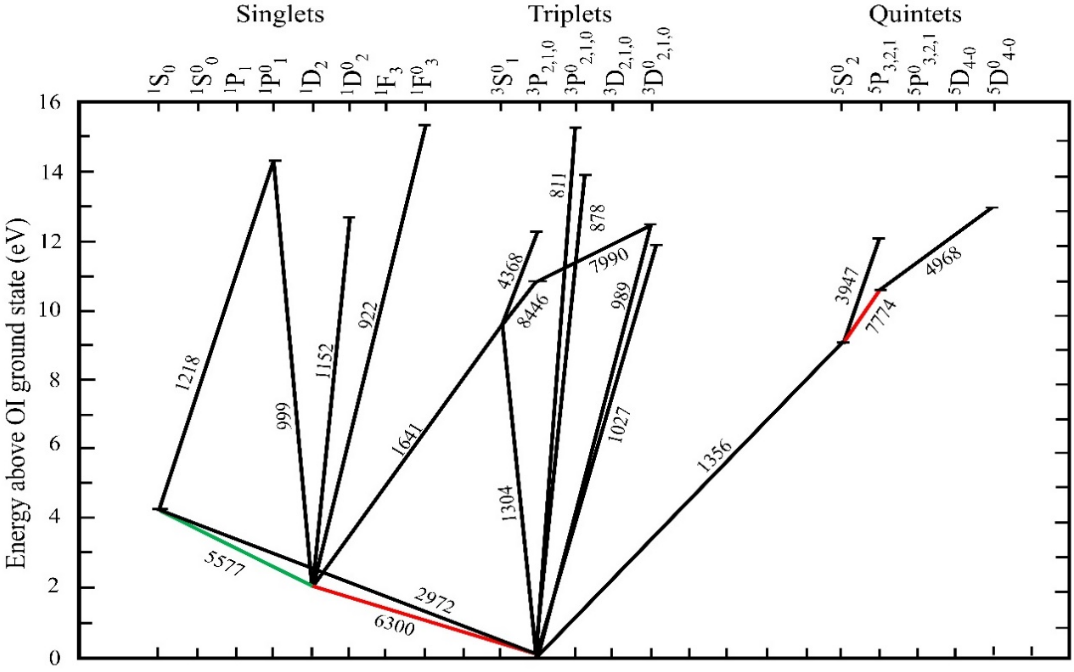

SOURCE: Adapted from (HARGREAVES, 1992)**.**

OI 557.7 nm green Line

The green line was the first nightglow emission observed at 557.7 nm. The green line emissions are from two distinct layers; 95-100 km in the middle and lower thermosphere (MLT) and 250-300 km in the F region. The production process of excited atomic oxygen O (^{1}S) in the F region is the dissociative recombination of molecular oxygen ions with electrons. The main reactions of the process involving OI 557.7 nm are:

$$O^+ + O_2 \xrightarrow{\gamma_1} O_2^+ + O \tag{15}$$

$$O_2^+ + e \xrightarrow{\alpha_s} O + O^*({}^1S) \tag{16}$$

$$O^*({}^1S) \xrightarrow{A_s} O({}^1D) + h\upsilon(557.7\ nm) \tag{17}$$

Red line OI 630.0 nm

The red line is used in nighttime ionospheric F-region irregularity studies. This emission line is produced in an ~ 50 km thick layer, between 250 and 300 km. This emission is used in the study of the generation, morphology, and dynamics of plasma bubbles. The dissociative recombination mechanism is the main process of production of excited oxygen O (^{1}D) in the F region that produces the red line. Recombination of molecular ions, O_2^+can produce the following oxygen in various excited states. Some of them are presented below:

$$O_2^+ + e \rightarrow O({}^3P) + O({}^3P) \tag{18}$$

$$O_2^+ + e \rightarrow O({}^3P) + O^*({}^1D) \tag{19}$$

$$O_2^+ + e \rightarrow O({}^3P) + O^*({}^1S) \tag{20}$$

$$O_2^+ + e \rightarrow O^*({}^1D) + O^*({}^1D) \tag{21}$$

$$O_2^+ + e \rightarrow O^*({}^1D) + O^*({}^1S) \tag{22}$$

When the excited atoms in ^{1}D state deexcite and fall to the ground state ^{3}P, the spontaneous releases of the excess energy in the form of photons occur according to the reaction below in equation (23):

$$O^*({}^1D) \rightarrow O({}^3P) + h\upsilon(630.0\ nm) \tag{23}$$

OI 777.4 nm Emission Line

It is one of the weakest emissions and occurs at all ionospheric heights. Two recombination mechanisms have been proposed for atomic oxygen emission that generates the 777.4 nm line, i.e., radiative recombination and ion-ion recombination.

The radiative recombination mechanism involves electron capture by atomic ions and the emission of photons of energy $h\upsilon$, the excess energy excites the neutral atom. The atom stores this surplus energy for some time, if there is no decay of the excited state through collisions, the atom falls into chain transitions. Possible transitions of this mechanism are:

$$O^* + (4p)^3P \rightarrow O^*(3s)^3S^0 + hv(436.8\ nm) \tag{24}$$

$$O^* + (3p)^3P \rightarrow O^*(3s)^3S^0 + hv(844\ nm) \tag{25}$$

$$O^*(3s)^3S^0 \rightarrow O\ (2P^4)^3P\ + hv(130.4\ nm) \tag{26}$$

$$O^*(4p)^5P\ \rightarrow O^*(3s)^5S^0 + hv(394.7\ nm) \tag{27}$$

$$O^*(3p)^5P\ \rightarrow O^*(3s)^3S^0 + hv(777.4\ nm) \tag{28}$$

$$O^*(3s)^5S^0\ \rightarrow O^*(2P^4)^3P + hv(135.6\ nm) \tag{29}$$

In this process, ionized atomic oxygen recombines radiatively to form an excited oxygen atom as

$$O^+(\,^4S) +\ e \rightarrow O^* + hv \tag{30}$$

that energy falls to the ground state,

$$O^+ \rightarrow O(\,^3P) + \sum hv \tag{31}$$

The ionization energy of the atomic oxygen ion recombination is divided between the excited oxygen atom and the irradiated photon if the excited oxygen atom is formed through ^5P state, then the emission of OI 777.4 nm observed is given by:

$$O^+(\,^5P) \rightarrow O^*(\,^5S) + hv(777.4\ nm) \tag{32}$$

The ion-ion recombination mechanism involves the mutual neutralization of positive and negative ions. Negative and positive ions are given, respectively, by

$$O +\ e \rightarrow O^- + hv \tag{33}$$

and

$$O^- + O^+ \rightarrow O^* + O + k_e \tag{34}$$

Appendix C

ASI Optics System

The all-sky imager (ASI) makes measurements by focusing the lens of the instrument upward toward the desired emission. The observed emissions enter the lens and are projected along the system of the lens' photosensitive cells that associate the luminous intensity with digital information. The ASI uses a fisheye lens that provides a 180^o field of view. The selection of the desired wavelengths of each emission is made by the interference filters, then the lens set projects the image onto the CCD-type camera. The Cooling System keeps the temperature at ~ - 35 °C to reduce thermal noise. The whole system is monitored by a microcomputer that also manages the storage of the data on a hard drive. The optics system of the all-sky imager is made up of the objective or primary (fisheye) lens, the telecentric optical lens, the filter wheel, and the reimaging optics. The descriptions of these components are below (See Figure 17).

Front Lens and shutter

The main lens, also the primary or objective lens, of the imager is a fisheye lens which determines the field of view (FOV) of the imager. This type of lens has a field of view (FOV) of up to 180^o, however, the FOV is most times limited to 150^o -170^o as a lot of times trees and buildings obstruct some of the horizon. Figure 61 shows an image of the fish-eye lens of the ASI used at one of UNIVAP's observing stations. A mechanical shutter is placed immediately after the lens to protect the intensifier and filter from direct sunlight (KELLEY, 2009). The system uses a 4-inch Mamiya RB67 37 mm/F4.5 medium-format achromatic fisheye lens. It has a focal length of 24 mm.

Figure 61: a) fish-eye lens attached to the main frame of the imager b) separated fish-eye lens of the ASI.

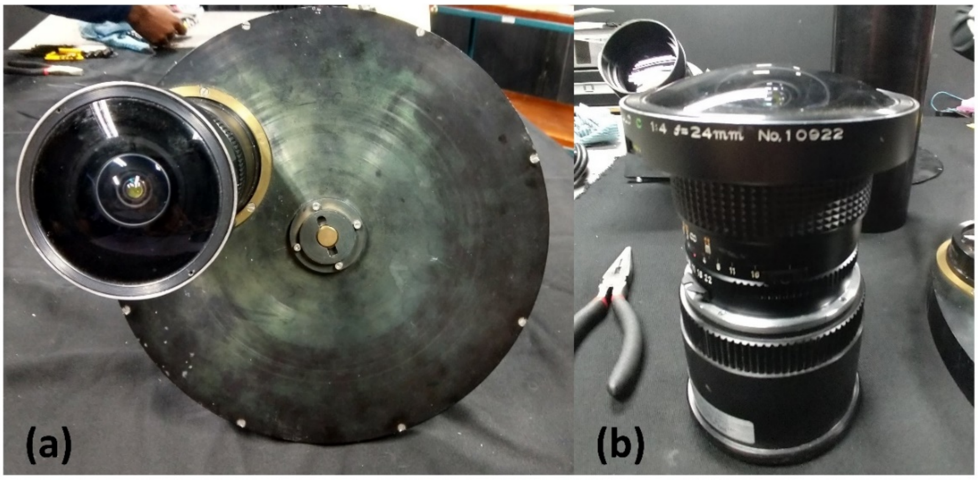

SOURCE: Author

Telecentric Optics

The transmission wavelength depends on the incident angle. Some of the principal light rays exiting the main lens are not parallel and also for normal camera lenses with large ray angles, the principal ray pass throughout the optical path. The interference filters are designed and constructed such that the wavelength of light transmitted through the filter depends almost completely on the incident angle. As the incidence angle to the filter increases, the transmitted wavelengths shift according to the square of the angle resulting quickly in larger ray angles. Such large angles will require wider band filters. Thus, it is necessary to use telecentric optic elements between the main lens and the filter wheel to provide the same incident angle at all image points on the filter. The telecentric optics is made up of the two plano-convex lenses placed to coordinate with the main lens. The placement and selection configuration has been found to be ideal enough to reduce to some fraction, of spherical aberration, and refract the principal rays just parallel to the principal axis of the camera lens.

Filter Wheel

The imager uses narrow band-pass interference filters. Currently, there are filters for 557.7 nm, 630.0 nm, and 427.8 nm with a full-width half-maximum (FWHM) of about 2-3 nm. The interference filters are manufactured by coating a glass plate 10 with several thin layers with known refractive indices. They are constructed from dielectric materials. These thin films are placed on the substrate that composes the film so that only the desired wavelength passes through. The dielectric material allows only part of the incident light to undergo constructive interference and enhance the desired wavelength. The main filters that are mostly utilized for airglow observations at this station are OI 557.7 nm, OI 630 nm, and OI 777.4 nm. Other filters in the wheel include Na 589.3 nm and OH band filters. This filter wheel has eight positions. Figure 62 shows the main frame of an imager affixed with a filter wheel and the inset is a) a schematic diagram, b) a photo of the filter wheel used, with some visible filters of specific wavelengths. Figure 63 shows airglow images of the red and green lines obtained from the Manaus and Jatai observation sites. The images show plasma density structures which could be plasma bubbles or waves.

Figure 62: Photo of filter wheel attached to the main frame of an imager. Inset: a) schematic diagram of filter wheel b) photo of a filter wheel with some filters.

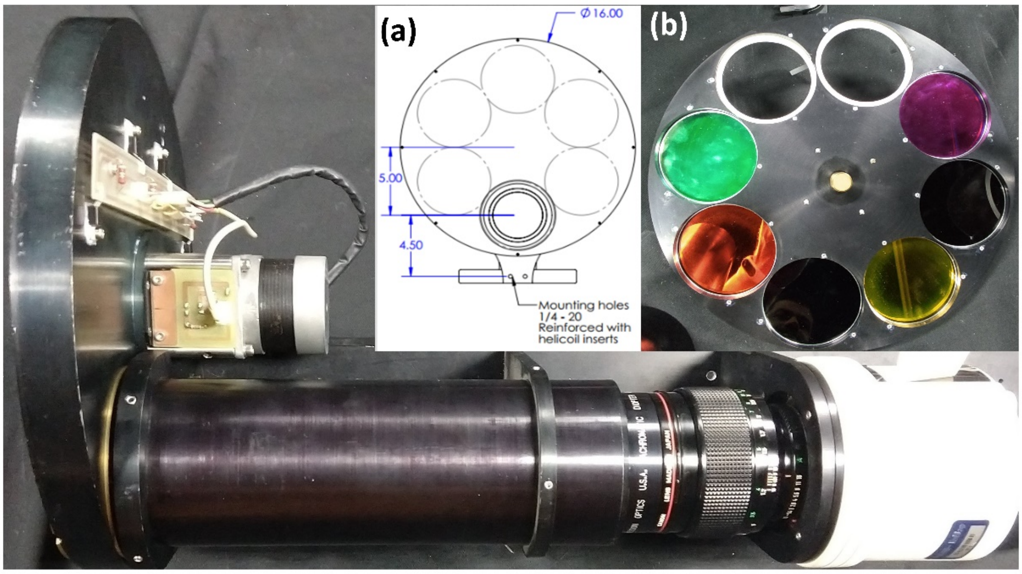

SOURCE: Author.

Table 10: Characteristics of principal interference filters average altitudes of airglow layers.

Filter	Wavelength (nm)	Bandwidth (nm)	Average height (km)
OI	557.7	2.65	~ 96
OI	630.0	3.3	~ 200-300
OI	777.4	2	~ 300-400
OH	715 – 930	215	~ 87
0_2 (0,1)	865.5	12	~ 94
BG	587	2.67	-

SOURCE: KEO Scientific.

Figure 63: Airglow images of the red (OI 630.0 nm) and green (OI 557.7 nm) lines from Manaus and Jatai observation stations showing possible plasma bubbles.

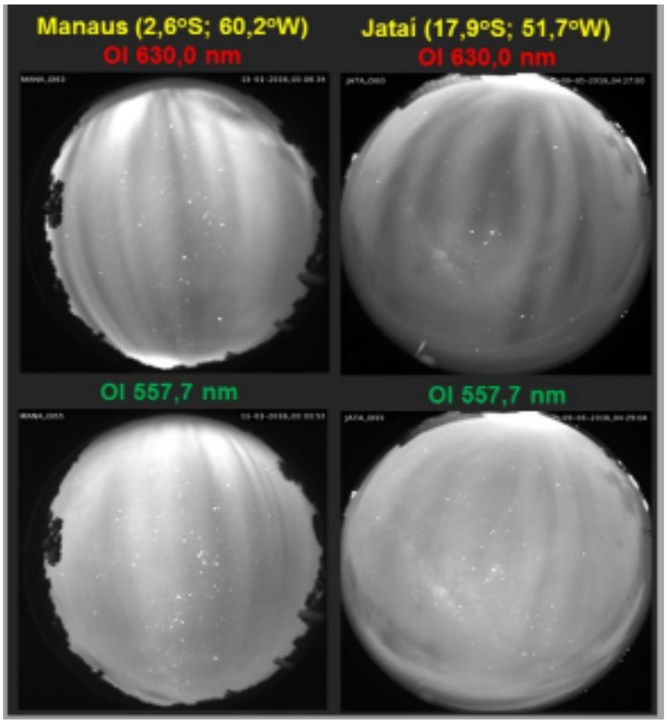

SOURCE: Author.

Re-imaging Optics

The re-imaging optics takes the rays from the telecentric optics passing through the interference filter and project them onto the CCD detector. The images that pass through the filter are approximately 75 mm on each side and have to be projected onto the CCD which is 24 mm. Therefore, these corrective lenses have 85 mm/F1.2 and the CCD camera has to be placed with an F-stop set to at least 1.2 because the reduction from 75 / F4.0 mm to 24 mm requires that the lenses have at least one F ≤ 1.3. The re-imaging optics provide the means for monochromatic images of wide-angle fields to be fashioned onto detectors at low effective F numbers onto the CCD detector.

CCD Camera

The first two-dimensional images with CCD cameras were made in 1974. Over time, astronomers have widely used CCDs because they provide high-quality celestial images. In recent times, CCD cameras are used more frequently in many areas including astronomy, and conventional photography. CCDs are also applied to X and infrared rays (as in the case of OH and O_2 emissions in the atmosphere (BARBOSA, 2018).

Princeton Instruments (PI) PIXIS 2048 cameras are fully integrated low-noise cameras expressly designed for quantitative scientific imaging applications. The cameras feature unique XP cooling technology, cooling up to -70° C, and are designed in thermically sealed metal, with guaranteed maintenance-free operation. High-efficiency quantum (QE) and ultra-low noise electronics make PIXIS series cameras (2048) ideal for low-light applications such as astronomy, Bose-Einstein condensate (BEC), solar cell inspection, chemiluminescence, and fluorescence images. The dual-speed operation of 100 kHz or 2 MHz allows these cameras to be used for steady-state kinetics as well as fast studies.

The Charge-couple device (CCD) is composed of thousands of light-sensitive elements arranged in a matrix. Each element is a semiconductor oxide capacitor (MOS). The photoelectric effect is responsible for the production of loads in this capacitor. The loads on each capacitor line are shifted to the output and each load is converted into a voltage. The advantage of CCD is that high voltage is not required, but the disadvantage is low time resolution (because it is a detector integrator type) and therefore it is not appropriate to look for very weak photon sources (without using a light amplifier). Quantum efficiency (QE) is typically 40 to 80% for a typical CCD. A typical CCD camera is shown in Figure 64. It is formed by a parallel and a serial recorder and has parallel and serial clocks, respectively, to control the transmission speed of electrons collected by the incidence of photons.

Each detector element (lower pixel division of the CCD) assesses the intensity of the received light and sends a signal proportional to the light intensity. Pixels are arranged in a typical 1024 x 1024 matrix and up to 2000 x 2000 pixels that contain 262,144 individual elements with independent potential barriers. The more pixels, the higher the resolution and the more complex and expensive the CCD. Modern pixel sizes are between 4 and 10 micrometers long and tall. When the CCD is exposed to light, loads are accumulated in the potential barriers of the parallel recorder. The total number of loads stored is proportional to the product of the incident light intensity at the time of exposure. Load accumulation is often called integration. The full pattern of stored loads corresponds to the focused image. Electronic circuits introduce unwanted noise into the CCD. The effect of this noise on performance is described by the signal-to-noise ratio (SNR). Photon noise, preamp noise, and dark current are three primary sources of noise in a CCD. Therefore, photonic noise is always present in an imaging system and is actually the uncertainty in the data.

Figure 64: A typical CCD camera.

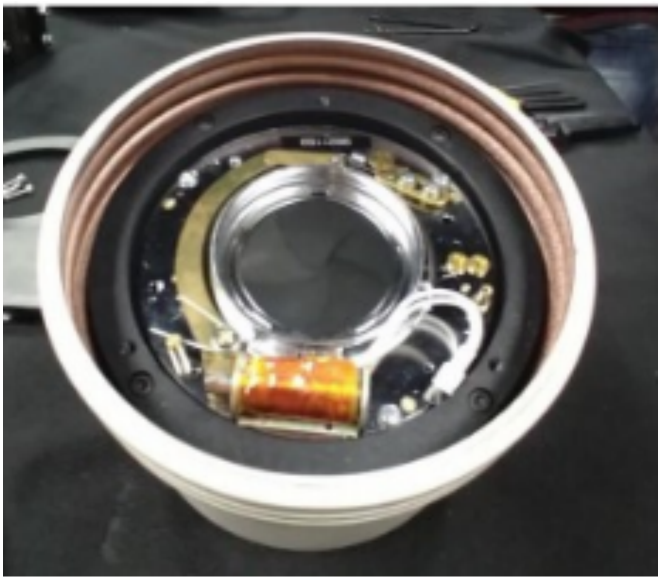

SOURCE: Author.

Cooling System

The dark count is the product of a "dark current", or rate per second of electrons created by the CCD, and the exposure time in seconds. A dark count occurs when a pixel registers an electron caused by thermal fluctuation rather than a photon. Thus, the amount of dark count present in a CCD image depends on the temperature of the CCD chip. Therefore, it is beneficial to run CCDs at lower temperatures as thermal energy is sufficient to excite electrons into pixels that cannot be distinguished from electrons produced by photons called dark current. This noise can be reduced by cooling the CCD to approximately - 35 ° C and for every 6-8 °C of cooling, there is about a 2X reduction in the total dark current generation rate up to about -120^{o} C where CCDs start to function less and less effectively since electron mobility is significantly reduced at this temperature.

One technique used is operation inversion which considerably reduces the rate of dark current. In many cases, this technique is sufficient to reduce the noise. A large part of the dark current is generated at the silicon dioxide interface. However, in this mode of operation, if used for a long period, potential barriers can disappear and compromise the functioning of the CCD. As such for long exposure times, a practical solution is to use a cooling system, which is usually made with liquid nitrogen through CCD. Liquid nitrogen was previously the primary method of cooling; however, today it is rarely used as LN2 affects camera orientation and can be cumbersome to work with. A Liquid Circulation Unit (LCU) is used by the "all-sky" imager. In the CCD used by the imager, there is a liquid unit of circulation. The LCU draws energy from CCD by pumping a mixture of ethylene glycol and distilled water. Other cooling techniques employed in the cooling of CCDs are thermometric coolers, mechanical pumps (cryo-coolers), and vacuum technology. Thermometric coolers have become more common in recent years. Thermometric cooling uses the Peltier effect to create a thermal difference between the junction of two different conducting materials. A Peltier cooler is a solid-state active heat pump that transfers heat from one side of the device to the other, with the consumption of electrical energy, depending on the direction of the current. Passive air, forced air, or circulating coolant tap water/ chilled coolant circulation is one of the several ways that heat can be removed from the hot end of the Peltier junction. The CCDs of the ASIs operated by UNIVAP are cooled by the Peltier cooling system which can cool down to an optimum operating temperature of ~ -60 ^{o} C.

6.2.1 Control Computer

The microcomputer manages and controls the entire imaging system. A great advantage of the ASI is that it can use a personal computer. The microcomputer makes the hardware connection with the software and monitors the filter wheel and exposure time of each image. The microcomputer also manages the start and end of observations and stores the data photographed by the CCD in a physical memory on the computer. A suitable electronic format is used.

In addition to hardware, the microcomputer has specific software that is designed to properly manage the hardware. These software scans are quite complex and have been developed in some programming languages that bring together the efficiency of managing the machine and the software sets themselves with agility and speed.

Image Visualization, Treatment, and Analysis

The airglow image files are collected and stored as *.tif files. Each of these images is an array of 1024 x 1024 elements (the number of elements depends on the resolution of the CCD). Consequently, an element of these arrays is one pixel. The information contained in each pixel refers to the intensity of airglow that the corresponding CCD cell has received. The information recorded in the matrix elements varies on a scale from 0 to 65536 degrees gray, where 0 corresponds to the absence of light and 65536 to maximum intensity. UNIVAP All-Sky Data Analysis (UASDA), shown in

Figure 18, has been developed at the UNIVAP to study airglow images obtained from all-sky imaging systems. The program has several useful features incorporated into it. It is used for the visualization, calibration, and linearization of airglow images among other features. And in Figure 19, a lecturer from the Space Physics Laboratory in practical class helps students to disassemble and mount an all-sky imaging system in a dark room.

Appendix D

Ionosonde

An ionospheric sounder or ionosonde is the oldest ground-based experimental technique for investigating the terrestrial ionosphere utilizing radio waves. It is a variable frequency radar that transmits a signal vertically with frequencies that vary from 1 to 30 MHz. It is used primarily to determine the electron density profile of the ionosphere. The ionosonde measures the time of flight of the signal when sent from the transmitter and is received by the receiver after reflection from a layer in the ionosphere. The ionosonde is limited, in that it can only sound the ionosphere up to the F-layer peak height from the bottomside. As a result, there is a lack of information above the peak height at any time from the ground-based sounder. The majority of the ionospheric studies done with ionosonde have been done from the ground, as such the results discussed have been from the bottomside ionosphere. Notwithstanding, there is a satellite-based ionospheric observation that mitigates to some extent the limitation of sounding the ionosphere using a ground-based sounder. The satellite-based ionosonde provides information at the topside – above the plasma density peak only. Thus, to get sounding information of the entire ionosphere (topside and bottom side), and to get a complete profile, there has to be a combined observation from both types of ionosondes. The topside sounding helps to study spatial variability, but temporal variability is not visible with this method. Ionosonde operates on the principle of total reflection of radio signals from a reflecting layer in the ionosphere.

Ionosonde operation principle

The ionosonde operates on the reflection of electromagnetic signals (see Table 2). These signals are transmitted at different frequencies from a transmitter on Earth toward the ionosphere. The echoes are directed to a receiver at some point on Earth. These signals travel to ionospheric heights where the transmitted radio wave frequency f equal to the local plasma frequency f_p reflected towards a receiver on Earth. The plasma frequency (f_p) is related to the electron density (N_e) of the reflecting layer as

$$f_p = \sqrt{\frac{1}{2\pi}\left(\frac{N_e e^2}{m_e \varepsilon_o}\right)} \tag{35}$$

Substituting the constants with their respective values gives

$$f_p = 9(N_e)^{1/2}\ \text{MHz} \tag{36}$$

The plasma density can then be determined as

$$N_e = 1.24 \times 10^4\, f_p^{\ 2} \tag{37}$$

Increasing electron density with height in the ionosphere corresponds to higher values of plasma frequency. As the electron density increases with height in the ionosphere, the value of plasma frequency (transmitted radio frequency) at which reflections take place also increases. Since the peak electron density in the ionosphere is a few times 10^6 cm $^{-3}$, the plasma frequency $f_p \leq 12\ \text{MHz}$ (PILLAT; FAGUNDES; GUIMARÃES, 2015). Transmitted radio signals with frequencies above the peak plasma frequency corresponding to peak plasma density, will penetrate through the ionosphere and escape into outer space without being reflected by any of the ionospheric layers. However, a dense E region (like Sporadic E) can absorb all the transmitted radio frequencies and prevent them from reaching the F-layer. The penetration frequency, which is the lowest frequency that can penetrate the ionospheric layer, can provide a measure of the electron density at the peak of the ionosphere.

By analyzing the received echo between the transmitted and received signals, the height called the virtual height ($h'f$), of the ionosphere at which the reflection happens, can be inferred. This height is not the actual height at the point of reflection but the height that would result if the signal were sent at the speed of light in a vacuum. As the ionosphere is not a vacuum, the velocity of the transmitted radio waves in the ionosphere cannot be equal to the speed of light in a vacuum. The virtual height can be converted into real height in vertical sounding (incidence) if required. The expression for the virtual height is stated as

$$h'f = \frac{c\Delta t}{2} \tag{38}$$

Where Δt is the time of flight of the signal, c is the speed of light in a vacuum and since the group velocity of the radio waves is less than the velocity of light in the ionosphere due to the presence of free electrons in their path, the virtual height is always greater than the actual height. Hence, the virtual height $h'f$ is always greater than the real height. Figure 65a is a schematic representation of ionospheric sounding using an ionosonde where radio signals of varied frequencies are sent vertically from the transmitter and upon contact with an ionospheric layer with equal frequency, the signal is reflected. After reflection at the ionosphere, the signal is received at the receiving antenna. Figure 65b shows a typical nighttime ionospheric plasma density profile and the height at which the frequency signal equal to the plasma frequency will be reflected. Figure 65c shows the transmitted signal and the echo received at 7 MHz from ~ 280 km altitude with Figure 65d showing a typical ionospheric profile on an ionogram.

Figure 65: a) Schematic demonstration of vertical ionospheric sounding, b) typical nighttime ionospheric profile and height at which signal 7 MHz frequency will be reflected, c) diagram showing transmitted and reflected signal, and d) typical nighttime F-layer profile on the ionogram.

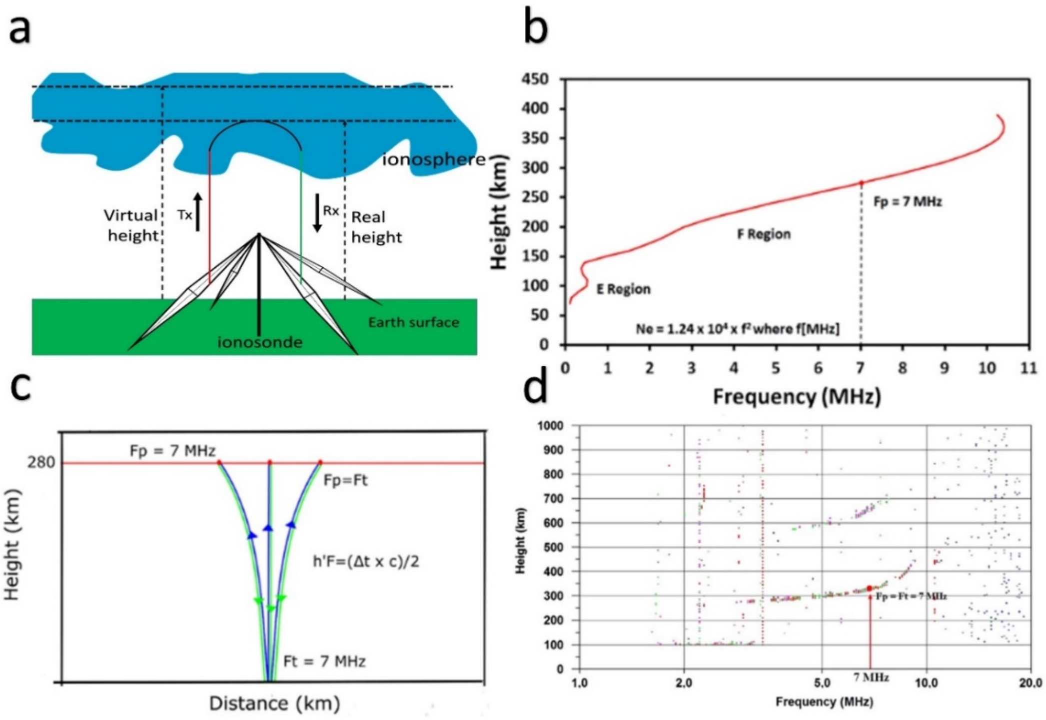

SOURCE: Adapted from PILLAT; FAGUNDES; GUIMARÃES (2015).

The plot of f versus $h'f$ produces what is known as the ionogram. Ionograms are scaled or analyzed for the different ionospheric parameters like Virtual height ($h'f$) of the ionospheric regions, critical frequency ($foF2$), and height of maximum electron density ($hpF2$), etc. and to detect the occurrence Spread-F. Figure 66 shows a generic ionogram depicting the E, F1, and F2 layers. It also shows the critical frequencies and virtual heights of these layers. Figure 67 and Figure 68 show ionograms from the CADI ionosonde located at Araguatins in Brazil. The different regions, structures, and parameters have been marked in the figures. The E region is visible at ~100 km (Figure 67). The separation between F1 and F2 can be clearly observed at ~ 325 km (Figure 67). In Figure 68, the Es is observed at ~ 120 km and the signature of ESF is visible.

Figure 66: A generic ionogram showing parameters for the layers of the ionosphere.

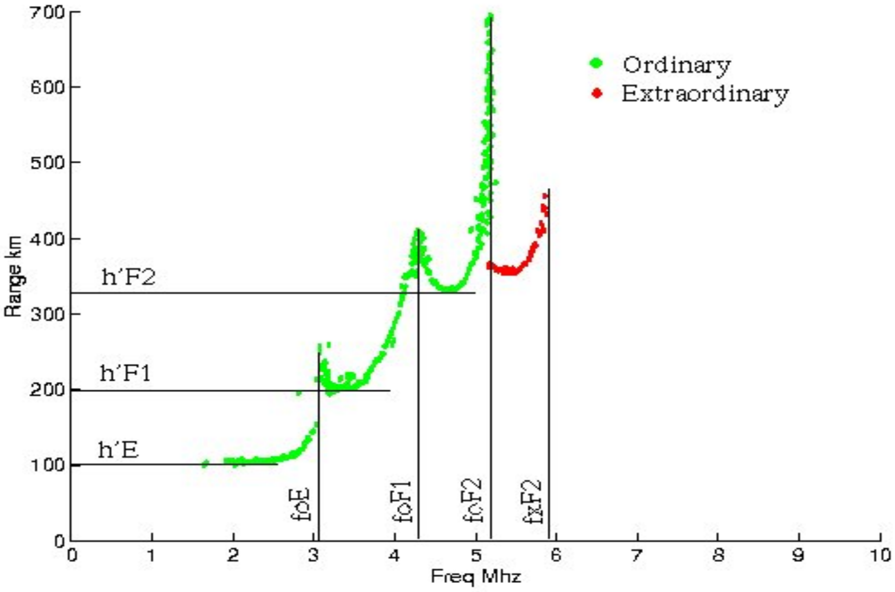

SOURCE: (BAMFORD, 2000).

Figure 67: UDIDA interface showing some ionospheric layers and parameters manually selected by the user.

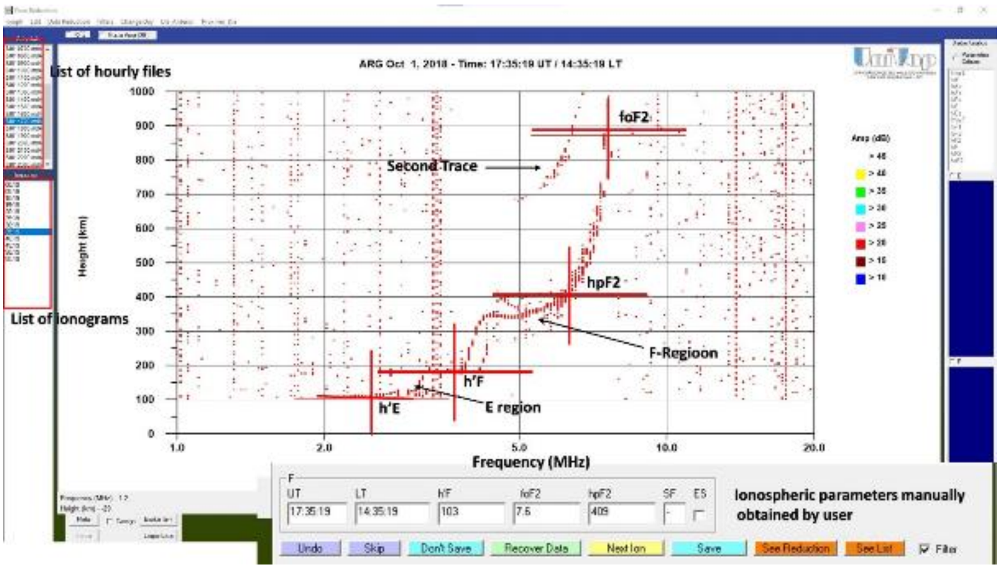
ARG Oct 1, 2018 - Time: 17:35:19 UT / 14:35:19 LT

F

UT: 17:35:19

LT: 14:35:19

h'F: 103

foF2: 7.6

hpF2: 409

SF: -

ES: ☐

☑ Filter

SOURCE: Author.

Figure 68: Ionogram showing ESF and Es occurrence.

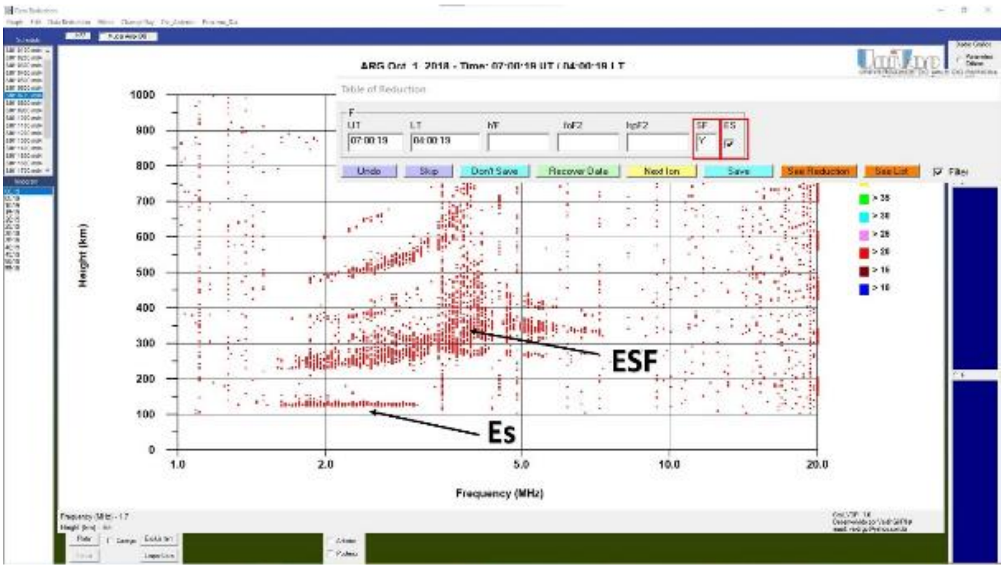

ARG Oct 1, 2018 - Time: 07:00:18 UT / 04:00:18 LT

Table of Reduction

F

UT: 07:00:19
LT: 04:00:19
hF:
foF2:
hpF2:
SF: Y
ES: ☑

SOURCE: Author.